Development of Neutron Tagging Algorithm and Search for Supernova Relic Neutrino in SK-Gd Experiment

September, 2023

Masayuki HARADA

Graduate School of
Natural Science and Technology
(Doctor's Course)
OKAYAMA UNIVERSITY

OKAYAMA UNIVERSITY

Abstract

Graduate School of Natural Science and Technology
Doctor's Course

Doctor of Philosophy

Development of Neutron Tagging Algorithm and Search for Supernova Relic Neutrino in SK-Gd Experiment

by Masayuki Harada

Observing neutrinos originating from supernovae is vital for deciphering the explosion mechanisms of core-collapse supernovae. Specifically, detecting supernova relic neutrinos (SRNs) can elucidate these mechanisms as well as the cosmic star formation history. The predominant signal within the SRN energy region corresponds to the inverse-beta decay ($\bar{\nu}_e + p \to e^+ + n$).

The Super-Kamiokande experiment, currently the most sensitive neutrino detector for the SRN energy region, has introduced the delayed coincidence method to the event selection using a neutron capture signal. This improvement has resulted in a more stringent upper limit. For the first discovery of SRN, the SK-Gd experiment was proposed in 2004. In the SK-Gd experiment, the SRN signal efficiency is significantly improved by loading gadolinium (Gd) in the detector tank. Gd has the largest cross-section for the thermal neutron capture among natural elements and emits a total of about 8 MeV gamma rays during the thermal neutron capture. This key advantage strengthens the correlation between the prompt positron and delayed neutron signal with enhanced neutron detection efficiency.

The SK-Gd experiment with about 0.011% mass concentration of Gd started in July 2020 and operated until May 2022. At first, an algorithm for detecting the neutron signal in SK-Gd is newly introduced. The algorithm is evaluated by the newly constructed Monte-Carlo simulation and neutron source measurement. Consequently, the neutron tagging efficiency is estimated to be 40.2%, with an uncertainty of 8.7%.

After that, the initial search was conducted using data from 552.2 days SK-Gd operation. This analysis employed the newly constructed neutron detection algorithm and Monte Carlo simulation. After eliminating the major background events, the remaining were consistent with the expected background within 1.1σ according to the p-value test across all investigated energy bins. In the absence of an SRN signal in this search, the observed and expected upper limits of SRN fluxes were respectively extracted to be 0.3–32.3 and 0.3–49.2 $\mathrm{cm}^{-2}\,\mathrm{sec}^{-1}\,\mathrm{MeV}^{-1}$, depending on the energy bins. These limits are commensurate with the most stringent limit determined by the search result in a pure-water phase of Super-Kamiokande.

For prospects, pragmatic improvements to the detector and analysis are contemplated for the SK-Gd experiment. The future sensitivity of the SK-Gd experiment is examined by assuming these enhancements. To demonstrate a potential approach for extracting physics parameters from the SRN flux, the formation rate of black holes and heavy neutron stars are highlighted.

Acknowledgements

I would like to express my gratitude to all those who supported me. First of all, I would like to express my sincere gratitude to my adviser, Prof. Yusuke Koshio, for giving me the great opportunity to study neutrino physics. I have learned a lot of things, not only physics but also the attitude toward research. We discussed physics, analysis, and so on. He not only taught me but also often had discussions. Also, he gave me several opportunities to visit European countries and the US and attend and make presentations at several conferences. Also, he introduced me to delicious foods in each country we went to. All of those experiences are wonderful and made me grow as a researcher. This thesis would never be without his kind comments and detailed suggestions.

I will never forget to thank those who worked with me on the analysis, Prof. Masayuki Nakahata, Prof. Hiroyuki Sekiya, Prof. Yasuhiro Nakajima, Dr. Guillaume Pronost, Dr. Alberto Giampaolo, Dr. Hiroshi Ito, and Dr. Sonia El Hedri. Their advice was always accurate and made me realize new insights. I owe my gratitude to the water team who operated the first Gd loading with me, Prof. Hiroyuki Sekiya, Prof. Yasuhiro Nakajima, Prof. Motoyasu Ikeda, and Prof. Kiseki Nakamura. I learned a lot from the hard work of everyone on site. I will never forget the days when I continued to knock on the pipe (and the impression when Nakajima-san found a yura-yura swing machine). I would like to thank Dr. Yuuki Nakano. He told me so much knowledge about low-energy physics analysis in SK. Not only that, he invited me to dinner and parties many times. A special gratitude I give to Dr. Takatomi Yano. We had many chances to discuss about Am/Be calibration analysis. I feel sorry that I was not able to go to Kamioka for calibration during the COVID period. But he took a lot of calibration data and shared me. I also would like to thank the people who worked with me in Kamioka, Sonoda-san, Akutsu-san, Takenaka-san, Okamoto-san, Imaizumi-kun, Chen-kun, Okada-kun, Nagao-kun, Han-kun, Shibata-kun, Izumiyama-kun, Shinoki-kun, Miki-kun, Kanemura-san, Watanabe-kun, Shimizu-kun, Kaneshima-kun, Kashiwagi-san, Yoshida-kun, Tomiya-kun, Shima-san, Shigeta-san, Kochi-kun, and Kaminaga-san. Although the Kamioka site is really isolated from the city, I had a pretty fun moment in Kamioka thanks to them. We enjoyed a lot of parties in Kenkyu-to, and driving to Toyama to have nice food with them. Especially, I was able to refresh myself by having many online drinking parties with colleagues in the same grade. I would like to say thank you to all Super-Kamiokande collaborators. All the people kindly lectured me when I had a question about even the basics of analysis, computing, etc.

I am grateful to the supernova theorists, Prof. Yudai Suwa, Prof. Ken'ichiro Nakazato, Prof. Kosuke Sumiyoshi, Prof. Shunsaku Horiuchi, and Dr. Masamitsu Mori. They have given me great theoretical insights since I started studying the supernova by joining the nuLC group.

I would thank the people who often had parties. Kaito Hagiwara, Yosuke Ashida, Hirotaka Nagata, and Toshiaki Horai. We had a number of times of the online and offline parties. Hagiwara-san is my first colleague who did the same research. We had a lot of discussions about the Geant4 and SKG4. That time was fun, like playing a game. Ashida-san told me about essential things of the SRN analysis. In addition to giving me advice about research, we enjoyed some things like parties and playing games. Nagata-san is a really kind and sincere person. Even though we were not in the lab during the same period, he talked to me a lot. Horai-san is the only colleague in the same grade. He had always taken care of deadlines and tasks of our homework and assignments. My attitude towards life as a PhD was very much based on him.

I would like to offer my special thanks to my friends at Okayama University, Wataru Hosoda, Yuji Kogame, Shotaro Nakano, and Takeshi Takahashi. We made some trips and on/off-line parties even after they graduated and went away from Okayama and were under a severe situation with COVID. They are the only friends with whom I can talk about research and physics other than researchers. I will never forget our graduate trip to Italy.

I would like to express my sincere gratitude to my club activity members of 'Five Stars' and 'Perfetto Partita.' The time spent playing basketball and playing with them was very relaxing.

I would like to thank everyone who worked with me at Okayama University, Hino-san, Sakai-san (Sakee-shi), Nakanishi-san, Shiraishi-kun, Tano-san, Tada-san, Takeya-kun, Higashi-kun, and Homma-san. Of course, I also would like to express my gratitude to all the past members of the lab. group and secretaries, Shintaro-san, Xu-san, Fukuda-san, Hagiwara-san, Yamasu-san, Takahira-san, Nakamura-san, Horai-san, Okada-kun (Oka-D), Wenjie, Kitagawa-kun, Tanaka-kun, and Shikaras-kun. I am very happy that I could join this group. I am also particularly grateful for the kind support to those who have previously or currently belonged to the Astro-physics Laboratory, Prof. Makoto Sakuda, Prof. Hirokazu Ishino, Ou-san, Pretam, Mandeep, Kida-san, Komatsu-san, Hidehira-san, Sudo-san, Tanaka-san, Yanagisawa-kun, Toda-kun, Nakao-kun, Nakajima-kun, Takase-kun, Nagano-kun, Kazehaya-kun, Doi-kun, Ishizaka-kun, Koeda-san, and Nagatsuna-san.

I owe my gratitude to my local friends, Kazuki Abe and Kaori, Jun'ichi Sakamoto, Kohei Yamasaki, Hiroyoshi Yamaoka, and Atsushi Nara. They gave me a lot of valuable time without research. That made me relax and have a fun time other than the research activity.

In addition, am grateful to everyone who involved me. I was able to enjoy my research life during the doctor period and write this thesis without feeling tired because of the support of my colleagues, including many professors, researchers, and friends. The years I spent with everyone were extremely fulfilling and enjoyable.

The works in this thesis have been achieved with support from the JSPS Young Scientist Fellowship (JP20J20189: "Search for Supernova relic neutrinos in Super-Kamiokande experiment").

At the end of acknowledgment, I would like to express my deepest gratitude to my family. In particular, my parents and my sister. They always supported me for a long time. Finishing this thesis wouldn't have been possible without all of you. Thank you very much!

Contents

1 Introduction **1**
1.1 Supernova Explosion . . . 1
1.1.1 Explosion Types and Mechanism Overview . . . 1
1.1.2 Explosion Mechanism of Core-Collapse Supernova . . . 2
1.1.3 Neutrinos from Core-Collapse Supernovae . . . 5
Neutrino Oscillations . . . 5
Neutrino Emission from Core-Collapse Supernova . . . 8
Neutrinos Observation from SN1987A . . . 10
1.2 Diffuse Supernova Neutrino Background . . . 11
1.2.1 Formulation of SRN Flux . . . 11
1.2.2 Contribution to the SRN flux . . . 12
Neutrino Oscillation Effects . . . 12
Modeling of Galaxy Evolution . . . 13
Other Contributions to the SRN Flux . . . 14
1.2.3 Flux Predictions . . . 15
1.3 Current Status of SRN Search . . . 17

2 Super-Kamiokande **21**
2.1 Detection Principle . . . 21
2.2 Super-Kamiokande Detector . . . 22
2.2.1 Detector Overview . . . 22
2.2.2 History of SK phase . . . 23
SK-I . . . 23
SK-II . . . 24
SK-III . . . 24
SK-IV . . . 24
SK-V . . . 24
SK-VI . . . 25
SK-VII . . . 25
2.2.3 ID PMT . . . 25
2.2.4 OD PMT . . . 26
2.2.5 Compensation Coils . . . 27
2.3 Water and Air purification system . . . 28
2.3.1 Water purification . . . 28
Water system at SK-IV . . . 28
Water system from SK-V . . . 29
2.3.2 Air purification system . . . 30
2.4 Electronics and Data Acquisition . . . 30
2.4.1 Electronics and DAQ from SK-IV . . . 30
2.4.2 Software Trigger . . . 31

3 Simulation **33**
3.1 Simulation for High-Energy Neutrino Event . . . 33
3.1.1 Atmospheric neutrino flux . . . 33
Primary cosmic-ray . . . 33
Hadronic interaction . . . 34
Neutrino Flux at the SK . . . 34
3.1.2 Neutrino Interaction . . . 36
Elastic and Quasi-elastic Scattering . . . 38
CC Meson Exchange Interaction . . . 38
Single Meson Production . . . 39
Deep Inelastic Scattering . . . 39
Coherent pion production . . . 39
3.2 Simulation for the IBD-like Event . . . 40
3.2.1 DSNB Signals MC creation . . . 40
3.3 Detector Simulation . . . 40
3.3.1 Particle tracking . . . 40
3.3.2 Optical Photon Emission and Tracking . . . 41
3.3.3 PMT response . . . 41

4 Event Reconstruction **43**
4.1 Low Energy Event Reconstruction . . . 43
4.1.1 Vertex reconstruction . . . 43
4.1.2 Direction Reconstruction . . . 45
4.1.3 Effective hit calculation . . . 46
4.1.4 Energy reconstruction . . . 49
4.1.5 Cherenkov angle reconstruction . . . 50
4.2 Muon Event Reconstruction . . . 50
4.2.1 PMT hit selection . . . 52
4.2.2 Initial Entry Point . . . 53
4.2.3 Direction Reconstruction . . . 53
4.2.4 Event classification . . . 55
Corner-clipping muons . . . 55
Stopping muons . . . 56
Multiple muons . . . 57
Classification summary . . . 58

5 Detector Calibration Measurement **61**
5.1 ID Detector Calibration . . . 61
5.1.1 High-Voltage determination . . . 61
5.1.2 Relative Gain Measurement . . . 62
5.1.3 Absolute Gain Measurement . . . 63
5.1.4 Relative QE measurement . . . 63
5.1.5 Timing Response Calibration . . . 64
5.2 Photon tracking . . . 67
5.2.1 Water Transparency Measurement . . . 68
5.2.2 Top-Bottom Asymmetry Measurement . . . 71
5.2.3 Photon Reflection on the Material Surface . . . 72
Reflection on PMT Surface . . . 72
Reflection on Black Sheet . . . 73
5.3 Energy Scale Calibration using LINAC . . . 73

6 Development of Neutron Tagging in SK-Gd **77**
6.1 Neutron Tagging Algorithm . . . 77
6.1.1 Neutron Tagging in Pure Water . . . 77
6.1.2 Neutron Tagging in SK-Gd . . . 77
6.1.3 Delayed Neutron Search . . . 78
Injection of Realistic Noise into MC . . . 78
Pre-selection . . . 78
Cut-based neutron selection . . . 78
6.1.4 Neutron Tagging Efficiency . . . 80
6.1.5 Misidentification rate . . . 81
6.2 Americium-Beryllium Calibration . . . 83
6.2.1 Measurement . . . 83
Source structure . . . 84
Data taking . . . 85
6.2.2 AmBe MC simulation . . . 85
Primary Particles . . . 86
Parameter tuning for BGO scintillator . . . 86
MC production procedure . . . 88
6.3 Neutron Tagging Efficiency Evaluation with AmBe Source . . . 89
6.3.1 Prompt event selection . . . 90
6.3.2 Neutron Signal Search . . . 90
6.3.3 Tagging Efficiency Estimation . . . 91
6.4 Discussion on Tagging Efficiency Measurement . . . 93
6.4.1 Random neutron intensity . . . 94
6.4.2 Probability of prompt event from neutron . . . 96
6.4.3 Trigger efficiency . . . 97
6.4.4 Result . . . 97
6.5 Systematic Uncertainty Extraction . . . 98
6.5.1 Prompt event selection . . . 98
6.5.2 Delayed event selection . . . 98
Vertex reconstruction goodness . . . 99
Direction reconstruction goodness . . . 99
Reconstructed energy . . . 99
Vertex resolution . . . 100
6.5.3 MC simulation settings . . . 101
Gd concentration . . . 102
Gamma-ray emission model of neutron capture on Gd . . . 102
Neutron excited state fraction . . . 102
Neutron energy spectrum of the first excited state . . . 103
6.5.4 Position Dependence . . . 104
6.5.5 Total Systematic Uncertainty . . . 104
6.6 Result . . . 104
6.6.1 Neutron Tagging Efficiency . . . 104
6.6.2 Time variation . . . 105
6.6.3 Conclusion . . . 106

7 Search for Diffuse Supernova Neutrino Background in SK-Gd **107**
7.1 Data Set . . . 107
7.2 Signal Energy Window . . . 107
7.3 Overview of Background Events . . . 108
7.3.1 Radioisotope Decays from Muon Spallation and Lithium-9 . . . 108
Isotopes accompanied by neutron . . . 108
7.3.2 Atmospheric Neutrinos . . . 110
7.3.3 Reactor Neutrinos . . . 112
7.3.4 Accidental Coincidence background . . . 114
7.4 MC Creation . . . 114

8 Event reduction **115**
8.1 First Reduction: Pre-cut . . . 115
8.1.1 Nonphysical Event and Invalid Triggered Event Cut . . . 115
8.1.2 Cosmic-ray muon-induced event cut . . . 115
8.1.3 Fiducial volume cut . . . 116
8.1.4 Fit-quality cut . . . 116
8.1.5 Trigger Requirement . . . 116
8.2 Second Reduction: Spallation Cut . . . 117
8.2.1 1-ms cut . . . 118
8.2.2 Multiple Spallation Cut . . . 119
8.2.3 Neutron Cloud Cut . . . 119
8.2.4 Spallation Likelihood Cut . . . 122
Spallation variables . . . 122
PDF and Likelihood . . . 124
8.2.5 Spallation Box Cut . . . 125
8.2.6 Spallation Cut Efficiency Estimation . . . 127
Efficiency for random event . . . 128
Efficiency for solar neutrino event . . . 128
Spallation remaining rate . . . 129
Efficiency for the Lithium-9 . . . 130
ROC curve . . . 130
Efficiencies above 16 MeV . . . 132
8.3 Third Reduction: Positron Event Selection . . . 133
8.3.1 Cherenkov angle . . . 133
8.3.2 Ratio of charge over the number of hits . . . 134
8.3.3 Pion likeness . . . 134
8.3.4 Pre-PMT activities and post-PMT activities . . . 135
8.3.5 Remaining Radioactivity cut using Effective wall distance . . . 136
8.3.6 Systematic Uncertainty Estimation with LINAC data . . . 137
Cherenkov angle . . . 138
Pion likeness . . . 139
q50/n50 . . . 139
8.3.7 Reduction summary . . . 139
8.4 Forth Reduction: Neutron Tagging . . . 139
8.4.1 Neutron misidentification rate . . . 140
8.4.2 Neutron tagging efficiency . . . 142
8.4.3 Tagged neutron multiplicity . . . 142
8.5 Reduction Summary . . . 142
8.5.1 Optimization of Spallation Cut Criteria . . . 142
8.5.2 Signal Efficiency . . . 143

9 Background Estimation **147**
9.1 Atmospheric neutrinos . . . 147
9.1.1 NCQE event . . . 147
Neutrino flux and flux shape . . . 148
Cross-section . . . 148
Neutron tagging efficiency and neutron multiplicity . . . 149
Spectrum shape of the observed event . . . 149
Total systematic uncertainty . . . 152
9.1.2 Non-NCQE like interactions . . . 153
9.2 Lithium-9 . . . 155
9.3 Reactor Neutrinos . . . 155
9.4 Accidental Fake background . . . 155
9.5 Expected Background Spectrum . . . 156

10 Results **159**
10.1 Search Result . . . 159
10.2 Upper Limit Extraction . . . 161
10.2.1 Upper limit on the number of signal events . . . 161
10.2.2 Flux Upper Limit Calculation . . . 162

11 Discussion and Conclusion **165**
11.1 Future Prospects on the SRN Search . . . 165
11.2 Future Sensitivity Calculation . . . 166
11.3 Limitation to the Failed Supernova Rate . . . 168
11.4 Conclusion . . . 172

A Theoretical prediction of SRN flux with integrated bins **173**

B Spallation Distributions **175**
B.1 Neutron cloud distributions . . . 175
B.2 PDF distributions . . . 182
B.3 ROC Curves for each energy bin . . . 186
B.4 Correlation between Spallation and Li9 efficiency . . . 187

C Third Reduction Cut Variables **189**
C.1 Effective wall distance distribution . . . 189
C.2 Third reduction variables in LINAC data . . . 190
C.2.1 Cherenkov Angle . . . 190
C.2.2 Cherenkov Angle . . . 191
C.2.3 Pion likeness . . . 192

List of Figures

1.1 Classification of the supernovae by these spectra. 2
1.2 Schematic of CCSN explosion procedure. Explosion proceeds from the smaller number. Neutrino-heating is assumed to be the mechanism for shockwave revival. 4
1.3 Typical theoretical calculation of timing development of neutrino luminosity and average energy [1]. 10
1.4 Timing and energy distribution of neutrinos observed by Kamiokande-II and IMB experiments. The figure is taken from [2]. 11
1.5 CSFRD distribution as a function of redshift. This plot is taken from [3]. 14
1.6 Difference of neutrino number spectrum of CCSN with $30M_{\odot}$ and $Z = 0.02$ for a progenitor depending on the shock revival time. The left, central, and right plots show the spectra corresponding to $\nu_e, \bar{\nu}_e$, and $\nu_x(\nu_\mu, \bar{\nu}_\mu, \nu_\tau, \bar{\nu}_\tau)$. This figure is sourced from [3]. 15
1.7 Summary of modern theoretical prediction of SRN flux [4, 5, 6, 7, 8, 3, 9, 10, 11, 12, 13, 14, 15, 16]. 17
1.8 Effective cross-section including the resolution and threshold effect of certain detectors for each process below 60 MeV. This plot is taken from [17]. 18
1.9 Upper limits on $\bar{\nu}_e$ flux from SK, KamLAND, and the Borexino experiment [18]. This figure is taken from [19]. 19
1.10 Upper limits on $\bar{\nu}_e$ flux from the SK [20]. 19

2.1 Schematic of view of the SK detector (cutaway view). This figure is taken from [21]. 22
2.2 Overall schematic of SK (Left) and magnified to each face of the support structure (Right)[22]. 23
2.3 Image of the shockwave prevention case for 20-inch PMT 24
2.4 Overview of Hamamatsu R3600 used for SK ID PMT [22]. 26
2.5 Wavelength dependence of QE (top), distribution of relative transit time (bottom left), and ADC charge count distribution(bottom right) for Hamamatsu R3600 PMT [22]. 26
2.6 Relationship between ID PMT and OD PMT [23]. 27
2.7 Schematic view of compensation coils wounding the SK tank [24]. . . . 28
2.8 Schematic diagram of the water purification system in SK-IV. This figure is taken from [25]. 29
2.9 Schematic of SK-Gd water system. This figure is taken from [26]. . . . 30
2.10 Schematic of the DAQ system with QBEE[27]. 31
2.11 Schematic of the DAQ system with QBEE[28]. 32

3.1 Illustration of atmospheric neutrino production. 34

3.2 Comparison between HARP data and the theoretical calculations of JAM and DPMJET-III for the cross-section of pion production. The figures are taken in [29]. 35
3.3 Comparison of muon flux between the theoretical calculations and experimental data. Dashed line represents the sum of the error in the calculation and observation at Mt. Tsukuba (blue squares), at Mt. Norikura(red triangles) using the BESS detector, and at CERN using the L3 detector(black circles). Results from the DEIS experiment [30] and MUTRON experiment [31] are presented as well. The figure is taken from [32]. 36
3.4 Zenith angle dependence of atmospheric neutrino flux, averaged over all azimuthal angles, for Kamioka. Here the θ is the zenith direction of coming neutrinos. The figure is taken from [29]. 36
3.5 Comparison of the atmospheric neutrino flux for some calculations: Honda prediction(solid red), previous Honda model(blue dotted-dashed line) [33], Bartol model[34], and the Fluka model[35]. The figure is taken from [29]. 37
3.6 Cross-section of CCQE scattering of muon neutrino (left panel) and anti-muon neutrino (right panel). Lines denote the NEUT calculation for the free target (solid) and the bound target(dashed). Data points are taken from ANL (crosses), BNL (triangles), SKAT (stars), Serpukhov (asterisks), and GGMs (circles). The figures are taken from [36]. 38
3.7 Comparison between measured data from ANNRI experiment and MC with ANNRI-Gd model. This figure was taken from [37]. 41

4.1 PDF distribution for the PMT hit timing residuals. Additional peaks surrounding 30 and 100 ns are caused by late pulse, which is caused by the photoelectrons reflected at the dynode and further incidence. . . . 44
4.2 Vertex resolution as a function of true electron energy for SK-I, II, III, IV by dotted, dot-dashed, dashed, and solid lines, respectively. This figure is taken from [38]. 44
4.3 Energy dependence of the directional resolution. This plot was taken from [39]. 45
4.4 Illustration of the definition of $\angle^i_{\rm uniform}$ and $\angle^i_{\rm data}$. Blue circles exhibit the PMT hits, and gray circles indicate the expected point if the hits are equally distributed at an azimuthal angle. 46
4.5 Definition of the incident angle θ and ϕ. This plot is referred from [40]. 48
4.6 $S(\theta, \phi)$ distribution for barrel PMTs (left) and top and bottom PMTs (right). The plots are taken from [40]. 48
4.7 Illustration defining the calculation of θ. Circles comprise unit vectors from the reconstructed vertex to the three PMT hits. 51
4.8 Example of θ distribution of three-hits combinations for electron-, and muon-like events. Plots are taken from [41]. 51
4.9 Illustration of muon categories for single-through (top, left), stopping (top, right), multiple (bottom, left), and corner-clipping (bottom, right) muons. 52
4.10 Illustration of the concept for the counting of $N_{\rm nn}$ with the case of $N_{\rm nn} = 5$ in the central PMT. 53
4.11 Flowchart of Muboy about the direction reconstruction with a part of event classification. 56

4.12 Histogram of typical dQ/dx distribution for considering the length along the muon track as the horizontal axis. This figure is taken from [42]. 57
4.13 Muon types and reconstruction goodness. The term 'single' represents the single-through muons. 59

5.1 Positions of the Standard PMTs (left) and schematic of the grouping of the PMTs (right). Red points indicate the location. The figures are taken from [43]. 62
5.2 Appearance of the Ni-Cf source geometry. The figures are taken from [43]. 63
5.3 Charge distribution taken using Ni-Cf source used in SK-III. The figures are taken from [43]. 64
5.4 Hit rate distribution as a function of PMT positions measured in SK-VI. Top: barrel PMTs, with the z-position of PMTs plotted in the horizontal axis. Bottom: two plots indicate top (left) and bottom (right) PMTs, where the horizontal axis denotes the square of the radial distance on the x-y plane. Black points indicate the data, and red points display MC. 65
5.5 Schematic view of the timing calibration system. The figures are taken from [43]. 66
5.6 Typical scatter plot of the timing and the charge. For the vertical axis, larger (smaller) T corresponds to the earlier (later) hits. The figures are taken from [43]. 67
5.7 Timing distribution and the function resulting from the fitting for the Qbin = 14. The figures are taken from [43]. 67
5.8 Distribution of timing resolution as a function of the charge, measured during in SK-IV. The figures are taken from [43]. 68
5.9 Schematic of the laser measurement system. The analysis uses PMTs pertaining to five segmented barrel regions B1-B5 and the top. The figures are taken from [43]. 69
5.10 Best-fitted timing distribution of data and MC for each PMT region in SK-IV measurement. The circle with the black line represents the data, and the red line indicates the MC. Both are normalized by total observed photoelectrons. The top panel represents the PMTs at the top of the ID wall, whereas the second-to-bottom panels correspond to the five segmented barrel regions B1–B5, as displayed in Figure 5.9. The region between the two blue-solid lines on the left-hand side was used to fit the attenuation coefficients. The region between the two blue-solid lines on the right-hand was utilized in the PMT reflection measurement. The figures are taken from [43]. 70
5.11 Distributions of the coefficient as functions of the wavelength. Each point represents the Best-fitted coefficients for each laser wavelength and interaction. Red, blue, and magenta points and the lines represent the α_{abs}, α_{sym}, and α_{asym}, respectively. Circles (triangles) and solid (dot-dashed) lines of the Geant4-based (GEANT3-based) simulation result are described in Section 3.3. 71

5.12 Variation of the TBA during the SK-V and SK-VI, taken by the Ni-Cf source and Xe light source (top), and differences of TBA between both measurements and between data and MC for Ni-Cf source measurement (bottom). Thick dotted-dashed line indicates the 0.5% difference region. 72
5.13 Schematic of a laser light injector to measure black sheet reflectivity. The figure is taken from [43]. 73
5.14 Comparison between laser data and MC in the black sheet measurement. The three left panels show the ratio of the charge between reflected and direct incident light, and the right panels show the ratio between data and MC for the left plots, for the wavelength at 337 nm (top), 400 nm (middle), and 420 nm (bottom). The figure is taken from [43]. 74

6.1 Schematic diagram of the procedure of noise production. The contents with the blue characters and lines are simulated in the detector MC, while those with red characters and lines are appended later. 79
6.2 Illustration of the primary selection. Dashed line indicates the N_{200} threshold. 79
6.3 Distribution of the g_{vtx} (left) and g_{dir} (right) for signals from neutron capture on Gd (magenta) and proton (cyan), and noise (gray) candidates. The red arrows show the cut criteria. These distributions are normalized by area. 80
6.4 Distributions of the d_{prompt} for the signal from neutron capture on Gd (magenta) and proton (cyan), and noise (gray) candidates. Red arrow indicates the threshold. These distributions are area-normalized. . . . 81
6.5 Distributions of the reconstructed energy for the signal from neutron capture on Gd (magenta) and proton (cyan), and noise (gray) candidates. Red arrow indicates the cut criteria. These distributions are normalized by area. 82
6.6 Capture time distribution of the neutron MC and the fitting result. . 82
6.7 Time variation of ϵ_{mis}. Black-dotted line denotes the weighted mean value for the entire period, and the gray-shaded region indicates the standard deviation. 83
6.8 Major final state of ^{13}C. A de-excitation from the second excited state was not observed in the Kamioka AmBe source. 84
6.9 Appearance of the Am/Be source (left) and the four pieces of BGO scintillator crystals (right). 84
6.10 Appearance and schematic of 1BGO geometry (left) and 8BGO geometry (right). 85
6.11 Illustration of measurement points. Orange squares exhibit measurement points, and the darker blue circle denotes calibration holes, where $x = -1237, 35.3, 1080$ cm $\sim -12, 0, +12$ m. 85
6.12 Kinetic energy spectrum of the emitted neutron from each state, calculated as the combination referring measurements of Guarrini and Malaroda [44], and ISO8529-1 [45]. 86
6.13 Correlation between scintillation time constant for each component with BGO temperature. This figure is taken from [46]. 87
6.14 QISMSK distribution of the AmBe MC with 8BGO at the center point for various scintillation yield parameters. 87

6.15 QISMSK distribution of the 8BGO at center point data with some light yield setting. 88
6.16 Correlation between yield and QISMSK in MC. Black circles denote the MC peak and its deviation for each yield setting in Figure 6.15. Red line indicates the QISMSK peak for the data in Figure 6.14. . . . 88
6.17 QISMSK distribution for the data and best-fitted MC; n^0, n^1, and n^2 MC indicates the MC simulation for each excited state of ^{12}C. 89
6.18 QISMSK distributions for center data (top left), (X= −12 m, Z= −12 m) data (top right), and (X= +12 m, Z= 0 m) data (bottom) obtained by 8BGO AmBe measurement; arrows indicate the threshold criteria for each source position. 91
6.19 Distribution of the number of delayed candidates passing $N_{200} \geq 25$. . 92
6.20 Distributions of neutron selection variables. Each color-filled histogram exhibits the MC, and solid point represents the data, which is aligned with the statistical error. Red arrow indicates the cut criteria for neutron selection. These distributions are normalized by the number of prompt events. 93
6.21 Capture timing distributions for measured data (left) and MC simulation (right). Dotted line only displayed in the data plot represents the flat component evaluated by exponential fitting. 94
6.22 Illustration of emission of the random neutron. 94
6.23 The probability of thermal neutron capture in the SK with AmBe source geometry for 8BGO (top) and 1BGO (bottom). These probabilities were calculated based on the result of the five million neutron MC, which uses ENDF.VII.1 as a nuclear data library [47]. 96
6.24 QISMSK cut criteria and the data-MC difference in the neutron tagging efficiency as a function of the higher side (left) and lower side (right). 98
6.25 QISMSK cut criteria and the data-MC difference in neutron tagging efficiency. Color depicts the difference between data and MC from the nominal criteria. 99
6.26 Distribution of g_{vtx} for data and MC. Solid green line indicates the smeared cut threshold. Both plots are normalized by area. 100
6.27 Distribution of g_{dir} for data and MC. Solid green line indicates the smeared cut threshold. Both plots are normalized by area. 100
6.28 Distribution of reconstructed energy for data and MC. Solid green line denotes the smeared cut threshold. Both plots are normalized by area. 101
6.29 Distribution of the distance between reconstructed delayed event vertex and the source position for data and MC. Solid green line denotes the smeared cut threshold. Both plots are normalized by area. 101
6.30 Correlation between the time constant and Gd mass concentration (left), and the Gd capture fraction and Gd mass concentration (right). 102
6.31 Neutron kinetic energy spectra from the first state of ^{12}C based on ISO (black) and measured (red). 103
6.32 Neutron tagging efficiency for each measured point. 104
6.33 Neutron tagging efficiency as a function of the surrounding BGOs. Efficiency without BGO (0BGO) is only estimated by MC because it cannot be estimated for actual data. 105
6.34 Neutron tagging efficiency as a function of the surrounding BGOs. . . 106

7.1 Correlation between end-point energies and half-lives (left) and that between half-lives and yield (right) for spallation isotopes detected in the DSNB search window and generated by cosmic-ray muons in water. Red circles in both figures represent undergoing beta decay with neutrons. For the isotopes undergoing decay with neutrons, the yield includes the fraction of decay with neutrons. The fraction of these plots referred from [48]. . . . 110
7.2 Decay scheme of ^{9}Li based on PDG [49]. . . . 110
7.3 True and reconstructed electron kinetic energy for the β-decay of ^{9}Li. 111
7.4 Illustration of decay electron background. In the figure, the decay electron from an invisible muon produced via CCQE interaction of atmospheric neutrino is displayed. . . . 111
7.5 Illustration of the visible muon and pion background. In the figure, the visible muon and the decay electron produced via the CCQE interaction of atmospheric neutrino are displayed. . . . 112
7.6 Illustration of the electron background event via CCQE interaction of the atmospheric electron neutrinos. . . . 112
7.7 Illustration of the NCQE background event. . . . 113
7.8 Activities of Japanese reactor from Apr. 2018 to Sep. 2022; dashed line indicates 100% operation time. . . . 113
7.9 Expected neutrino energy flux from Japanese reactors at the SK site, considering the neutrino oscillation effect. . . . 114

8.1 Reconstruction goodness and reconstructed energy distribution for data (left) and signal MC (right). Vertical magenta line exhibits the energy threshold of 7.49 MeV, and the horizontal magenta line presents the g_{vtx} threshold. . . . 116
8.2 Illustration of muon concept for the spallation. . . . 118
8.3 Minimum distance between the SHE event and the low-energy event within $\pm$60 s, obtained from the SHE event and randomized vertex (left) and the subtracted distribution (right). . . . 119
8.4 Number of neutrons after muons for pre (black) and post (red) samples. 120
8.5 Time difference between muons and the SHE event. Each color exhibits the number of neutrons after muons. . . . 120
8.6 Distance between neutron cloud position and the SHE event. Each panel exhibits the difference in N_{ncloud}. . . . 121
8.7 Illustration of definition for the variables used in the neutron cloud cut. 121
8.8 Two-dimensional distribution of Δ_x, Δ_y, and Δ_z. Left column represents the pre-samples, and right column indicates the post-samples. Magenta lines indicate the cut criteria. These are clouds with $N_{\mathrm{ncloud}} \geq 10$. . . . 123
8.9 Two-dimensional distribution of $\log|dt|$ and Δl for the pre-sample (left) and the post-sample (right). Magenta lines are cut criteria in this plane. These are for clouds with $N_{\mathrm{ncloud}} \geq 10$. . . . 124
8.10 Illustration for variables related to spatial correlation 125
8.11 Random (red) and spallation (blue) PDFs for dt (top, left), ℓ_t (top, right), ℓ_l (middle, right), Q_{res} (middle, right), and Q_μ (bottom). These muons belong to the single through-going muons with the dt region of 0–0.05 s and the ℓ_t region of 0–300 cm. . . . 126

8.12 Spallation likelihood distributions of pre (blue) and post (red) samples, for misfit (top, left), stop (top, right), single through-going with dt = 0–0.05 sec (middle, left), and ℓ_t = 0–200 cm (middle, right), and multiple muons with dt = 0–0.05 sec (bottom left), and ℓ_t = 0–100 cm (bottom, right). These findings correspond to the reconstructed energy in the 8–10 MeV region. 127
8.13 Schematic of definition of $\theta_{\rm sun}$ and $\cos\theta_{\rm sun}$. 129
8.14 Correlation between $\varepsilon_{\rm random}$ and $\varepsilon_{\rm solar}$. 129
8.15 ROC curve representing the correlation between spallation remaining rate and random event efficiency for 8–10 MeV region. 131
8.16 Correlation between spallation remaining rate and lithium-9 event efficiency for 8–10 MeV region. 131
8.17 Mis-reconstruction of the Cherenkov ring owing to the multiple Cherenkov ring. 133
8.18 Distribution of the Cherenkov angle. Color plot describe the type of atmospheric neutrino interaction, and black line denotes the DSNB signal MC assuming the Horiuchi+09 flux model [10]. These are obtained from the events after only passing the first reductions. 134
8.19 Distribution of the $q50/n50$ with the linear (left) and logarithmic (right) for the vertical axis. Color plot exhibits the type of atmospheric neutrino interaction, and black line denotes the DSNB signal MC assuming the Horiuchi+09 flux model [10]. These are made from the events after passing only the first reductions. 134
8.20 Distribution of $\mathcal{L}_{\rm pion}$. Color plot denotes the type of atmospheric neutrino interaction, and black line exhibits the DSNB signal MC assuming the Horiuchi+09 flux model [10]. These are made from the events after passing only the first reductions. 135
8.21 Distribution of $N_{\rm pre}^{\rm max}$. Color plot exhibits the type of atmospheric neutrino interaction. These are made from the events after passing only the first reductions. 136
8.22 Distribution of $N_{\rm decay\text{-}e}$ with the linear (left) and logarithmic (right) for the vertical axis. Color plot exhibits the type of atmospheric neutrino interaction. These are made from the events after passing only the first reductions. 136
8.23 Illustration of definition of $d_{\rm eff}$. 137
8.24 Comparison of $d_{\rm eff}$ after 1st reduction between data and MC. 137
8.25 Comparison of Cherenkov angle distribution between data and MC (top) and the data/MC ratio (bottom) for the E =12 MeV LINAC run. 138
8.26 Comparison of $\mathcal{L}_{\rm pion}$ distribution between data and MC (top) and the data/MC ratio (bottom) for the E =12 MeV LINAC run. 139
8.27 Comparison of $q50/n50$ distribution between data and MC (top) and the ratio of data/MC (bottom) for the E =12 MeV LINAC run. 140
8.28 Distribution of $\epsilon_{\rm mis}$ as a function of the cut criteria for the $d_{\rm prompt}$ (left) and the $E_{\rm delayed}$ (right). Color for the left (right) plot exhibits the cut criteria of $E_{\rm delayed}$ ($d_{\rm prompt}$). 141
8.29 Time variation of $\epsilon_{\rm mis}$. Black-dotted line depicts the weighted mean value for the entire period, and the gray-shaded region indicates the standard deviation. Horizontal axis represents the same factor as that in Figure 6.7. 141

8.30 Distribution of number of tagged neutrons for the IBD MC and atmospheric neutrino MC, after first to third reductions, in the signal energy region. Histograms of atmospheric neutrino MC are stacked with each other. . . . 142
8.31 Signal efficiency as a function of kinetic energy E_{rec}. . . . 143

9.1 Total cross-section for neutrino (left) and antineutrino (right) for $^{16}\mathrm{O}(\nu, \nu'\mathrm{N})$ interaction. . . . 148
9.2 Average of the number of tagged neutrons in the T2K CC-dominant samples, as a function of reconstructed Q^2, for FHC (left) and RHC (right). Plots are taken from [41], and the original work was done by [50]. . . . 149
9.3 Neutron multiplicity distribution for $Q^2 < 0.25$ GeV^2 (upper left), $Q^2 = 0.25$–0.5 GeV^2 (upper right), $Q^2 = 0.5$–$0.0.75$ GeV^2 (bottom left), and $Q^2 = 0.75$–3.0 GeV^2. . . . 150
9.4 Illustration of the NCQE interaction and subsequent nuclear interactions. . . . 151
9.5 Reconstructed Cherenkov angle distribution in the T2K FHC (left) and RHC (right) measurements. These plots are recited from [51]. . . . 151
9.6 Weighting factor $\varepsilon_{\nu(\bar{\nu})}$ of neutrino (left) and antineutrino (right), each 2 MeV bin. . . . 152
9.7 Weighting factor $\varepsilon_{\nu+\bar{\nu}}$ each 2 MeV bin. . . . 153
9.8 Energy distribution before and after reweighting by $\varepsilon_{\nu+\bar{\nu}}$, after the third reduction. . . . 153
9.9 Energy spectrum in the side-band region of 31.49–79.49 MeV for the reconstructed kinetic energy. . . . 154
9.10 χ^2 distribution as a function of the scaling factor. . . . 154
9.11 Expected background spectrum with these total systematic uncertainties (hatched) for each 2 MeV bin. Dotted-dashed red line denotes the expected SRN signal based on [10]. . . . 156
9.12 Expected background spectrum with these total systematic uncertainty (hatched) for each merged bin (hatched). Dotted-dashed red line portrays the expected SRN signal based on [10]. . . . 157

10.1 Observed and expected background spectrum with these total systematic uncertainties (hatched) with linear scale (top) and logarithmic (bottom). The dot-dashed red line shows the expected SRN signal based on [10]. . . . 160
10.2 Toy MC result for calculating the p-value for each energy bin above 11.49 MeV (bottom, right). Red line exhibits the actual observed event in this analysis. . . . 161
10.3 N_{sig} distribution for $E_{\mathrm{rec}} = 9.49$–11.49 MeV bin as an example of N_{90}^{limit}. The region between $N_{\mathrm{sig}} = 0$ and $N_{\mathrm{sig}} = N_{90}^{\mathrm{limit}}$ contains 90% of the total of $N_{\mathrm{sig}} > 0$ events. . . . 162

10.4 Upper limits on the $\bar{\nu}_e$ flux. Solid lines denote the observed upper limit for SK-IV (blue), SK-VI (red), and KamLAND (green), respectively. Dot-dashed lines represent the expected sensitivity based on the expected background for SK-IV (black) and SK-VI (yellow). Gray-shaded region represents the range of the modern theoretical expectation. The expectation drawn in the figure includes DSNB flux models [15, 16, 14, 12, 11, 10, 9, 3, 8, 6, 5, 4, 52]. Ando+03 model was updated in [13]. 163

11.1 Expected future sensitivity for 9.3–11.3 MeV (left) and 11.3–13.3 MeV energy bins with various background conditions, such as nominal case (black), and further higher neutron tagging efficiency (red), 70% of NCQE background (green), 50% of the error on the NCQE background (blue), 50% of the error on the ^{9}Li (Orange), 50% of the CCQE background and their error (Magenta). Thick-dotted line denotes the most optimistic theoretical expected flux. In the 9.3–11.3 MeV region, the theoretical expectation is excluded from this figure as it is smaller than the sensitivity. 166

11.2 Expected future sensitivity for 13.3–17.3 MeV (left) 17.3–25.3 MeV (middle), and 25.3–31.3 MeV (right) energy bins with the same assumption as Figure 11.1; colors represent the assumptions listed in Table 11.1. Two thick-dotted lines exhibit the range of model expectations. 167

11.3 Event rate spectra of DSNB $\bar{\nu}_e$ for SK 22.5 kton water per year. The EOS model is assumed to be (a) Togashi EOS, (b) LS220 EOS, (c) Shen EOS, respectively. Colors correspond to the remnant types and mass hierarchy of the neutrino oscillation. These plots are sourced from [53]. 168

11.4 Two-dimensional map of the DSNB $\bar{\nu}_e$ flux as a function of $f_{\rm BH}$ and $f_{\rm HNS}$ in normal mass hierarchy. Dotted-dashed line reports the 3σ expected sensitivity derived from the 10 years of future SK-Gd operation. These are estimated as the integrated flux for the neutrino energy $13.3 < E_\nu < 31.3$ MeV (top) and $17.3 < E_\nu < 31.3$ MeV (bottom) with distinct EOS models such as Togashi EOS (left), LS220 EOS (middle), and Shen EOS (right), respectively. 170

11.5 Distributions with the same manners as Figure 11.4, in case of inverted mass hierarchy. 170

11.6 3σ detectable areas on the $f_{\rm BH}$-$f_{\rm HNS}$ plane assuming NH for three distinct EOS models in the energy range of 13.3–31.3 MeV (left) and 17.3–31.3 MeV (right) according to the future flux limit at 10 year of the SK-Gd observation. 171

11.7 Distributions with the same manners as Figure 11.6 but assuming IH. 171

B.1 Two-dimensional distribution of $\log|dt|$ and Δl for the pre-sample (left) and the post-sample (right). Magenta lines are cut criteria in this plane. These are for clouds with $N_{\rm ncloud} = 2$. 175

B.2 Two-dimensional distribution of $\log|dt|$ and Δl for the pre-sample (left) and the post-sample (right). Magenta lines are cut criteria in this plane. These are for clouds with $N_{\rm ncloud} = 3$. 175

B.3 Two-dimensional distribution of $\log|dt|$ and Δl for the pre-sample (left) and the post-sample (right). Magenta lines are cut criteria in this plane. These are for clouds with $N_{\rm ncloud} = 4$-5. 176

B.4 Two-dimensional distribution of $\log|dt|$ and Δl for the pre-sample (left) and the post-sample (right). Magenta lines are cut criteria in this plane. These are for clouds with $N_{\rm ncloud}$ = 6-9. 176
B.5 Two-dimensional distribution of $\log|dt|$ and Δl for the pre-sample (left) and the post-sample (right). Magenta lines are cut criteria in this plane. These are for clouds with $N_{\rm ncloud} \geq 2$. 176
B.6 Two-dimensional distribution of Δ_x, Δ_y, and Δ_z. The left column shows the pre-samples and the right column shows the post-samples. Magenta lines are cut criteria. These are clouds with $N_{\rm ncloud} = 2$. . . 177
B.7 Two-dimensional distribution of Δ_x, Δ_y, and Δ_z. The left column shows the pre-samples and the right column shows the post-samples. Magenta lines are cut criteria. These are clouds with $N_{\rm ncloud} = 3$. . . 178
B.8 Two-dimensional distribution of Δ_x, Δ_y, and Δ_z. The left column shows the pre-samples and the right column shows the post-samples. Magenta lines are cut criteria. These are clouds with $N_{\rm ncloud}$ = 4-5. . 179
B.9 Two-dimensional distribution of Δ_x, Δ_y, and Δ_z. The left column shows the pre-samples and the right column shows the post-samples. Magenta lines are cut criteria. These are clouds with $N_{\rm ncloud}$ = 6-9. . 180
B.10 Two-dimensional distribution of Δ_x, Δ_y, and Δ_z. The left column shows the pre-samples and the right column shows the post-samples. Magenta lines are cut criteria. These are clouds with $N_{\rm ncloud} \geq 2$. . . 181
B.11 Random (blue) and spallation (red) PDFs for dt (top), and ℓ_t (second from the top to bottom). ℓ_t PDF distributions are separated for the muon with dt region of 0–0.05 sec (second from top), 0.05–0.5 sec (third from top), and 0.5-60 sec (bottom). These muons belong to the stopping (left) and multiple (right) muons. 182
B.12 Random (blue) and spallation (red) PDFs for ℓ_l with dt region of 0–0.05 sec (top), 0.05–0.5 sec (middle), 0.5-60 sec (bottom), and ℓ_t region of 0–300 cm (left), 300–1000 cm (middle), and more than 1000 cm (right). These muons belong to the single through-going muons. . . . 183
B.13 Random (blue) and spallation (red) PDFs for $Q_{\rm res}$ with dt region of 0–0.05 sec (top), 0.05–0.5 sec (middle), 0.5-60 sec (bottom), and ℓ_t region of 0–300 cm (left), 300–1000 cm (middle), and more than 1000 cm (right). These muons belong to the single through-going muons. . . . 184
B.14 Random (blue) and spallation (red) PDFs for $Q_{\rm mu}$ with dt region of 0–0.05 sec (top), 0.05–0.5 sec (middle), 0.5-60 sec (bottom), and ℓ_t region of 0–300 cm (left), 300–1000 cm (middle), and more than 1000 cm (right). These muons belong to the single through-going muons. . . . 185
B.15 ROC curve for each 2 MeV bin below 16 MeV. 186
B.16 Correlation between spallation remaining rate and ^9Li efficiency for each 2 MeV energy bin below 16 MeV. 187

C.1 $d_{\rm eff}$ wall distribution for the data (black) and MC (blue). Each panel show the reconstructed energy E for $E > 8$ MeV (left-top), $E > 10$ MeV (right-top), $E > 12$ MeV (left-middle), $E > 14$ MeV (right-middle), $E > 16$ MeV (left-bottom), and $E > 20$ MeV (right-bottom). 189

C.2 Reconstructed Cherenkov angle distribution for LINAC data (black) and MC (blue). For each plot, the lower panel shows the ratio of data over MC. For the LINAC position, figures show the $z = -12$ m (top), $z = 0$ m (middle), and $z = 12$ m (bottom). For the LINAC energy, figures show the $E = 8$ MeV (left), $E = 12$ MeV (middle), and $E = 15$ MeV (right). 190
C.3 Ratio of charge over number of hits in 50 ns distribution for LINAC data (black) and MC (blue). For each plot, the lower panel shows the ratio of data over MC. For the LINAC position, figures show the $z = -12$ m (top), $z = 0$ m (middle), and $z = 12$ m (bottom). For the LINAC energy, figures show the $E = 8$ MeV (left), $E = 12$ MeV (middle), and $E = 15$ MeV (right). 191
C.4 Pion likeness distribution for LINAC data (black) and MC (blue). For each plot, the lower panel shows the ratio of data over MC. For the LINAC position, figures show the $z = -12$ m (top), $z = 0$ m (middle), and $z = 12$ m (bottom). For the LINAC energy, figures show the $E = 8$ MeV (left), $E = 12$ MeV (middle), and $E = 15$ MeV (right). . . 192

List of Tables

1.1 Best-fitted neutrino oscillation parameters. These values are taken by [54]. . . . 9

2.1 The detector situation for each observation period of SK. . . . 25
2.2 Detectable dynamic range and charge resolution for each range. . . . 31
2.3 Threshold for each type of trigger in SK-VI . . . 32

4.1 Parameter settings for the reconstructed energy calculation in SK-VI. 50
4.2 Charge thresholds for ID PMT corresponding to the number of ID PMT hits. . . . 52
4.3 N_{nn} thresholds for ID PMT corresponding to the number of ID PMT hits. . . . 53

6.1 Summary of thermal neutron capture on ^{155}Gd and ^{157}Gd [37] . . . 78
6.2 Summary of neutron selection variables. . . . 80
6.3 Summary of selection and reduction efficiency for the neutron event and background. . . . 81
6.4 Parameters determined from the measurements, including the rise time parameters and resolution scale parameter. . . . 89
6.5 Summary of capture time constant and neutron tagging efficiency for the DATA and MC for each BGO geometry. Errors only include only statistical uncertainty. . . . 92
6.6 Summary of contents in the calculation for the tagging efficiency of 4.4 MeV gamma-ray. . . . 95
6.7 Break down the contents in the calculation of random neutron intensity. 95
6.8 Summary of the contents of the dummy prompt event. . . . 97
6.9 Summary of contents in dummy prompt event. . . . 97
6.10 Summary of excited state fraction and neutron tagging efficiency . . . 103
6.11 Summary of systematic uncertainty on AmBe measurement. . . . 105
6.12 Summary of neutron tagging efficiencies for the DATA and MC for each BGO geometry. . . . 106

7.1 Trigger conditions and live-time during SK-VI. . . . 107
7.2 Summary of the muon spallation products in the water. This table is taken from Ref. [35]. . . . 109

8.1 AFT trigger efficiency calculated using 2 MeV energy bins. These values are calculated by considering the average of the entire SK-VI period. . 117
8.2 Cut criteria of neutron cloud cut. The signature (+) in the multiplicity column signifies equal or more than the value. . . . 122
8.3 Summary of cut criteria of spallation box cuts for each reconstructed energy E region. . . . 128
8.4 Summary of the cut efficiency of spallation cut above 16 MeV. . . . 132
8.5 LINAC positions and target energies used in the evaluation . . . 138

8.6 Summary of the cut criteria and efficiencies. 140
8.7 Summary of the signal efficiencies at each cut stage for energy E = 8–16 MeV. 143
8.8 Summary of the signal efficiencies at each cut stage for the $E_{\rm rec}$ = 7.49–15.49 MeV. 145
8.9 Summary of the signal efficiencies at each cut stage for $E_{\rm rec}$ =15.49–23.49 MeV. 145
8.10 Summary of the signal efficiencies at each cut stage for $E_{\rm rec}$ = 23.49–29.49 MeV. 145

9.1 Ratio of the number of observed neutrons $N_{\rm obs}^{\rm T2K}$ over the predicted by MC $N_{\rm pred}^{\rm T2K}$ in each Q^2 region. 150
9.2 Break down the systematic uncertainty on the NCQE interaction events. 153
9.3 Breakdown of the expected background events and these systematic errors at each merged bin. 156

10.1 Breakdown the event reduction and signal efficiency at each merged bin. 159
10.2 Summary table of upper limits, sensitivity. 162

11.1 Assumptions for calculating future sensitivity. Titles about color indicate the line color for each panel shown in Figure 11.1. 167

A.1 Summary of model projections of average flux and obtained sensitivity in each bin. The future sensitivity in SK-VII represents the magenta line in Figure 11.1. The unit of each value is $\rm cm^{-2}\,sec^{-1}\,MeV^{-1}$. . . . 173

Chapter 1

Introduction

Massive stars, with a gravitational mass exceeding about eight solar masses, end their life in an intense explosion known as a *Supernova*. Supernova is one of the most dynamic phenomena in the universe, and the energy released at the explosion is about 10^{53} erg. Consequently, supernovae are pivotal in the fields of astrophysics and particle physics. Contemporary theory suggests that a large part of this formidable explosion energy is emitted via neutrinos, rendering their detection crucial for deciphering the physics of supernovae.

In this chapter, the initial section presents a discussion on the supernova explosion and the consequent emission of neutrinos. After that, supernova relic neutrinos, which constitute an integrated flux of neutrinos originating from past supernovae, are introduced. Finally, the past experimental approach utilized in the detection of supernova relic neutrinos, culminating with a summary of the current status of sensitivity toward these neutrinos, is outlined.

1.1 Supernova Explosion

Supernova is predicted to occur a few times in our galaxy [55]. The light emission from a supernova, reaching approximately 10^{51} erg, is primarily observable via optical surveys. Despite numerous observations of supernovae across various galaxies, significant mysteries persist surrounding supernovae and their underlying explosion mechanisms.

1.1.1 Explosion Types and Mechanism Overview

Supernovae can be categorized based on their optically observed spectra, including types Ia, Ib, IIP, and IIL, as illustrated in Figure 1.1. A supernova devoid of hydrogen lines (Balmer series) in its spectrum is classified as Type-I, whereas those featuring such lines are designated as Type-II. Those exhibiting silicon lines within the Type-I supernova category are further classified as Type-Ia. The explosion mechanism of these supernovae is attributed to thermo-nuclear interactions.

The supernovae with weak silicon lines are classified as either Type-Ib or Type-Ic, contingent upon the presence of a helium line. Type-II supernovae are differentiated based on their light curves. A supernova displaying a stable period in its light curve is designated Type-IIP (Plateau), whereas a linearly decreasing light curve characterizes a Type-IIL (Linear) supernova. The explosion mechanism for supernovae apart from Type-Ia is attributed to the core collapse of the star, leading to the nomenclature 'Core-Collapse Supernova' (CCSN). The neutrino emitted via this mechanism is focused on in this thesis as the explosion is accompanied by enormous neutrino emission.

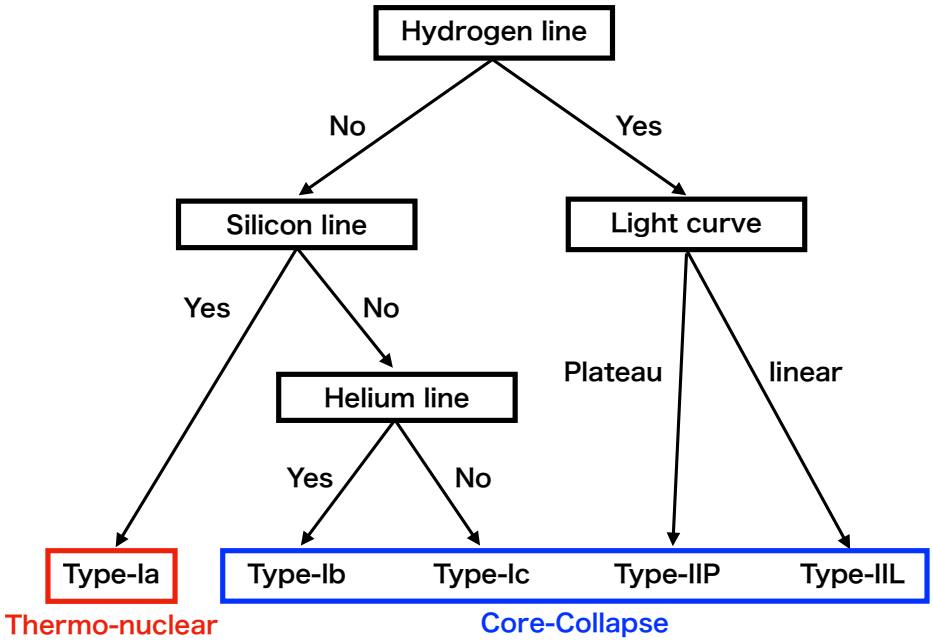

FIGURE 1.1: Classification of the supernovae by these spectra.

The kinetic energy propelling an explosion emanates from two primary sources. The first pertains to the energy derived from nuclear fusion. Assuming a rapid nuclear fusion reaction transitioning from carbon atoms to iron atoms within a star of mass M, the energy released, represented as $E_{\rm nuc}$, can be expressed as follows:

$$E_{\rm nuc} \sim 2 \times 10^{51} {\rm erg} \left(\frac{M}{M_\odot} \right), \tag{1.1}$$

where $M_\odot$ denotes the solar mass[1]. The second source of energy is gravitational. Assuming a star of radius R contracts to a final radius $R_{\rm f}$, comparable to the size of a neutron star ($\sim$ 10 km), the gravitational energy $E_{\rm g}$ can be calculated as follows:

$$E_{\rm g} \sim 3 \times 10^{53} {\rm erg} \left(\frac{M}{M_\odot} \right)^2 \left(\frac{R_{\rm f}}{10 \text{ km}} \right) \tag{1.2}$$

Type-Ia supernovae are fueled by nuclear fusion reactions, whereas core-collapse supernovae are driven by gravitational energy.

1.1.2 Explosion Mechanism of Core-Collapse Supernova

This section describes the mechanism through which a star concludes its life with a CCSN explosion. Figure 1.2 illustrates a schematic view of the CCSN explosion process.

The formation of stars commences when the interstellar medium condenses due to gravity, forming a core. Surrounding materials are continuously accreted to the core, causing it to grow. Simultaneously, the gravitational energy from the accreted materials is converted into thermal energy, resulting in increasing internal pressure. When the central temperature of the star reaches $T \approx 10^5$ K, the radiation spectrum

[1] $M_\odot \sim 1.9884 \times 10^{30}$ kg

bears an optical range. Stars in this stage are referred to as primitive stars. Once the temperature surpasses $T > 10^7$ K, the conditions are favorable for nuclear fusion and the subsequent production of heavier elements. Hereinafter, the progenitor mass of the star constrains the maximum mass of the created element. In instances where the star mass $M > 8M_\odot$, neon and magnesium serve as the fuel for nuclear fusion, such as 1.3. If the density exceeds 4×10^9 g/cm^3, magnesium occurs electron capture, which results in a decreased electron density (as indicated in stages (1) and (2) in Figure 1.2).

$$^{24}\mathrm{Mg} + \mathrm{e}^- \longrightarrow {}^{24}\mathrm{Na} + \nu_e \tag{1.3}$$

As the density continues to rise, the generated nuclei start to capture electrons.

$$^{24}\mathrm{Na} + \mathrm{e}^- \longrightarrow {}^{24}\mathrm{Ne} + \nu_e \tag{1.4}$$

$$^{24}\mathrm{Ne} + \mathrm{e}^- \longrightarrow {}^{24}\mathrm{F} + \nu_e \tag{1.5}$$

$$^{24}\mathrm{F} + \mathrm{e}^- \longrightarrow {}^{24}\mathrm{O} + \nu_e \tag{1.6}$$

The decrease in electron density reduces the electron degeneracy pressure, triggering a gravitational contraction at the central core (as depicted in stage (3) in Figure 1.2). Eventually, the mass density of the central core becomes sufficiently dense to cause a gravitational collapse. If $M > 12M_\odot$, magnesium undergoes nuclear fusion under nondegenerate pressure, culminating in the creation of the Iron nucleus (^{56}Fe). Given that ^{56}Fe is the most stable nucleus formed in this process, further nuclear fusion to create heavier elements does not take place. Consequently, the iron core stops providing energy, and gravitational force is counterbalanced by electron degeneracy pressure. The temperature becomes sufficiently high to create the iron core, and high-energy photons disintegrate the nucleus in a process called photodisintegration.

$$^{56}\mathrm{Fe} + \gamma \longrightarrow 13\,\alpha + 4n - 124.4 \text{ MeV} \tag{1.7}$$

$$\alpha + \gamma \longrightarrow 2p + 2n - 28.3 \text{ MeV} \tag{1.8}$$

As this reaction progresses, the electron density diminishes. The photodisintegration process is activated at the $T \sim 5 \times 10^9$ K, and the internal core achieves a thermodynamic equilibrium between nuclear fusion and the photodisintegration. The continuous contraction and rising temperature eventually lead to the core collapse of the iron core, accompanied by explosive photodisintegration.

The collapse halts when the density reaches $\sim 10^{14}$ g/cm^3 due to nuclear forces, resulting in the creation of an outward shockwave ((5) in Figure 1.2). This shockwave heats the surrounding material and dissipates its energy. Following the passage of the shockwave, a proto-neutron star (PNS) forms within the core. The PNS is an incredibly dense object with an inner core packed with neutron-rich nuclei and free neutrons. The gravity acting on the PNS is offset by the neutron degeneracy pressure, yielding a radius of ~ 10 km. The material remaining after the passage of the shockwave collapses onto the PNS (as depicted in stage (7) in Figure 1.2). Although the shockwave is considered the engine of the supernova explosion, it eventually stalls due to energy loss from the accretion of the surrounding matter. This shockwave was believed to be revived through a neutrino-heating mechanism (as indicated in (8) in Figure 1.2) [56]. In this mechanism, the matter behind the shockwave absorbs neutrinos emitted from the PNS, reenergizing the shockwave. Although only simple neutrino transportation does not revive the shockwave [57], recent studies propose that the shockwave instability and the convection in the progenitor may accelerate

the neutrino-heating [58, 59].

As the outer layer of a star is weakly bound to the core, the shockwave ejects the outer layer, leaving a neutron star after the explosion (as displayed in stage (9) in Figure 1.2). Although the gravity of a neutron star is balanced by the degeneracy pressure of neutrons, stars with $M > 12M_{\odot}$ can occasionally exceed the neutron degeneracy pressure, referred to as the Tolman-Oppenheimer-Volkoff limit. In such cases, these stars ultimately form a black hole.

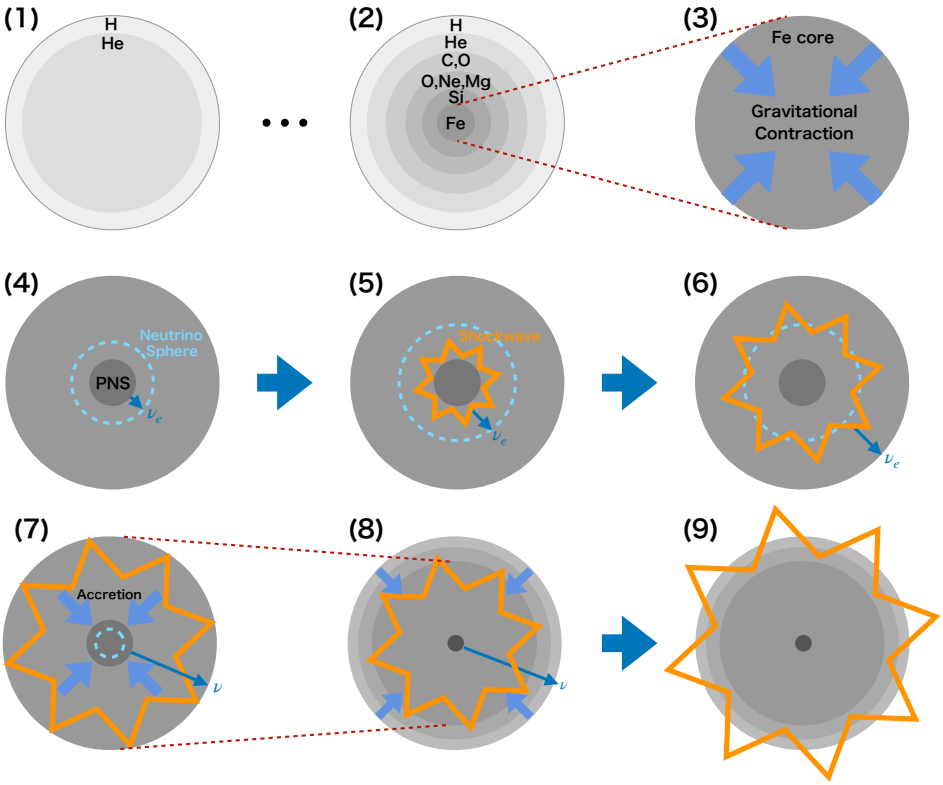

FIGURE 1.2: Schematic of CCSN explosion procedure. Explosion proceeds from the smaller number. Neutrino-heating is assumed to be the mechanism for shockwave revival.

1.1.3 Neutrinos from Core-Collapse Supernovae

Neutrinos are fundamental particles, possessing no electric charge and a spin of 1/2, making them fermions. They are categorized into three leptonic flavors: electron, muon, and tau, including their antiparticles. They only interact with matter via weak forces (and gravity) due to their lack of charge and minuscule masses. This characteristic plays a pivotal role in the mechanism of supernova explosions. This section first elucidates the neutrino oscillation, a key property of neutrinos, before detailing the mechanisms and neutrino emissions from Core-Collapse Supernovae.

Neutrino Oscillations

The discrepancy between the observed and the expected flux of neutrinos was a long-standing mystery because neutrino was first believed to be mass-less. However, this assumption of mass-less was contradicted, and the mystery was resolved by observing a key characteristic of neutrinos, known as Neutrino Oscillation[60, 61]. This evidence suggests that neutrinos possess extremely minute masses below 1 eV. The theory of neutrino oscillation was first proposed by Pontecorvo[62, 63] for neutrinos and anti-neutrinos, and has since been further developed quantitatively[64, 65]. This theory demonstrates the transition of neutrino types by assuming that the neutrino flavor eigenstates differ from their mass eigenstates and that the flavor state eigenstate comprises a mix of three types of mass eigenstates. Initially, the fundamental concept of neutrino oscillation in a vacuum is discussed, as material affects neutrino oscillation until it is observed. The impact of the material will be discussed later in this section.

In a vacuum, the neutrino flavor state eigenstates $|\nu_\alpha\rangle\,(\alpha = e, \mu, \tau)$ are correlated linearly with three types of neutrino mass eigenstates $|\nu_i\rangle\,(i = 1, 2, 3)$:

$$|\nu_\alpha\rangle = \sum_{i=1}^{3} U^*_{\alpha i}\,|\nu_i\rangle \tag{1.9}$$

Here, U represents the 3×3 matrix called Pontecorvo-Maki-Nakagawa-Sakata(PMNS) matrix [64]. PMNS matrix can be usually described by three unitary matrices as follows:

$$\begin{pmatrix} 1 & 0 & 0 \\ 0 & c_{23} & s_{23} \\ 0 & -s_{23} & c_{23} \end{pmatrix} \begin{pmatrix} c_{13} & 0 & s_{13}e^{-i\delta_{CP}} \\ 0 & 1 & 0 \\ -s_{13}e^{-i\delta_{CP}} & 0 & c_{13} \end{pmatrix} \begin{pmatrix} c_{12} & s_{12} & 0 \\ -s_{12} & c_{12} & 0 \\ 0 & 0 & 1 \end{pmatrix}, \tag{1.10}$$

where the $s_{ij} = \sin\theta_{ij}$ and $c_{ij} = \cos\theta_{ij}$ denote the sine and cosine of mixing angle θ_{ij} between two distinct mass eigenstates, and δ_{CP} represents the charge-parity violating phase of the CP asymmetry for the lepton sector.

The evolution of the flavor eigenstate over time is described with the energy eigenvalue of each eigenstate for ν_i as follows:

$$|\nu_\alpha(t)\rangle = \sum_{i=1}^{3} U^*_{\alpha i} e^{-iE_i t}\,|\nu_i(t=0)\rangle\,, \tag{1.11}$$

and the probability amplitude, $A_{\nu_\alpha \to \nu_\beta}(t)$, when a neutrino is produced at a time $t = 0$ with the state, is detected at the time t can be described as

$$\begin{aligned} A_{\nu_\alpha \to \nu_\beta}(t) &\equiv \langle \nu_\beta | \nu_\alpha(t) \rangle \\ &= \sum_j \langle \nu_\beta | U^*_{\alpha j} e^{-iE_j t} | \nu_j \rangle \\ &= \sum_j \sum_{\gamma=e,\mu,\tau} \langle \nu_\beta | U^*_{\alpha j} e^{-iE_j t} U_{\gamma j} | \nu_\gamma \rangle \\ &= \sum_j \sum_{\gamma=e,\mu,\tau} U^*_{\alpha j} U_{\gamma j} e^{-iE_j t} \langle \nu_\beta | \nu_\gamma \rangle \\ &= \sum_j U^*_{\alpha j} U_{\beta j} e^{-iE_j t}. \end{aligned} \tag{1.12}$$

Therefore, the flavor oscillation probability $P_{\nu_\alpha \to \nu_\beta}(t)$ is expressed as

$$\begin{aligned} P_{\nu_\alpha \to \nu_\beta}(t) &= \left| A_{\nu_\alpha \to \nu_\beta}(t) \right|^2 \\ &= \left(\sum_j U^*_{\alpha j} U_{\beta j} e^{-iE_j t} \right) \left(\sum_k U^*_{\alpha k} U_{\beta k} e^{-iE_k t} \right)^* \\ &= \sum_j \sum_k U^*_{\alpha j} U_{\beta j} U_{\alpha k} U^*_{\beta k} e^{-i(E_j - E_k)t} \\ &= \sum_j U^*_{\alpha j} U_{\beta j} U_{\alpha j} U^*_{\beta j} + \sum_{j \neq k} U^*_{\alpha j} U_{\beta j} U_{\alpha k} U^*_{\beta k} e^{-i(E_j - E_k)t}. \end{aligned} \tag{1.13}$$

In the case that neutrino moves relativistically, the energy difference between two energy eigenstates E_i and E_j is denoted as follows:

$$\begin{aligned} E_i - E_j &= \sqrt{\boldsymbol{p}_i^2 - m_i^2} - \sqrt{\boldsymbol{p}_j^2 - m_j^2} \\ &\simeq \boldsymbol{p}_i \left(1 + \frac{m_i^2}{2\boldsymbol{p}_i^2} \right) - \boldsymbol{p}_j \left(1 + \frac{m_j^2}{2\boldsymbol{p}_j^2} \right) \qquad (1.14) \\ &= \frac{m_i^2 - m_j^2}{2E}. \qquad (1.15) \end{aligned}$$

Here $E \cong |\boldsymbol{p}_i| = |\boldsymbol{p}_j|$ represents the neutrino energy of relativistic neutrinos. With the transportation distance $L = ct$, Equation 1.13 can be rewritten as

$$\begin{aligned} P_{\nu_\alpha \to \nu_\beta}(t) &= \sum_j U^*_{\alpha j} U_{\beta j} U_{\alpha j} U^*_{\beta j} + \sum_{j \neq k} U^*_{\alpha j} U_{\beta j} U_{\alpha k} U^*_{\beta k} \exp\left(-i \frac{\Delta m^2_{jk} L}{2E} t \right) \\ &= \sum_j U^*_{\alpha j} U_{\beta j} U_{\alpha j} U^*_{\beta j} + \sum_{j \neq k} U^*_{\alpha j} U_{\beta j} U_{\alpha k} U^*_{\beta k} \\ &\quad - 2 \sum_{j \neq k} U^*_{\alpha j} U_{\beta j} U_{\alpha k} U^*_{\beta k} \sin^2 \left(\frac{\Delta m^2_{jk} L}{4E} \right) \\ &\quad + i \sum_{j \neq k} U^*_{\alpha j} U_{\beta j} U_{\alpha k} U^*_{\beta k} \sin \left(\frac{\Delta m^2_{jk} L}{2E} \right) \\ &= P_1 + P_2 - 2P_3 + iP_4, \end{aligned} \tag{1.16}$$

where Δm_{jk} is defined as $\Delta m^2_{jk} = m^2_j - m^2_k$. P_1 and P_2 are summarized as

$$\begin{aligned} P_1 + P_2 &= \sum_j \sum_k U^*_{\alpha j} U_{\beta j} U_{\alpha k} U^*_{\beta k} \\ &= \sum_j (U^*_{\alpha j} U_{\beta j}) \sum_k (U_{\alpha k} U^*_{\beta k}) \\ &= \left| \sum_j U^*_{\alpha j} U_{\beta j} \right|^2 \\ &= \delta_{\alpha\beta}, \end{aligned} \tag{1.17}$$

where the $\delta_{\alpha\beta}$ denotes Kronecker delta. Moreover, P_3 and P_4 can be transformed as

$$\begin{aligned} P_3 &= \sum_{j>k} (U^*_{\alpha j} U_{\beta j} U_{\alpha k} U^*_{\beta k} + U^*_{\alpha k} U_{\beta k} U_{\alpha j} U^*_{\beta j}) \sin^2 \left(\frac{\Delta m^2_{jk} L}{4E} \right) \\ &= 2 \sum_{j>k} \mathrm{Re}[U^*_{\alpha j} U_{\beta j} U_{\alpha k} U^*_{\beta k}] \sin^2 \left(\frac{\Delta m^2_{jk} L}{4E} \right) \end{aligned} \tag{1.18}$$

$$\begin{aligned} P_4 &= \sum_{j>k} (U^*_{\alpha j} U_{\beta j} U_{\alpha k} U^*_{\beta k} - U^*_{\alpha k} U_{\beta k} U_{\alpha j} U^*_{\beta j}) \sin \left(\frac{\Delta m^2_{jk} L}{2E} \right) \\ &= -2i \sum_{j>k} \mathrm{Im}[U^*_{\alpha j} U_{\beta j} U_{\alpha k} U^*_{\beta k}] \sin \left(\frac{\Delta m^2_{jk} L}{2E} \right). \end{aligned} \tag{1.19}$$

Finally, $P_{\nu_\alpha \to \nu_\beta}(t)$ can be denoted using Equations 1.16, 1.17, 1.18, and 1.19 as

$$\begin{aligned} P_{\nu_\alpha \to \nu_\beta}(t) =& \delta_{\alpha\beta} - 4 \sum_{i>j} \mathrm{Re}[U^*_{\alpha j} U_{\beta j} U_{\alpha k} U^*_{\beta k}] \sin^2 \left(\frac{\Delta m^2_{jk} L}{4E} \right) \\ &+ 2 \sum_{j>k} \mathrm{Im}[U^*_{\alpha j} U_{\beta j} U_{\alpha k} U^*_{\beta k}] \sin \left(\frac{\Delta m^2_{jk} L}{2E} \right). \end{aligned} \tag{1.20}$$

From Equation 1.20, it is clear that the neutrino oscillation occurs if any mass eigenstate differs from other states.

From now on, we consider the scenario where neutrinos interact with surrounding matter. The oscillation effect of neutrinos changes when propagating through matter due to the interactions between neutrinos and matter. This effect is called the Mikheyev-Smirnov-Wolfenstein (MSW) effect [66, 67, 68], or simply the matter effect.

All three generations of neutrinos undergo neutral-current coherent scattering with protons, neutrons, and electrons. In addition, only electron-type neutrinos are affected by the charged-current coherent interaction with abundant electrons in matter. Therefore, the neutral-current interaction does not impact the manifestation of neutrino oscillation for each flavor since the neutral-current interaction happens in all flavors with equal probability. Conversely, charged-current interaction influences oscillation by adding potential V_{CC} to only electron-type neutrinos:

$$V_{CC} = \pm \sqrt{2} G_F n_e, \tag{1.21}$$

where the G_F denotes the weak-coupling constant, and n_e indicates the number density of electrons in the matter; the $\pm$ symbol represents the charge of neutrinos, i.e., the positive sign corresponds to neutrinos, while the negative sign corresponds to the anti-neutrinos.

Assuming a two-flavor oscillation $\nu_e \to \nu_\mu$, a Hamiltonian can be expressed as

$$H = \frac{\Delta m_M^2}{4E_\nu} \begin{pmatrix} -\cos(2\theta_M) & sin(2\theta_M) \\ \sin(2\theta_M) & \cos(2\theta_M) \end{pmatrix}, \tag{1.22}$$

where Δm_M^2 denotes the square difference of the effective mass with considering matter effect, θ_M symbolizes the effective mixing angle, and E_ν represents neutrino energy. Both Δm_M^2 and θ_M are expressed using mixing angle θ and mass difference Δm^2 between ν_e and ν_μ as

$$\Delta m_M^2 = \Delta m^2 \sqrt{\sin^2 2\theta + (\cos 2\theta - x)^2} \tag{1.23}$$

$$\sin^2 2\theta_M = \frac{\sin^2 2\theta}{\sin^2 2\theta + (\cos 2\theta - x)^2} \tag{1.24}$$

$$(x \equiv \frac{2\sqrt{2} G_F N_e E_\nu}{\Delta m^2}), \tag{1.25}$$

In the case of the two-flavor oscillation of $\nu_e \to \nu_\mu$, the survival probability $P_{\nu_e \to \nu_e}$ and transition probability $P_{\nu_e \to \nu_\mu}$ can be expressed as

$$P_{\nu_e \to \nu_e} = 1 - \sin^2 2\theta_M \sin^2 \left(\frac{\Delta m_M^2 L}{4E} \right), \tag{1.26}$$

$$P_{\nu_e \to \nu_\mu} = \sin^2 2\theta_M \sin^2 \left(\frac{\Delta m_M^2 L}{4E} \right). \tag{1.27}$$

In the study of neutrino oscillation in a vacuum, six parameters need to be considered: three mixing angles (θ_{12}, θ_{23}, θ_{13}), two mass-splitting parameters ($\Delta m_{21}^2 = m_2^2 - m_1^2$, $\Delta m_{32}^2 = m_3^2 - m_2^2$), and a CP violating phase parameter δ_{CP}. These are extensively measured primarily through reactor, atmospheric, solar, and long-baseline neutrino experiments.

θ_{12} and Δm_{21}^2 are measured from solar and reactor neutrino observations, by Super-K[69], SNO[70], and KamLAND[71] experiments. θ_{23} and Δm_{32}^2 are explored from ν_μ disappearance measurement by the atmospheric and long-baseline neutrino experiment such as Super-K[72, 73], T2K[74, 75], NOvA[76, 77] experiments, and so on. θ_{13} is measured by the reactor experiment such as KamLAND[71], DayaBay[78], Double Chooz[7] experiment, and so on.

The current best-fitted parameters are summarized in Table 1.1 [54].

Neutrino Emission from Core-Collapse Supernova

This section describes the neutrino emissions from CCSN. As described in 1.1.1, an energy surmounting to $E \sim 10^{53}$ erg is emitted from CCSN, with approximately 99% of this energy propagated out by neutrinos. The interaction responsible for the neutrino production varies with the time sequence of CCSN, so here, the emission processes are described in accordance with this sequence.

1. At the commencement of the collapse

   As the core contracts, the Fermi energy of its electrons increases. During this

TABLE 1.1: Best-fitted neutrino oscillation parameters. These values are taken by [54].

	Normal ordering	Inverted ordering
$\sin^2\theta_{12}$	0.304 ± 0.012	$0.304^{+0.013}_{-0.012}$
$\sin^2\theta_{23}$	$0.573^{+0.016}_{-0.020}$	$0.575^{+0.016}_{-0.019}$
$\sin^2\theta_{13}$	$0.02219^{+0.00062}_{-0.00063}$	$0.02238^{+0.00063}_{-0.00062}$
δ_{CP} [deg]	197^{+27}_{-24}	282^{+26}_{-30}
$\Delta m^2_{21}[/10^{-5}$ eV]	$7.42^{+0.21}_{-0.20}$	$7.42^{+0.21}_{-0.20}$
$\Delta m^2_{32}[/10^{-3}$ eV]	$+2.517^{+0.026}_{-0.028}$	-2.498 ± 0.028

stage, neutrinos are created by electron capture (Equations 1.3–1.6, and 1.28) and the photodisintegration (Equations 1.7 and 1.8), which collectively cause the core to collapse. Initially, after the collapse, the density of the core is relatively low, allowing neutrinos to escape freely ((3) in Figure 1.2).

$$e^- + A(N, Z) \longleftrightarrow \nu_e + A(N + 1, Z - 1). \tag{1.28}$$

2. Neutrino Trapping
As density increases, the core becomes opaque to the neutrinos. Despite neutrinos having extremely high transparency in the matter, their escape from the dense core is delayed due to coherent scattering. When density reaches $\rho \sim 10^{12}$ g/cm^3, the time scale of neutrinos leaving the core becomes equivalent to the time scale of the core collapse. The optical thickness τ of the materials outside the core radius r is defined for the neutrino mean free path l_{mfp} as

$$\tau = \int_r^\infty \frac{1}{l_{\text{mfp}}} dr. \tag{1.29}$$

This formulation implies neutrinos require τ times longer to diffuse than to travel straight forward. The sphere with a radius where $\tau = 2/3$ is specifically termed the 'Neutrino Sphere.' This serves as the boundary of the region where neutrinos truly interact with matter.

When the density of the core reaches nuclear density, $\rho \sim 10^{14}$ g/cm^3, contraction ceases due to the resistance offered by neutron degeneracy pressure, and the core starts to expand–an event termed 'core-bounce.' The expanding core collides with the outer layers still contracting, which generates a shockwave. The remaining central core stabilizes and forms a PNS ((4) in Figure 1.2).

3. Neutronization burst
The shockwave heats the core materials, causing nuclei to decompose into nucleons due to photodisintegration (1.7). As the electron capture interaction exhibits a significantly larger cross-section for nucleons than for nuclei, electron capture processes proceed rapidly. The electron capture of nuclei can be expressed as

$$e^- + p \longrightarrow \nu_e + n. \tag{1.30}$$

This process can be summarized as the 'neutronization' of the core. The neutronization burst lasts for about 1 ms, during which the neutrino luminosity escapades to 10^{53} erg s^{-1}. Given the short duration, the energy emission is $\lesssim 10^{51}$ erg, less than 1% of the total energy emission ((6) in Figure 1.2).

4. PNS Cooling
   Post explosion, matter from the outer layers accretes onto the PNS, converting gravitational energy into thermal energy. This energy is subsequently emitted as the neutrinos via the following processes, eventually cooling the PNS.

$$\begin{aligned} e^- + n &\longleftrightarrow \bar{\nu}_e + p, \\ e^- + e^+ &\longleftrightarrow \nu_X + \bar{\nu}_X, \\ e^{\pm} + N &\longleftrightarrow e^{\pm} + N + \nu_X + \bar{\nu}_X, \\ N + N &\longleftrightarrow N + N + \nu_X + \bar{\nu}_X, \\ \gamma &\longleftrightarrow \nu_X + \bar{\nu}_X, \\ \gamma + e^{\pm} &\longleftrightarrow e^{\pm} + \nu_X + \bar{\nu}_X. \end{aligned} \tag{1.31}$$

   These processes result in the creation of all types of neutrinos.

Figure 1.3 presents a typical theoretical calculation of the time evolution of the neutrino luminosity and the average energy [1]. The sharp peak caused by the neutronization burst is clearly visible. A complex timing structure persists for the first 1 second, followed by a simpler structure representing the PNS cooling phase. Several analytical approaches focusing on this cooling phase have recently been proposed based on theoretical expectations-[79, 80, 81].

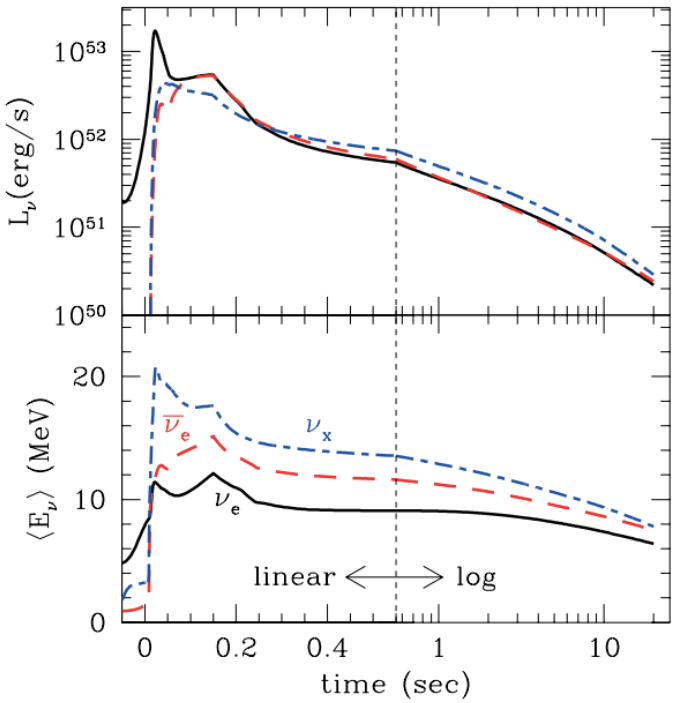

FIGURE 1.3: Typical theoretical calculation of timing development of neutrino luminosity and average energy [1].

Neutrinos Observation from SN1987A

To date, only a single recorded observation of neutrinos from a supernova. In total, 24 neutrinos were concurrently observed by the Kamiokande-II, IMB, and Baksan experiments [82, 83, 84], during a supernova event dubbed SN1987A, which occurred

in the Large Magellanic Cloud. Figure 1.4 displays the energies of observed neutrinos as a function of the observed time, recorded by the Kamiokande-II (12 events) and IMB (8 events) experiments. The total energy and timeframe of neutrino emission derived from SN1987A were confirmed to align with theoretical expectations [85]. Although the theory of supernovae was corroborated, it proved challenging to delve into the fundamental physics and constrain of the supernova model due to the limited statistical data. Several next-generation neutrino detectors exist worldwide, including Super-Kamiokande, all on the lookout for the next nearby supernova burst to gain insight into the mechanics of supernovae.

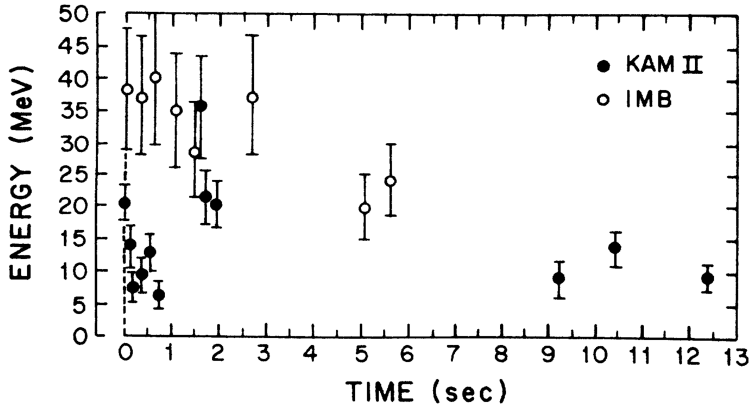

FIGURE 1.4: Timing and energy distribution of neutrinos observed by Kamiokande-II and IMB experiments. The figure is taken from [2].

1.2 Diffuse Supernova Neutrino Background

Presumably, neutrinos from all past CCSNe compose the background flux of our universe. This is called 'Diffuse Supernova Neutrino Background (DSNB)' or 'Supernova Relic Neutrinos (SRNs). ' Observing this flux could provide us with variable information, not only on the explosion mechanism of CCSN but also on the history of star formation in our universe. This section outlines the theoretical prediction of the SRN flux based on Ref. [3].

1.2.1 Formulation of SRN Flux

The number density of SRNs at present, which are emitted at redshift $z \sim z + dz$ with energies $E'_\nu \sim E'_\nu + dE'_\nu$, where E'_ν denote the energy at emission timing, can be described as

$$dn(E'_\nu) = R_{\mathrm{CCSN}}(z)\frac{dt}{dz}dz\frac{dN(E'_\nu)}{dE'_\nu}dE'_\nu, \tag{1.32}$$

where $R_{\mathrm{CCSN}}(z)$ denotes the CCSN rate in unit volume at redshift z, $dN(E'_\nu)/dE'_\nu$ denotes the number density of neutrinos from each CCSN, and the variables with a prime sign represent the quantities at the neutrino emission period. The energy is redshifted to $E'_\nu = (1+z)E_\nu$ and the redshift z is related to the time t based on the

Friedmann equation as

$$\frac{dt}{dz} = \frac{1}{H_0(1+z)\sqrt{\Omega_m(1+z)^3+\Omega_\Lambda}}, \tag{1.33}$$

where H_0 denotes the Hubble constant, Ω_m and Ω_Λ indicate the matter density and cosmological constant, respectively. Using the redshift evolution of the CCSN rate $R_{\mathrm{CCSN}}(z)$ and $dN(E'_\nu)/dE'_\nu$, the flux of SRNs $d\Phi(E_\nu)/dE_\nu$ can be denoted as:

$$\frac{d\Phi(E_\nu)}{dE_\nu} = c\int_0^\infty \frac{dz}{H_0(1+z)\sqrt{\Omega_m(1+z)^3+\Omega_\Lambda}} R_{\mathrm{CCSN}}(z)\frac{dN(E'_\nu)}{dE'_\nu}. \tag{1.34}$$

As the number density of neutrino emission depends on the metallicity Z and the initial mass M of each progenitor, the SRN flux can be expressed according to [3] as follows:

$$\begin{aligned}\frac{d\Phi(E_\nu)}{dE_\nu} =& c\int_0^\infty dz \frac{R_{\mathrm{CCSN}}(z)}{H_0(1+z)\sqrt{\Omega_m(1+z)^3+\Omega_\Lambda}} \\ &\times \int_0^{Z_{\max}} \psi_{\mathrm{ZF}}(z,Z)\int_{M_{\min}}^{M_{\max}} \psi_{\mathrm{IMF}}(M)\frac{dN(M,Z,E'_\nu)}{dE'_\nu} dM dZ\end{aligned}, \tag{1.35}$$

where the $\psi_{\mathrm{ZF}}(z,Z)$ and the $\psi_{\mathrm{IMF}}(M)$ represent the metallicity function and the initial mass function of the progenitor (IMF), respectively. These are normalized as follows:

$$\int_{M_{\min}}^{M_{\max}} \psi_{\mathrm{IMF}}(M)dM = 1, \tag{1.36}$$

$$\int_0^{Z_{\max}} \psi_{\mathrm{ZF}}(z,Z)dZ = 1. \tag{1.37}$$

Although the flux is formed by all flavors of neutrinos and anti-neutrinos, hereafter, only electron anti-neutrinos are considered because the experiment generally searches through the SRN signal as the inverse beta decay of electron anti-neutrinos.

1.2.2 Contribution to the SRN flux

As discussed earlier, the SRN flux comprises various theories, parameters, and models on neutrinos and galactic cosmology. This section describes the modeling of compositions for SRN flux.

Neutrino Oscillation Effects

The number spectrum of $\bar{\nu}_e$, which forms the detection target of SRN for the neutrino detector, is influenced by the matter effect of neutrino oscillation up to the surface of the explosion, and the spectrum is a combination of all flavors, such as:

$$\begin{aligned}\frac{dN_{\bar{\nu}_e}}{E_\nu} &= \bar{P}_{ee}\frac{dN^0_{\bar{\nu}_e}}{E_\nu} + \bar{P}_{\mu e}\frac{dN^0_{\bar{\nu}_\mu}}{E_\nu} + \bar{P}_{\tau e}\frac{dN^0_{\bar{\nu}_\tau}}{E_\nu} \\ &= \bar{P}\frac{dN^0_{\bar{\nu}_e}}{E_\nu} + (1-\bar{P})\frac{dN^0_{\bar{\nu}_x}}{E_x},\end{aligned} \tag{1.38}$$

where $\bar{P}_{\alpha e}$ represents the probability that a neutrino with flavor α is converted to the electron type ($\alpha = e, \mu, \tau$), satisfying $\sum^{\alpha} \bar{P}_{\alpha e} = 1$, and $\frac{dN^0_{\bar{\nu}_\alpha}}{E_\nu}$ indicates the initial number spectrum as a function of M, Z, and E_ν when the neutrinos are created in the supernova, and $\bar{P} = \bar{P}_{ee}$ denotes the survival probability of $\bar{\nu}_e$ after traveling through stellar envelopes and space. As discussed in Section 1.1.3, using the PMNS matrix of Equation 1.10, the Equation 1.38 can be transformed into:

$$\begin{aligned}\frac{dN_{\bar{\nu}_e}}{dE_\nu} &= |U_{e1}|^2 \frac{dN_{\bar{\nu}_1}}{dE_\nu} + |U_{e2}|^2 \frac{dN_{\bar{\nu}_2}}{dE_\nu} + |U_{e3}|^2 \frac{dN_{\bar{\nu}_3}}{dE_\nu} \\ &= \cos^2\theta_{12}\cos^2\theta_{13}\frac{dN_{\bar{\nu}_1}}{dE_\nu} + \sin^2\theta_{12}\cos^2\theta_{13}\frac{dN_{\bar{\nu}_2}}{dE_\nu} + \sin^2\theta_{13}\frac{dN_{\bar{\nu}_3}}{dE_\nu},\end{aligned} \tag{1.39}$$

where the $U_{ei} (i = 1, 2, 3)$ denotes the corresponding matrix element noted in Equation 1.10, and $dN_{\bar{\nu}_i}/dE_\nu$ denotes the number spectrum of i-type neutrinos. According to Ref. [86], the lowest energy eigenstate corresponds to $\bar{\nu}_e$, and other states in the supernova core are assumed to be mixtures of the remaining types. Therefore, $dN_{\bar{\nu}_1}/dE_\nu$ can be approximated as $dN_{\bar{\nu}_1}/dE_\nu \sim dN^0_{\bar{\nu}_e}/dE_\nu$, $dN_{\bar{\nu}_2}/dE_\nu \sim dN^0_{\bar{\nu}_x}/dE_\nu$, and $dN_{\bar{\nu}_3}/dE_\nu \sim dN^0_{\bar{\nu}_x}/dE_\nu$ in case of normal hierarchy. These relations result in the following approximation in Ref. [3]:

$$\frac{dN_{\bar{\nu}_e}}{dE_\nu} \sim 0.68\frac{dN^0_{\bar{\nu}_e}}{dE_\nu} + 0.32\frac{dN^0_{\bar{\nu}_x}}{dE_\nu}. \tag{1.40}$$

Comparing with Equation 1.38, $\bar{P} \sim 0.68$ for the normal hierarchy is obtained. In contrast, under the inverted hierarchy, the $dN_{\bar{\nu}_i}/dE_\nu$ can be transformed as $dN_{\bar{\nu}_1}/dE_\nu \sim dN^0_{\bar{\nu}_x}/dE_\nu$, $dN_{\bar{\nu}_2}/dE_\nu \sim dN^0_{\bar{\nu}_x}/dE_\nu$, and $dN_{\bar{\nu}_3}/dE_\nu \sim dN^0_{\bar{\nu}_e}/dE_\nu$, based on which Equation 1.38 can be rewritten as

$$\frac{dN_{\bar{\nu}_e}}{dE_\nu} \sim \frac{dN^0_{\bar{\nu}_x}}{dE_\nu}, \tag{1.41}$$

where the terms with $\sin^2\theta_{13}$ is neglected owing to its negligibly small value. This results in $\bar{P} = 0$, indicating a complete transition. At this instant, the approximation assumes that the stellar density profiles are not sufficiently steep and do not consider the breaking of adiabaticity owing to the shockwave propagation. Furthermore, the neutrino-neutrino collective effect in the dense core is neglected.

Modeling of Galaxy Evolution

As described in Equation 1.35, the SRN flux depends on $R_{\mathrm{CCSN}}(z)$, and it can be expressed by a cosmic star formation rate density (CSFRD) ($\dot{\rho}_*(z)$) and the IMF $\psi_{\mathrm{IMF}}(M)$ as follows:

$$R_{\mathrm{CCSN}}(z) = \dot{\rho}_*(z) \times \frac{\int_{M_{\mathrm{min}}}^{M_{\mathrm{max}}} \psi_{\mathrm{IMF}}(M)dM}{\int_{0.1M_\odot}^{100M_\odot} M\psi_{\mathrm{IMF}}(M)dM}, \tag{1.42}$$

where M_{min} and M_{max} denote the minimum and maximum masses of the progenitor causing CCSN, respectively. The CSFRD $\dot{\rho}_*(z)$ denotes the mass density of the star

formation for all galaxies at given z and is obtained from

$$\dot{\rho}_*(z) = \int_0^\infty \dot{M}_*(M_*, z)\phi(M_*, z)dM_*, \tag{1.43}$$

where the $\dot{M}_*(M_*, z)$ indicates the star formation rate of a galaxy (SFR), M_* denotes the stellar mass, and $\phi(M_*, z)$ represents the stellar mass function (SMF). The measured data and the results obtained using model CSFRD are comparatively presented in Figure 1.5 as a function of the redshift. According to [3], the differences between each model increase for $z > 0.5$, corresponding to the lower energy region of the SRN flux.

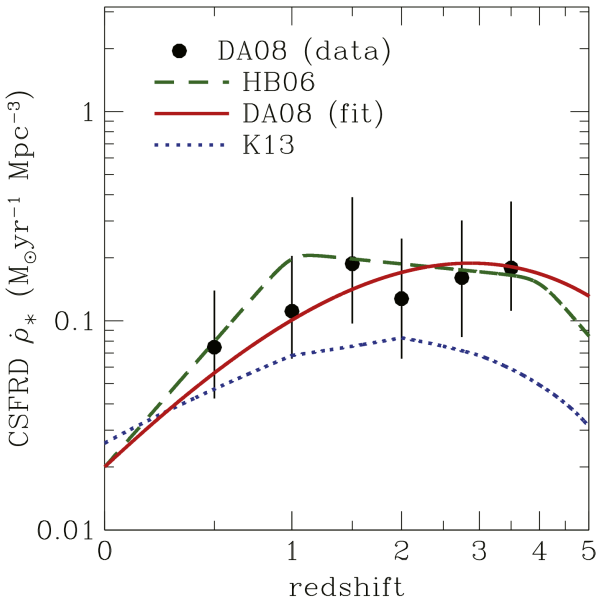

FIGURE 1.5: CSFRD distribution as a function of redshift. This plot is taken from [3].

The metallicity of the progenitor affects both star formation and evolution. According to [3], the relation between $\psi_{\mathrm{ZF}}(z, Z)$ and the SFR and SMF can be described as

$$\int_0^Z \psi_{\mathrm{ZF}}(z, Z')dZ' = \frac{\int_0^{M_*(z,Z)} \dot{M}_*(M'_*, z)\phi_{\mathrm{SMF}}(M'_*, z)dM'_*}{\int_0^\infty \dot{M}_*(M'_*, z)\phi_{\mathrm{SMF}}(M'_*, z)dM'_*}, \tag{1.44}$$

where $M_*(z, Z)$ denotes the stellar mass of a galaxy with metallicity Z at redshift z.

Other Contributions to the SRN Flux

The shockwave stalling duration, called the 'shock revival time,' affects the SRN flux. As described in Section 1.1.3, a shockwave is generated during CCSN. Although the shockwave typically stalls only once, it is revived by a specific mechanism. This revival time is estimated to be $\mathcal{O}(100)$ ms from the core bounce. A longer revival time increases the neutrino emission and neutrino energy because more material is accreted onto the core, and a significant amount of gravitational energy is released. The variations in the neutrino number spectra from CCSN with some assumed revival time are shown in Figure 1.6. The effect is critical for larger energy regions.

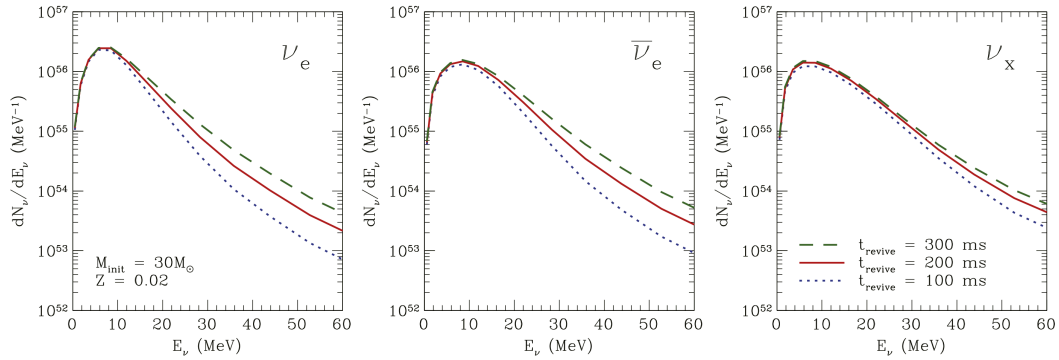

FIGURE 1.6: Difference of neutrino number spectrum of CCSN with $30M_\odot$ and $Z = 0.02$ for a progenitor depending on the shock revival time. The left, central, and right plots show the spectra corresponding to $\nu_e, \bar{\nu}_e$, and $\nu_x(\nu_\mu, \bar{\nu}_\mu, \nu_\tau, \bar{\nu}_\tau)$. This figure is sourced from [3].

The formation of black holes is correlated with the SRN flux. Stars that fail to explode and become black holes are called 'failed supernovae.' In the case of failed supernovae, the matter accretion continues until black hole formation, and generally, requires a longer period than the standard CCSN scenario. Therefore, the rate of progenitors forming black holes contributes to the SRN flux, especially in the higher energy region. Furthermore, the evolution of galactic metallicity is connected to the black hole formation rate.

Another significant contribution related to the failed supernovae to the SRN flux arises from the Equation-Of-State (EOS) of the progenitor and neutron star. A stiffer EOS results in a larger maximum mass of neutron stars and more substantial mass accretion, leading to a longer black hole formation time. Recent observations [87, 88] indicate that many stars form binaries with companion stars. These binary interactions, strongly affecting the CCSN rate, especially due to mass transfers and mergers, must be considered. It is a combined effect of the increasing and decreasing massive star and black hole-forming star.

1.2.3 Flux Predictions

Various SRN flux predictions have been proposed thus far. In this section, several of them are reviewed. The corresponding $\bar{\nu}_e$ fluxes are summarized in Figure 1.7. The difference among these flux predictions is approximately one order of magnitude.

- Hartmann+97 [16]
  To calculate the SRN flux, this model considers the cosmic chemical evolution in the calculation of the SRN flux. The evolution models are obtained from observations of a damped Ly α system.

- Malaney+97 [15]
  This model calculates the flux, including the redshift evolution of the cosmic gas, based on the observations of the absorption lines.

- Kaplinghat+00 [14]
  This calculation aims to minimize the dependence of any model on SRN flux by directly associating the supernova rate and its evolution with the observation of the metal enrichment history [89]. This model adopts conservative values for other uncertain parameters to establish a robust upper bound on the SRN flux.

- Ando+03 [12]
  This model considers a realistic neutrino oscillation into account for the first time and uses a numerical SRN spectrum [90] instead of the Fermi-Dirac distribution. In addition, the normal hierarchy and a vacuum oscillation are considered for the oscillation. The SRN flux displayed in Figure 1.7 is an updated version released at the NNN2005 conference [13].

- Lunardini09 [11]
  This model is the first model that accounted for the failed supernova rate to the SRN flux and separately considered the SRN flux originating from the failed supernovae rather than the neutron star-forming supernovae. As such, the flux from the failed supernovae contributes to the higher energy side and tends to be more luminous than the nominal supernovae.

- Horiuchi+09 [10]
  This calculation procedure of this model determines the CCSN rate based on the cosmic star formation history from the data [91] and cross-checks the various astrophysics and CCSN neutrino emission parameters at that instant. As depicted in Figure 1.7, the effective $\bar{\nu}_e$ temperature is assumed to be 6 MeV.

- Galais+10 [9]
  This research conducted comparative analytical solutions and numerical simulations, suggesting that the shockwave introduces significant modifications to the SRN flux. Consequently, the flux evaluated upon considering the shockwave effects is lower than that obtained without considering its effect.

- Nakazato+15 [3]
  This model considers the black-hole forming failed supernovae, including the cosmic metallicity evolution for the first time. In addition, the model investigates various effects on the SRN flux, such as the CSFRD, shock revival time, and EOS. As observed in Figure 1.7, two predictions estimated with varying combinations of CSFRD, shock revival time, and EOS were accounted as the largest and smallest fluxes.

- Horiuchi+18 [8]
  This model introduces critical compactness, which is a threshold for whether the core will become a neutron star or a black hole. The SRN flux assuming the critical compactness $\xi_{2.5,\mathrm{crit}} = 0.1$, is depicted in Figure 1.7.

- Kresse+20 [6]
  With state-of-the-art simulation, this model considers black hole formation along with the contributions from the helium stars to the SRN flux.

- Tabrizi+20 [5]
  This model considers the effect of additional neutrino transformation induced by the neutrino decay [92] to the nominal neutrino oscillation theory of it in a vacuum and the MSW effect, based on the Horiuchi+18 model[8].

- Horiuchi+21 [4]
  This model assesses the impact of the binary interaction of progenitors forming binary systems, such as mass transfer and mergers, on the SRN flux. In Figure 1.7, the SRN flux in the case of the envelope parameter $\alpha\lambda$, which determines the difficulty of unbinding the envelope, to be standard $\alpha\lambda = 0.1$ is shown.

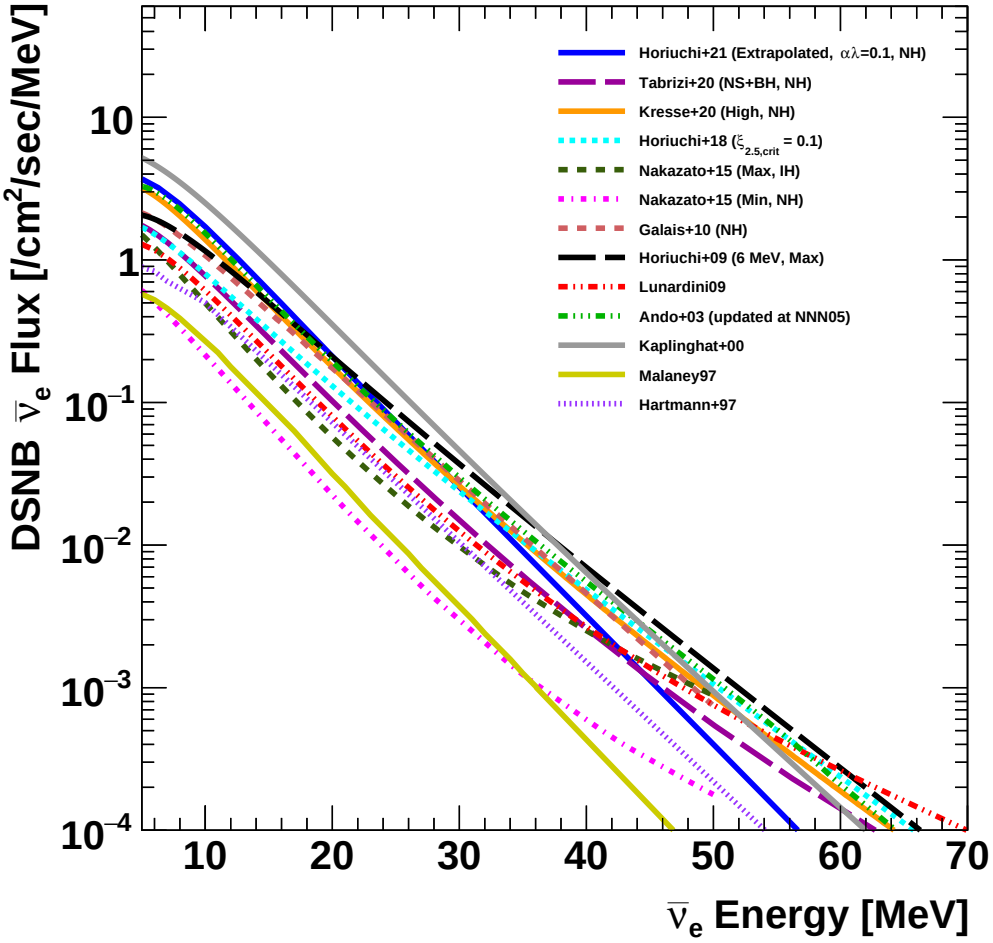

FIGURE 1.7: Summary of modern theoretical prediction of SRN flux [4, 5, 6, 7, 8, 3, 9, 10, 11, 12, 13, 14, 15, 16].

1.3 Current Status of SRN Search

Observation of the SRN can provide valuable information to support and enhance the theoretical understanding of supernovae and neutrino physics. Despite concerted efforts by neutrino experiments worldwide to detect the SRN, it is yet to be definitively identified. As discussed in Section 1.2, most experiments searched the positron signal via inverse-beta decay (IBD) of electron antineutrinos, as its cross-section is the largest in the O(10) MeV region (Figure 1.8).

Globally, the Super-Kamiokande (SK) Water Cherenkov experiment and the KamLAND Liquid Scintillator experiment provide the most stringent upper limit on the SRN flux. For the SK, the first search was performed over 1496 days of live time by fitting the spectrum for various backgrounds and the spectrum shape of each signal model [93]. The search is limited to the neutrino energy region of $E_\nu > 19.3$ MeV to prevent noise contamination from the large background from the muon spallation events. This search was updated with a longer exposure of 2853 days and a lowered energy threshold of $E_\nu > 17.3$ MeV by updating the analysis techniques [94]. Since

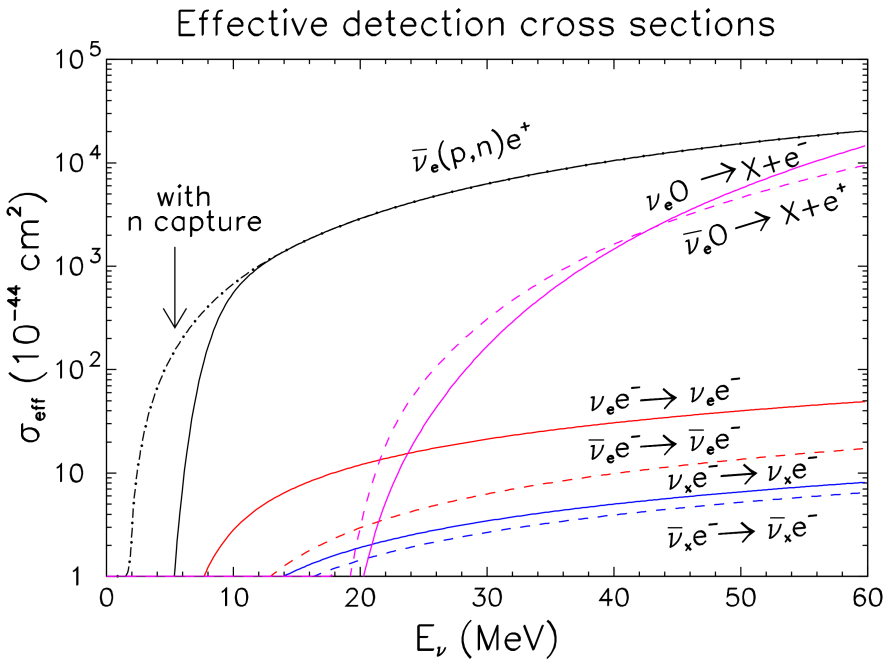

FIGURE 1.8: Effective cross-section including the resolution and threshold effect of certain detectors for each process below 60 MeV. This plot is taken from [17].

2008, an electronics upgrade has enabled longer recording periods after a primary trigger, as described in Chapter 2. This improvement has facilitated the tagging of a neutron from IBD interaction and the reduction of large backgrounds in the low-energy region, especially muon spallation events, which dominate in the energy region of $E_\nu < 17.3$ MeV. Consequently, the first energy binned search with the energy threshold lowered to $E_\nu > 13.3$ MeV was performed for 960 days [48]. The result of $E_\nu < 17.3$ MeV is practically inferior to the KamLAND results [19] owing to the lower statistics associated with the lower neutron tagging efficiency in SK, which is approximately 20%. Similarly, due to lower statistics in the energy region above 17.3 MeV, the limit was also inferior to the spectral analysis result of the combination of SK-I, II, and III.

The SRN search for SK during the pure water period was completed in 2021 with a live time of 2970 days along with neutron tagging [20]. The result is comparable with KamLAND results [19] in the region of $E_\nu < 17.3$ MeV and the SK spectral analysis results [94] observed at $E_\nu > 17.3$ MeV. In addition, the upper limits from the SK spectral analysis were also calculated for the modern SRN flux models over 5823 days of live time without neutron tagging. The result showed that the Totani+95 model [95] and the most optimistic prediction of the Kaplinghat model [14] could be excluded with above a 90% confidence level (C.L.). The upper limits on the $\bar{\nu}_e$ flux from the experiments are displayed in Figures 1.9 and 1.10.

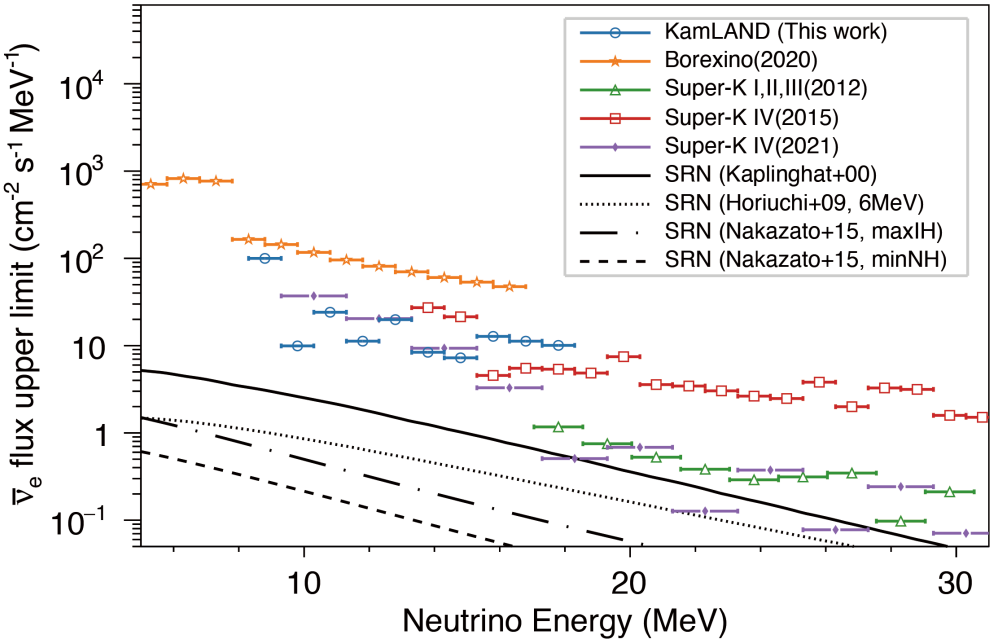

FIGURE 1.9: Upper limits on $\bar{\nu}_e$ flux from SK, KamLAND, and the Borexino experiment [18]. This figure is taken from [19].

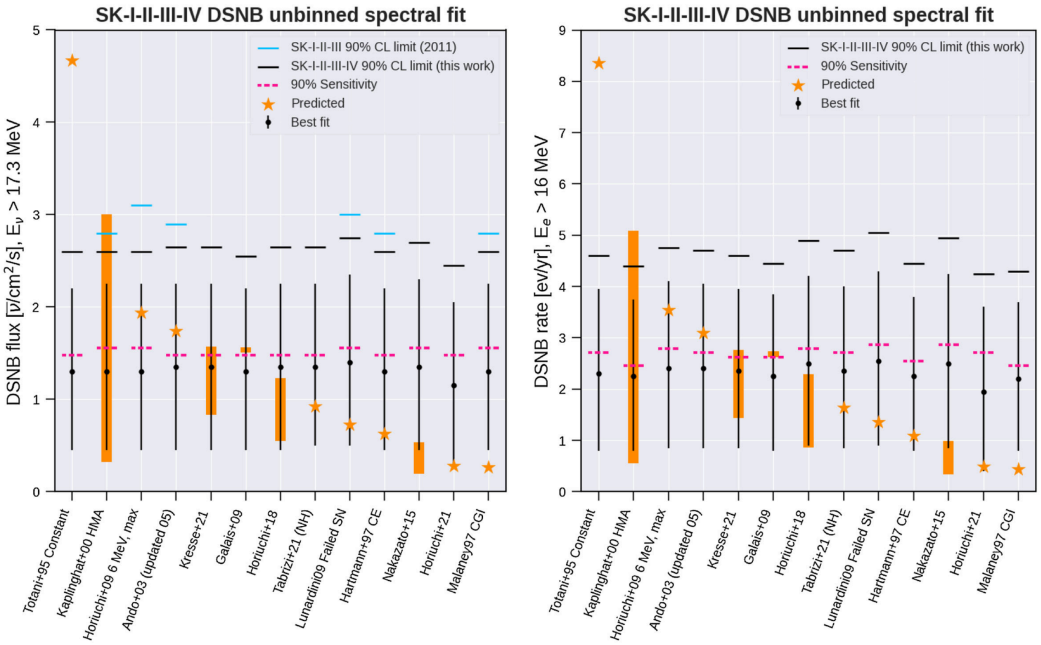

FIGURE 1.10: Upper limits on $\bar{\nu}_e$ flux from the SK [20].

Chapter 2

Super-Kamiokande

The Super-Kamiokande (SK) detector is the world's largest underground water Cherenkov detector[22].

2.1 Detection Principle

When a charged particle passes through a dielectric medium with a refractive index of greater than 1, at a velocity surpassing the speed-of-light within the medium, an electromagnetic shock, termed 'Cherenkov radiation,' transpires.

$$v > \frac{c}{n}, \tag{2.1}$$

where v denotes the velocity of the charged particle and n indicates the refractive index of the medium. The energy of the radiation light prevails in the optical region, and it is emitted in the cone shape with the half angle θ_{C}, which is calculated as

$$\cos\theta_{\mathrm{C}} = \frac{1}{n\beta}, \tag{2.2}$$

where β represents the ratio of the velocity of charged particles to the speed of light in a vacuum; n of the ultrapure water in the SK is ~ 1.33. Thus, the θ_{C} for an electron is $\sim 42^{\circ}$ because the speed of the electron can be approximated to the speed of light. In contrast, heavier particles such as muons and charged pions travel at speeds lower than electrons owing to their mass. Thus, the θ_{C} tends to be smaller than that of electrons. Based on Equation 2.1, β for the charged particles exhibit a minimum speed with Cherenkov emission (β_{thr}):

$$\beta_{\mathrm{thr}} = \frac{1}{n}, \tag{2.3}$$

Therefore, a threshold E_{thr} exists for the minimum energy of the charged particle (called 'Cherenkov threshold'), expressed as

$$E_{\mathrm{thr}} = mc^2\gamma = \frac{mc^2}{\sqrt{1-1/n^2}}, \tag{2.4}$$

where γ denotes Lorentz factor, $\gamma = (1-\beta^2)^{-1/2}$, and m indicates the mass of the charged particle.

The number of emitted photons N can be expressed in the form of a derivative of unit length L and photon wavelength λ as

$$\frac{d^2N}{dLd\lambda} = 2\pi\alpha\left(1-\frac{1}{n^2\beta^2}\right)\frac{1}{\lambda^2}, \tag{2.5}$$

where α indicates the fine-structure constant. Thus, the number of Cherenkov photons for the SK can be estimated to reach hundreds per centimeter.

2.2 Super-Kamiokande Detector

2.2.1 Detector Overview

The SK detector is situated at a depth of 1,000 m (2,700 m water equivalent) beneath Mt. Ikenoyama in Gifu Prefecture, Japan. Owing to the 1,000 m of overburden above the detector, the cosmic-ray muon background is diminished by a factor of 10^{-5} relative to the mountain's surface. The detector comprises a cylindrical tank with a 39.3 m diameter and 41.4 m height. The tank accommodates 50 kilotons of ultrapure water, serving as both the target material and dielectric medium for Cherenkov radiation. The layout of the detector is depicted in Figure 2.1.

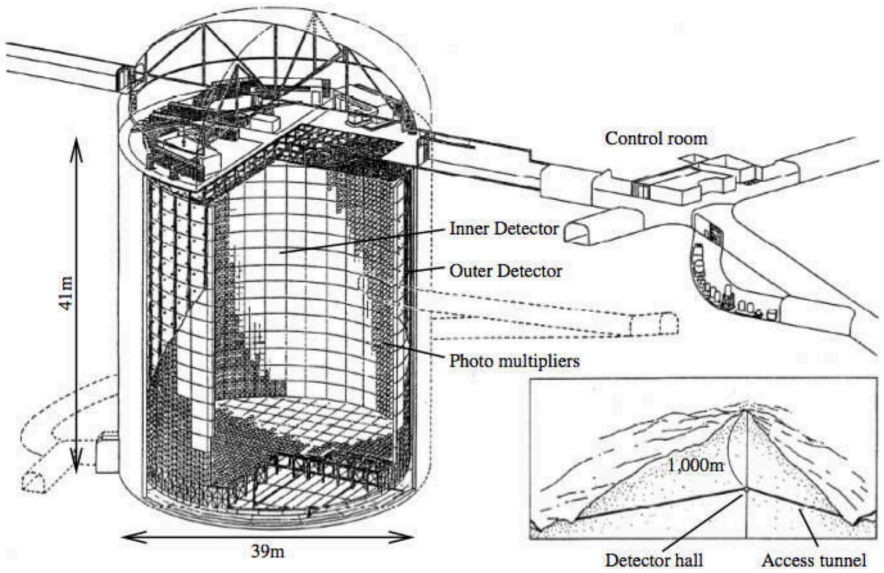

FIGURE 2.1: Schematic of view of the SK detector (cutaway view). This figure is taken from [21].

The water tank of the SK is optically partitioned into an inner tank (ID) and an outer tank (OD), with approximately 60 cm width of a stainless steel structure separating the ID and the OD. The ID has a diameter of 33.8 m and a height of 36.2 m, with a total water mass of approximately 32.5 kilotons. Additionally, 11,129 20-inch photomultiplier tubes (PMTs) are mounted on the ID wall, top, and bottom structures directed inwards. The photo-cathode coverage for the entire ID surface is $\sim$ 40%. The gap between each PMT is concealed by a black sheet that exhibits minimal light reflectance and restricts the reflection of light on the ID surface. Consequently, ID and the stainless-steel structure remain optically isolated.

The thickness of the OD is $\sim$ 2 m, encompassing a total water mass of $\sim$ 17.5 kilotons. In total, 1,885 8-inch PMTs are affixed to the ID-OD separation structure, oriented outwards. The inner surface of the OD is covered by a white Tyvek sheet, exhibiting high photon reflectivity, on the OD side, and a black sheet on the opposing side. Similar to the gaps between PMT, those between the OD and the stainless-steel structure are also optically separated by the white Tyvek and black sheets. Additionally, the photon collection efficiency is enhanced by the elevated reflectivity of

the Tyvek sheet. A structure comprising 12 ID PMTs, 2 OD PMTs, an OD Tyvek sheet, and an ID black sheet is termed a Super-Module. The schematic cross-sectional views of the ID, OD, and separation structure for the top, side, and bottom of the Super-Module, are displayed in Figure 2.2.

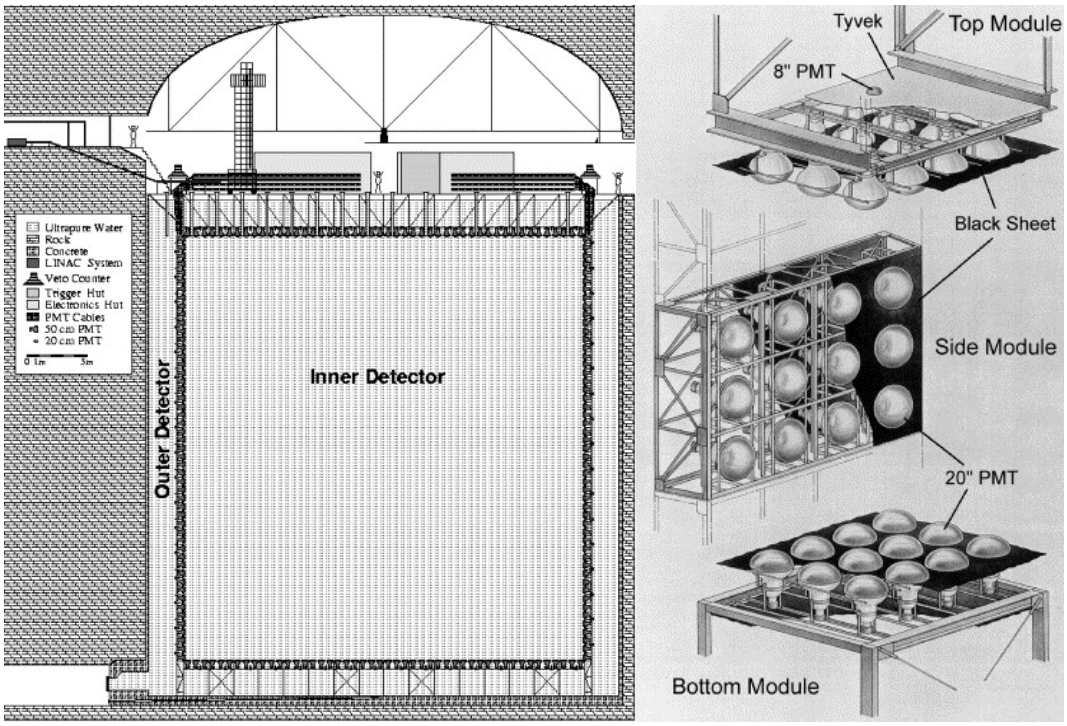

FIGURE 2.2: Overall schematic of SK (Left) and magnified to each face of the support structure (Right)[22].

2.2.2 History of SK phase

The SK experiment commenced in April 1996, with the observational phase segmented into seven periods: SK-I through SK-VII. Each period is distinguished by alterations in the geometry, electronics, and post-dissolution of gadolinium. The state of the detector for each phase is summarized in Table. 2.1

SK-I

SK-I commenced in April 1996 and was terminated in July 2001, employing the initial electronics system called ATM. During this period, certain preliminary observational results were published regarding solar and atmospheric neutrinos and the search for proton decay search within the SK. Most notably, the evidence demonstrating neutrino oscillation for the atmospheric neutrinos was revealed, which is deemed as one of the world's most significant results.

In July 2001, the replacement work for damaged PMTs was conducted. However, on November 12, 2001, a PMT at the bottom imploded, triggering a chain reaction that destroyed more than half of the PMTs–approximately 7,900 in total.

SK-II

Following the accident, the experiment was temporarily halted. The remaining ID PMTs were relocated during this pause, and new OD PMTs were installed. Additionally, each ID PMT was encased in an acrylic and Fiberglass Reinforced Plastic (FRP) case, enhancing the water pressure resistance of PMT and mitigating the risk of chain destruction if damage occurred. The part covering the photo-cathode is constructed from high-transparency acrylic, whereas its other components are fabricated from FRP. An image of the case is displayed in Figure 2.3. The experiment resumed in October 2002 with 5,182 ID PMTs in place, amounting to 19% photo-cathode coverage. This period is known as SK-II.

FIGURE 2.3: Image of the shockwave prevention case for 20-inch PMT

SK-III

Between SK-II and SK-III, new ID PMTs were manufactured and installed. SK-III commenced in July 2006, at which point 40% of photo-cathode coverage was recovered. During this period, 17 ID PMTs installed at the top and bottom edges of the tank during SK-I were removed due to the conflict with the acrylic cover. Consequently, the SK has operated with 11,129 ID PMTs and 1,885 OD PMTs from this period onward.

SK-IV

In September 2008, a new data acquisition(DAQ) system known as QBEE was installed instead of the ATM, enabling the recording of extended PMT signal time windows for neutron search. The specifications of the QBEE are described in Section 2.4.

SK-V

In May 2018, a tank refurbishment was initiated in preparation for loading gadolinium into the SK tank. The process was completed by the end of January of the following year, initiating the new SK-V phase. Various preparations for the forthcoming SK-Gd

experiment were carried out during this period, such as changes to the water flow, water leakage repairs, and PMT replacements.

SK-VI

In July 2020, the SK experiment was reincarnated as the 'SK-Gd' experiment by loading 13 tons of $Gd_2(SO_4)_3 \cdot 8H_2O$, equivalent to about 0.011 ppm of Gd, into the ultrapure water of SK. Loading Gd enhances the neutron signal, achieving higher neutron identification efficiency than in the previous period. This phase continued until the end of May 2022 and is referred to as SK-VI.

SK-VII

From June 2022, three times the amount of Gd was loaded into the SK detector, concluding the loading process in July. The additional loading increased the neutron capture fraction on Gd to approximately 1.5 times higher than that in SK-VI. This period is designated as SK-VII.

TABLE 2.1: The detector situation for each observation period of SK.

Phase	SK-I	SK-II	SK-III
Start	Apr. 1996	Oct. 2002	Jul. 2006
End	Jul. 2001	Oct. 2005	Aug. 2008
Live days	1496 days	791 days	548 days
Num. of ID PMT (Coverage)	11146 (40%)	5182 (19%)	11129 (40%)
Electronics		ATM	
Analysis threshold	5 MeV	7 MeV	4.5 MeV

Phase	SK-IV	SK-V	SK-VI	SK-VII
Start	Sep. 2008	Feb. 2019	Jul. 2020	Jun. 2022
End	May. 2018	Jul. 2020	May. 2022	–
Live days	3235 days	530 days	623 days	–
Num. of ID PMT (Coverage)	11129 (40%)			
Electronics	QBEE			
Analysis threshold	3.5 MeV			

2.2.3 ID PMT

The PMT used on the ID is the Hamamatsu R3600, produced by Hamamatsu Photonics K.K. This PMT has a diameter of 20-inches (about 50 cm). Figure 2.4 provides an overview of the Hamamatsu R3600 PMT. The photocathode of the PMT consists of bialkali(Sb-K-Cs), which offers excellent quantum efficiency for the wavelength of Cherenkov light. The sensitivity range of this PMT extends from 280 to 660 nm, and the quantum efficiency (QE) peaks at about 22% at the peak of $\sim$ 390 nm, as illustrated at the top of Figure 2.5.

The average collection efficiency at the first dynode is around 70%, and the PMT gain is approximately 10^7 at around 2000 V of HV. The transit time is roughly 10 ns, with a relative spread of about 2.2 ns at one sigma. The nominal distribution of the transit time can be observed in the bottom left panel of Figure 2.5. The single photo-electron (p.e.) peak is visible in the ADC charge distribution, depicted in the

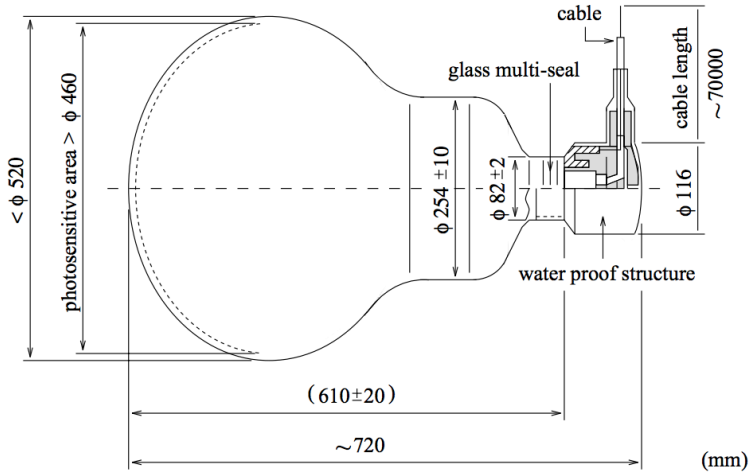

FIGURE 2.4: Overview of Hamamatsu R3600 used for SK ID PMT [22].

bottom right panel of Figure 2.5. The distributions illustrated in Figure 2.5 were obtained from tests conducted with the 410 nm wavelength light.

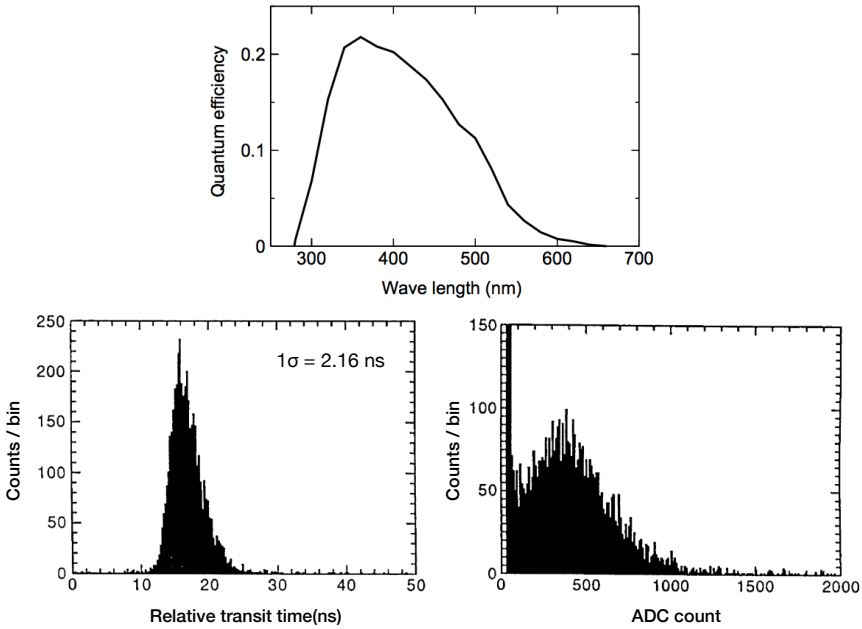

FIGURE 2.5: Wavelength dependence of QE (top), distribution of relative transit time (bottom left), and ADC charge count distribution(bottom right) for Hamamatsu R3600 PMT [22].

2.2.4 OD PMT

The PMT installed on the OD surface has a diameter of 8 inches (about 22 cm). These were repurposed from the IMB experiment [96] during the SK-I period. After the 2001 accident, most of OD PMTs were replaced with new ones, the Hamamatsu R5912. These PMTs are of similar size and possess comparable photon sensitivity

characteristics to the IMB PMTs. To compensate for the smaller coverage of OD PMT, each PMT is affixed to a wavelength shifter (WS) plate measuring 60 cm × 60 cm × 1.3 cm. The WS is an acrylic plate impregnated with 50 mg/L of bis-MSB($C_{24}H_{22}$), which absorbs light in the wavelength of ultraviolet range and emits light in the blue to the green range, which is close to the peak of QE for the OD PMT. Thanks to the WS, the collection efficiency of the OD increases to 60%. However, the timing resolution has decreased from 13 ns to 15 ns. Presently, 1,275 OD PMTs are evenly distributed on the OD walls, with 308 on the bottom and 302 on the top. An overview of the OD PMT setting and the relationship between ID and OD PMT is illustrated in Figure 2.6.

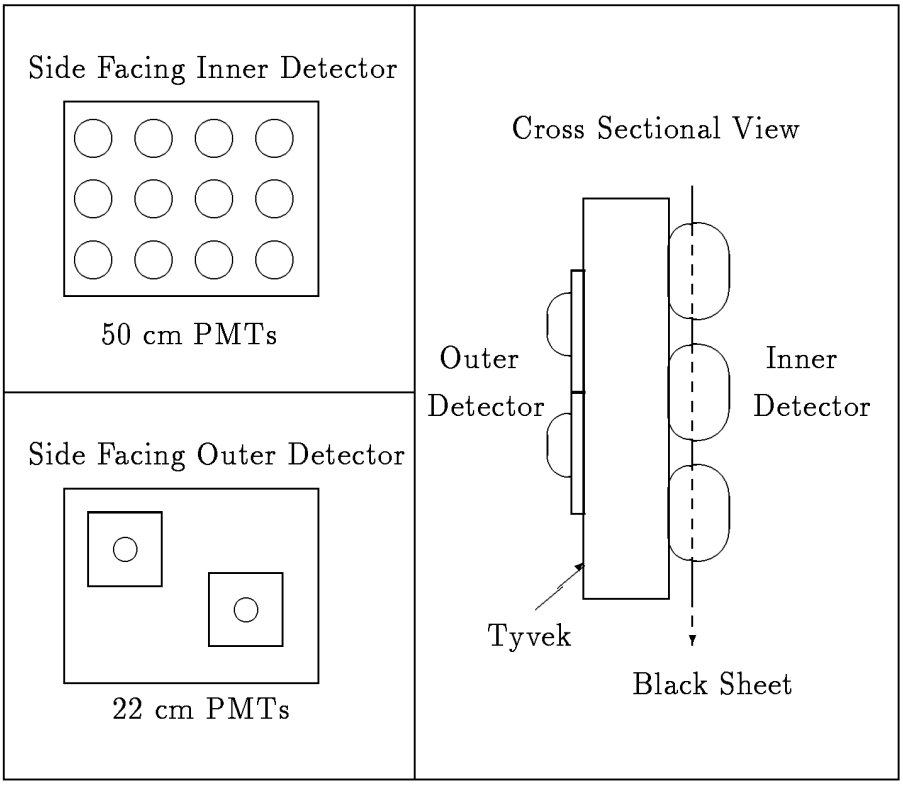

FIGURE 2.6: Relationship between ID PMT and OD PMT [23].

2.2.5 Compensation Coils

The photo-electron emitted on the surface of the photocathode is collected by the electric field of the PMT. During this process, the geomagnetic field can affect the collection efficiency. To mitigate this effect, 26 sets of coils are wound around the tank to compensate for the geomagnetic field within the tank. Thanks to these coils, the magnetic field within the tank is kept below 100 mG. The schematic view of the compensation coils is illustrated in Figure 2.7.

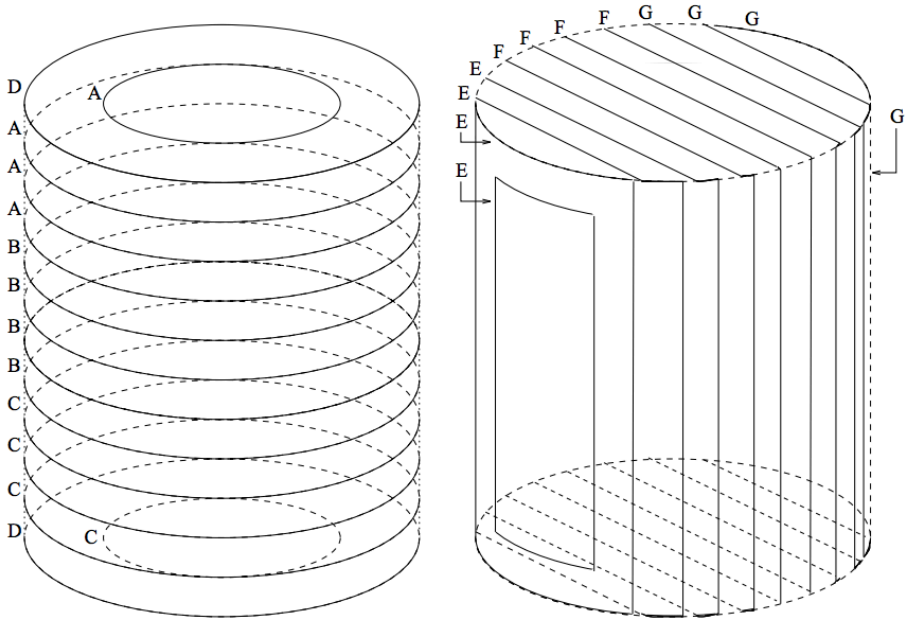

FIGURE 2.7: Schematic view of compensation coils wounding the SK tank [24].

2.3 Water and Air purification system

2.3.1 Water purification

Water system at SK-IV

Until the end of the SK-V phase, the SK tank was filled with ultrapure water transported from the Kamioka mine. Dust, radioactive contaminants, and bacteria can cause low-energy background events and degrade water transparency. As a result, a water purification system is implemented, circulating water at a rate of roughly 60 tons/hour to eliminate these impurities. Since the water flow and PMT noise rates are highly sensitive to the water temperature, the system maintains the water at approximately 13°C. The schematic of the water purification of SK-IV is illustrated in Figure 2.8.

The flow of water purification is detailed as follows:

- 1 μm mesh filter: Removes dust and larger impurities
- Heat exchanger (HE): Exchange heat from the water circulation pump and maintain the water temperature at approximately 13 °C. This aids in preventing increased PMT dark noise, stabilizing water flow, and hindering bacteria growth that occurs at high water temperatures.
- Ion exchanger: Eliminates heavy ions that can decrease water transparency, including radioactive contaminants.
- UV sterilizer: Kills bacteria present in the water by irradiating ultraviolet light.
- Radon-free Air Dissolving system: Dissolves radon-free air into the water to enhance the radon removal efficiency in the subsequent vacuum degasification step.

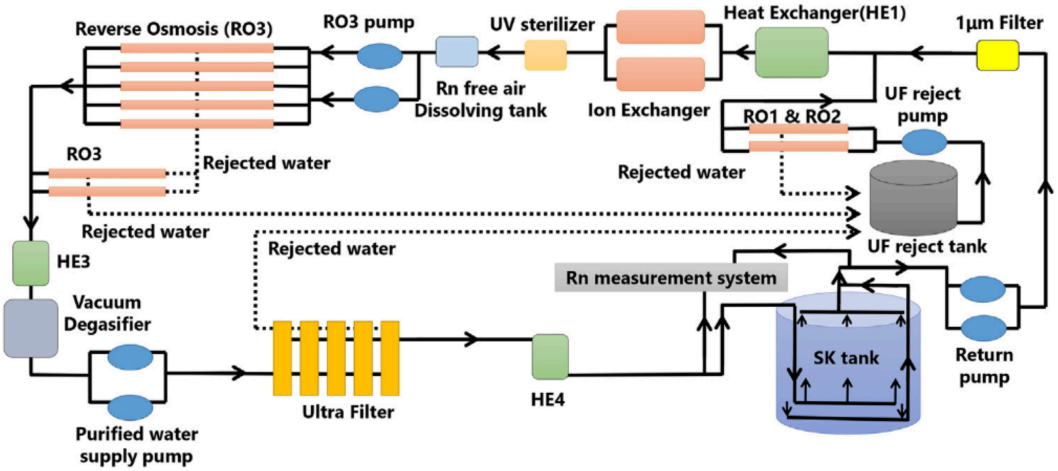

FIGURE 2.8: Schematic diagram of the water purification system in SK-IV. This figure is taken from [25].

- Reverse Osmosis filter(RO): Further removes organic contaminations with molecular weights of about 1000.
- Vacuum degasifier: Removes gases dissolved in the water with an efficiency of 96% for radon and 99% for oxygen gas.
- Ultra filter(UF): Removes small particles that are larger than the size of 10 nm.
- Membrane Degasifier: Reduces the radon gas dissolved in the water with an efficiency of approximately 83%.

After these steps, the radon concentration in the supply water entering the SK tank is estimated to be 1.74 ± 0.14 mBq/m^3, whereas that of the return water is 9.06 ± 0.58 mBq/m^3. The water resistivity entering the purification system is typically 11 MΩ · cm. However, because of these meticulous purification steps, the resistivity of water entering the SK tank increases to about 18.2 MΩ · cm.

Water system from SK-V

In the SK-V phase, the water purification system was entirely revised in preparation for the subsequent SK-Gd experiment. Figure 2.9 illustrates the new water circulation system for SK-Gd. In this experiment, it is crucial to eliminate contaminants at the same level as in the SK-IV phase, while preserving the gadolinium and sulfate ions dissolved in the water.

During the Gd-dissolving process, a high-concentration Gd solution first passes through the pretreatment system. This system comprises three filters, UV light, and Ion-exchange resins (yellow dotted box in Figure 2.9). The ion exchanger (Anion and Cation resins) used in SK-Gd is specifically designed to prevent the loss of dissolved gadolinium and sulfur ions. The main recirculation system is branched into two identical parts, each with a water flow capacity of ~ 60 m^3/h. The water flow rate can be controlled up to 120 m^3/h using both branches. The design also allows continuous circulation with one line while the other is under maintenance.

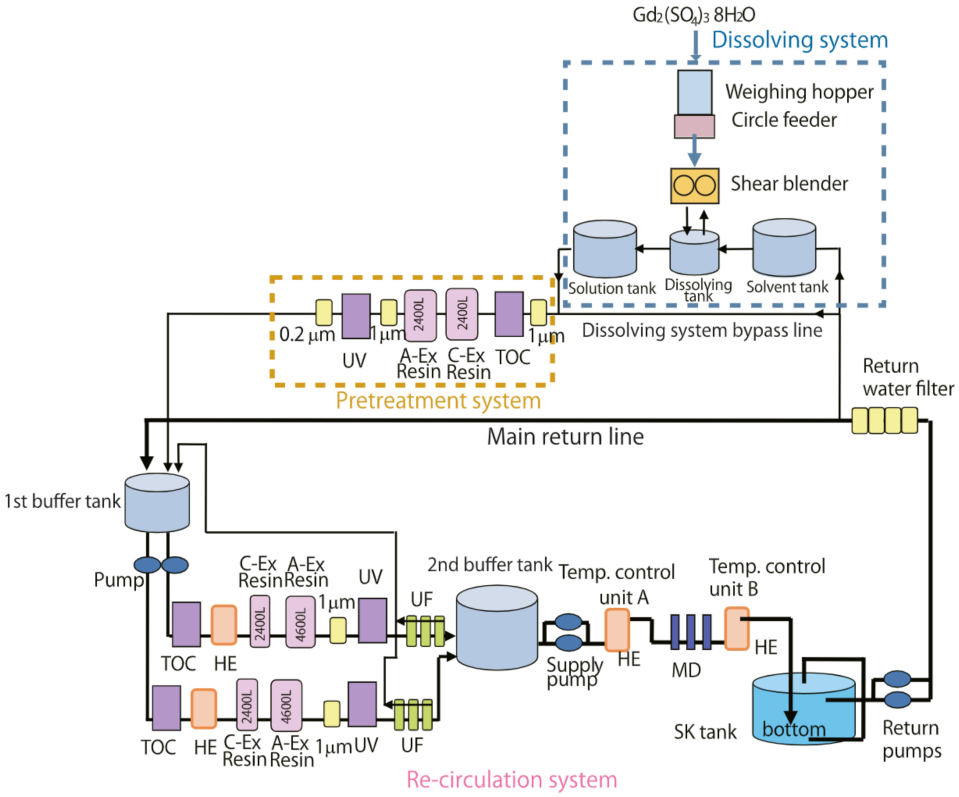

FIGURE 2.9: Schematic of SK-Gd water system. This figure is taken from [26].

2.3.2 Air purification system

As the rock is Rn-rich, the air in the mine is abundant in Rn gas, substantially more than the Rn gas concentration in the air outside of the mine. Radon gas concentrations in the mine air fluctuate between 1000 and 2000 Bq/m^3 during summer and between 100 and 300 Bq/m^3 during winter because of the variation in airflow inside the mine induced by the outside temperature. Accordingly, the air purification system is utilized to reduce Rn in the air inside the mine and produce Rn-free air. This system comprises three compressors, a buffer tank, dryers, filters, and activated charcoal filters, and it reduces the Rn concentration in the Rn-free air to < 3 mBq/m^3. Post-purification, Rn-free air is introduced into the space between the water surface and the top of the inside of the SK tank.

2.4 Electronics and Data Acquisition

The electronics for data acquisition were uploaded from SK-IV to a new system named QBEE [28]. The data used in this study were acquired during the period of these newer electronics. Thus, the detailed explanations of the older ATM system are omitted.

2.4.1 Electronics and DAQ from SK-IV

From SK-IV, the DAQ system was switched to QTC-based Electronics with Ethernet (QBEE), replacing the older Analog-Timing-Module (ATM). Figures 2.10 and 2.11 provide schematic diagrams of the QBEE electronics and the entire DAQ system of SK.

Each QBEE module is fitted with eight QTCs designed for Application-Specific Integrated Circuits (ASIC) [27]. Each QBEE processes 24 PMT signals because each QTC has three channels. When a charge, exceeding the threshold equivalent to 1/4 p.e., is sent to a QBEE module, the QTC integrates the charge and emits a rectangular pulse proportional to the integrated charge. The leading edge of the pulse signifies the timing of the signal. Each QTC has three different gain ranges, labeled 'Small,' 'Medium,' and 'Large,' to enhance charge resolution and expand the charge range from ATM. The gain ratio for each gain range is set at 1, 1/7, and 1/49. The total charge range is 0.2–2500 pC, roughly five times larger than the ATM module. The detectable dynamic ranges, including the charge resolution for each range, are listed in Table 2.2.

The pulse generated in QTC is transmitted to the TDC and digitized. The digitized charge and timing information is then processed by an FPGA before being transmitted to the front-end PC via Ethernet, as depicted in Figure 2.11. These front-end PCs are connected to Merger PCs via a 10-Gigabit Ethernet cable. This connection initiates the event-building process, during which a software trigger is applied to signals, and selected candidates are used for analysis. Ultimately, the event information is gathered by the Organizer PC and stored on the Disk.

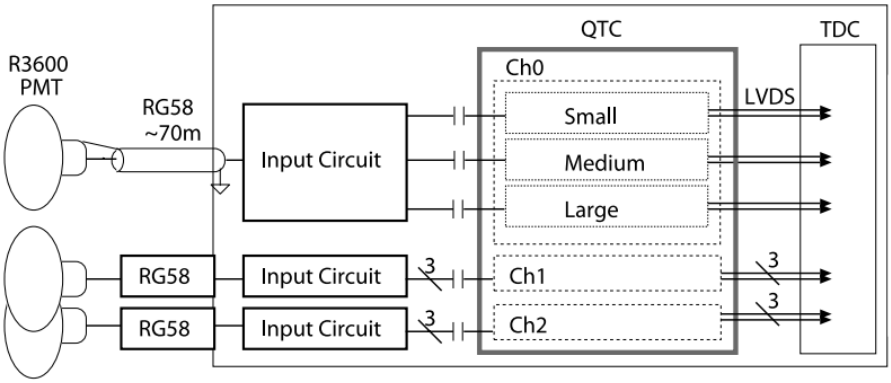

FIGURE 2.10: Schematic of the DAQ system with QBEE[27].

TABLE 2.2: Detectable dynamic range and charge resolution for each range.

Gain channel	Dynamic range [pC]	Charge resolution [pC/Count]
Small	0.2-51	0.1
Medium	1-357	0.7
Large	5-2500	4.9

2.4.2 Software Trigger

With the high-speed signal digitization capabilities of the QBEE system, all PMT hits can tentatively be collected on the merger PC. As a result, the signals gathered in the Merger PC can be processed by the software trigger and formed into an event. The software trigger initiates a trigger when the number of hits within a 200 ns window, corresponding to the time for light to travel from one edge of the tank to the other, exceeds a specific threshold. There are four types of triggers for ID: SHE(Super High

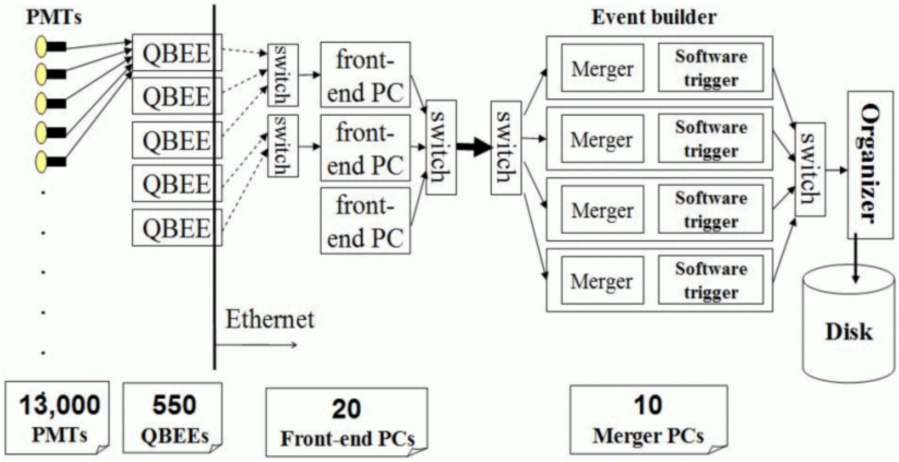

FIGURE 2.11: Schematic of the DAQ system with QBEE[28].

Energy), HE(High Energy), LE(Low Energy), SLE(Super Low Energy), and one OD trigger. Table 2.3 displays the standard trigger conditions in SK-VI. When a trigger is issued, all hits from -5 μsec to $+35$ μsec are recorded for SHE, HE, and LE, as a larger time window makes it easier to efficiently tag subsequent signals such as Michel electrons from muon decays. Due to their high rate, only PMT hits around 1.5 μsec are saved for SLE events.

A special trigger, AFT, was implemented from SK-IV onward to save delayed neutron capture signals. Following the issuance of the SHE trigger, a 500 μsec window opens, during which all hits are recorded. To conserve data capacity and transfer rate, the AFT trigger is issued only after an event with the SHE trigger and without the OD trigger, i.e., the trigger is not issued by muon until SK-IV. The AFT rate limit is set to 50 Hz, as this trigger was originally designated for the Inverse-Beta decay of electron anti-neutrinos. However, owing to increased interest in neutron events caused by muon events, including muon spallation, the condition of no OD trigger was removed from the AFT trigger conditions from the commencement of SK-V. Moreover, the limit of the AFT rate was further broadened by upgrading the online system from the middle of SK-VI onwards.

TABLE 2.3: Threshold for each type of trigger in SK-VI

Trigger type	N_{200} Threshold [/μsec]	Event window [μsec]	Trigger rate [Hz]
SLE	34	1.5 [-0.5,+1.0]	3.0-4.0
LE	49	40 [-5,+35]	80
HE	52	40 [-5,+35]	30
SHE	60	40 [-5,+35]	3
OD	22(Only OD)	40 [-5,+35]	2

Chapter 3

Simulation

This chapter describes the Monte Carlo (MC) simulation and the tools used in the SK analysis. The events studied in the SK are divided into low-energy and high-energy events, with the boundary set at an energy level of approximately 100 MeV. The simulation stage of a neutrino event is divided into three primary parts: neutrino flux calculation, neutrino interaction, and detector simulation. Notably, the neutrino flux calculation and neutrino interaction components are characteristic of each event type.

3.1 Simulation for High-Energy Neutrino Event

High-energy neutrino events are predominantly composed of Atmospheric neutrinos, making their simulation complex due to various types of neutrinos and secondary products that span a wide energy range. The main visible energy range for the DSNB search is around a few tens of MeV. However, some events resulting from the atmospheric neutrino interaction and subsequent secondary interaction extend into the search region. Hence, precisely simulating of the atmospheric neutrino events is crucial for the DSNB search.

3.1.1 Atmospheric neutrino flux

Atmospheric neutrinos are produced in the Earth's atmosphere via the decay of mesons and muons from cosmic rays, as illustrated in Figure 3.1. Despite various atmospheric neutrino flux models, the flux calculation for the SK is based on the Honda-Kajita-Kasahara-Midorikawa(HKKM) model [97, 98, 99, 33, 29]. This model primarily comprises three parts: primary cosmic-ray flux, hadronic interaction models, and a virtual detector.

Primary cosmic-ray

The primary cosmic-ray flux has been measured by several experiments to date. The flux below 100 GeV is accurately estimated by the BESS experiment [100, 101] and the AMS experiment [102]. For flux above 100 GeV, the flux curve is effectively calibrated by data obtained from the emulsion chamber [103, 104]. The primary cosmic-ray flux at the Earth's surface is influenced by solar activity. Given the periodicity of solar activity, the cosmic-ray flux is classified by high and low activity periods. Depending on solar activity intensity, cosmic rays at around 1 GeV can fluctuate by a factor of 2 or more, while at 10 GeV and above, the difference is about 10%.

Additionally, the incoming cosmic-ray particles are influenced by the geomagnetic field. This effect is calculated based on the position and direction of the incoming particle, and the calculation employs the IGRF2005 model https://www.ngdc.noaa.gov/IAGA/vmod/igrf.html. The cosmic rays penetrating the atmosphere interact

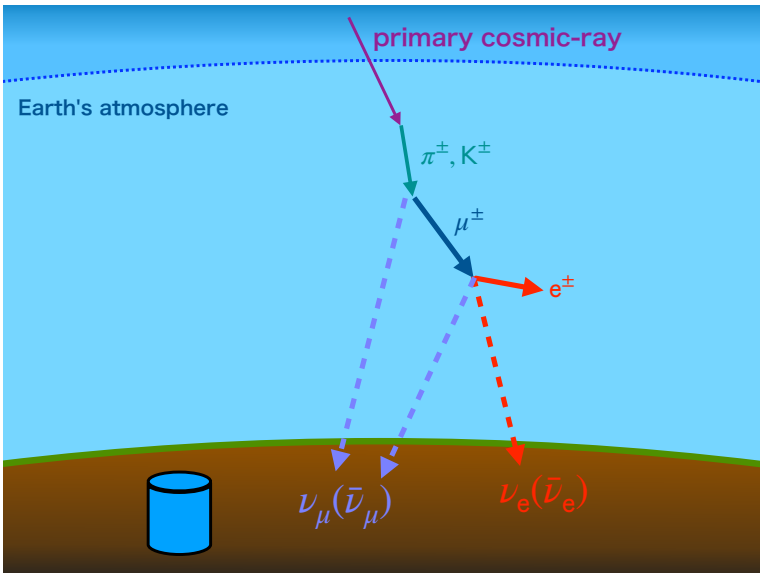

FIGURE 3.1: Illustration of atmospheric neutrino production.

with air molecules, primarily generating mesons. The calculation adopts the U.S. standard'76 model for the atmospheric environment. This model provides atmospheric data such as pressure, temperature, density, and viscosity, encompassing a vast range of altitudes and elevations globally.

Hadronic interaction

Two models for cosmic-ray interaction with molecules are implemented, with 32 GeV as the dividing line. Below 32 GeV, the JAM model [105] is utilized, whereas above 32 GeV, the DPMJET-III [106] is applied for calculation. The JAM model is a hadronic cascade model employed for Particle and Heavy-Ion Transport code Systems (PHITS) [107]. DPMJET-III is a code system based on the Dual Parton Model (DPM) [108] capable of calculating interactions such as those involving hadrons above a few GeV, nuclei, and high-energy photons. The JAM, DPMJET-III, and the results of the Hadron Production (HARP) experiment are comparatively presented in Figure 3.2 [109, 110]. The HARP experiment examined the hadronic interactions of protons on N_2 and O_2 targets at a few GeV/c momentum regions.

The mesons resulting from the hadronic interaction of cosmic rays further decay into secondary muons referred to as cosmic-ray muons. The flux of cosmic-ray muons from the simulation is compared with some experimental results. The flux of cosmic-ray muon was measured by BESS [101][111] and L3+C experiment [112]. The DPMJET-III was refined based on these results. Figure 3.3 displays the comparison of the flux of cosmic-ray muon between various experimental data and simulation, displaying an agreement within 10% for the 1–100 GeV range.

Neutrino Flux at the SK

Figure 3.4 illustrates the zenith angle dependence of the atmospheric neutrino flux at the Kamioka site, computed using the Honda flux model. The peaks depicted in Figure 3.4 are due to the greater travel distance for muons and pions from the horizontal than the vertical direction. The up-down asymmetry in the lowest energy region is induced by the geomagnetic field for the charged cosmic-ray particles.

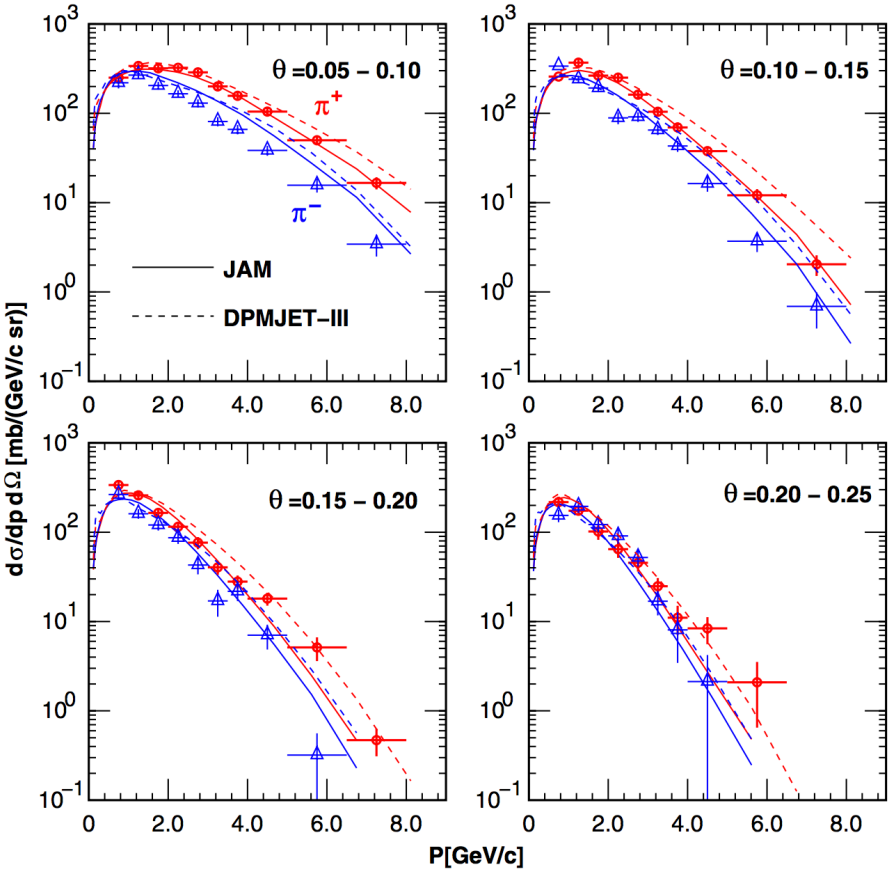

FIGURE 3.2: Comparison between HARP data and the theoretical calculations of JAM and DPMJET-III for the cross-section of pion production. The figures are taken in [29].

The spectra of the atmospheric neutrinos coming to Kamioka using various models are displayed in Figure 3.5. Since the cosmic-ray muon, which is the source of electron neutrinos, reaches the Earth's surface before decaying into electron neutrinos, a faster drop in electron neutrinos appears in the higher energy region as depicted in Figure 3.5.

The atmospheric neutrino events are simulated based on the expected flux at Kamioka. It should be noted that the neutrino oscillation effect is not considered at this stage. It is assumed that the neutrino created in the atmosphere reaches the SK while maintaining its original flavor. Then, the neutrino oscillation effect is taken into account by calculating weight based on the latest neutrino oscillation analysis result [72] for each MC event at the analysis stage.

The oscillation parameters used in this study are listed as follows:

$$\Delta m^2_{21} = 7.53 \times 10^{-5}\ \text{eV}^2 \text{ (fixed in fit)} \tag{3.1}$$
$$\Delta m^2_{32} = 2.50 \times 10^{-3}\ \text{eV}^2 \text{ (fixed in fit)} \tag{3.2}$$
$$\sin^2\theta_{12} = 0.304 \text{ (fixed in fit)} \tag{3.3}$$
$$\sin^2\theta_{13} = 0.0219 \text{ (fixed in fit)} \tag{3.4}$$
$$\sin^2\theta_{23} = 0.588 \text{ (fitted)} \tag{3.5}$$
$$\delta_{CP} = 4.18 \text{ (fitted)} \tag{3.6}$$

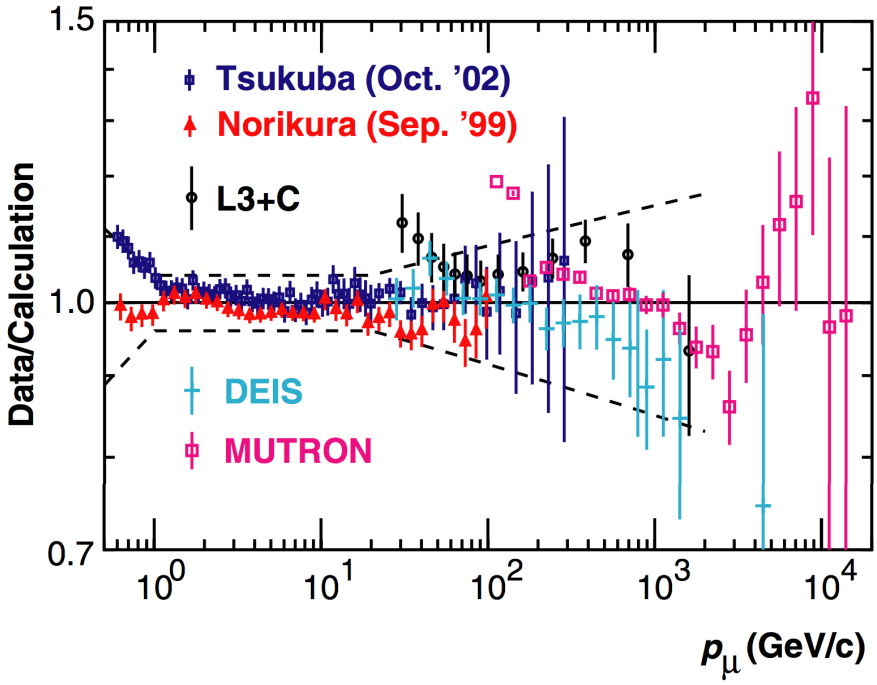

FIGURE 3.3: Comparison of muon flux between the theoretical calculations and experimental data. Dashed line represents the sum of the error in the calculation and observation at Mt. Tsukuba (blue squares), at Mt. Norikura(red triangles) using the BESS detector, and at CERN using the L3 detector(black circles). Results from the DEIS experiment [30] and MUTRON experiment [31] are presented as well. The figure is taken from [32].

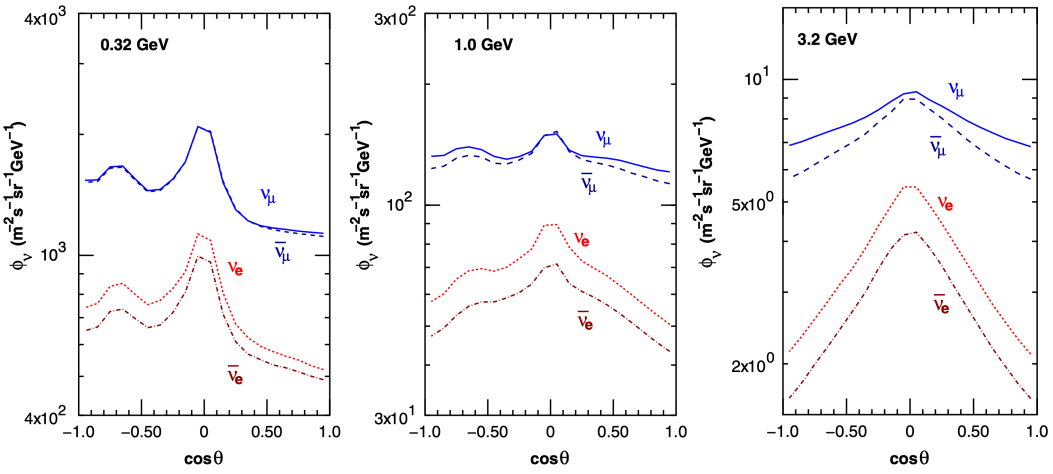

FIGURE 3.4: Zenith angle dependence of atmospheric neutrino flux, averaged over all azimuthal angles, for Kamioka. Here the θ is the zenith direction of coming neutrinos. The figure is taken from [29].

3.1.2 Neutrino Interaction

The neutrino interaction at the SK is calculated based on NEUT [36] [113]. NEUT manages the neutrino interaction with the water (H_2O) and the rocks around the detector (SiO_2) as the target material for the energy range of a few tens MeV to a

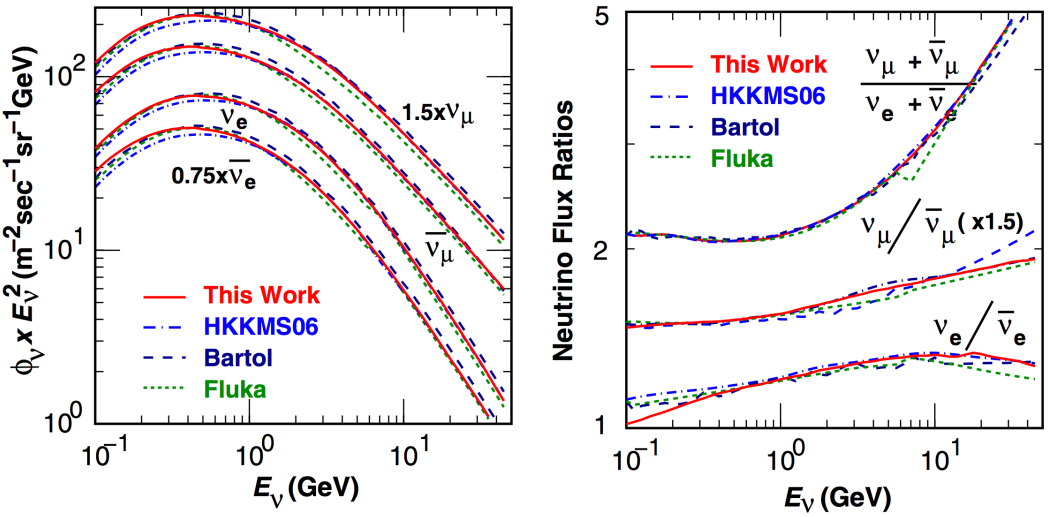

FIGURE 3.5: Comparison of the atmospheric neutrino flux for some calculations: Honda prediction(solid red), previous Honda model(blue dotted-dashed line) [33], Bartol model[34], and the Fluka model[35]. The figure is taken from [29].

hundred TeV. The interaction with the electron is disregarded in the calculation since the cross-section is 10^{-3} smaller than the interaction with the nucleus.

The neutrino interaction is primarily categorized into two types: charged-current (CC) and neutral-current (NC) interactions. Although the flavor of neutrinos can be identified based on the types of charged lepton produced for the CC interaction, no information regarding the neutrino flavor will be retained on NC interaction as no charged leptons are produced. In the NEUT, five reactions are evaluated based on CC and NC interaction.

- CC/NC (Quasi-)inelastic scattering: $\nu_\ell + N \to \ell + N'$,
- CC meson exchange interaction: $\nu_\ell + NN' \to \ell + N''N'''$,
- CC/NC single meson production: $\nu_\ell + N \to \ell + N' + Meson$,
- CC/NC deep inelastic scattering: $\nu_\ell + N \to \ell + N' + Hadrons$,
- CC/NC coherent pion production $\nu_\ell + N \to \ell + N' + pion$,

where N, N' (N'', N''') represent the nucleon states before and after an interaction, and ℓ denotes a lepton and neutrino.

The flavor of the original neutrino flux produced in the atmosphere is composed of only muon and electron types. Nonetheless, the tau neutrino also arrives at the SK because of neutrino oscillation. The CC interaction of tau neutrino occurs beyond a few GeV of energy owing to its large mass (1.78 GeV/c^2). Consequently, the number of tau neutrino interactions is significantly smaller than that of electron neutrinos and muon neutrinos. The production and decay of tau particles are calculated using TAUOLA [114].

Elastic and Quasi-elastic Scattering

NC elastic scattering is a process wherein a neutrino scatters and transfers momentum to the target nucleon, without generating any new particles. Conversely, CC quasi-elastic scattering process (CCQE) results in a charged lepton and modifies the target nucleon, conserving charge and momentum but not leading to fragmentation. NC elastic and CCQE interactions can be represented as follows:

$$\text{NC elastic scattering} : \nu_\ell(\bar{\nu}_\ell) + N \rightarrow \nu_\ell(\bar{\nu}_\ell) + N', \tag{3.7}$$

$$\text{CCQE} : \nu_\ell(\bar{\nu}_\ell) + N \rightarrow \ell(\bar{\ell}) + N'. \tag{3.8}$$

The CCQE interaction in NEUT is calculated by [115], and the differential cross-section can be expressed as

$$\frac{d\sigma^{\text{CCQE}}}{dq^2} = \frac{M^2 G_F^2 \cos\theta_{\text{C}}}{8\pi E_\nu^2}\left[A(q^2) \mp B(q^2)\frac{s-u}{M^2} + C(q^2)\frac{(s-u)^2}{M^4}\right], \tag{3.9}$$

where the E_ν denotes the energy of the incoming neutrino, M represents the mass of the target nucleon (~ 0.938 GeV), G_F represents the Fermi coupling constant($= 1.1663787 \times 10^{-5}$ GeV^{-2}), θ_{C} indicates Cabibo-angle, $q = q_\ell - q_\nu$ accounts for the momentum transfer, m denotes the lepton mass, and s, u denote the Mandelstam variables. Definitions of A, B, and C are referred from [115]. Furthermore, the relativistic Fermi gas model [116] is used for the neutrino-nucleon interaction at the boundary of the oxygen nucleus. Figure 3.6 presents a comparison of the cross-section for CCQE scattering interaction among NEUT computation and certain experimental results.

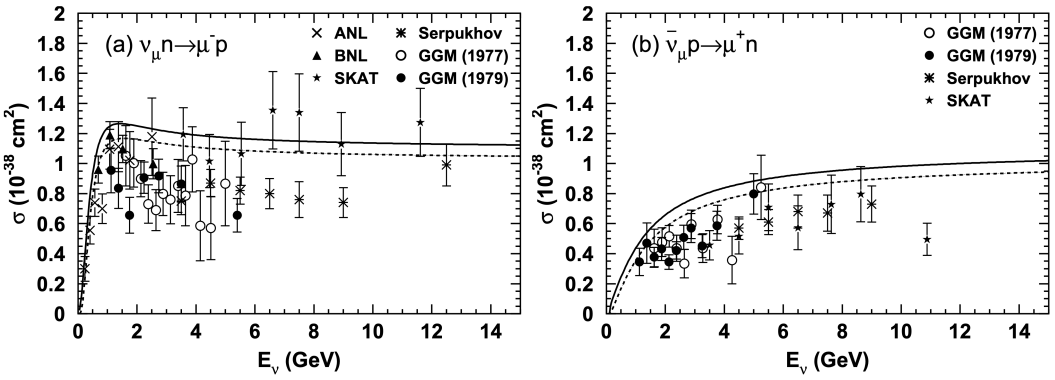

FIGURE 3.6: Cross-section of CCQE scattering of muon neutrino (left panel) and anti-muon neutrino (right panel). Lines denote the NEUT calculation for the free target (solid) and the bound target(dashed). Data points are taken from ANL (crosses), BNL (triangles), SKAT (stars), Serpukhov (asterisks), and GGMs (circles). The figures are taken from [36].

CC Meson Exchange Interaction

The calculation of the CCQE scattering interaction outlined above is based on an approximation that there are no relations among individual nucleons in a nucleus. However, it is necessary to account for the interaction between a neutrino and multiple nucleons simultaneously. The Mini-BooNE results suggests the existence of this

process [117]. Thus, the meson exchange current (MEC) model deviseed by Nieves et al. [118] is integrated into NEUT. This is a prominent model that expands the existing CCQE model. The incident neutrino interacts with a pair of nucleons as follows:

$$\nu_\ell + NN' \rightarrow \ell + N'' + N''', \tag{3.10}$$

where N, N', N'', and N''' denote the nuclei before and after interaction. Although other multi-nucleon correlations may exist for any neutrino interaction on a bound of the nucleon, only the CC MEC interaction is considered in the NEUT calculation.

Single Meson Production

A nucleus can exist in the baryon resonance state, resulting in the production of a single meson for the final state, as follows:

$$\nu + N \rightarrow \ell(\nu) + N^*, \tag{3.11}$$

$$N^* \rightarrow N' + \text{meson}, \tag{3.12}$$

where N^* represents the baryon resonance state, and a meson emerges as the final state of N^*. When the invariant mass in the hadron system W is less than approximately 2 GeV/c^2, this process becomes the primary mechanism for hadron production. Above 2 GeV/c^2, the interactions are simulated as deep inelastic scattering, which will be described in the following section. The process in NEUT is grounded in the Rein-Sehgal [119] model, and an enhanced model that includes the lepton mass correction [120] has also been incorporated. New form factors have since been developed [121] and employed in NEUT. The angular calculation for the interaction leading to an intermediate state $\Delta(1232)$, the primary channel of single pion production, is based on Rein's prescription [122]. For other channels, the angular distribution is presumed to be uniform.

Deep Inelastic Scattering

The interaction of the neutrinos with the quarks composing nucleons results in multiple hadrons via CC deep inelastic scattering (DIS). This process is dominant for $W > 1.3$ GeV/c^2 in NEUT calculation. When $W > 2$ GeV/c^2, all interactions producing at least one meson are simulated by PYTHIA/JETSET [123]. For interactions with $W < 2.0$ GeV/c^2, only pions are produced as the hadrons in the final state. To prevent double counting with single meson production, only multiple pion production is considered in this mass region. The nucleon structure is modeled based on the Parton Distribution Function. The default function is derived from the GRV98 [124] and corrected by the Bodel and Yang model [125].

Coherent pion production

The process of pion production interaction with the whole oxygen nucleus, preserving charge, is referred to as coherent pion production interaction. This interaction can be defined as follows:

$$\nu + {}^{16}\text{O} \rightarrow \ell + {}^{16}\text{O} + \pi, \tag{3.13}$$

Until the previous NEUT version 5.3.6, this process had been simulated based on the Rein-Sehgal model [126]. However, the interaction model was updated to the Berger-Sehgal model [127], incorporating improved elastic pion-carbon cross-section

data and considering the lepton-mass effect. This improvement allows NEUT to apply this interaction to neutrinos with energies below 10 GeV. Due to the low momentum transfer to the oxygen in this interaction, both the produced lepton and pion tend to move in forward directions.

3.2 Simulation for the IBD-like Event

3.2.1 DSNB Signals MC creation

Although all three flavors of neutrinos and their anti-neutrinos are emitted from supernovae, as described in Section 1.2, the most detectable signal in SK is the inverse-beta decay (IBD) of the electron anti-neutrinos ($\bar{\nu}_e + p \rightarrow e^+ + n$) owing to its largest cross-section below 30 MeV, as depicted in Figure 1.8. As described in Section 1.2.3, various SRN flux shapes are proposed, and it is challenging to create DSNB signal MC simulations for each flux model. Therefore, the DSNB signal MC simulation is produced uniformly in the positron energy and isotropically for the positron and neutron directions across the entire ID. The energy will later be normalized by the actual fluxes derived from model predictions. This normalization considers the differential cross-section of IBD, referred to as the Strumia-Vissani model [128].

In addition to the DSNB signals, backgrounds with the energy of $\mathcal{O}$(1–10) MeV and the same event structure, such as an $e^+(e^-) + n$-like signal, cannot be distinguished from IBD by the SK, and are normalized by their spectrum shape. These details will be further explained in Chapter 7.

3.3 Detector Simulation

Currently, the transport of the secondary particles from neutrino interactions is currently computed by a Monte-Carlo simulation toolkit. Traditionally, SK DETector SIMulation (SKDETSIM) based on GEANT3 [129, 130] toolkit is used in the SK analysis. SKDETSIM, developed in the FORTRAN programming language, is grounded in a suite of simulation tools, such as GEometry ANd Tracking(GEANT), originally developed by CERN, the final version was released in 1994. Given that the last update of GEANT3 occurred in 1994, implementing the latest physics model in a GEANT3-based simulation is problematic. Consequently, a new simulation based on Geant4 (SKG4) was developed to utilize the most current physics model and interpolate new functionality into the SK simulation. In 1998, the successor to GEANT3 was launched as Geant4 [131, 132, 133], and it is regularly updated and programmed in C++.

SK detector simulation accounts for particle tracking and interactions throughout the detector, the generation and propagation of photons emitted through scintillation and the Cherenkov radiation effect, PMT responses to photons, and electronic digitization. Calibration of parameters for detector conditions, such as water and PMT conditions, are performed using known light sources. The detector calibration will be described in Chapter 5, whereas this section will focus on physics and how to track the particles in the detector simulation.

3.3.1 Particle tracking

The Geant4 package offers various interaction models for hadrons, charged leptons, and photons. FTFP_BERT_HP physics list[133] is the package of hadronic physics,

except for the gamma-ray emission of thermal neutron capture on Gd and pion interactions below 500 MeV/c. For the pion interaction below 500 MeV/c, a custom program [134] based on an experiment of π-^{16}O scattering [135] and π-p scattering [136] is employed. As the gamma-ray emission from thermal neutron capture on Gd in SK-Gd is crucial, a model based on experimental results of ANNRI(ANNRI-Gd) [137, 37] is applied for gamma-ray emission from neutron capture on Gd. Figure 3.7 provides a comparison between data and MC in the ANNRI experiment, wherein the proposed model reproduced the measured data within 17% tolerance.

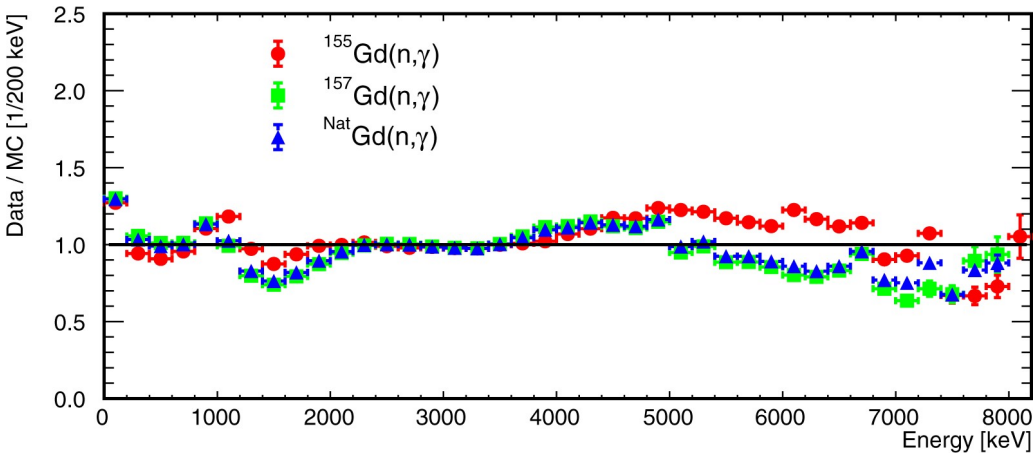

FIGURE 3.7: Comparison between measured data from ANNRI experiment and MC with ANNRI-Gd model. This figure was taken from [37].

3.3.2 Optical Photon Emission and Tracking

SK measures the physical phenomena by detecting the optical photons generated by the Cherenkov effect and scintillation. In particular, the emission of Cherenkov photons is a crucial aspect of the SK simulation. The process of Cherenkov emission in the simulation is described in Chapter 2. In the simulation, only the photons with wavelengths of 300–700 nm are generated, which correspond to the sensitive region of SK PMT, considering the optical photon propagation, scattering, absorption, and boundary effects. The probability of these processes depends on parameters reproducing the properties of water. For the scattering process, the simulation considers two types of scattering: Rayleigh and Mie scattering. As described in Chapter 5, these parameters are calibrated using laser measurement [43].

3.3.3 PMT response

When a photon reaches the PMT, the behaviors occurring on the PMT surface, including the photoelectric effect, are simulated. The probability of photoelectric effect, reflection, and absorption on the PMT surface is based on measurements. If photons are converted into a signal, the process of signal integration and digitization of charge and timing are also simulated as well. Finally, the simulated data are reformatted and stored in the output file, enabling them to be analyzed in the same manner as the observed data.

Chapter 4

Event Reconstruction

In the SK analysis, an event reconstruction is performed according to the target physics events, including electrons, muons, and other hadronic particles. This chapter outlines the event reconstruction algorithms used to estimate event energy, vertex, and direction for each physics target, with a particular emphasis on electron-like particles and muons.

4.1 Low Energy Event Reconstruction

In the SK analysis, the total energy of low-energy electron-like events (e.g., the electrons, positrons, and gamma rays) is reconstructed using the number of PMT hits. This section describes the algorithm used for reconstructing the vertex, direction, and energy of events.

4.1.1 Vertex reconstruction

The event vertex for low-energy events is reconstructed using the timings of the PMT hits. Considering an electron-like event with the energy of $\mathcal{O}(10)$ MeV moves only ~ 10 cm in water, which is shorter than the timing resolution of SK PMT, the track can be considered as the vertex. It is determined by the likelihood method. The likelihood $\mathcal{L}$ is defined as

$$\mathcal{L}(\boldsymbol{x}, t_0) \equiv \sum_{i=1}^{N_{\mathrm{hit}}} \log P(t_{\mathrm{res}}, i), \tag{4.1}$$

$$t_{\mathrm{res},i} = t_i - t_{\mathrm{tof},i} - t_0. \tag{4.2}$$

Here, $\boldsymbol{x}$ denotes the candidate of the reconstructed vertex, N_{hit} denotes the number of PMT hits, t_0 indicates the candidate of the event time, t_{i} represents the PMT hit timing, and $t_{\mathrm{tof},i}$ denotes the time of flight from vertex to PMT for i-th hit. $P(t_{\mathrm{res},i})$ denotes the Probability Density Function (PDF) for $t_{\mathrm{res},i}$. The PDF distribution of timing residuals is illustrated in Figure 4.1. The event's vertex and timing are determined as these with a maximum likelihood by scanning the entire tank.

The reconstructed vertex resolution is presented in Figure 4.2 as a function of the true electron energy evaluated by MC [38]. The resolution can be improved by enhancing the reconstruction and timing resolution.

The goodness of the event vertex and timing g_{vtx} is evaluated as follows

$$g_{\mathrm{vtx}} = \frac{1}{\sum^{N_{\mathrm{hits}}} 1/w^2(t_{\mathrm{res},i})} \times \sum_{i}^{N_{\mathrm{hits}}} \frac{1}{w^2(t_{\mathrm{res},i})} \exp\left[-\frac{t_{\mathrm{res},i}^2}{2\sigma^2(t_{\mathrm{res},i})}\right]. \tag{4.3}$$

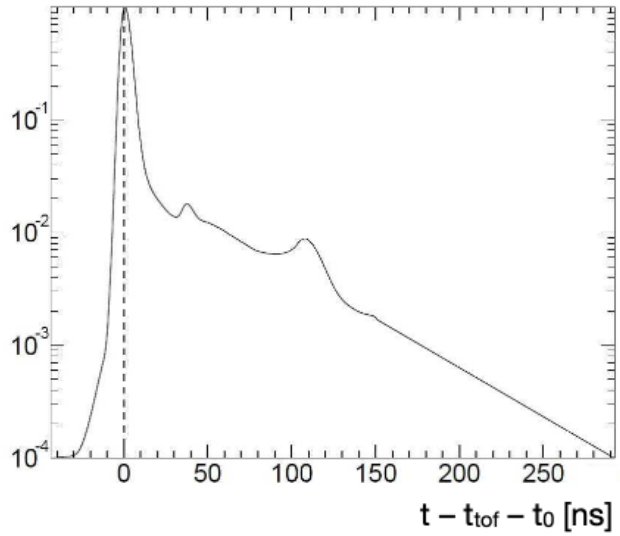

FIGURE 4.1: PDF distribution for the PMT hit timing residuals. Additional peaks surrounding 30 and 100 ns are caused by late pulse, which is caused by the photoelectrons reflected at the dynode and further incidence.

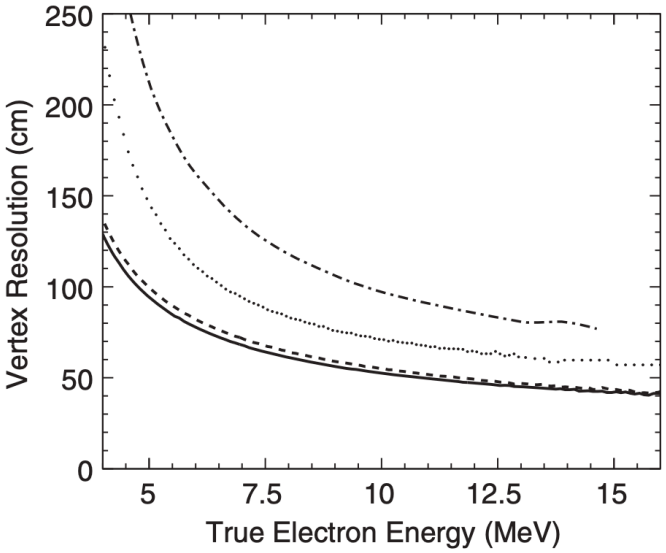

FIGURE 4.2: Vertex resolution as a function of true electron energy for SK-I, II, III, IV by dotted, dot-dashed, dashed, and solid lines, respectively. This figure is taken from [38].

Here, the $w(t_{\mathrm{res},i}) = \exp\left[-t_{\mathrm{res},i}/\sqrt{2}\omega\right]$ denotes the resolution function of the $t_{\mathrm{res},i}$ distribution with ω set of 60 s, and $\sigma(t_{\mathrm{res},i})$ denotes the same form with the w with replacing ω to the PMT timing resolution of 5 ns.

4.1.2 Direction Reconstruction

The event direction is determined by the Cherenkov light pattern to maximize likelihood as follows

$$\mathcal{L}(\boldsymbol{d}) \equiv \sum_{i=1}^{N_{20}} \log\{f(\cos\theta_i, E)\} \times \frac{\cos\theta_i}{a(\theta_i)}, \tag{4.4}$$

where the N_{20} denotes the number of hits that $t_{\mathrm{res},i}$ are within 20 ns from the t_0, $f(\cos\theta_i, E)$ indicates the expected distribution of the opening angle for the event energy E, and the cosine of the angle between PMT direction and the reconstructed event direction $\cos\theta_i$, and $a(\theta_i)$ is a factor correcting the PMT acceptance. In particular, $a(\theta_i)$ depends on the geometry of the PMT and acrylic case, and it is extracted by the MC as follows:

$$a(\theta_i) = 0.205 + 0.524\cos\theta_i + 0.390\cos^2\theta_i - 0.132\cos^3\theta_i. \tag{4.5}$$

Consequently, the resolution at 10 MeV is evaluated to be 25°. Figure 4.3 represents the energy dependence of the 1σ directional resolution estimated by SK-I MC.

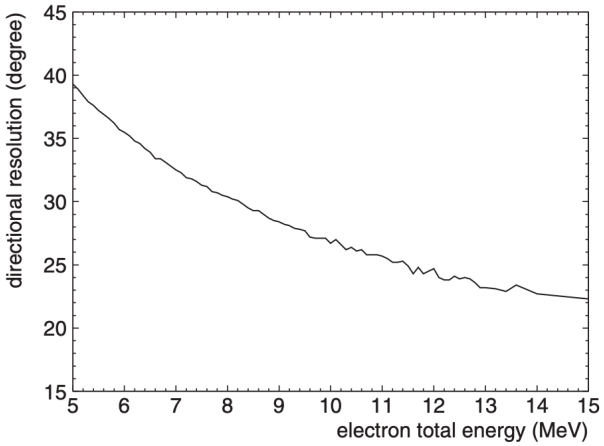

FIGURE 4.3: Energy dependence of the directional resolution. This plot was taken from [39].

A parameter, g_{dir}, which is the KS test result for the azimuthal angle uniformity, with the z-axis representing the reconstructed direction, can be calculated as

$$g_{\mathrm{dir}} = \frac{\max\left[\angle^i_{\mathrm{uniform}} - \angle^i_{\mathrm{data}}\right] - \min\left[\angle^i_{\mathrm{uniform}} - \angle^i_{\mathrm{data}}\right]}{2\pi}, \tag{4.6}$$

where the $\angle^i_{\mathrm{uniform}}$ denotes the expected azimuthal angle of the i-th hit along the Cherenkov angle of electrons, and $\angle^i_{\mathrm{data}}$ indicates the azimuthal angle of the i-th hit from a certain start point. The $\angle^i_{\mathrm{uniform}}$ is calculated by $i \times \angle^i_{\mathrm{uniform}} = 2\pi/N_{\mathrm{hits}}$. Figure 4.4 represents the calculation of the $\angle^i_{\mathrm{uniform}}$ and $\angle^i_{\mathrm{data}}$. The azimuthal angle is distributed equally if the PMT hits are more likely to be the Cherenkov ring. In contrast, if these are accidental clusters like PMT flasher, then the equality is inadequate. Thus, the parameter g_{dir} exhibits a smaller value when the hits are akin to electrons, whereas it displays a larger value if the event contains a clustered hit pattern.

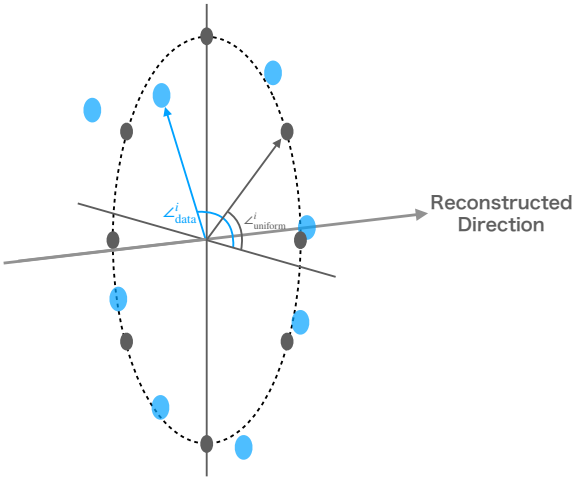

FIGURE 4.4: Illustration of the definition of $\angle^i_{\text{uniform}}$ and $\angle^i_{\text{data}}$. Blue circles exhibit the PMT hits, and gray circles indicate the expected point if the hits are equally distributed at an azimuthal angle.

4.1.3 Effective hit calculation

The number of PMT hits can vary depending on factors like water transparency, PMT noise rate, and PMT signal efficiency, including QE and the gain, for a given reconstructed vertex and direction. All these factors must be taken into account during energy reconstruction. Consequently, an effective number of hits, N_{eff}, that does not depend on these parameters is computed. N_{eff} is defined as follows:

$$N_{\text{eff}} \equiv \sum_{i}^{N_{50}} \left[(X_i + \epsilon_{\text{tail}} - \epsilon_{\text{dark}}) \times \frac{N_{\text{all}}}{N_{\text{alive}}} \times \frac{1}{S(\theta_i, \phi_i)} \times \exp\left(\frac{r_i}{L^i_{\text{eff}}}\right) \times \frac{1}{QE_i(1 + C \cdot G_i(t))} \right]. \tag{4.7}$$

Here, N_{50} indicates the number of hits in which the timing residual is within 50 ns from the t_0, and $N_{\text{all}}/N_{\text{alive}}$ denotes the inverse proportion of the number of functioning PMTs to the number of all PMTs (=11,129). QE_i indicates the relative QE described in Section 5.1.4. Other parameters are listed below, wherein the notation i represents the i-th hit PMT.

- **Multiple hit correction X_i:**
  If multiple photons hit one PMT within the same PMT gate (multiple photoelectrons), the number of photons is counted as a single hit, whereas the charges are integrated. If the event occurs proximate to the wall and the direction is toward the wall, this effect becomes crucial for energy reconstruction. Therefore,

the occupancy correction of neighboring PMT hits is expressed as

$$X_i = \begin{cases} \dfrac{\log\{1/(1-x_i)\}}{x_i} & (x_i < 1) \\ 3.0 & (x_i = 1) \end{cases} \tag{4.8}$$

$$x_i = N_{\text{neighbor}}/N_{\text{total}} \tag{4.9}$$

where x_i denotes the occupancy of these hits, N_{neighbor} indicates the number of hits for the surrounding 3×3 PMTs patch surrounding the target PMT, and N_{total} denotes the total number of hits.

- **Delayed hit correction ϵ_{tail}:**
  A number of Cherenkov photons fall out from the signal window because of the delay induced by the reflection on the PMT and the black sheet. To include these leaked hits in the N_{eff}, the factor ϵ_{tail} is defined as

$$\epsilon_{\text{tail}} = \frac{N_{100} - N_{50} - N_{\text{alive}} \times R^{\text{ave}}_{\text{dark}} \times 50 \text{ nsec}}{N_{50}}, \tag{4.10}$$

  where the N_{100} denotes the number of hits that the timing residual is within 100 ns from the t_0, and R_{dark} is the averaged dark noise rate of all PMT. This correction estimates the number of hits originating from sources other than the dark noise during 50 ns after the N_{50} window.

- **Dark noise correction ϵ^i_{dark}:**
  The dark noise stemming from the Cherenkov light owing to the thermionic emission of PMT and the radio activities should be considered when evaluating N_{eff}. As the dark noise rate for each PMT varies over time, the correction is calculated using the dark rate at the time of observation as follows:

$$\epsilon^i_{\text{dark}} = \frac{R^{\text{ave}}_{\text{dark}} \times 50 \text{ ns} \times N_{\text{alive}}}{N_{50}} \times \frac{r^i_{\text{dark}}}{\sum_i^{N_{50}} \frac{r^i_{\text{dark}}}{N_{50}}}. \tag{4.11}$$

  Here, the r^i_{dark} denotes the dark rate for each PMT, depending on the time. The first term represents the averaged fraction of dark noise hits in 50 ns, and the second term represents the variation from the averaged dark noise rate.

- **Correction for the actual photo coverage $S(\theta, \phi)$:**
  As ID PMTs are mounted on the inner surface of the ID, the actual photo coverage is varied depending on the photon incident angle θ and ϕ as displayed in Figure 4.5.

  The actual photo coverage $S(\theta, \phi)$ is evaluated by injecting optical photons from a uniform vertex and isotropic direction into SKG4. The $S(\theta, \phi)$ is defined as

$$S(\theta, \phi) = N_{\text{obs}}(\theta, \phi)/N_{\text{inc}}(\theta, \phi), \tag{4.12}$$

  where $N_{\text{obs}}(\theta, \phi)$ denotes the number of total photoelectrons incident from (θ, ϕ), and the $N_{\text{ph}}(\theta, \phi)$ represents the total number of photons reaching the PMT with the incident angle (θ, ϕ). The evaluation using SKG4 enables the consideration

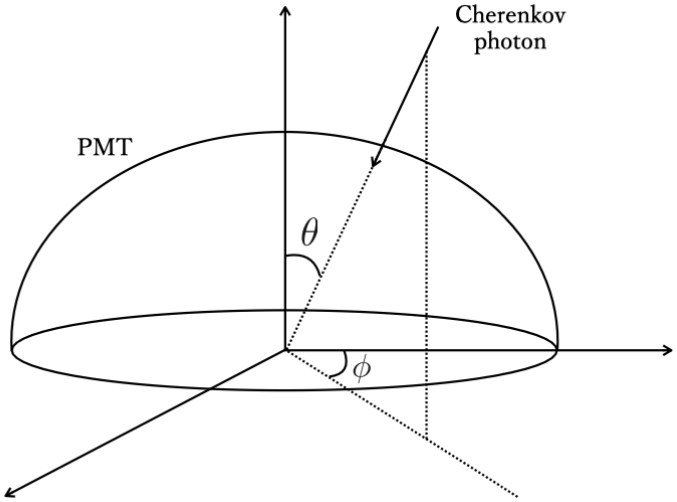

FIGURE 4.5: Definition of the incident angle θ and ϕ. This plot is referred from [40].

of the QE dependence on the incident angle. As the angle range varies between the barrel PMT, and top and bottom PMT, two types of the $S(\theta, \phi)$ are calculated as displayed in Figure 4.6.

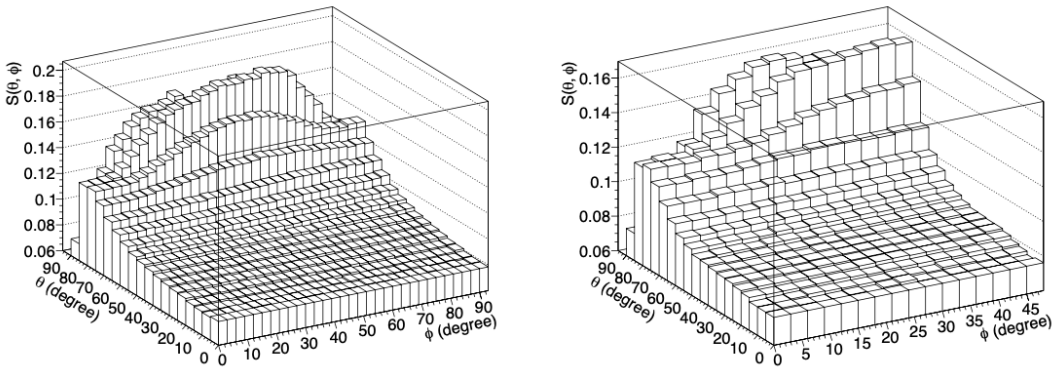

FIGURE 4.6: $S(\theta, \phi)$ distribution for barrel PMTs (left) and top and bottom PMTs (right). The plots are taken from [40].

- **Water transparency correction** $\exp\left(\frac{r_i}{L^i_{\text{eff}}}\right)$**:**
  The correction is performed to consider the light attenuation in the water. r_i denotes the distance between the event vertex and the PMT. λ^i_{eff} indicates the effective transmission length considering the variation of water quality from the event vertex to the PMT. As described in Section 5.2.2, the water transparency exhibits an asymmetry along with the z-position. The photon transmission length L is modeled as

$$L(\lambda, z) \equiv \frac{1}{\alpha_{\text{abs}}(\lambda) \times (1 + \beta z) + \alpha_{\text{sym}}(\lambda) + \alpha_{\text{asym}}(\lambda)} \tag{4.13}$$

where λ denotes the wavelength of photons, β represents the slope parameter describing non-uniformity of water transparency, and α_{abs}, α_{sym}, and α_{asym} represent the attenuation coefficient of the absorption, symmetric scattering, and asymmetric scattering, respectively, as described in Section 5.2.1, respectively. Furthermore, the cross-section with the water in the case of the photon travels a distance r_i, $\sigma_i(\lambda)$ is denoted as

$$\sigma_i(\lambda) = \alpha_{\text{abs}}(\lambda)\left[1 + \beta\left(z + \frac{1}{2}\, r_i \cdot dz_i\right)\right] + C_{\text{sca}} \cdot (\alpha_{\text{sym}}(\lambda) + \alpha_{\text{asym}}(\lambda)) \quad (4.14)$$

where the dz_i indicates the z component of photon direction, and C_{sca} represents the correction of the scattering effect. C_{sca} is estimated to minimize the position variation of N_{eff} using 10 MeV SKG4 MC simulation as $C_{\text{sca}} \sim 0.44$. According to these equations, the probability that the photon generated by the event vertex reaches the PMT, $p_i(\lambda)$, is calculated as

$$p_i(\lambda) = \int_{\lambda_{\text{min}}}^{\lambda_{\text{max}}} w_0(\lambda) \exp(-\sigma_i(\lambda) \cdot r_i) d\lambda \quad (4.15)$$

where $w_0(\lambda)$ denotes the PDF of the wavelength for the Cherenkov photons, $\lambda_{\text{max}} = 650$ nm, and $\lambda_{\text{min}} = 300$ nm. Therefore, $p_i(\lambda)$ can be rewritten as

$$p_i(\lambda) = \exp\left(-\frac{r_i}{L^i_{\text{eff}}}\right), \quad (4.16)$$

and the effective transmission length L^i_{eff} can finally be expressed as

$$L^i_{\text{eff}} = -\frac{r_i}{\ln\left(\int_{\lambda_{\text{min}}}^{\lambda_{\text{max}}} w_0(\lambda) \exp(-\sigma_i(\lambda) \cdot r_i) d\lambda\right)}. \quad (4.17)$$

- **Relative QE and gain correction** $1/[QE_i \times (1 + C \cdot G_i(t))]$**:**
  The PMT QE varies for each PMT, as does the gain, described later in Section 5.1.4. The parameter C is introduced to reproduce the gain increase over time, assuming a proportional relationship. In the SK-V, the tank refurbishment was conducted, and the PMT high voltage (HV) and gain were tuned during that period. As no increase in gain has been observed to date, we assigned $C = 0$ for SK-V and SK-VI.

4.1.4 Energy reconstruction

After calculating N_{eff}, the total energy of the event can be estimated by a combination of the 5th-order polynomial function and linear function. The energy reconstruction E_{tot} function can be described as

$$E_{\text{tot}} = \begin{cases} \sum_{i=0}^{5} p_i (N_{\text{eff}})^i & (N_{\text{eff}} \leqq N_{\text{thr}}) \\ \sum_{i=0}^{5} p_i (N_{\text{thr}})^i + a \times (N_{\text{eff}} - N_{\text{thr}}) & (N_{\text{eff}} > N_{\text{thr}}) \end{cases}. \quad (4.18)$$

Here, p_i denotes the coefficient of the polynomial function as a fitting parameter, N_{thr} indicates the connection point of two functions, and a denotes the first derivative of the upper function in order to ensure the continuity of functions. To determine parameters, the electron MC simulations were conducted across an energy range of 3–100 MeV, and accordingly, the N_{eff} was calculated. The parameters were determined by fitting the correlation between N_{eff} and true total energy. The parameters for the energy reconstruction are summarized in Table 4.1. After evaluating p_0–p_5, N_{thr} was determined to be 2.202×10^2 for SK-VI.

TABLE 4.1: Parameter settings for the reconstructed energy calculation in SK-VI.

p_0	p_1	p_2	p_3	p_4	p_5
0.702	0.131	-2.35×10^{-4}	2.640×10^{-6}	-1.188×10^{-8}	1.930×10^{-11}

4.1.5 Cherenkov angle reconstruction

In the DSNB search, the Cherenkov angle of the event is used to filter out non-electron-like events, such as muon, pion, those involving muons, pions, and multiple gamma rays. The Cherenkov angle is determined using the pattern of PMT hits to achieve this separation. Only PMT hits with timing residuals from the reconstructed vertex within 15 ns are considered for this process. All three-hit combinations of three PMT hits are explored because, theoretically, a circle can be drawn given any three points on its circumference. According to the theorems of sine and cosine, if a, b, and c in Figure 4.7 are given, the opening angle θ for each three-hit combination can be calculated in the following:

$$\frac{a}{\sin A} = 2R, \tag{4.19}$$

$$\therefore R = \frac{a}{2\sqrt{1-\cos^2 A}} = \frac{a}{2\sqrt{1-\left(\dfrac{b^2+c^2-a^2}{2bc}\right)^2}},$$

$$\sin\theta = R = \frac{abc}{\sqrt{2(a^2b^2+b^2c^2+c^2a^2)-(a^4+b^4+c^4)},} \tag{4.20}$$

$$\therefore \theta = \sin^{-1}\left\{\frac{abc}{\sqrt{2(a^2b^2+b^2c^2+c^2a^2)-(a^4+b^4+c^4)}}\right\}$$

The angle θ for each combination is stored for each 0.9° bin. The central value of the maximum continuous 7 bins is identified as the reconstructed Cherenkov angles. Figure 4.8 presents an θ distribution created from three-hit combinations for electron-like and muon-like events. Peaks are observed around these typical Cherenkov angles.

4.2 Muon Event Reconstruction

A muon event generally has more energy than an electron-like event, resulting in much more PMT hits and charges in SK. The trajectory of a muon event is also more track-like than electron events. This section details the algorithm for identifying muons and

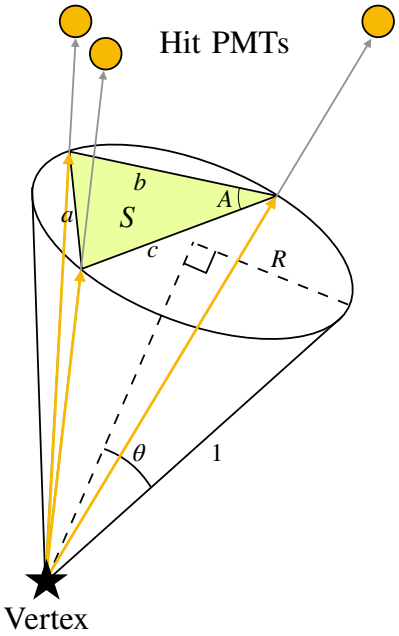

FIGURE 4.7: Illustration defining the calculation of θ. Circles comprise unit vectors from the reconstructed vertex to the three PMT hits.

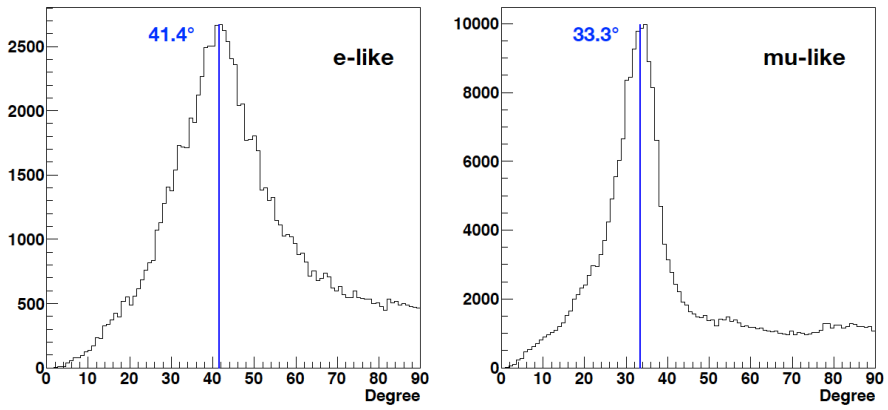

FIGURE 4.8: Example of θ distribution of three-hits combinations for electron-, and muon-like events. Plots are taken from [41].

reconstructing their direction and trajectory.

Cosmic-ray muon events observed at SK are usually identified by ID triggers paired with OD-triggered events. These events are classified into five categories: single-through going, stopping, multiple, corner-clipping, and misfit muons. Figure 4.9 provides illustrations of each muon type. Multiple muons are further divided into two types: those where only one track can be fitted or those where multiple tracks can be fitted.

A muon reconstruction algorithm, called 'Muboy' fitter, works depending on the

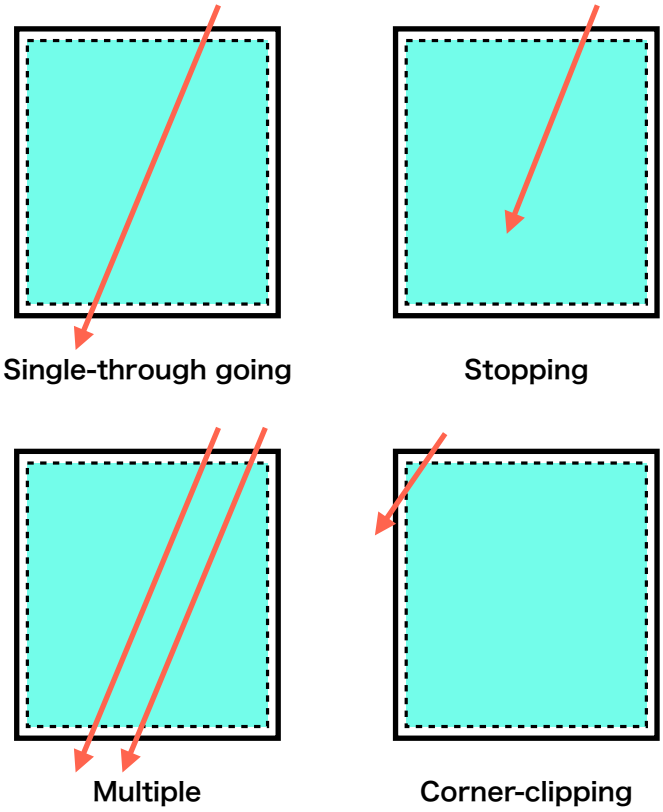

FIGURE 4.9: Illustration of muon categories for single-through (top, left), stopping (top, right), multiple (bottom, left), and corner-clipping (bottom, right) muons.

category of each muon. At first, Muboy looks at the muon type, whether the event has a single track or multiple tracks in the ID, then identifies whether the muon stopped in the ID. This section describes the overview of the Muboy fitter, and more detail can be found in [23, 138]

4.2.1 PMT hit selection

Typically, a cosmic-ray muon deposits more charge per PMT than electrons due to its high energy and distinct Cherenkov ring pattern. Therefore, the ID PMT hits used in reconstruction are pruned by applying a certain charge threshold for each PMT, depending on the number of PMT hits (first cleaning cut), as summarized in Table 4.2.

TABLE 4.2: Charge thresholds for ID PMT corresponding to the number of ID PMT hits.

Number of PMT hits	Threshold charge to select ID PMT
< 8000	2.0 p.e.
8000 – 10000	2.5 p.e.
> 10000	3.0 p.e.

Following the first cleaning cut, Muboy calculates the nearest neighbor hits N_{nn}, which consists of PMT hits from eight surrounding PMTs and own, within 15 ns for

each PMT. Figure 4.10 displays the example of the counting of N_{nn}.

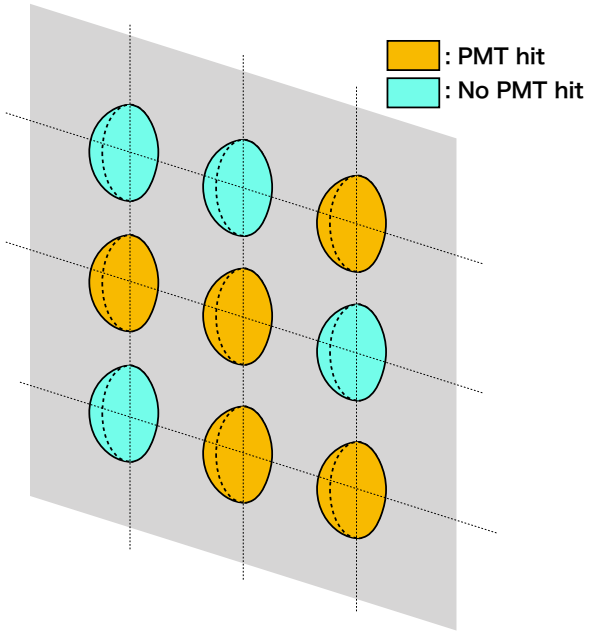

FIGURE 4.10: Illustration of the concept for the counting of N_{nn} with the case of $N_{\mathrm{nn}} = 5$ in the central PMT.

For further PMT hit reduction, the PMT is selected by a certain threshold relating to N_{nn}, as listed in Table 4.3.

TABLE 4.3: N_{nn} thresholds for ID PMT corresponding to the number of ID PMT hits.

Number of PMT hits after first cleaning	N_{nn} threshold to select ID PMT
≤ 500	1
500–2500	7
2500–5000	8
5000–7500	9
> 7500	10

4.2.2 Initial Entry Point

The entry point and timing — the location and instant the muon enters the ID tank — is estimated by the earliest hit PMT with $N_{\mathrm{nn}} > 3$. If no PMT hit has three neighbor hits, the threshold is decreased by one neighbor. The entry point is determined as the coordinate of the earliest hit PMT, and entry time is the timing of the earliest PMT hit. Moreover, the tentative exit point was determined as the position of the PMT with maximal Q_{nn}, representing the total charge among the surrounding PMTs.

4.2.3 Direction Reconstruction

For the direction reconstruction, further constraints regarding hit timing are applied to the PMT hits. In the case of a single-through going muon, the PMT hit timing cannot be advanced in comparison to the muon travel distance of the muon in the

water. Furthermore, the photon directly produced from the muon should arrive at the PMT prior to the period in which the light travels from the muon entry point. Therefore, the hit timing constraint to the earlier side T_{early} and later side T_{later} can be described as,

$$T_{\text{early}} = T_{\text{entry}} + \frac{D}{v_1}, \tag{4.21}$$

$$T_{\text{later}} = T_{\text{entry}} + \frac{D}{v_2}, \tag{4.22}$$

where T_{entry} denotes the PMT hit timing of the enter point, D indicates the distance for each hit PMT, and v_1 and v_2 denote the speed of muon and light in the water, expected to be 34 cm/ns and 18 cm/ns, respectively. Muboy performs the direction fit based on the PMT hits between T_{early} and T_{later}. Accordingly, the number of PMT hits before the T_{early} (N_{early}) is counted. If $N_{\text{early}} > 45$, the event is classified as the multiple muons because the constraint by T_{early} cannot be applied to the multiple muons (called MultiMu-1). The reconstruction of multiple muons is treated separately for estimating the entry point and direction reconstruction, which will be described later. To assert that the direction from the entry point towards the PMT hit is within the Cherenkov angle, either or both of the following conditions should be satisfied:

1. $\vec{d} \cdot \vec{r} > 0.74$, where the $\vec{d}$ denotes the unit vector from the entry point to hit PMT, and $\vec{r}$ indicates the muon track direction.
2. $D < 2$ m.

Using the selected hits, Muboy estimates the direction to maximize the goodness of fit (GOF). The GOF is defined as follows,

$$\text{GOF}(f_{\text{cone}}) = \frac{C_{\text{cone}}}{N} \sum_{i=1}^{N} g(\delta t_i), \tag{4.23}$$

where f_{cone} denotes the number fraction of hit PMTs in the Cherenkov cone, δt_i indicates the time difference between the measured time t_i of the i-th PMT hits and the expected timing at which the PMT hit should be hit from a given muon track and direction. Furthermore, C_{cone} presumes the following form:

$$C_{\text{cone}} = \begin{cases} f_{\text{cone}} \dfrac{0.9}{C_{\text{cut}}} & (f_{\text{cone}} < 0.75) \\ \dfrac{0.1 f_{\text{cone}} + 0.9 - C_{\text{cut}}}{1 - C_{\text{cut}}} & (f_{\text{cone}} > 0.75) \end{cases}, \tag{4.24}$$

where $C_{\text{cut}} = 0.74$. The function $g(\delta t_i)$ is defined as follows,

$$g(\delta t_i) = \begin{cases} \exp\left[-\dfrac{\delta t_i}{\lambda(q_i)} \right] & (\delta t_i < 0), \\ \exp\left[-\dfrac{(\delta t_i - t_{\text{mean}}(q_i))^2}{2\sigma(q_i)^2} \right] & (\delta t_i > 0 \text{ or } q_i > 30 \text{ p.e.}), \end{cases} \tag{4.25}$$

where q_i denotes the charge for i-th hit PMT, $t_{\mathrm{mean}}(q_i)$, $\sigma(q_i)$, and $\lambda(q_i)$ can be defined as follows:

$$t_{\mathrm{mean}}(q) = 2.563 - 0.029 \cdot q \tag{4.26}$$

$$\sigma(q) = 1.691 + 2.514 \exp\left[-\frac{q}{2.453}\right] \tag{4.27}$$

$$\lambda(q) = 1.254 + 14.863 \exp\left[-\frac{q}{2.316}\right]. \tag{4.28}$$

$$\tag{4.29}$$

Direction estimation is conducted by iterating around the first tentative direction while keeping the entry point and timing constant. After identifying the maximized direction, a second iteration is performed. At this stage, the entry time is permitted to change with the direction changes. The entry time can be smeared within a range of 26.7 nsec around the track. Subsequently, the GOF(f_{cone}) is again optimized with $C_{\mathrm{cut}} = 0.74$ replaced by $C_{\mathrm{cut}} = 0.65$. After the second iteration, Muboy counts the number of early PMT hits with the condition of $\delta t_i - t_{\mathrm{mean}}(q_i) > 250$ ns under the optimized direction and entry time. If the count exceeds 35, the muon is categorized as a multiple muon (MultiMu-2). If the number of PMT hits is less than 10, under any timing of hit reduction, the muon is considered a misfit muon. All other remaining events are categorized as the through-going muons. The track length of these muons is calculated geometrically using the direction and entry point. Figure 4.11 illustrates the flowchart of hit reduction for the direction reconstruction.

4.2.4 Event classification

As discussed in the previous section, the muons are separated into misfit muons, two types of multiple muons, and single-through going muons. Muboy subsequently investigates single-through-going muons to further divide them into two other types: corner-clipping and stopping muons. A different reconstruction approach is used for the multiple muons.

Corner-clipping muons

Corner-clipping muons, which merely scrape the edge of the ID, typically exhibit short track lengths and minimal PMT hits. As such, any muon with a track length under 7 m and fewer than 2,000 ID PMT hits is investigated to determine if it qualifies as a corner-clipping muon. As the entry point of the corner-clipping muon is typically near the top or bottom corner, a muon is tested using the following conditions:

$$\begin{cases} \dfrac{X_{\mathrm{entry}} \cos\theta_x + Y_{\mathrm{entry}} \cos\theta_y}{\sqrt{X_{\mathrm{entry}}^2 + Y_{\mathrm{entry}}^2}} > 0.05 \\ \sqrt{X_{\mathrm{entry}}^2 + Y_{\mathrm{entry}}^2} > 1500 \text{ cm} \end{cases} \quad (Z_{\mathrm{entry}} > 1750 \text{ cm}), \tag{4.30}$$

$$\begin{cases} (\text{Distance between entry and exit point}) < 4 \text{ m} \\ \sqrt{X_{\mathrm{entry}}^2 + Y_{\mathrm{entry}}^2} > 1600 \text{ cm} \end{cases} \quad (Z_{\mathrm{entry}} < -1600 \text{ cm}), \tag{4.31}$$

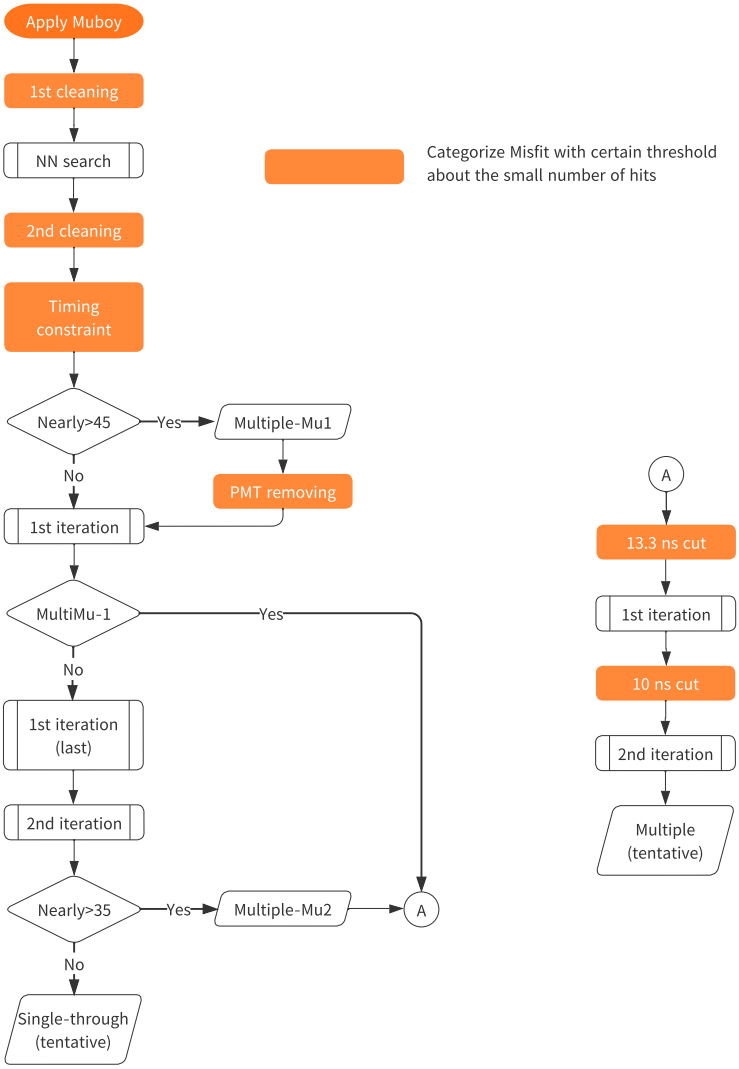

FIGURE 4.11: Flowchart of Muboy about the direction reconstruction with a part of event classification.

where the X_{entry} (Y_{entry}, Z_{entry}) denotes the x (y, z) coordinates of the muon entry point, and θ_x (θ_y) indicates the x (y) direction of the muon. The muons satisfying the conditions mentioned earlier are categorized as corner-clipping.

Stopping muons

Finally, Muboy determines whether the muons qualify as Stopping muons. To analyze the muon events, the number of p.e.s generated within 2 m from the exit point in the ID (Q_{ID}) and within 4 m from the exit point in the OD (Q_{rmOD}), are counted. If a muon meets any of the following conditions, it is classified as a Stopping muon.

- $Q_{\text{ID}} < 200$ p.e.
- $Q_{\text{ID}} < 400$ p.e. and $Q_{\text{OD}} < 30$ p.e.

- $Q_{\mathrm{ID}} < 150$ p.e. and $Q_{\mathrm{OD}} > 30$ p.e.
- $Q_{\mathrm{ID}} > 300$ p.e. and No OD PMT hit data.

For Stopping muons, The track length and stopping point are estimated. The track length is determined by the energy deposit per unit track length dE/dx, correlating to the quantity of detected Cherenkov light per geometrically estimated unit track length dQ/dE. A typical dE/dx distribution for a muon event is depicted in Figure 4.12. The track length is determined up to the point where the dQ/dx reduces to less than 40% of the average value of the first 1.5 m. For the case presented in Figure 4.12, the stopping point is defined as 25 m.

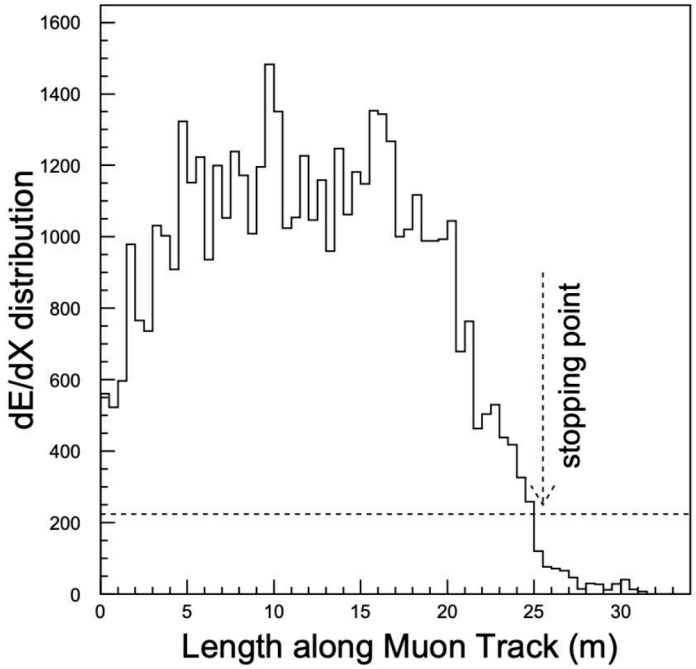

FIGURE 4.12: Histogram of typical dQ/dx distribution for considering the length along the muon track as the horizontal axis. This figure is taken from [42].

Multiple muons

There are two times when Muboy classifies muon into Multiple muons, such as for MultipleMu-1 and -2. After the MultipleMu-1 branch, these muons are subject to a stricter hit timing cut, identical in approach to T_{early} and T_{later}, whereas $v1$ and v_2 are altered to 32 and 19.5, respectively. Furthermore, before the final maximization of the first iteration, with a fixed entry time, all hits are further pruned to remove any hit time residuals outside 13.3 ns. This hit reduction is also applied to MultipleMu-2.

After this, two types of multiple muons are merged. The first iteration, with a fixed entry time, is repeated using a new set of PMT hits, and the second iteration is also repeated, but only using hits with a timing residual inside 10 ns. At this instant, the direction fitting is completed for one track of the multiple muons.

After that, for Multiple muons, additional entry points and directions for other muons are sought. Initially, the PMT hits, removed by the cut after cleaning described in Section 4.2.1, are recovered. This search assumes that these muons are moving in a

track parallel with the first determined track. To sample the PMT hits, these PMTs require the following direction from the first track:

$$\vec{n}_{\mathrm{PMT,i}} \cdot \vec{d}_{\mathrm{track}} > 0, \tag{4.32}$$

where $\vec{n}_{\mathrm{PMT},i}$ denotes the normal vector of i-th hit PMT, and $\vec{d}_{\mathrm{track}}$ indicates the direction of the first track. The remaining PMTs are further selected to gather the hits close to the muon tracks using the 'plane wave time' t_{plane}. t_{plane}, indicating the time at which the PMT would have been hit if the light was a plane wave traveling at c, denoted as

$$t_{\mathrm{plane}} = T_{\mathrm{entry}} + \frac{|\vec{r}_{\mathrm{PMT},i} - \vec{r}_{\mathrm{entry}} \cdot \vec{d}_{\mathrm{track}}|}{c} \tag{4.33}$$

where $\vec{r}_{\mathrm{PMT},i}$ indicates the PMT position, and $\vec{r}_{\mathrm{entry}}$ denotes the entry point. If the time difference $T_{\mathrm{plane}} - t_i$ is beyond the range of -33.3 ns and 16.6 ns, the hits are eliminated.

To locate the additional tracks, Muboy iterates the procedure stated below until the number of remaining tubes is less than t or 9 tracks are detected by eliminating the PMT hits with $0 < T_{\mathrm{expected}} - t_i < 10$ ns, and they are within 12 m from the track.

1. Locate the earliest PMT hit. It becomes an entry point for an additional track.
2. Remove PMT hits that are located closer than 12 m and with $0 < T_{\mathrm{expected}} - t_i < 10$ ns.
3. Count the number of clustered hits. If the count is greater than 5, the track is valid.
4. Subtract the number of clustered hits. If ≥ 6 PMT hits remain, revert to search further (to (1)).

Classification summary

Figure 4.13 portrays the muon types and reconstruction goodness g_μ defined as the maximized GOF. The majority of the muons are classified as the single-through going muons. The misfit muons tend to exhibit a lower value of goodness than other types.

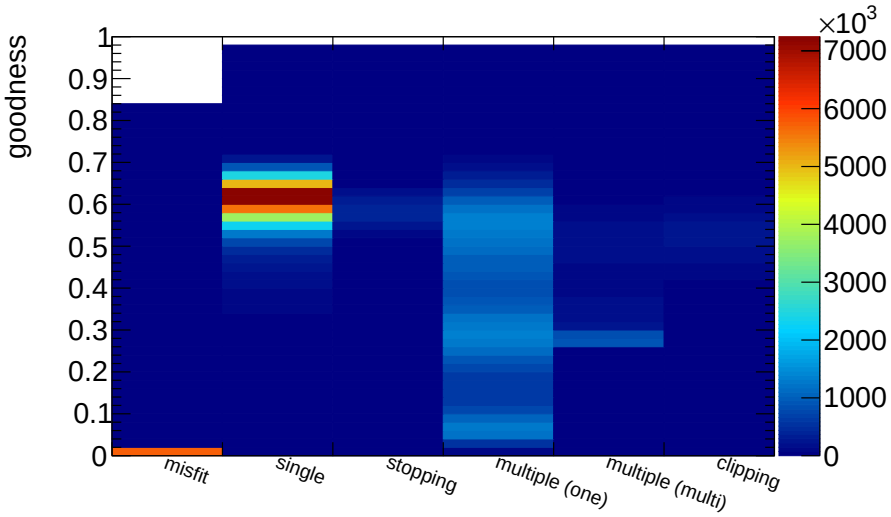

FIGURE 4.13: Muon types and reconstruction goodness. The term 'single' represents the single-through muons.

Chapter 5

Detector Calibration Measurement

In SK, periodic detector calibrations are essential to investigate the functionality of the detector behavior and ensure accurate signal measurement. Results from these calibration measurements feed into the analysis software, detector tuning, and the detector simulation, as described in Section 3.3.

The data procured at SK primarily comprises timing and the charge information captured by PMTs and consolidated through electronics. The integrity of the signal is influenced by the QE and the gain characteristics of each PMT. Additionally, photon behaviors such as absorption and scattering by the water and other materials in the tank must be well-understood and integrated into the detector simulation and analysis software. Evaluating attributes such as PMT response and water properties from calibration measurements is critical for event reconstruction and physics analysis. This is especially true for low-energy analyses, such as $\mathcal{O}$(1–10) MeV range, where calibration data is vital for the event energy reconstruction given the low photon yield, as outlined in Section 4.1.3. This chapter describes calibration measurements performed in SK and the utilization of parameters obtained from calibration.

5.1 ID Detector Calibration

As physics analyses in SK are based on signals detected by the ID, a detailed understanding of the PMT in ID is essential for evaluating the functionality of SK. This section explains the measurement process and the parameters obtained for each calibration.

5.1.1 High-Voltage determination

The amplitude of photoelectrons on the dynode, stemming from the photoelectric effect on the PMT, is influenced by the High-Voltage (HV) applied to the PMT. For consistent gains across all PMTs, individual HV adjustments ensure uniform outputs. To facilitate this, an isotropic light source, created by injecting light from a Xe lamp into a 5 cm diameter acrylic diffuser ball via a UV filter, is employed. Positioned at the center of the tank, measurements from this diffused light are susceptible to factors like PMT position, water properties, and PMT glass surface reflectivity. To ensure accuracy, 420 pre-calibrated PMTs, termed Standard PMTs, are evenly placed within the ID. Prior to their SK introduction, the HV of these standard PMTs is calibrated using an identical light source and DAQ system. Figure 5.1 illustrates the placement of Standard PMTs and their associated PMT grouping.

For all PMTs, except the Standard ones, HV is adjusted to align the charge from the light source with the average charge of a corresponding group's Standard PMT. The consistency of the HV is verified to be within a 1.3% range, which is also aligned

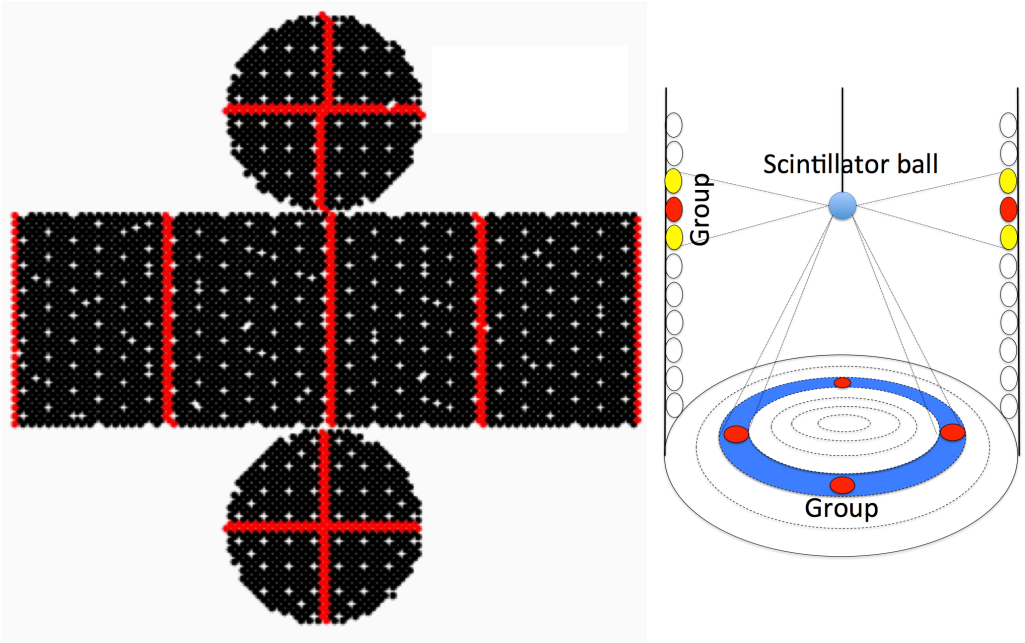

FIGURE 5.1: Positions of the Standard PMTs (left) and schematic of the grouping of the PMTs (right). Red points indicate the location. The figures are taken from [43].

with the measurement outcomes of the Standard PMTs. Given the permanent placement of the light source in the tank, routine HV measurements are feasible.

5.1.2 Relative Gain Measurement

The gain for each PMT is determined by the output charge relative to the amount of input light intensity. This gain can be ascertained from the average gain across all PMTs (Absolute gain) and individual PMT deviations from this average (Relative gain). A two-step measurement process using the aforementioned isotropic light source is employed for relative gain calculation.

Initially, light is introduced in abundance to ensure adequate illumination for all PMTs. Following this, a minuscule light quantity is introduced allowing PMTs to capture a single photon, registering a 1 p.e. signal. From this, the average charge under intense light (Q_{obs}) and the instances the PMT charge exceeds a set threshold (N_{obs}) are determined for each PMT. Upon conducting the two measurements at the same location, Q_{obs} and N_{obs} can be described as

$$Q_{\mathrm{obs}}(i) \propto I_{\mathrm{H}} \times a(i) \times \epsilon(i) \times G(i), \tag{5.1}$$

$$N_{\mathrm{obs}}(i) \propto I_{\mathrm{L}} \times a(i) \times \epsilon(i). \tag{5.2}$$

Here, $I_{\mathrm{H}}(I_{\mathrm{L}})$ denotes the averaged light intensity of the larger (smaller) light, a denotes the acceptance of each PMT, ϵ indicates a relative QE described below, and G denotes gain. The notation i represents i th PMT. Thus, the gain for each PMT can be calculated as

$$G(i) \propto \frac{Q_{\mathrm{obs}}(i)}{N_{\mathrm{obs}}(i)}. \tag{5.3}$$

The relative gain indicates the deviation from the average of G. In this case, the standard deviation is $\sim 5.9\%$. This deviation arises from the QE variability of each PMT, given the HV adjustments for uniform PMT charge. Relative gain serves as a coefficient for the charge to the p.e. conversion.

5.1.3 Absolute Gain Measurement

Absolute gain is determined from the charge distribution of 1 p.e. signal. The measurement is performed using apparatus consisting of a Cf source and a surrounding NiO_2 sphere, called a Ni-Cf source. The appearance is shown in Figure 5.2. The Ni-Cf source emits multiple gamma rays totaling 9 MeV by the thermal neutron capture on the ^{58}Ni. Neutrons are emitted from the spontaneous decay of the ^{252}Cf, and their half-life is 2.56 years, resulting in an average of 3.76 neutrons producing with an average energy of 2.1 MeV. The spontaneous decay of ^{252}Cf is only 3% of the decay fraction, and the remaining 97% is alpha decay. By placing the Ni-Cf source into the center of the tank, each PMT detected an average of 0.004 p.e./event so that over 99% of PMT signals are 1 p.e..

FIGURE 5.2: Appearance of the Ni-Cf source geometry. The figures are taken from [43].

After the correction of relative gain, described above, the charge distribution is made like Figure 5.3. The highest peak, around 0 pC, is formed by the photoelectrons not amplified at the first dynode. The second peak at 3 pC represents the averaged 1 p.e. peak. This measurement results in the conversion factor between pC and p.e. being 2.055, 2.297, 2,243, 2.645, 2.46 [pC/p.e.] for SK-I to SK-V, respectively. The factor in SK-VI is the same as SK-V since HV tuning for SK-VI is not changed from SK-V. The charge distribution shown in Figure 5.3 is also used in the detector simulation as the PMT response for the photoelectrons.

5.1.4 Relative QE measurement

For the low energy hit, such as the charge for each PMT being 1 p.e., the variation of QE for each PMT affects the physics measurement. Thus, we define the relative QE for each PMT. That is used for the energy reconstruction of particles (which appeared as QE in Equation 4.8) and reproduction of PMT response in the detector

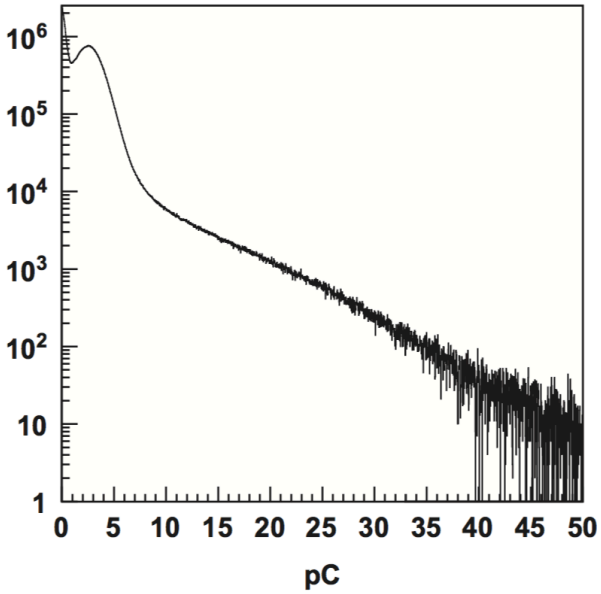

FIGURE 5.3: Charge distribution taken using Ni-Cf source used in SK-III. The figures are taken from [43].

simulation. The measurement also uses the Ni-Cf source described above. As shown in Equation 5.2, the averaged number of hits in the low luminosity is proportional to the relative QE. Consequently, the relative QE is discerned by comparing deviations in the average hit counts between actual data and an MC model, which does not account for individual PMT relative QE. Comparing with the MC model neutralizes effects like geometry, water interactions, individual PMT acceptances, and other PMT responses. Concurrently, hit counts must be adjusted for relative gain, PMT acceptance, and source proximity. The discrepancy from the amended hit average, termed the 'hit rate' (R_{hit}), can be defined as follows:

$$R_{\mathrm{hit}}(i) = N_{\mathrm{corr}}(i) \times \frac{1}{\sum^{N_{\mathrm{PMT}}} N_{\mathrm{corr}}(i)/N_{\mathrm{PMT}}}, \tag{5.4}$$

$$N_{\mathrm{corr}}(i) = N_{\mathrm{hit}} \times \frac{r^2}{a(\theta)} \times \frac{1}{G(i)}, \tag{5.5}$$

where N_{PMT} denotes the number of appropriately functioning PMT, N_{hit} indicates the number of hits obtained surrounding the event timing, $G(i)$ denotes the relative gain, r indicates the distance between PMT and the source, and $a(\theta)$ represents the acceptance function, similar to that in Equation 4.5. The position dependence of the hit probability is exemplified in Figure 5.4.

5.1.5 Timing Response Calibration

The timing response of a PMT varies due to factors like cable length, intrinsic PMT response, and the processing time of the electronic circuit. Additionally, the timing response is influenced by the amplitude of the PMT signal waveform, a phenomenon referred to as 'Time walk.' The purpose of timing response calibration is to establish a correction function that considers the comprehensive processing time of the detector

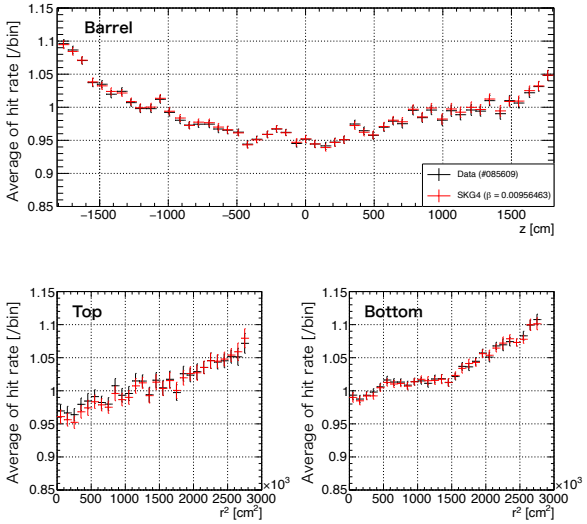

FIGURE 5.4: Hit rate distribution as a function of PMT positions measured in SK-VI. Top: barrel PMTs, with the z-position of PMTs plotted in the horizontal axis. Bottom: two plots indicate top (left) and bottom (right) PMTs, where the horizontal axis denotes the square of the radial distance on the x-y plane. Black points indicate the data, and red points display MC.

for each PMT. Correcting for the time walk is vital for the accurate reconstruction of particle tracks and vertices.

Figure 5.5 illustrates the design of the light source apparatus employed for this calibration. Monochromatic pulsed light, emanating from Nitrogen lasers, exhibits a 337 nm wavelength and a full-width at half maximum (FWHM) of 0.4 ns. This light is monitored and triggered by a fast-response 2-inch PMT. The wavelength of the laser light is shifted to 398 nm by a dye, which is within the combined response range of the PMT to Cherenkov emission, photon absorption, and PMT QE peaks. After that, the modified light attains a diffuser ball situated at the center of the tank. Any directional discrepancies in photon emission time from the diffuser ball are negligible, staying under 0.2 ns. Adjusting the intensity of light with a filter facilitates measurement of the timing response across various PMT signal amplitudes. As the PMT pulse height corresponds to the charge, this calibration is referred to as the TQ calibration.

Two-dimensional histograms plotting the timing against the charge for every PMT are exemplified in Figure 5.6, wherein the timing T denoted in the vertical axis is calculated as $T = T_{\text{obs}} - TOF - T_{\text{2-inch}}$, where the T_{obs} denotes the hit time of PMT, TOF indicates the time-of-flight (TOF) between each PMT and the light source, and $T_{\text{2-inch}}$ is the trigger timing of the monitoring 2-inch PMT. Calibration constants, termed 'TQmap' are extracted by fitting the TQ distributions to polynomial functions. The charge displayed on the horizontal axis in Figure 5.6 is segmented into 180 bins (Qbins). EachQbin is defined on a linear scale below 10 pC with a width of 0.2 pC/Qbin and on a logarithmic scale $\geq$ 10 pC with a width of 50 log(pC)/Qbin. After determining the timing peak for each Qbin, the time peaks for respective charges

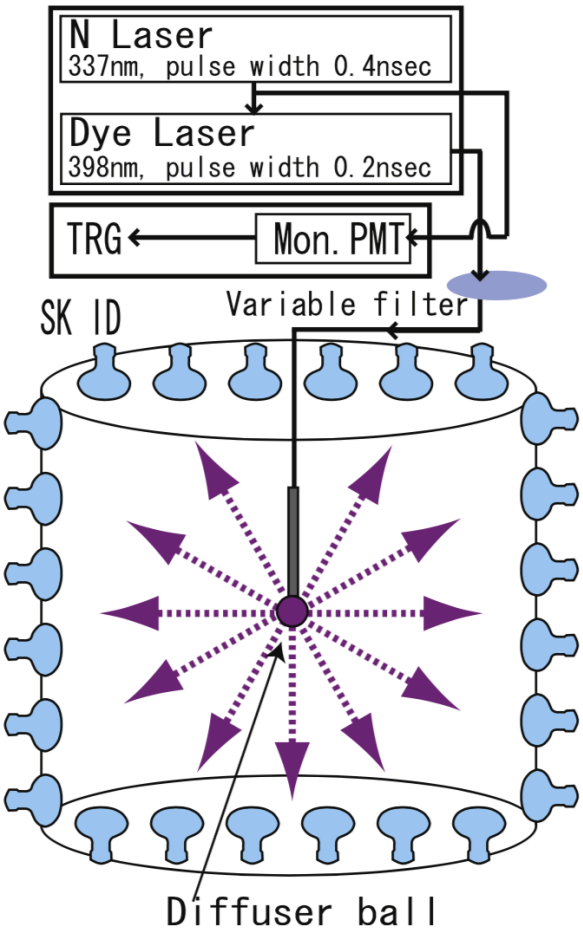

FIGURE 5.5: Schematic view of the timing calibration system. The figures are taken from [43].

are fitted by polynomial functions depending on Qbin as follows:

$$\mathrm{pol}N(x) \equiv p_0 + p_1 x + p_2 x^2 + \cdots + p_N x^N, \tag{5.6}$$

$$\mathrm{Qbin} \leq 10 : F_1(x) \equiv \mathrm{pol3}(x), \tag{5.7}$$

$$\mathrm{Qbin} \leq 50 : F_2(x) \equiv F_1(10) + (x-10)[F_1'(10) + (x-10)\mathrm{pol3}(x-10)], \tag{5.8}$$

$$\mathrm{Qbin} > 50 : F_3(x) \equiv F_2(50) + (x-50)\mathrm{pol6}(x-50), \tag{5.9}$$

where F_1' denotes a derivation of F_1 that is introduced to ensure continuity between $F_1(x)$ and $F_2(x)$. In total, 15 fitting parameters are determined for each PMT.

The timing resolution of each PMT, contingent upon the charge, can also be investigated using the same TQ calibration dataset. To gauge this resolution, timing distributions for all PMTs — corrected via the TQmaps — are compiled for every Qbin. These timing distributions are then modeled by an asymmetric Gaussian, characterized as follows:

$$f(t; t > T_{\mathrm{peak}}) \equiv A_1 \cdot \exp(-(t - T_{\mathrm{peak}})^2/\sigma_t^2) + B_1, \tag{5.10}$$

$$f(t; t \leq T_{\mathrm{peak}}) \equiv A_2 \cdot \exp(-(t - T_{\mathrm{peak}})^2/\sigma_t'^2) + B_2, \tag{5.11}$$

where the A_{i}, B_{i}, σ_t, and σ_t' represent the fit parameters that should satisfy a boundary condition of $A_1 + B_1 = A_2 + B_2$ to connect two Gaussians at $t = T_{\mathrm{peak}}$. An example

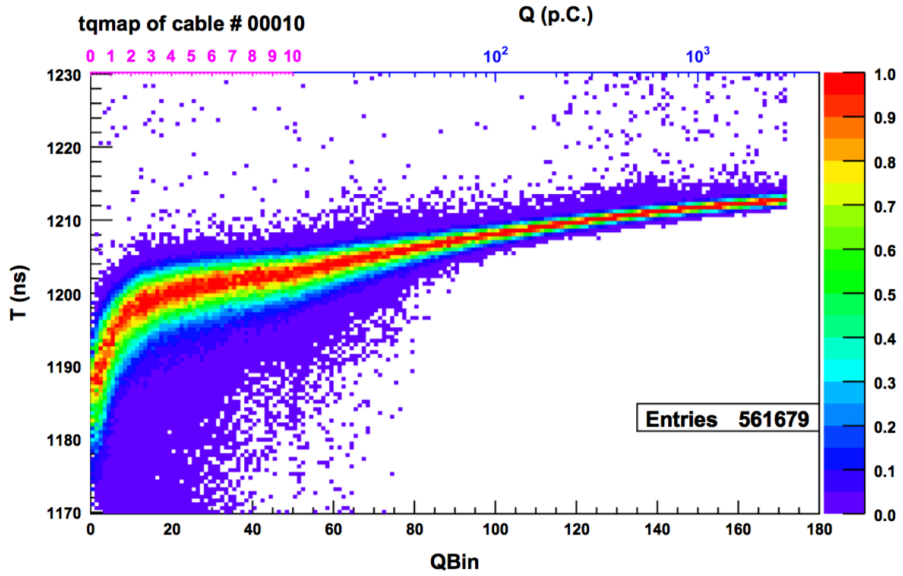

FIGURE 5.6: Typical scatter plot of the timing and the charge. For the vertical axis, larger (smaller) T corresponds to the earlier (later) hits. The figures are taken from [43].

of the timing distribution and the function resulting from the fitting for the Qbin=14 is presented in Figure 5.7, and the distribution of timing resolution is displayed in Figure 5.8 as a function of the charge. For lower charges, the two resolutions are observed to be more distributed. Thus, the timing resolution is implemented in the detector simulation.

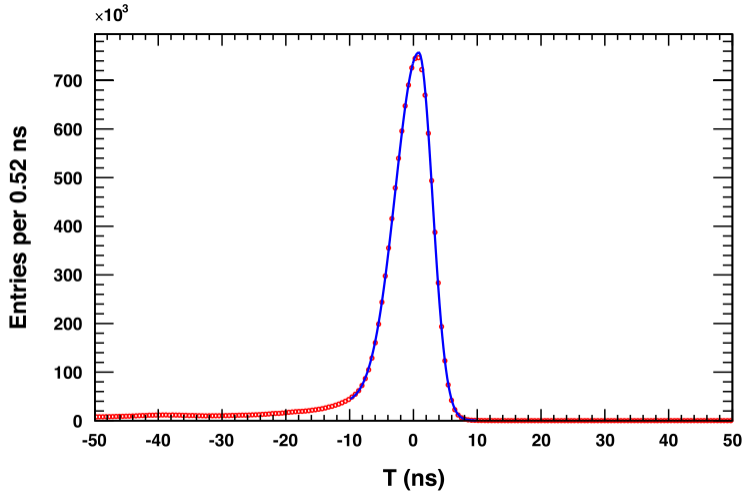

FIGURE 5.7: Timing distribution and the function resulting from the fitting for the Qbin = 14. The figures are taken from [43].

5.2 Photon tracking

A comprehensive understanding of photon tracking is pivotal for accurate data replication in detecter simulation. Moreover, refining the correction for photon absorption

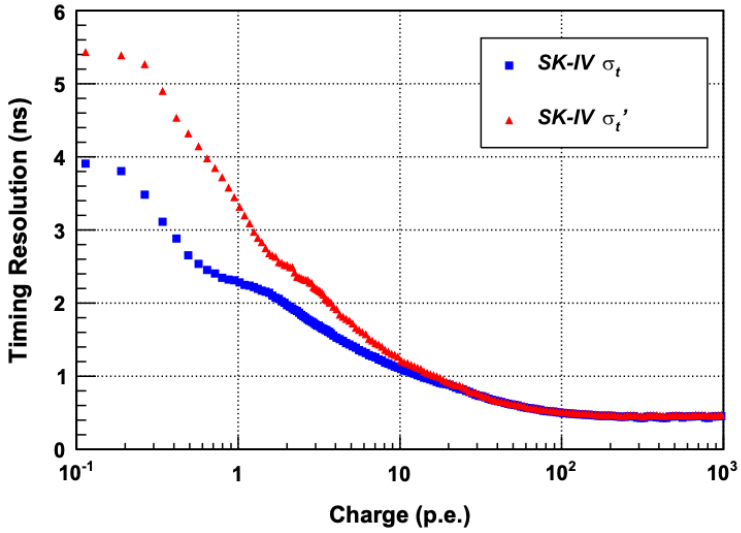

FIGURE 5.8: Distribution of timing resolution as a function of the charge, measured during in SK-IV. The figures are taken from [43].

enhances energy reconstruction. Thus, multiple parameters are evaluated to refine both the detector simulation and energy reconstruction in the SK.

5.2.1 Water Transparency Measurement

For photon tracking in the detector simulation, accounting for material properties like scattering and absorption within the tank is crucial. Light attenuation is represented using an attenuation length $L(\lambda)$ of a photon at wavelength λ and light path length l as the $\exp(-l/L(\lambda))$. In the SK analysis, the $L(\lambda)$ is defined as

$$L(\lambda) = \frac{1}{\alpha_{\text{abs}}(\lambda) + \alpha_{\text{sym}}(\lambda) + \alpha_{\text{asym}}(\lambda)}. \tag{5.12}$$

Here, the $\alpha_{\text{abs}}(\lambda)$, $\alpha_{\text{sym}}(\lambda)$, and $\alpha_{\text{asym}}(\lambda)$ denote the attenuation coefficient for the absorption, symmetric scattering, and asymmetric scattering, respectively. $\alpha_{\text{asym}}(\lambda)$ is introduced to consider the forward Mie scattering easily. $\alpha_{\text{sym}}(\lambda)$ is used to consider the symmetric Rayleigh scattering and the remaining symmetric components of Mie scattering. To measure three attenuation length variables, we injected the monochromatic laser with some wavelength from the top of the tank downward. The schematic illustration of the measurement is depicted in Figure 5.9.

To understand wavelength dependence, the measurement uses lasers of five distinct wavelengths (337, 375, 405, 445, and 473 nm). The PMT hit timings are subtracted by the TOF from the light-blue area displayed in Figure 5.9. After that, the optimal attenuation coefficient is identified by comparing TOF subtracted time across various PMT regions between measured data and simulations while tweaking the coefficients. Figure 5.10 presents the TOF subtracted timing distribution for each PMT zone along with the best-fit outcome in the SK-IV. The region pinched in the two blue lines on the right-hand side is considered the hits after reflection on the PMT, acrylic surface, and the black sheet at the bottom of the ID tank.

After the three best coefficients with minimum χ^2, representing the discrepancy between data and MC, are determined for each wavelength, the attenuation coefficients are evaluated as functions of the wavelength by fitting to discrete coefficients for five

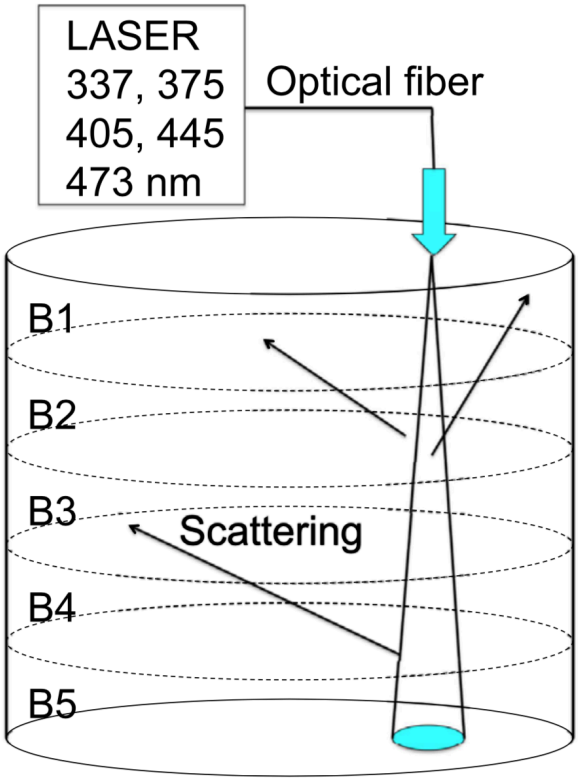

FIGURE 5.9: Schematic of the laser measurement system. The analysis uses PMTs pertaining to five segmented barrel regions B1-B5 and the top. The figures are taken from [43].

wavelengths. The attenuation coefficients are calculated using 9 parameters P_0-P_8 as follows:

$$\alpha_{\mathrm{abs}}(\lambda) \equiv P_0 \times \frac{P_1}{\lambda^4} + C \tag{5.13}$$

$$C \equiv P_0 \times P_2 \times (\lambda/500)^{P_3} \ (\text{for } \lambda < \lambda_{\mathrm{thr}}) \tag{5.14}$$

$$\alpha_{\mathrm{sym}}(\lambda) \equiv \frac{P_4}{\lambda^4} \times \left(1 + \frac{P_5}{\lambda^2}\right) \tag{5.15}$$

$$\alpha_{\mathrm{asym}}(\lambda) \equiv P_6 \times \left(1 + \frac{P_7}{\lambda^4} \times (\lambda - P_8)^2\right) \tag{5.16}$$

The parameters P_0–P_8 are called 'water parameters.' C can be calculated using Equation 5.14 until $\lambda < \lambda_{\mathrm{thr}}$. In contrast, for wavelength exceeding λ_{thr}, the experimental result of Pope and Fry's model [139] is invoked. λ_{thr} is determined as the wavelength at the intersection between our numerical calculation and the Pope-Fry model.

The best-fitting results of the water parameters recorded by the laser measurement in SK-VI are summarized in Figure 5.11.

We compared two types of simulation to review whether any deviation is detected in the asymmetric scattering. It can be concluded based on the modeling variations of the angular dependence of asymmetric scattering. SKG4 refers to the angular dependence of Mie scattering as a 'Henyey-Greenstein'(HG) approximation [140], whereas SKDETSIM assumes that the probability increases linearly increased along with $\cos\theta$.

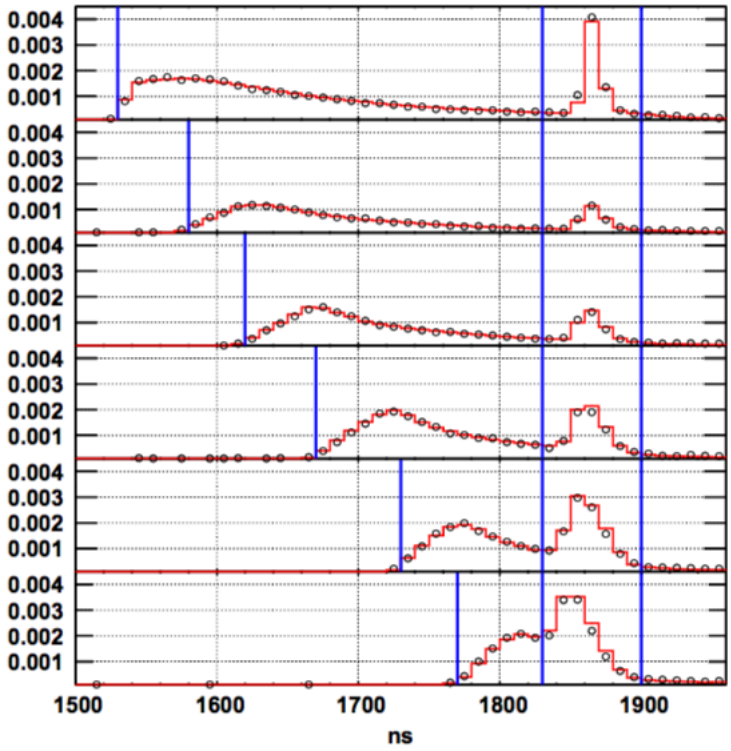

FIGURE 5.10: Best-fitted timing distribution of data and MC for each PMT region in SK-IV measurement. The circle with the black line represents the data, and the red line indicates the MC. Both are normalized by total observed photoelectrons. The top panel represents the PMTs at the top of the ID wall, whereas the second-to-bottom panels correspond to the five segmented barrel regions B1–B5, as displayed in Figure 5.9. The region between the two blue-solid lines on the left-hand side was used to fit the attenuation coefficients. The region between the two blue-solid lines on the right-hand was utilized in the PMT reflection measurement. The figures are taken from [43].

According to the HG approximation, the differential cross-section of the Mie scattering can be approximated as

$$\frac{d\sigma}{d\Omega} \sim \frac{1-g^2}{(1+g^2-2g\cos\theta)^{3/2}}, \tag{5.17}$$

where $d\Omega = d\cos\theta\phi$, σ denotes the cross-section, θ represents the scattering angle, and g indicates the cosine of the mean angle. Therefore, the normalized density function $P(\cos\theta_0)$ can be expressed as follows:

$$\begin{aligned} P(\cos\theta_0) &= \frac{\int_{-1}^{\cos\theta_0} \frac{d\sigma}{d\Omega} d\cos\theta}{\int_{-1}^{1} \frac{d\sigma}{d\Omega} d\cos\theta} \\ &= \frac{1-g^2}{2g}\left(\frac{1}{1+g^2-2g\cos\theta_0} - \frac{1}{1+g}\right) \end{aligned} \tag{5.18}$$

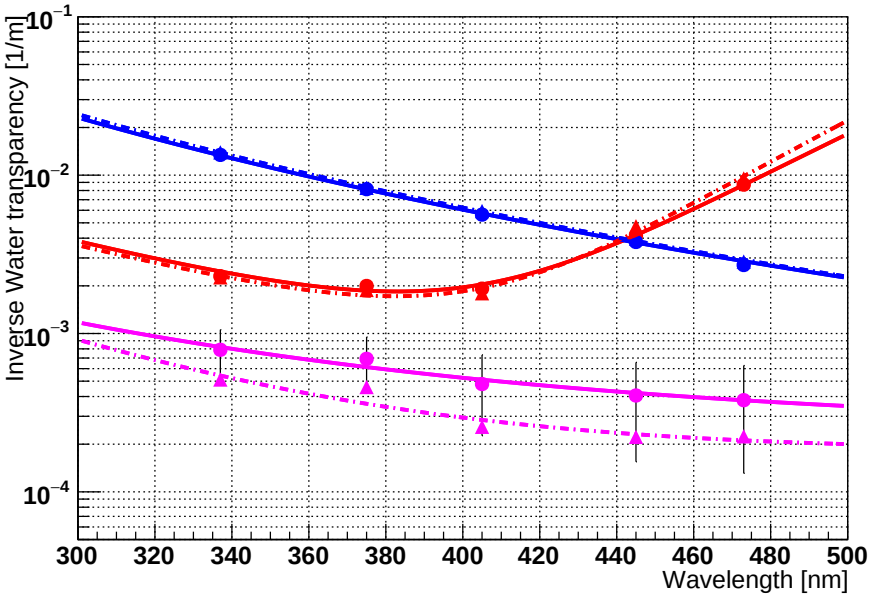

FIGURE 5.11: Distributions of the coefficient as functions of the wavelength. Each point represents the Best-fitted coefficients for each laser wavelength and interaction. Red, blue, and magenta points and the lines represent the α_{abs}, α_{sym}, and α_{asym}, respectively. Circles (triangles) and solid (dot-dashed) lines of the Geant4-based (GEANT3-based) simulation result are described in Section 3.3.

It yields the angular distribution of HG approximation, computed using the random number p between 0 and 1, as follows:

$$\begin{aligned}\cos\theta &= \frac{1}{2g}\left(1+g^2-\frac{1-g^2}{1-g+2gp})^2\right) \\ &= 2p\frac{(1+g)^2(1-g+gp)}{(1-g+2gp)^2}-1\end{aligned} \tag{5.19}$$

5.2.2 Top-Bottom Asymmetry Measurement

The water under $z = -11$ m in the SK tank is continuously circulated to maintain water transparency. However, above this depth, the water temperature with height, with a maximum variation in temperature at 0.2 °C. This increase in temperature also affects water quality, causing up to a 5% discrepancy in transparency. Due to these factors, the water in the tank is not uniform. Understanding the nonuniformity along the z-axis becomes critical. To estimate this, we examine the top-bottom asymmetry of water transparency (TBA) using both the Ni-Cf and Xe isotropic light sources.

TBA α_{tba} is calculated as

$$\alpha_{\mathrm{tba}} \equiv \frac{\langle N_{\mathrm{top}}\rangle - \langle N_{\mathrm{bottom}}\rangle}{\langle N_{\mathrm{barrel}}\rangle}, \tag{5.20}$$

where the $\langle N_{\mathrm{top}}\rangle$, $\langle N_{\mathrm{bottom}}\rangle$, and $\langle N_{\mathrm{barrel}}\rangle$ denote the average of hit rate R_{hit} for the PMT on the top, bottom, and wall of the tank, respectively. The variation of the TBA during the SK-V and the SK-VI is represented in Figure 5.12, in which variation ranges

up to $\sim 5\%$. A notable decrease in TBA was observed post the water convection period when relative QE measurements were operated in March 2020. With the introduction of Gd, the pattern of TBA remained consistent. Almost daily measurements of TBA are performed using the Xe light source, whereas the Ni-Cf source is utilized monthly.

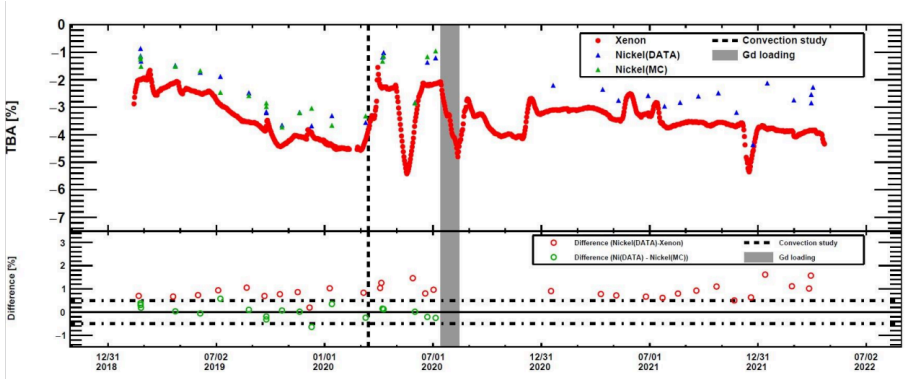

FIGURE 5.12: Variation of the TBA during the SK-V and SK-VI, taken by the Ni-Cf source and Xe light source (top), and differences of TBA between both measurements and between data and MC for Ni-Cf source measurement (bottom). Thick dotted-dashed line indicates the 0.5% difference region.

Given that TBA variation is assumed to emerge as the absorption effect, the coefficient α_{abs} is adjusted by multiplying the factor $A(z,t)$, which is denoted as

$$A(z,t) \equiv \begin{cases} 1 + z \cdot \beta & \text{for } z \geq -11 \text{ m}, \\ 1 - 11 \cdot \beta & \text{for } z < -11 \text{ m}, \end{cases} \tag{5.21}$$

where the $\beta(t)$ denotes the time-dependent slope of the water transparency along with the z-axis. To estimate the correlation between β and TBA, the optimization of the parameter β for all Ni-Cf source data in the SK-VI period by scanning various β to determine the β that most accurately reproduces the TBA of the actual data. Consequently, the correlation between Ni-Cf data and MC is estimated as

$$\beta(t)\ [\text{cm}^{-1}] = 0.01 \times (-0.006322 \times 100 \times \text{TBA} - 0.004130). \tag{5.22}$$

Here, the time dependence of $\beta(t)$ is derived from the daily measured TBA by the Xe light source. The correlation is introduced into the MC and the energy reconstruction.

5.2.3 Photon Reflection on the Material Surface

For an accurate photon transportation simulation, it is crucial to incorporate photon reflection on the material surfaces into the MC. In particular, the reflectivity of PMTs and the black sheet is evaluated using two types of laser systems.

Reflection on PMT Surface

The simulation considers four refractive index layers from the surface inwards towards the PMT: water, glass, bi-alkali, and vacuum. Their refractive indices are 1.33, $1.472+3670/\lambda^2$, $n_{\text{real}} + i \cdot n_{\text{img}}$, and 1.0, respectively. Here, λ denotes the wavelength of the photon, n_{real}, and n_{img} denote the real and imaginary parts of the complex refractive

index. The light reflection of the PMT surface in the MC is adjusted using the same laser data from Section 5.2.1. The best pair of parameters for n_{real} and n_{img} are searched by comparing the timing distribution of the region between the two blue lines on right-hand side in Figure 5.10. For the wavelengths 337, 375, 405, and 445 nm, the optimized pairs are (2.8, 1.4), (3.2, 1.5), (3.4, 1.6), and (3.6, 1.7), respectively, in both SK-V and SK-VI.

Reflection on Black Sheet

Although the majority of the photons are absorbed by the black sheet, a minority gets reflected. This reflectivity is gauged using a light injector. Figure 5.13 depicts the schematic representation of the measurement setup.

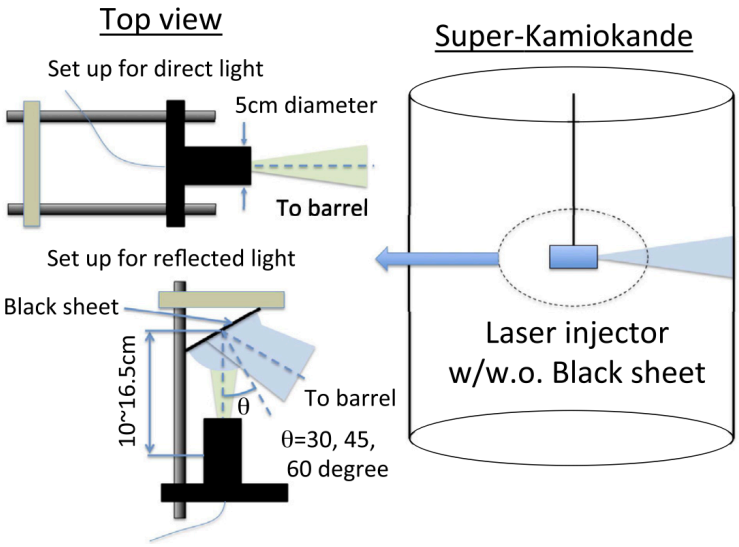

FIGURE 5.13: Schematic of a laser light injector to measure black sheet reflectivity. The figure is taken from [43].

The apparatus is inserted into the central region of the tank. The laser is injected into the black sheet at the incident angle θ of $\theta = 30$, 45, and 60 degrees such that the ID PMTs detect the reflected light. The reflected charge $Q_{\text{scattered}}$ is measured for wavelengths of 337, 400, and 420 nm. In addition, a direct charge in the absence of the black sheet (Q_{direct}) is measured for reference purposes. Reflectivity (R) is tuned using the equation $R = Q_{\text{scattered}}/Q_{\text{direct}}$. The comparison of R between the laser data and laser MC with the best-tuned reflectivity is depicted in Figure 5.14. Both the actual data and MC results align within a 1% margin across all wavelengths and angles.

5.3 Energy Scale Calibration using LINAC

To calculate the energy scaling factor for low-energy MC simulations, the electron linear accelerator (LINAC) is employed. The LINAC is capable of producing mono-energetic electron beams. As depicted in Figure 5.15a, these electrons are bent by the D1–D3 magnet, directing them above the tank and then downward. The LINAC is positioned above the tank, and its beam pipe extends into the tank through a calibration hole approximately 18 cm in diameter. As indicated in Figure 5.15a, the

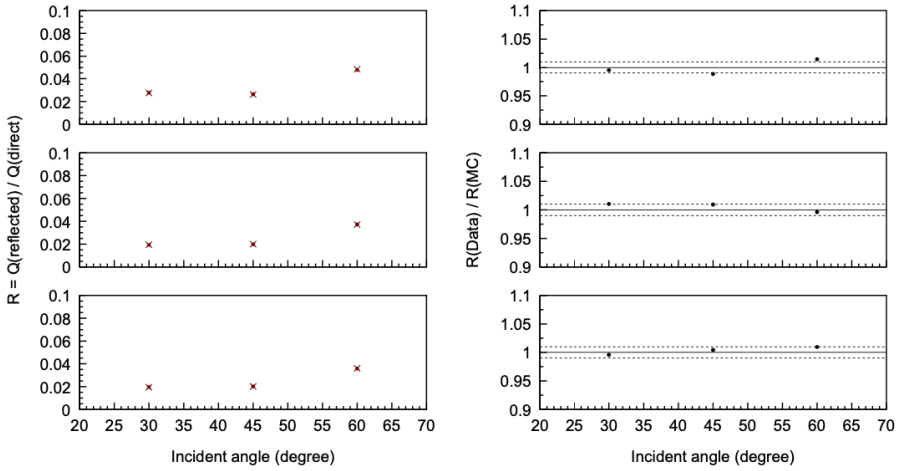

FIGURE 5.14: Comparison between laser data and MC in the black sheet measurement. The three left panels show the ratio of the charge between reflected and direct incident light, and the right panels show the ratio between data and MC for the left plots, for the wavelength at 337 nm (top), 400 nm (middle), and 420 nm (bottom). The figure is taken from [43].

x-position of the beam can be shifted by moving the tower on top of the tank, whereas its z-position can be modified by extending or retracting the beam pipe. The energy is discretely selected from kinematic energies of 5–18 MeV. Thus, the LINAC is utilized to estimate the scaling factor, review the uniformity of energy reconstruction, and evaluate systematic uncertainty on the energy reconstruction up to several tens of MeV.

After optimizing the parameters for evaluating N_{eff} and the detector simulation, N_{eff} for the LINAC data should be ideally comparable to the LINAC MC at each energy point and beam position. Any remaining discrepancies can be attributed to intricate PMT property reproductions, like PMT collection efficiency, which poses challenges for individual estimations. By comparing the N_{eff} of the LINAC data with MC across beam positions and energies, an overarching scaling factor for MC application is deduced. Typically, this scaling factor is multiplied by the QE of the ID PMT. In SK-VI, this factor is estimated to be ~ 0.88.

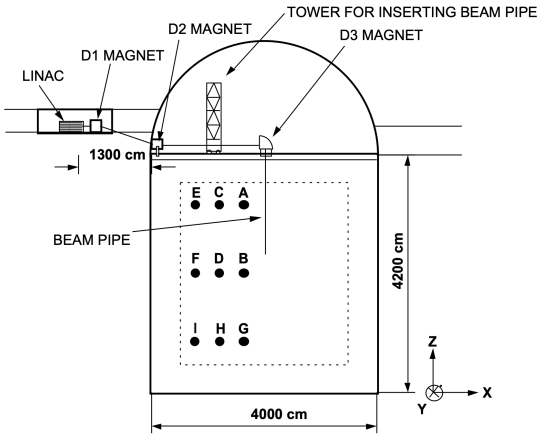

(A) Schematic of the LINAC calibration geometry. The marker A-I is the injection position.

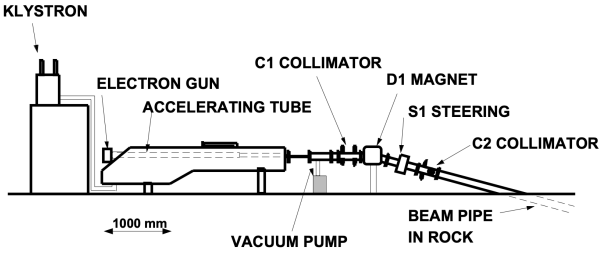

(B) Schematic of the part of the electron acceleration for LINAC calibration.

Chapter 6

Development of Neutron Tagging in SK-Gd

Detecting a neutron signal, i.e., the gamma rays resulting from thermal neutron capture, is the key aim of the SK-Gd experiment. The event identification using a prompt signal and delayed-neutron signal is called a 'delayed coincidence method.' This chapter begins by outlining the method of neutron tagging during the pure water period, progressing to a description of a newly constructed tagging algorithm, and concluding with its application to actual neutron source data.

6.1 Neutron Tagging Algorithm

6.1.1 Neutron Tagging in Pure Water

As introduced in Section 2, the SK detector was upgraded from SK-IV onward to record all PMT hits post-SHE triggers. Within SK, the event triggering SHE has been designated as the prompt signal. Until SK-VI, the neutron signal was represented by a single 2.2 MeV gamma ray, a product of thermal neutron capture on the proton. Initially, neutron tagging was implemented through a series of rectangular cuts [48]. Given the challenge of detecting the low 2.2 MeV signal in SK, a machine learning (ML) based algorithm was developed to maximize the efficiency of neutron signal identification. Notably, in the SRN search during SK-IV [20], the Boosted Decision Tree (BDT) discriminator [141] with 22 characteristic variables was applied, which delivered $\sim 20\%$ efficiency with approximately 12.5% relative uncertainty.

6.1.2 Neutron Tagging in SK-Gd

In SK-Gd, the neutron signal is augmented by the thermal neutron capture on Gd, resulting in multiple gamma-ray emissions totaling ~ 8 MeV. Moreover, the Gd isotope possesses one of the highest cross-sections for thermal neutron capture among natural isotopes. Consequently, even at minute concentrations, the capture fraction is considerable. Additionally, the capture time constant is reduced compared to pure water. The cross-sections of thermal neutron capture for ^{155}Gd and ^{157}Gd are summarized in Table 6.1, which predominantly contain large cross-sections.

In SK-VI, where the Gd mass concentration is around 0.011%, the capture time constant is ~ 115 μs, leading to $\sim 50\%$ of the neutrons being captured on Gd [26]. This short lifetime ensures that over 99% of neutrons are captured by the end of the AFT window. Given the augmented neutron capture signal on Gd (Gd-capture), there should be a marked improvement in neutron tagging efficiency. Measurements by weight and Atomic Absorption Spectrometer (AAS) have estimated the Gd mass concentration at 109.7 ± 0.7 ppm and 114 ± 2 ppm, respectively [26]. The capture

TABLE 6.1: Summary of thermal neutron capture on ^{155}Gd and ^{157}Gd [37]

	Abundance [%]	Cross-section σ_{NC} [barn]	Total γ energy [MeV]
^{155}Gd	14.80	60,900	8.45
^{157}Gd	15.65	254,000	7.86
$^{\mathrm{nat}}$Gd	–	$\sim 49,000$	–

time constant, reported as 115 ± 1(syst.+stat.) μs in Ref [26], is correlated with the cross-section of neutron capture and the Gd concentration. Nevertheless, the variations in neutron transportation computation in Geant4.10.5 indicate that the capture probability of Gd surpasses the actual calculation based on cross-section values. Thus, in detector MC simulations, the Gd mass concentration is adjusted to align the capture time constant with the data acquired from the measured radioactive source, as detailed in [26].

6.1.3 Delayed Neutron Search

This section delves into the process of neutron selection and the corresponding efficiency. The efficiency is estimated from neutron MC simulations, which produce a million neutrons with a kinetic energy of 0.1 MeV within the entire ID tank. In this study, the neutron signals are searched between 4 μs to 535 μs post the prompt event to mitigate the thermalization effect and any prompt event influences in SK. This search window captures over 95% of the neutron capture.

Injection of Realistic Noise into MC

Assessing the potential inaccuracies of the algorithm, especially when it misconstrues noise hits as neutrons, is essential for evaluating the neutron tagging algorithm. Nevertheless, simulating random noise, particularly from radioactive decay, poses challenges. As a result, SKG4 does not produce these hits. Instead, the real noise hits are introduced into the MC after a delay of 2.7 μs. This real noise hit data is sourced from the 'T2K dummy spill data' and the 'SK wide random trigger data.' The former is collected using the T2K trigger when the T2K beam is inactive within a 1024 μs time frame. The latter is gathered during regular SK normal runs every $\sim$ 30 seconds over a time span of 1000 μs. From these datasets, a 532 μs noise segment is trimmed and appended to the MC. Figure 6.1 illustrates the schematic diagram of noise hit generation for each event.

Pre-selection

The search window primarily contains a number of PMT hits attributable to the dark noise. To address this, the initial criteria require a N_{200} (number of hits within 200 ns) between 25 and 200 hits in the SHE and AFT time window (535 μs). Hit clusters that meet this requirement are retained. The primary selection is visually represented in Figure 6.2.

Cut-based neutron selection

For the subsequent step, low-energy reconstruction (Section 4.1) is applied to all candidates passing the pre-selection, because the Gd-capture signal can be reconstructed

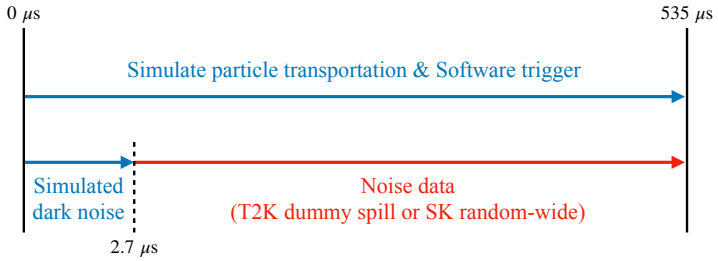

FIGURE 6.1: Schematic diagram of the procedure of noise production. The contents with the blue characters and lines are simulated in the detector MC, while those with red characters and lines are appended later.

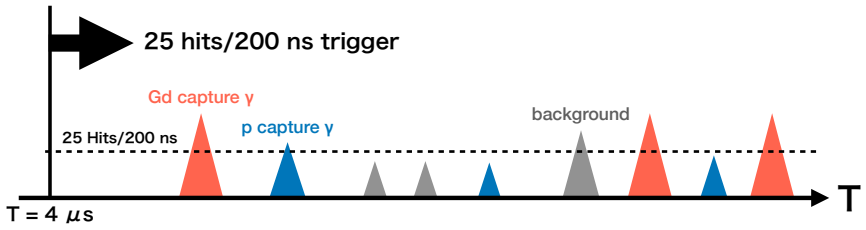

FIGURE 6.2: Illustration of the primary selection. Dashed line indicates the N_{200} threshold.

using a nominal low-energy reconstruction algorithm owing to its high-energy gamma-ray emission. Mis-reconstructed events and low-energy events resulting from radioactive decay products are typically situated closer to the perimeter of the tank wall. To filter out these events, a fiducial volume cut is implemented using the d_{wall}, representing the distance between the event vertex and the ID wall. Only the events with $d_{\text{wall}} > 200$ cm are considered after this.

The remaining events are further reduced through two threshold values related to event quality, i.e., g_{vtx} and g_{dir}; these variables are defined in Section 4.1. Distributions of both event quality variables are presented in Figure 6.3. To ensure optimal event quality, only events that satisfy the criteria $g_{\text{vtx}} > 0.4$ and $g_{\text{dir}} < 0.4$ are advanced to the subsequent stage.

In the final step of distinguishing noise events, the Gd(n, γ) event is chosen based on energy and vertex criteria. Given the spallation correlation between the prompt and delayed events, the distance from the reconstructed vertex to the prompt event vertex, termed d_{prompt}, can serve as an effective classifier. As such, a d_{prompt} criteria of less than 300 cm is implemented. In this MC study, the prompt event vertex is presumed to be the accurate neutron-generated vertex. The d_{propmt} distribution is illustrated in Figure 6.4. Here, the Gd-captured event appears to be accurately reconstructed in proximity to the prompt event vertex.

Finally, the reconstructed energy is considered the basis for selecting Gd-capture. Figure 6.5 illustrates the reconstructed energy distribution of gamma rays captured from Gd, protons, and noise candidates. While the Gd signal comprises the combination of multiple gamma rays, whose individual energies are not discernible in SK, the visible energy in SK is typically less than that of a single gamma ray with an energy equivalent to the sum of the multiple gamma rays. Nonetheless, it remains a reliable

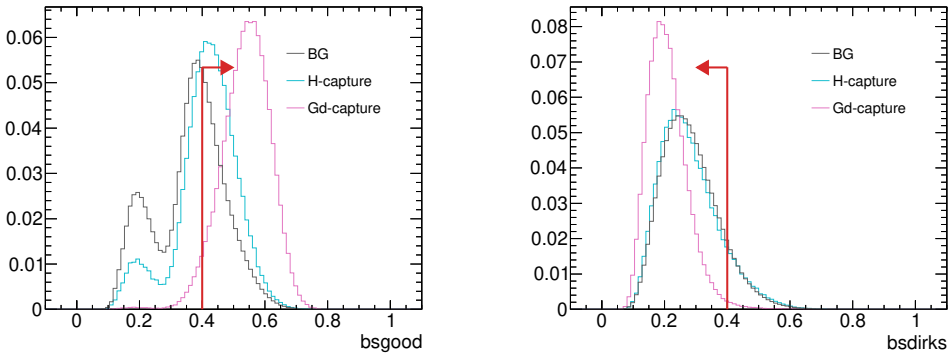

FIGURE 6.3: Distribution of the g_{vtx} (left) and g_{dir} (right) for signals from neutron capture on Gd (magenta) and proton (cyan), and noise (gray) candidates. The red arrows show the cut criteria. These distributions are normalized by area.

indicator for distinguishing the Gd signal from the background noise. Thus, an energy threshold of $E > 3$ MeV is set for the reconstructed energy in this analysis.

The cut variables and criteria of the Gd-capture signal are summarized in Table 6.2.

TABLE 6.2: Summary of neutron selection variables.

Cut variables	Criteria
Capture time t	$t > 4$ μs
N_{200}	$N_{200} \geq 25$
Fiducial volume cut	$dwall > 2$ m
Vertex reconstruction goodness g_{vtx}	$g_{\mathrm{vtx}} > 0.4$
Direction reconstruction goodness g_{dir}	$g_{\mathrm{dir}} < 0.4$
Distance from prompt vertex d_{prompt}	$d_{\mathrm{prompt}} < 300$ cm
Reconstructed energy E	$E > 3$ MeV

6.1.4 Neutron Tagging Efficiency

Table 6.3 summarizes the selection efficiency for p-capture, Gd-capture, and the reduction power of background for each cut. Events with a prompt vertex located outside the fiducial volume are omitted from the initial event count. The cut criteria aim to maximize Gd-capture selection and minimize background. Consequently, the efficiency of p-capture is compromised. In the end, the implemented criteria successfully diminish the background signal to 10^{-5} while retaining a Gd-capture efficiency of 78.6%.

Therefore, the neutron tagging efficiency for true neutrons $\epsilon_{\mathrm{n}}^{\mathrm{true}}$, which was calculated as

$$\epsilon_{\mathrm{n}}^{\mathrm{true}} = \frac{\text{Number of remaining neutron capture events}}{\text{Number of initial capture events}}, \tag{6.1}$$

and which was calculated as $39.5 \pm 0.1\%$.

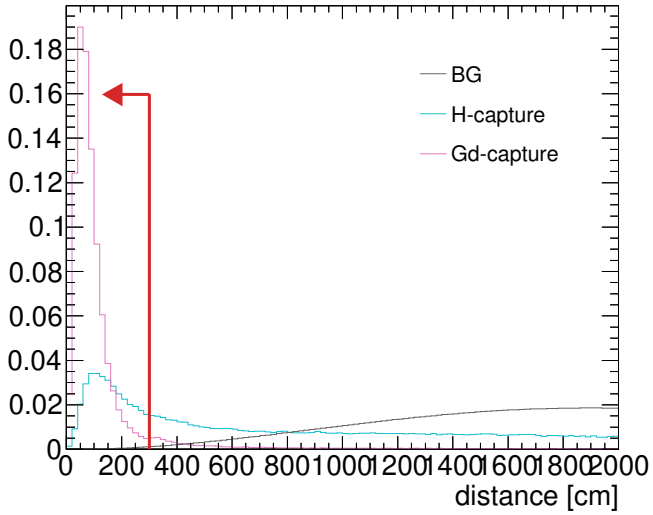

FIGURE 6.4: Distributions of the d_{prompt} for the signal from neutron capture on Gd (magenta) and proton (cyan), and noise (gray) candidates. Red arrow indicates the threshold. These distributions are area-normalized.

TABLE 6.3: Summary of selection and reduction efficiency for the neutron event and background.

Cut criteria	p-capture	Gd-capture	Background
Initial	355360	336046	–
$t > 4$ μs and $N_{200} \geqq 25$	41.2%	95.0%	100%
$dwall > 200$ cm	29.8%	88.8%	47.0%
$bsgood > 0.4$	18.8%	85.4%	11.6%
$bsdirks < 0.4$	16.8%	84.6%	10.3%
$d_{\text{prompt}} < 300$ cm	8.0%	81.9%	0.06%
$E > 3$ MeV	2.4%	78.6%	0.002%
Final	8521	264276	–

The capture time distribution is illustrated in Figure 6.6. The time constant is ascertained by fitting the range from 20 μs to 500 μs using an exponential function.

$$f(t) = A \cdot \exp(-x/\tau) + B \tag{6.2}$$

where A denotes the scale for fitting, B indicates the constant component, and τ signifies the capture time constant. The obtained value of 115.3 ± 0.5 μs is strongly consistent with the measured data [26].

6.1.5 Misidentification rate

The misidentification refers to the rate of the algorithm falsely recognizing non-neutron events as neutrons. Accurate event search analysis hinges on this, given the necessity for a minimal background rate when searching low-intensity events. To gauge the misidentification rate per event, termed ε_{mis}, the neutron search algorithm is utilized

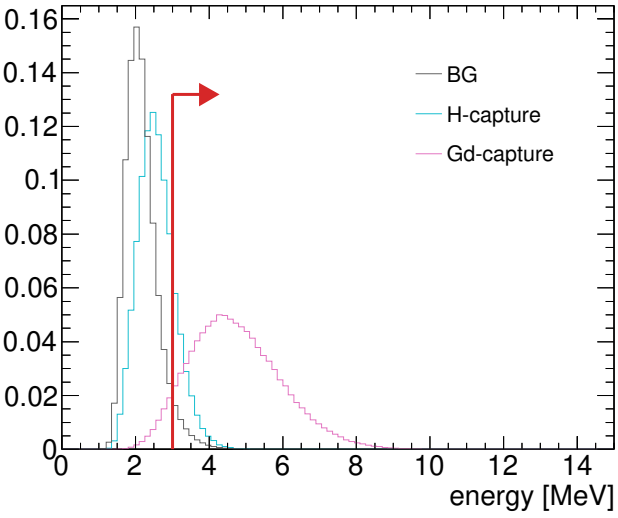

FIGURE 6.5: Distributions of the reconstructed energy for the signal from neutron capture on Gd (magenta) and proton (cyan), and noise (gray) candidates. Red arrow indicates the cut criteria. These distributions are normalized by area.

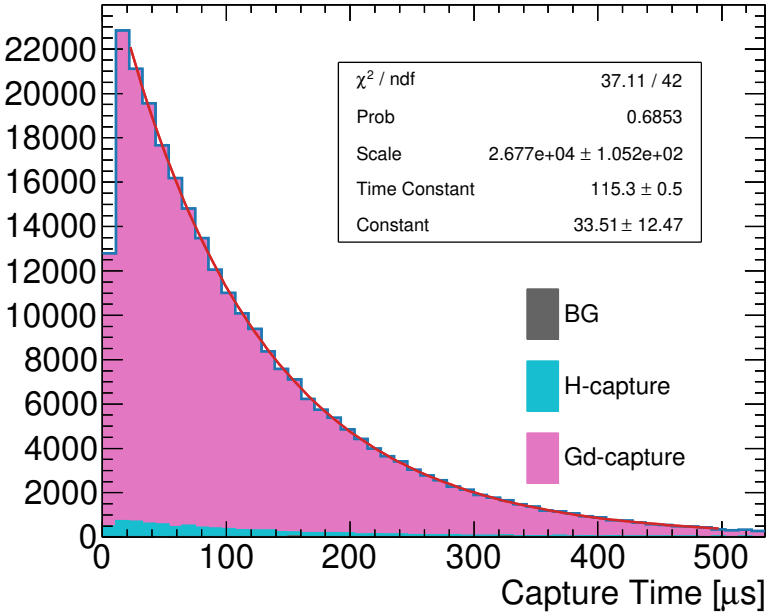

FIGURE 6.6: Capture time distribution of the neutron MC and the fitting result.

on the random trigger data detailed in Section 6.1.3. The vertex of the prompt event is assumed to be $(x, y, z) = (35.3, -70.7, 0)$ cm, which is the center calibration hole

for x, y and the center for z position. The value for ε_{mis} was calculated as follows:

$$\varepsilon_{\text{mis}}\ [/\text{event}] = \frac{N_{\text{delayed}} \cdot T_{\text{delayed}}}{N_{\text{random}} \cdot T_{\text{random}}}, \tag{6.3}$$

where N_{delayed} denotes the number of selected events as neutrons, N_{random} indicates the number of random trigger data, T_{delayed} denotes the time width of delayed neutron search (531 μs), and T_{random} indicates the time duration of the random trigger data. The consistency of ε_{mis} is assessed across all random trigger data from SK-VI. Figure 6.7 portrays the ε_{mis} distribution based on the observation period. When considering the entirety of the live time of SK-VI, it is classified into 20 uniform segments. Throughout the SK-Vi period, the mean ε_{mis} value stands at $(1.83 \pm 0.03) \times 10^{-3}$ per event.

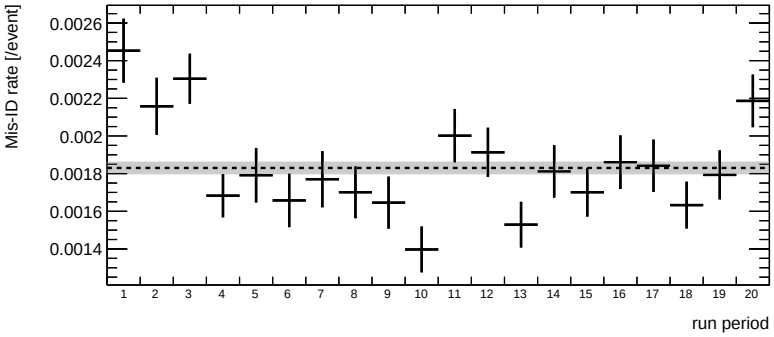

FIGURE 6.7: Time variation of ϵ_{mis}. Black-dotted line denotes the weighted mean value for the entire period, and the gray-shaded region indicates the standard deviation.

6.2 Americium-Beryllium Calibration

An accompanying prompt event for the neutron is required to evaluate the neutron tagging within actual SK data. Consequently, neutron detection was undertaken utilizing the Americium-241/Beryllium-9 (AmBe) radioactive source, renowned for emitting neutrons along with gamma rays. The main reaction chain can be described as follows:

$$^{241}\text{Am} \rightarrow {}^{237}\text{Np} + \alpha \tag{6.4}$$

$$^{9}\text{Be} + \alpha \rightarrow {}^{12}\text{C} + \text{n} + \gamma(4.4\ \text{MeV}), \tag{6.5}$$

where the gamma-ray emission is sourced from the de-excitation of the first excited state of ^{12}C. Figure 6.8 exhibits the major final state of the AmBe source. In this measurement, the pair of a neutron and a prompt 4.4 MeV gamma ray are used as the target of the delayed coincidence.

6.2.1 Measurement

The AmBe source employed in this study is near-cylindrical, with dimensions of $\sim$ 1.2 cm diameter and height, as depicted in Figure 6.9a. Due to the low energy of the Cherenkov light from the 4.4 MeV gamma ray, which is not sufficient to trigger SHE,

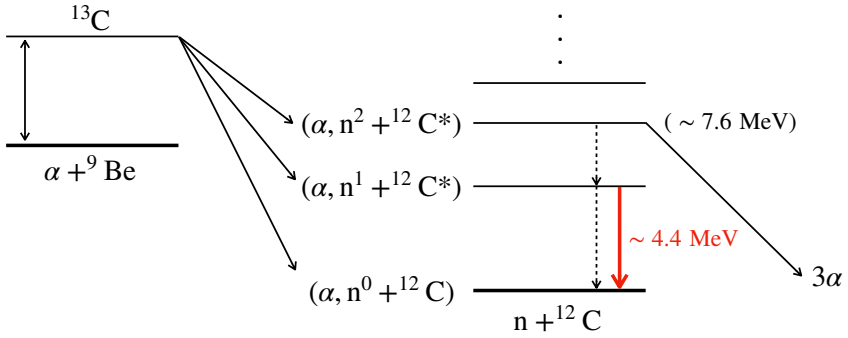

FIGURE 6.8: Major final state of ^{13}C. A de-excitation from the second excited state was not observed in the Kamioka AmBe source.

a unique setup was adopted. In this arrangement, the source was combined with a BGO scintillator crystal to boost the gamma-ray light yield. The BGO crystals utilized in this measurement are cubic-shaped, though one corner is missing. Figure 6.9b displays the appearance of BGO crystal.

(A) Appearance of the AmBe source.

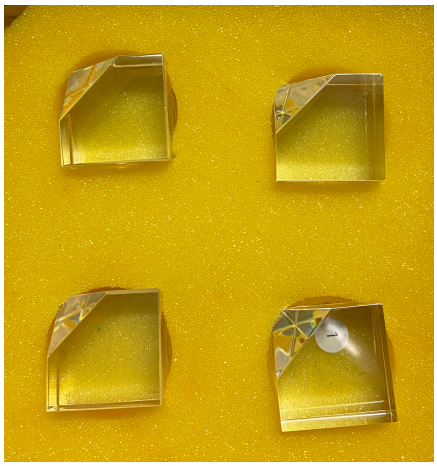

(B) Appearance of the four pieces of BGO scintillator crystals.

FIGURE 6.9: Appearance of the Am/Be source (left) and the four pieces of BGO scintillator crystals (right).

Source structure

The data was collected from two distinct source geometries to examine the influence of BGO on tagging efficiency: '1BGO' and '8BGO.' The 8BGO configuration entirely envelopes the source with eight BGO crystals, creating a cube with the missing corner at its center. On the other hand, the 1BGO setup positions the source atop a single BGO crystal, resulting in the source being only partially enveloped by BGO. All source components are housed within the acrylic casing. The visual and schematic of source geometries can be observed in Figure 6.10.

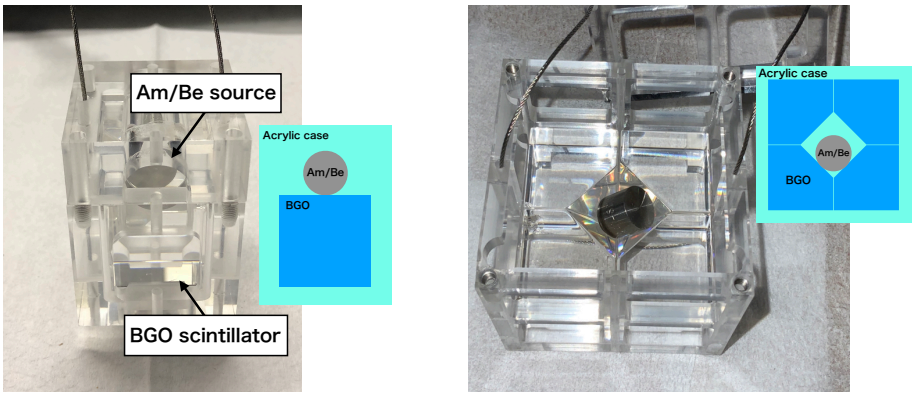

(A) Appearance and Schematic of the 1BGO geometry.

(B) Appearance and Schematic of the 8BGO geometry.

FIGURE 6.10: Appearance and schematic of 1BGO geometry (left) and 8BGO geometry (right).

Data taking

In January 2021, data from nine distinct AmBe points were taken. Figure 6.11 visualizes the measurement points. At the central point, 8BGO data was gathered over 1 hour, while 1BGO data spanned 2 hours. Measurements at other off-center points were conducted over a 30-minute interval, primarily to evaluate position dependence of efficiency. Note that 1BGO data was exclusively taken at the center point.

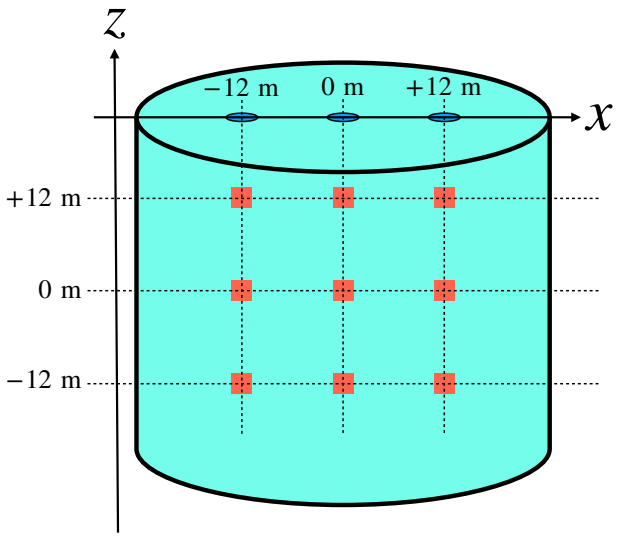

FIGURE 6.11: Illustration of measurement points. Orange squares exhibit measurement points, and the darker blue circle denotes calibration holes, where $x = -1237, 35.3, 1080$ cm $\sim -12, 0, +12$ m.

6.2.2 AmBe MC simulation

To compare the neutron tagging efficiency between the measured data and MC, the AmBe source geometry was reproduced by Geant4 and introduced to the SKG4 detector simulation.

Primary Particles

As introduced at the beginning of this chapter and depicted in Figure 6.8, the AmBe source decay typically culminates in one of three states: the emission of n^0, the emission of n^1, accompanied by 4.4 MeV gamma-ray, and the emission of n^2. As the dominant channel of the second excited state of ^{12}C is $^{12}C^* \rightarrow 3\alpha$ reaction, which cannot be observed in the SK, only a neutron is simulated from the n^2 state. In the MC simulation, the proportional representation of these three states is given as $(n^0 : n^1 : n^2) = (0.498, 1.0, 0.26)$, as cited in Ref. [45]. The kinetic energy of neutrons across each spectrum examined in this analysis is portrayed in Figure 6.12.

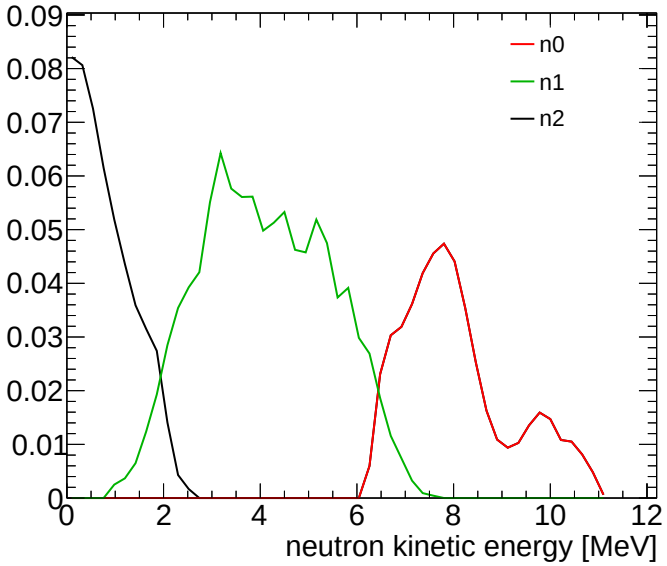

FIGURE 6.12: Kinetic energy spectrum of the emitted neutron from each state, calculated as the combination referring measurements of Guarrini and Malaroda [44], and ISO8529-1 [45].

Parameter tuning for BGO scintillator

To ensure a realistic simulation, certain scintillation, — parameters such as the light yield and the decay time constant of the scintillation light, should be tuned. The parameters were evaluated using the AmBe data at the center point. As such, the BGO scintillator exhibits two types of decay constant: slow (τ_s) and fast (τ_f). , which are estimated by fitting the PMT hit timings with the following function:

$$f(t) = \frac{H(t-T_0)}{2}(\mathrm{erf}((t-T_0-\mu)/(\sqrt{2}\times\sigma))+1) \times \left[A_f(e^{-(t-T_0)/\tau_f} - e^{-(t-T_0)/r_f}) + A_s(e^{-(t-T_0)/\tau_s} - e^{-(t-T_0)/r_s})\right] + C, \tag{6.6}$$

where the A_f and A_s denote the amplitudes, T_0 indicates the time offset, r_f and r_s represent the rise time for fast and slow components, respectively, and C denotes a constant component. $\mathrm{erf}(t)$ represents the error function, and μ and σ indicate the parameters of the error function. By assuming $A_f : A_s = 10\% : 90\%$ as described in Ref. [142], the decay constants were estimated as $\tau_s = 440$ ns and $\tau_f = 100$ ns. As

indicated in Figure 6.13, these results are consistent with the measurements recorded at 13.5 °C (SK water temperature) [46].

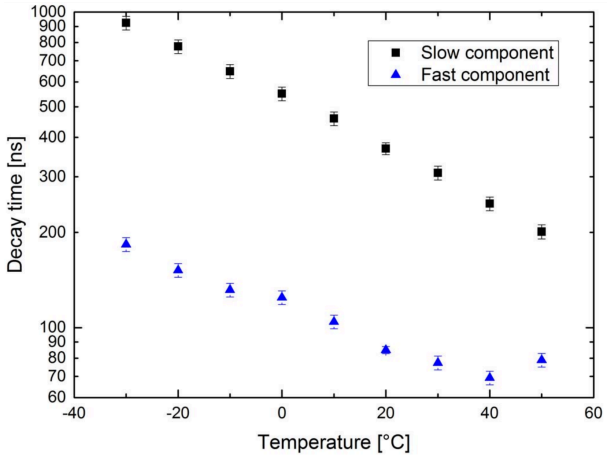

FIGURE 6.13: Correlation between scintillation time constant for each component with BGO temperature. This figure is taken from [46].

After calibrating the decay time constant, the scintillation light yield is tuned by comparing the total PMT charge within 1.3 μs around the SHE trigger (QISMSK). The QISMSK distribution of events triggered with the SHE and without the OD trigger is displayed in Figure 6.14. The prominent peak nearing 1000 highlights the 4.4 MeV scintillation photo-peak, while the trough near QISMSK $\sim$ 300 reveals the tapering section of the low-energy background event.

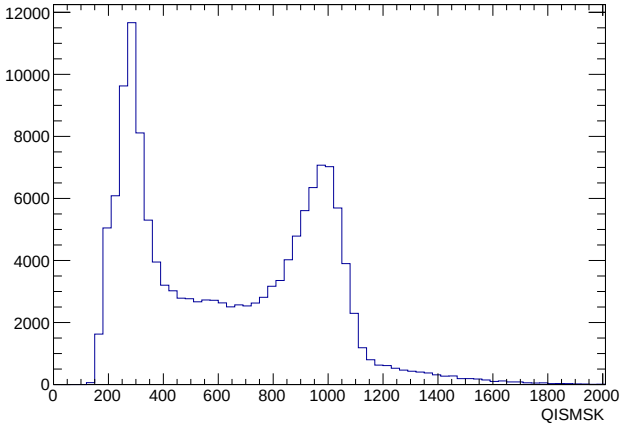

FIGURE 6.14: QISMSK distribution of the AmBe MC with 8BGO at the center point for various scintillation yield parameters.

Given that the total charge of the photo-peak of 4.4 MeV gamma-ray should be relatively proportional to the scintillation photon yield, optimization ensures that the QISMSK mirrors the data. Figure 6.15 illustrates the QISMSK distribution across various yield settings, with the higher side of the peak varying in line with the yield. After fitting these peaks using a Gaussian distribution, the interrelation between the

yield and QISMSK is gauged through a linear function, as observed in Figure 6.16. Consequently, the yield parameter is determined to be 5900 MeV^{-1}.

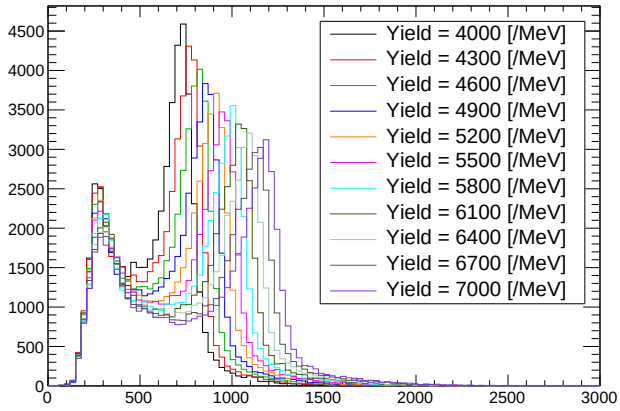

FIGURE 6.15: QISMSK distribution of the 8BGO at center point data with some light yield setting.

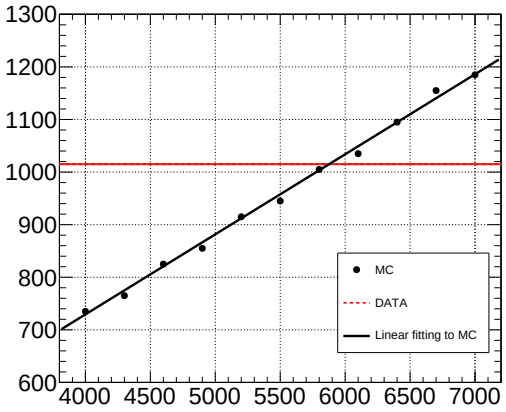

FIGURE 6.16: Correlation between yield and QISMSK in MC. Black circles denote the MC peak and its deviation for each yield setting in Figure 6.15. Red line indicates the QISMSK peak for the data in Figure 6.14.

QISMSK distribution data at the center point and the best-fitted MC data are comparatively presented in Figure 6.17.

Table 6.4 summarizes the parameters determined from the measurements.

MC production procedure

The procedure for noise data injection, detailed in Section 6.1.3, is employed to gauge noise contamination precisely. The creation process of the data structure for the AmBe MC comprises the following steps:

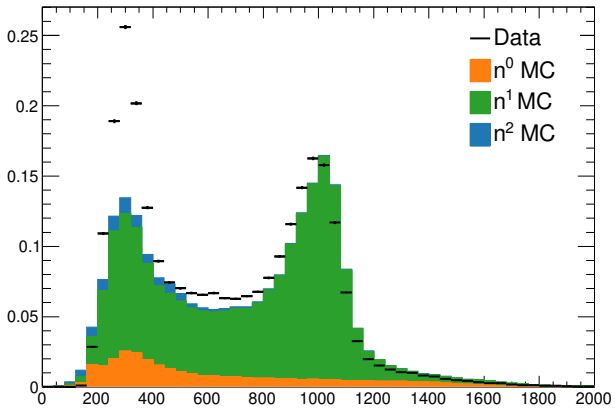

FIGURE 6.17: QISMSK distribution for the data and best-fitted MC; n^0, n^1, and n^2 MC indicates the MC simulation for each excited state of ^{12}C.

TABLE 6.4: Parameters determined from the measurements, including the rise time parameters and resolution scale parameter.

Parameter	Name in Geant4	Value
Fast time constant τ_f	FASTTIMECONSTANT	100 ns
Slow time constant τ_s	SLOWTIMECONSTANT	440 ns
Rise time of fast component	FASTSCINTILLATIONRISETIME	1.0 ns
Rise time of slow component	SLOWSCINTILLATIONRISETIME	1.0 ns
Photon yield	SCINTILLATIONYIELD	5900 MeV^{-1}
Resolution scaling factor	RESOLUTIONSCALE	1.0
Fraction of fast component	YIELDRATIO	0.1

- Simulate primary particles within the Am/Be geometry and record PMT hits up to 535 μs.
- Calculate noise hits sporadically between 0–2.7 μs, considering the primary trigger due to scintillation ends at 1μs.
- Produce software triggers up to 300 ns from generating time to prevent erroneous triggers due to Gd-capture gamma-ray activating the SHE.
- Append noise data (T2K or SK random-wide) into simulated PMT hits from 2.7 μs to 535 μs.

6.3 Neutron Tagging Efficiency Evaluation with AmBe Source

Evaluating the neutron tagging efficiency is essential to estimate the physics sensitivity in the SK-Gd experiment. To assess the performance of the neutron tagging algorithm and estimate the reproducibility of the actual neutron tagging by the MC, the neutron tagging efficiency calculated from AmBe measurements was compared between the measured data and MC results.

6.3.1 Prompt event selection

To accurately extract the neutron tagging efficiency, rigorous prompt event selection is essential. The obtained data undergoes processing to select the 4.4 MeV gamma-ray using these criteria meticulously:

- Events triggered by SHE and that do not trigger the OD, followed by an AFT event.
- Time differences exceed 1 ms from the previous SHE.
- Number of OD hits is less than 11.
- QISMSK values are contained within an acceptable region.

The first cut criterion ensures that the neutron signal is recorded over an extended time window and sidesteps significant charge events caused by muons. The second cut criterion helps to prevent interference from lingering signals of the previous prompt event and scintillation light. The third one ensures that the prompt event does not originate from the cosmic muons. The final criterion is tailored to single out scintillation prompt events compatible with the 4.4 MeV gamma-ray. The QISMSK distribution for specific measurement points is presented in Figure 6.18.

Given that QISMSK varies based on the distance between the source position and the ID wall, the selection criteria are segmented into three categories based on measurement locations: central data (both x and z coordinates at 0 m), edge data (either x or z at $\pm$ 12 m while the other remains at 0 m), and corner data(both x and z coordinates $\pm$ 12 m). Suitable criteria for each dataset are implemented, as depicted in Figure 6.18.

6.3.2 Neutron Signal Search

The neutron detection algorithm, as detailed in Section 6.1.3, is applied to both AmBe data and MC. The distribution of the number of delayed candidates surpassing the $N_{200} \geqq 25$ threshold for the central source position is illustrated in Figure 6.19. For MC, the peak value is 92.0, whereas for the data, it was 94.5. This difference arises from the drift of neutrons from a different event originating from the AmBe source, termed 'random neutrons,' and the capacity of the MC to reproduce noise hits.

All conditions for neutron selection, elaborated in Section 6.1.3, are applied to all candidates filtered by the N_{200} selection threshold. Figure 6.20 illustrates the distributions of variables used for selection. Each distribution has already applied thresholds other than the variable itself.

The data shapes largely align with the outcomes from the MC. Owing to the more expansive photon emission time scale of scintillation light emission, scintillation events generally exhibit a lower g_{vtx} compared to Chernekov events. This indicates a potential flaw in replicating scintillation, as the observed data contain more events with reduced g_{vtx} than the MC does for the g_{vtx} distribution. The majority of this variation is rectified by the imposed cut.

The timing distribution of the final neutron candidates, after passing all the requirements, is presented in Figure 6.21. These distributions are fitted with a range of 5 to 500 μs by the exponential function $f(t)$ as

$$f(t) = A\exp(-t/\tau)\cdot(1-\exp(-x/\mu)) + B, \tag{6.7}$$

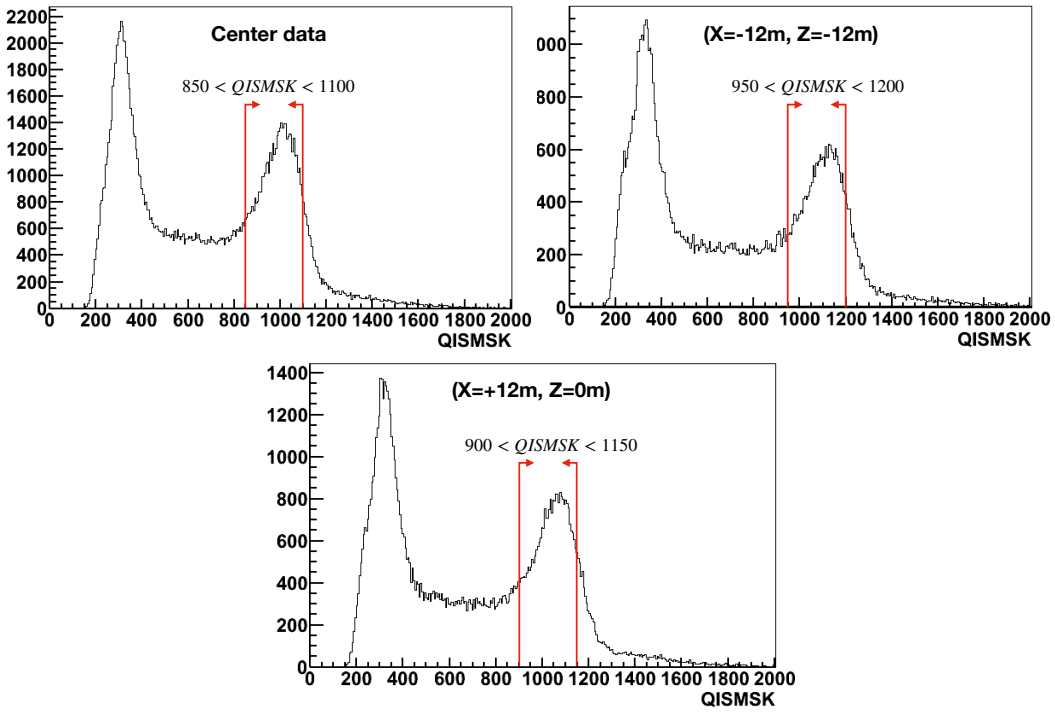

FIGURE 6.18: QISMSK distributions for center data (top left), (X= −12 m, Z= −12 m) data (top right), and (X= +12 m, Z= 0 m) data (bottom) obtained by 8BGO AmBe measurement; arrows indicate the threshold criteria for each source position.

where A denotes an amplitude parameter, τ indicates the decay time constant, μ refers to the thermalization time constant, and B indicates the constant component. In this analysis, μ is set to 4.3 μs. The time constant for the data (τ_{data}) and MC (τ_{MC}) were $\tau_{\text{data}} = 115.1 \pm 2.3$ μs, and $\tau_{\text{data}} = 118.1 \pm 0.9$ μs, respectively. The constant offset B observed only in data, primarily containing the random neutron, was evaluated as $B = 26.2$ events/bin.

6.3.3 Tagging Efficiency Estimation

The neutron tagging efficiency ϵ_n^{data} for AmBe data can be calculated as

$$\epsilon_n^{\text{data}} = \frac{N_{\text{tagged}} - N_{\text{uncorr}}}{N_{\text{prompt}}}, \tag{6.8}$$

where N_{tagged} denotes the total remaining neutron candidates after neutron selection, N_{uncorr} indicates the number of events without time correlation with the prompt events, and N_{prompt} represents the number of prompt events. N_{uncorr} is estimated by the constant component B that appeared in Equation 6.7 as follows:

$$N_{\text{uncorr}} = T_{\text{width}} \cdot B / T_{\text{bin}}, \tag{6.9}$$

where T_{width} denotes the neutron search window as $[4, 535]$ μs, B is a constant component presented in Figure 6.21a, and T_{bin} refers to the bin width of the capture timing distribution used for fitting. N_{uncorr} can be estimated to reduce the effect of the random neutron event from tagging efficiency.

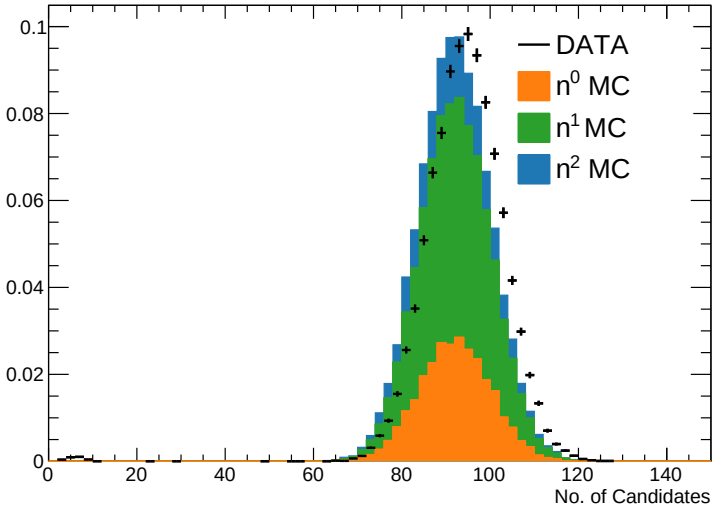

FIGURE 6.19: Distribution of the number of delayed candidates passing $N_{200} \geq 25$.

In contrast, for the MC, as all neutron events are correlated with the prompt event and the potential misidentification is negligible, N_{uncorr} should be zero. Therefore, the ϵ_n^{MC} can be estimated as

$$\epsilon_n^{\text{MC}} = \frac{N_{\text{tagged}}}{N_{\text{prompt}}}. \tag{6.10}$$

Considering each excited state, ϵ_n^{MC} can be modified to

$$\epsilon_n^{\text{MC}} = \frac{\sum_i^{state} N_{\text{tagged}}^i \times W_i}{\sum_i^{state} N_{\text{prompt}}^i \times W_i}, \tag{6.11}$$

where the N_{tagged}^i denotes the number of tagged candidates for the i-th state, N_{prompt}^i indicates the number of prompt events for the i-th state, and W_i refers to the fraction of each state, respectively. The estimated capture time constant and the tagging efficiency obtained from the 1BGO and 8BGO source data and MC are listed in Table 6.5, wherein the neutron tagging efficiency of the data was relatively 12% lower than that derived by the MC for 8BGO and 9% for 1BGO.

TABLE 6.5: Summary of capture time constant and neutron tagging efficiency for the DATA and MC for each BGO geometry. Errors only include only statistical uncertainty.

	Capture time constant [μs]		Tagging efficiency[%]	
	1BGO	8BGO	1BGO	8BGO
Data	118.9 ± 3.1	115.1 ± 2.3	36.4 ± 0.7	34.0 ± 0.5
MC	115.9 ± 1.2	118.1 ± 0.9	39.7 ± 0.3	38.3 ± 0.2
(Data-MC)/Data	–	–	-0.088	-0.123

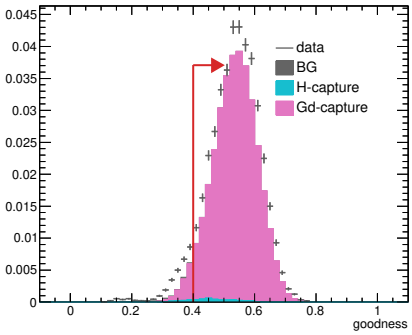

(A) Distribution of the g_{vtx}.

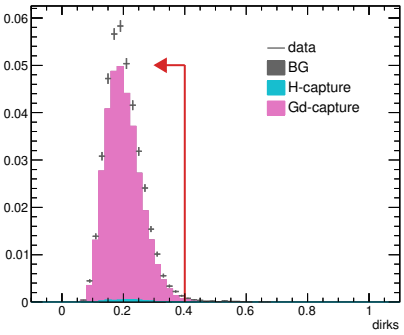

(B) Distribution of the g_{dir}.

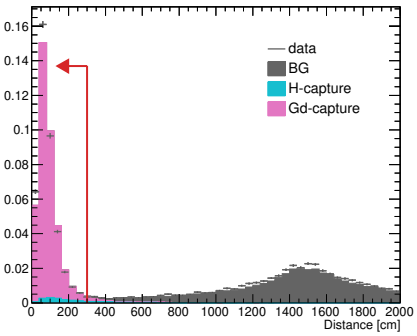

(C) Distribution of the distance from prompt event vertex.

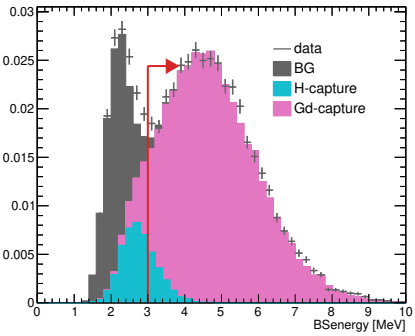

(D) Distribution of the reconstructed energy.

FIGURE 6.20: Distributions of neutron selection variables. Each color-filled histogram exhibits the MC, and solid point represents the data, which is aligned with the statistical error. Red arrow indicates the cut criteria for neutron selection. These distributions are normalized by the number of prompt events.

6.4 Discussion on Tagging Efficiency Measurement

The results listed in Table 6.5 indicate about 10% discrepancy between the data and MC. Compared to the 1 BGO, this difference is more pronounced in the 8 BGO case, suggesting that the BGO might be a contributor to the variance.

A potential explanation for this discrepancy can be attributed to the effect of creating a 'dummy prompt event.' In the measured data, neutron capture tends to occur in the vicinity of the BGO scintillator. Therefore, the gamma rays from neutron capture on the nucleus might sometimes trigger a SHE due to scintillation. This can reduce the neutron tagging efficiency as there is no subsequent neutron. This effect has not been incorporated in the MC, necessitating an assessment of the impact of this dummy prompt event on efficiency. At this time, the effect is estimated using

$$\begin{aligned}(\text{Dummy prompt event}) &= (\text{Measurement time [s]}) && (6.12)\\ &\times (\text{Random neutron intensity [Hz]}) && (6.13)\\ &\times (\text{Probability of prompt event from neutron}) && (6.14)\\ &\times (\text{SHE trigger efficiency}) && (6.15)\\ &\times (\text{AFT trigger efficiency}), && (6.16)\end{aligned}$$

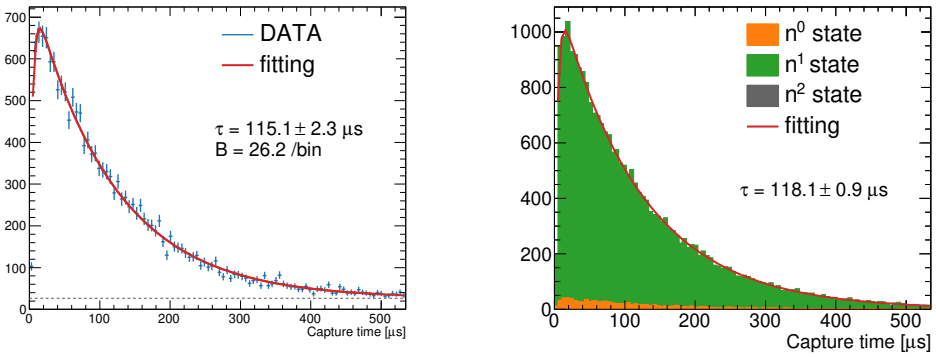

(A) Capture timing distribution for measured data. (B) Capture timing distribution for MC simulation.

FIGURE 6.21: Capture timing distributions for measured data (left) and MC simulation (right). Dotted line only displayed in the data plot represents the flat component evaluated by exponential fitting.

The measurement times of the center data for 1BGO and 8BGO configurations were 7329 s and 4002 s, respectively.

6.4.1 Random neutron intensity

Random neutrons lack a timing correlation with any prompt event, as depicted in Figure 6.22. They might produce the dummy prompt event if the 4.4 MeV gamma ray from the AmBe source does not trigger a SHE event. This random neutron intensity manifests as a portion of the constant component in the neutron capture time distribution. The timing fit is detailed in Section 6.3.2. However, several of the 4.4

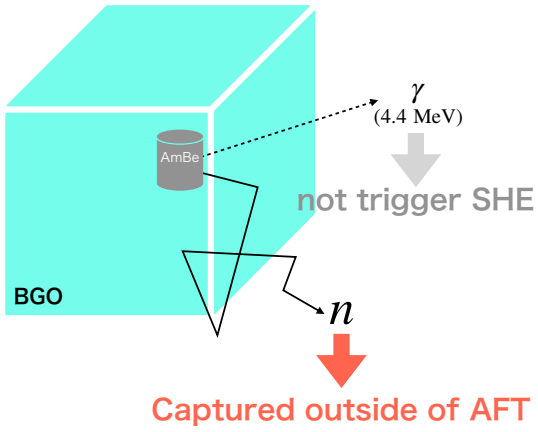

FIGURE 6.22: Illustration of emission of the random neutron.

MeV gamma-ray events were also accidentally tagged by a delayed neutron selection, as described in Section 6.1.3. Thus, this constant component encompasses these unintentional events. Consequently, when considering the random neutron intensity, the count of tagged 4.4 MeV gamma rays must be factored in. The intensity can be

determined as:

$$(\text{Random neutron intensity [Hz]}) = \frac{N_{\text{const}} - N_{4.4\text{MeV}}}{N_{\text{prompt}} \times T_{\text{bin}}\ [\text{s}] \times \epsilon_n^{\text{MC}}}. \tag{6.17}$$

Here, N_{const} [/bin] (B in Equation 6.7) denotes the constant component in the timing distribution, and $N_{4.4\text{MeV}}$ [/bin] represents the number of tagged 4.4 MeV gamma-ray events per bin. The constant component obtained by the timing distribution of tagged-neutron candidates is 26.2 [events/bin] for 8BGO and 17.4 events[/bin] for 1BGO. The bin width for all data is 5.35×10^{-6} [s].

After that, the number of tagged 4.4 MeV gamma-ray events per bin $N_{4.4\text{MeV}}$ is expressed as follows:

$$N_{4.4\text{MeV}} = R_{\text{n}^1} \times T_{\text{bin}} \times N_{\text{prompt}} \times \epsilon_{4.4\text{MeV}}^{\text{MC}}, \tag{6.18}$$

where R_{n^1} [Hz] denotes the emission rate of the 4.4 MeV gamma ray from the first excited state of the AmBe source, and $\epsilon_{4.4\text{MeV}}^{\text{MC}}$ signifies the survival probability of the 4.4 MeV gamma ray. This is estimated by applying the same neutron event selection cut to its MC simulation. Survival probabilities for each cut are summarized in Table 6.6. The probability of tagging 4.4 MeV gamma-ray as a neutron signal is 33.8% for 8BGO, and 59.7% for 1BGO, respectively. R_{n^1} is assumed to be 110.1 Hz from the result of the external experiment [143]. Consequently, the random neutron intensity for 8BGO is estimated to be 187.2 Hz, and for 1BGO, is estimated to be 149.2 Hz, as summarized in Table 6.7.

TABLE 6.6: Summary of contents in the calculation for the tagging efficiency of 4.4 MeV gamma-ray.

Content	Efficiency	
	8BGO	1BGO
$N_{200} > 25$	97.2%	90.8%
FV cut	61.4%	92.0%
goodness cut	68.1%	87.5%
dirks cut	99.3%	99.3%
energy cut	92.2%	90.7%
distance cut	90.9%	90.7%
Total probability	33.8%	59.7%

TABLE 6.7: Break down the contents in the calculation of random neutron intensity.

Content	Survival probability	
	8BGO	1BGO
N_{const} [/bin]	26.6	17.3
$N_{4.4\text{MeV}}$ [/bin]	11.4	11.6
N_{prompt}	44960	25873
T_{bin} [μs]	5.35	5.35
ϵ_n^{MC}	38.3%	39.7%
Random neutron intensity [Hz]	187.2	149.2

6.4.2 Probability of prompt event from neutron

The probability of the gamma-ray from neutron capture on Gd$(n, \gamma s)$Gd evolving into a prompt event is calculated. The 2.2 MeV gamma ray from hydrogen capture should not influence the prompt event selection, given that the QISMSK is likely half that of the 4.4 MeV gamma ray. Instead, we examined the captures from other isotopes, with Ge$(n, \gamma s)$Ge being the primary candidate, as illustrated in Figure 6.23.

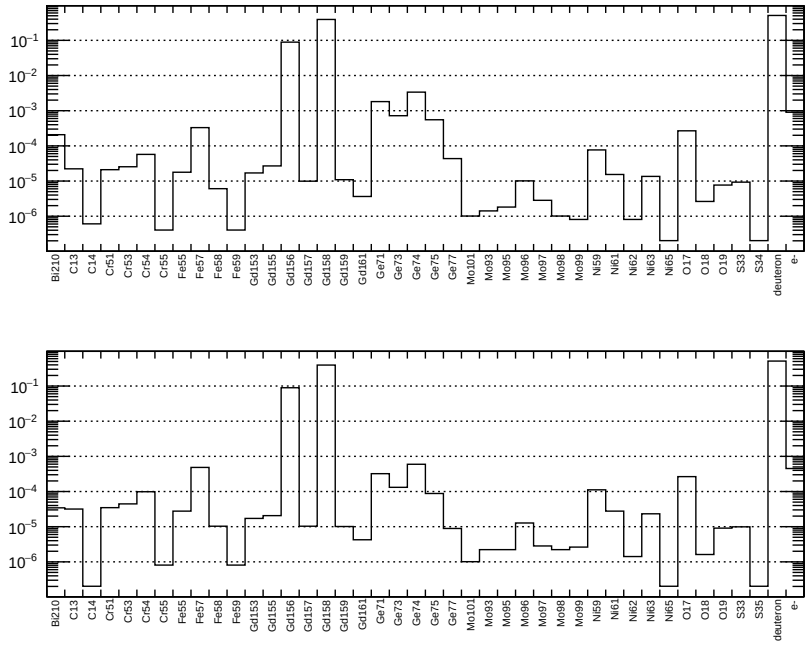

FIGURE 6.23: The probability of thermal neutron capture in the SK with AmBe source geometry for 8BGO (top) and 1BGO (bottom). These probabilities were calculated based on the result of the five million neutron MC, which uses ENDF.VII.1 as a nuclear data library [47].

To ascertain the probability, these steps are followed:

1. Generate 5 million neutron MC.
2. Store neutron capture data, like vertex, capture nucleus, and energy of each capture gamma-ray.
3. Based on this data, generate millions of gamma-ray MC for Gd$(n, \gamma s)$Gd and 30,000 MC events for Ge$(n, \gamma s)$Ge.
4. Determine the likelihood by applying identical cuts as the prompt event selection.

The outcomes indicate that the Gd$(n, \gamma s)$Gd probability is 0.285%, and for Ge$(n, \gamma s)$Ge, it was 10.2%. MC calculations yield neutron capture fractions of 48.1% for Gd and 0.7% for Ge. Thus, the final estimated probability stands at 0.2% (Table 6.8). Using the same calculations for the 1BGO setup, neutron capture fractions are 48.4% on Gd and 0.1% on Ge. The associated probabilities for a neutron emerging as a prompt event on Gd and Ge capture are 0.026% and 1.4%, respectively, resulting in an overall probability of 0.014% for 1BGO.

Table 6.8: Summary of the contents of the dummy prompt event.

Content	Probability			
	8BGO		1BGO	
	Gd	Ge	Gd	Ge
Trigger SHE	10.65%	88.61%	5.81%	79.08%
pass QISMSK cut	2.68%	11.17%	0.54%	7.23%
Total remaining	0.285%	9.90%	0.0311%	5.72%
Capture fraction	48.15%	0.65%	48.43%	0.11%
Final prob.	0.137%	0.045%	0.015%	0.006%
	0.182%		0.021%	

6.4.3 Trigger efficiency

To determine the number of dummy prompt events, the SHE and AFT trigger efficiencies must be accounted for and derived from the SHE and AFT trigger rates. For the central data measurements, the rates of SHE and AFT are 81.7 Hz and 37.7 Hz for 8BGO, and 25.8 Hz and 19.8 Hz for 1BGO, respectively. Occasionally, a SHE event might be overlooked due to overlap with another SHE or AFT event window. The inefficiency arising from this overlap can be assessed by the combined SHE and AFT window duration per second. Consequently, the dead time of the SHE trigger, induced by the AFT event, was recorded at 22 ms/sec for 8BGO and 11 ms/sec for 1BGO, translating to SHE trigger efficiencies of 97.8% for 8BGO and 98.9% 1BGO.

From the DAQ setup in January 2021, the AFT rate is limited to once every 20 ms. This constraint may lead to overlooked AFT events, essentially SHE events not followed by an AFT event. The proportion of such instances is deduced from the ratio of SHE to AFT events, resulting in values of 46.1% for 8BGO and 76.7% for 1BGO.

6.4.4 Result

As discussed in this section, the potential components of the dummy prompt events by the captured gamma-ray from neutron capture are estimated as defined by Equation 6.12. The terms in Equation 6.12 are summarized in Table 6.9.

Table 6.9: Summary of contents in dummy prompt event.

Content	Values	
	8BGO	1BGO
Measurement time [s]	4002	7329
Random neutron intensity [Hz]	187.2	149.2
Probability that neutron will be the prompt event	0.182%	0.021%
SHE trigger efficiency	97.8%	98.9%
AFT trigger efficiency	46.1%	76.7%
Estimated number of events	614.8	174.2
Dummy event probability	1.368%	0.673%

Consequently, we can express the expected neutron tagging efficiency for MC ϵ'_n as follows:

$$\epsilon'_n = \epsilon_n \times \frac{1}{1 + (\text{Dummy event probability})}. \tag{6.19}$$

Based on the findings presented in Table 6.5, only about 1.5% and 0.7% in 8BGO and 1BGO of relative discrepancy in absolute value can be attributed to dummy prompt events caused by source neutrons. This discrepancy will be factored into the MC efficiency correction.

6.5 Systematic Uncertainty Extraction

The systematic uncertainty contingent on the MC simulation is also gauged. It is broadly categorized into four areas: prompt event selection, delayed event selection, MC simulation settings, and position dependence. All these uncertainties are derived from the 8BGO central data and its MC counterpart.

6.5.1 Prompt event selection

As described in Section 6.3.1, the prompt event selection encompasses four conditions. Among these, only the QISMSK cut significantly impacts the tagging efficiency. Therefore, uncertainty arising from the QISMSK cut criteria needs assessment. This uncertainty is gauged by varying the QISMSK cut parameters at the central point, as depicted in Figure 6.18. For the lower threshold, the range is scanned from 700 to 850 [p.e.], whereas the upper limit varies from 1100 to 1250 [p.e.]. The most extensive criteria span is double the nominal range. The uncertainty is assigned as the maximum deviation in the neutron tagging ratio between data and MC when compared to the nominal cut criteria. Figures 6.24 and 6.25 display these comparative results. From this analysis, the largest discrepancy from nominal criteria is found within the [700, 1150] range, leading to an assigned uncertainty of 0.47%.

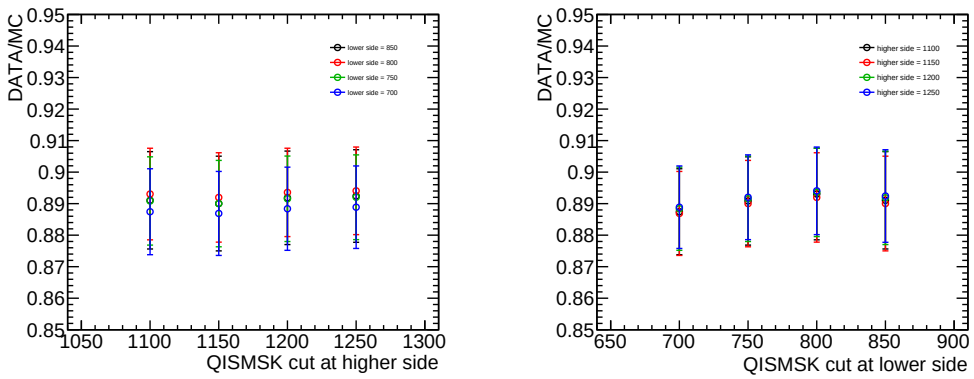

FIGURE 6.24: QISMSK cut criteria and the data-MC difference in the neutron tagging efficiency as a function of the higher side (left) and lower side (right).

6.5.2 Delayed event selection

The delayed event selection is associated with four distinct variables. Thus, the uncertainty for each variable is combined to determine the overall uncertainty of the delayed event selection. In this evaluation, the variation in tagging efficiency is considered equivalent to efficiency shifts when altering neutron selection criteria.

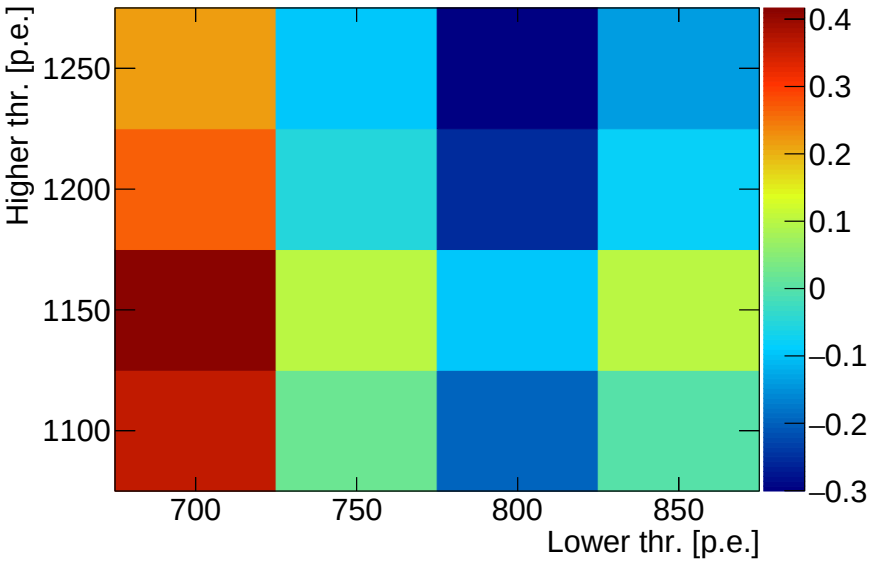

FIGURE 6.25: QISMSK cut criteria and the data-MC difference in neutron tagging efficiency. Color depicts the difference between data and MC from the nominal criteria.

Vertex reconstruction goodness

The uncertainty surrounding the vertex reconstruction goodness g_{vtx} is determined by contrasting the distribution between data and MC after imposing all cuts, except for the g_{vtx} cut. Figure 6.26 indicates a noticeable shift in the g_{vtx} distribution of MC, corresponding to about 2.1% towards a lower g_{vtx} side compared to the data. Thus, survival efficiency was calculated by applying a g_{vtx} threshold adjusted based on the difference between data and MC peak. The subsequent uncertainty was ascertained by comparing the survival efficiencies of MC for the nominal and shifted cut. Consequently, the g_{vtx} dependent uncertainty was evaluated to be 0.94%.

Direction reconstruction goodness

Similarly, the uncertainty from the g_{dir} cut is estimated. This evaluation follows the method used for g_{vtx}. Figure 6.27 depicts the g_{dir} distributions and cut criteria. The MC peak deviating from the data is 0.7%, and the resultant uncertainty was estimated at 0.03%.

Reconstructed energy

The variations in the energy scale between data and simulation should be considered for systematic uncertainty. This deviation is gauged by examining the distribution of reconstructed energy after applying all cuts, bar the energy cut, across data and MC. As displayed in Figure 6.28, the average discrepancy between the data and MC was 0.32%. By smearing the cut threshold to examine the impact of this difference, the uncertainty was determined as 0.23%.

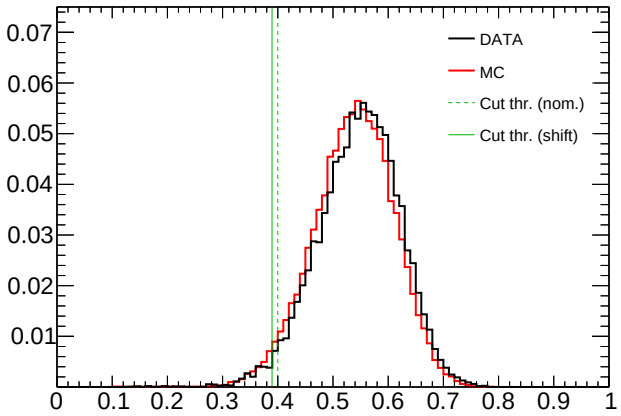

FIGURE 6.26: Distribution of g_{vtx} for data and MC. Solid green line indicates the smeared cut threshold. Both plots are normalized by area.

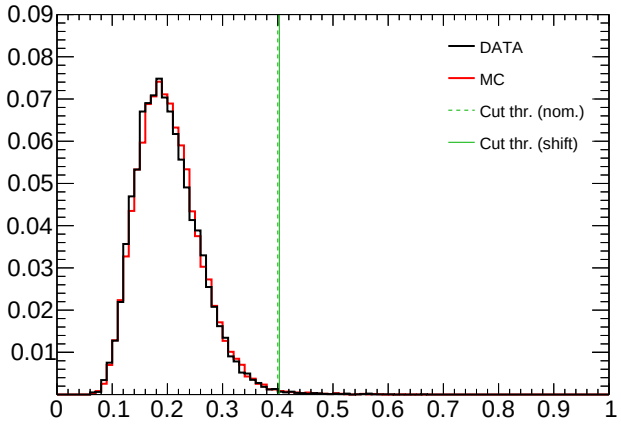

FIGURE 6.27: Distribution of g_{dir} for data and MC. Solid green line indicates the smeared cut threshold. Both plots are normalized by area.

Vertex resolution

Vertex reconstruction manifests as the distance from the source cut in neutron selection. Any discrepancy in vertex resolution between data and MC inherently introduces a systematic uncertainty in tagging efficiency. Accordingly, vertex resolution is analyzed. For this study, vertex resolution is defined as r satisfying the following equation:

$$\frac{\int_{0\mathrm{cm}}^{r\mathrm{cm}} dr' h(r')}{\int_{0cm}^{500\mathrm{cm}} dr' h(r')} = 1\sigma \sim 68.27\%, \tag{6.20}$$

where $h(r')$ denotes the distance distribution between the reconstructed vertex and source position. These distributions for data and MC are illustrated in Figure 6.29.

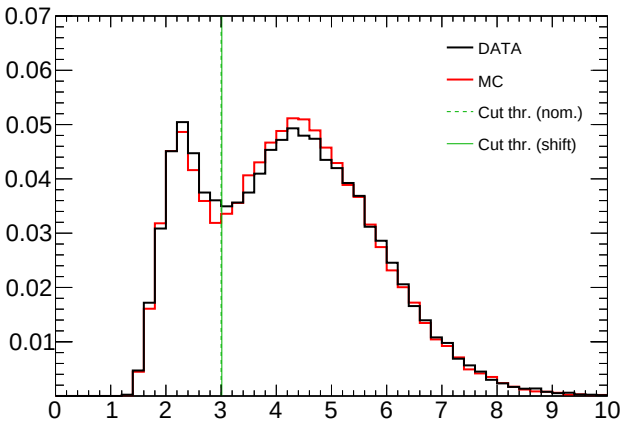

FIGURE 6.28: Distribution of reconstructed energy for data and MC. Solid green line denotes the smeared cut threshold. Both plots are normalized by area.

The resolution was 97.85 and 103.15 cm for data and MC, respectively.

The systematic uncertainty associated with vertex resolution can be calculated based on the efficiency differential between data and MC when altering the source distance cut criteria based on the vertex resolution discrepancies. This yields an uncertainty estimate of 0.44%.

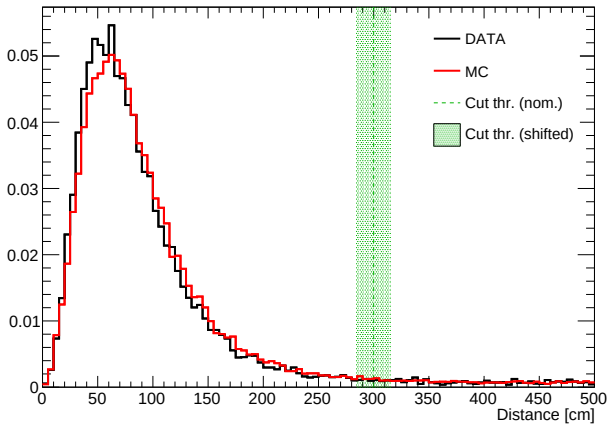

FIGURE 6.29: Distribution of the distance between reconstructed delayed event vertex and the source position for data and MC. Solid green line denotes the smeared cut threshold. Both plots are normalized by area.

6.5.3 MC simulation settings

MC simulation operates on various parameters. While the majority have a limited effect on tagging efficiency, certain settings related to the neutrons and their capture

play a significant role. Therefore, their influence requires further assessment.

Gd concentration

The uncertainty of Gd concentration is anticipated to impact neutron tagging efficiency, which can be ascertained by examining the tagging efficiency of Gd capture and the Gd capture fraction in SK-VI. Figure 6.30 displays the time constant (left) and the Gd capture efficiency (right) as a function of Gd mass concentration. These plots stem from fitting data points measured by the AmBe MC simulation based on the Geant4.10.5 using an inverse polynomial function. Recent studies posit the average time constant at SK-VI to be 116.5 ± 0.2 μs. Consequently, the corresponding Gd mass concentration stands at 105.0±0.4 ppm, derived from the function in the left panel of Figure 6.30. After that, the capture fraction on Gd nuclei is estimated to be $47.8 \pm 0.1\%$, obtained from the right panel of Figure 6.30.

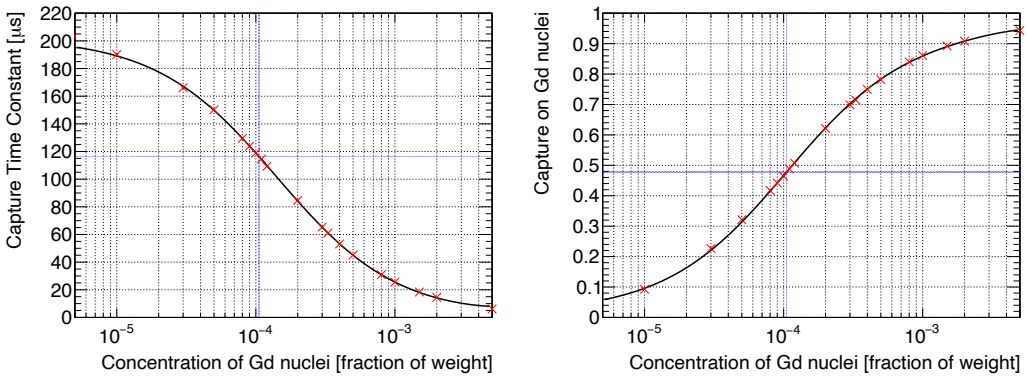

FIGURE 6.30: Correlation between the time constant and Gd mass concentration (left), and the Gd capture fraction and Gd mass concentration (right).

The relative error concerning the Gd nuclei capture fraction is deduced to be 0.21%. Referring to Table 6.3, 78.6% of Gd are tagged by the selection. Thus, the relative uncertainty of Gd mass concentration on the neutron tagging uncertainty is 0.17%. Generally, the effect of hydrogen capture is negligible owing to low tagging efficiency.

Gamma-ray emission model of neutron capture on Gd

As described in Section 3.3, the gamma-ray emission following neutron capture on Gd employs the ANNRI-Gd model. Variabilities in this model necessitate careful consideration. Consequently, the gamma-ray emission model for Gd capture is transitioned from ANNRI-Gd to the Photon-Evaporation model — a pre-installed model in Geant4. Subsequent MC simulations reveal that the energy distribution under the Photo-Evaporation model deviates significantly from that of the original ANNRI-Gd model, making a discrepancy of 1.7%.

Neutron excited state fraction

As expressed in Section 6.2.2 and Equation 6.11, the neutron tagging efficiency for MC was calculated considering the excited state branches of ^{12}C (0.498, 1.0, 0.26) determined according to ISO [45]. By examining potential extreme fractions, the

influence of state fraction on neutron tagging efficiency becomes apparent. Table 6.10 collates the state fraction patterns assumed for this analysis alongside neutron tagging efficiency. The external measurement conducted by Ito et al. [143] aligns with these assumptions. The most significant deviation from the nominal branch ratio of the state is identified as 0.39%, and this value is designated as the associated uncertainty.

TABLE 6.10: Summary of excited state fraction and neutron tagging efficiency

State fraction (n^0:n^1:n^2)	Neutron tagging efficiency	Relative difference
(0.498, 1.000, 0.260) (Default)	$38.31 \pm 0.37\%$	–
(0.760, 1.000, 0.000)	$38.30 \pm 0.36\%$	0.03%
(0.500, 1.000, 0.000)	$38.46 \pm 0.34\%$	0.39%
(0.650, 1.000, 0.000)	$38.36 \pm 0.36\%$	0.13%

Neutron energy spectrum of the first excited state

As the prompt event selection focuses on selecting the gamma-ray event from the first excited state of ^{12}C, the primary impact of the neutron energy spectrum on tagging efficiency stems from the spectrum of the first excited state. As such, the influence of only the first excited state is deemed relevant for uncertainty regarding the uncertainty on the neutron energy spectrum. Analysis of the spectrum variation uses data from experiments conducted in Kamioka [143]. Figure 6.31 displays the differential neutron spectrum for the first excited state between the default MC and the measured version. When substituting the default first excited state MC with the measured spectrum,

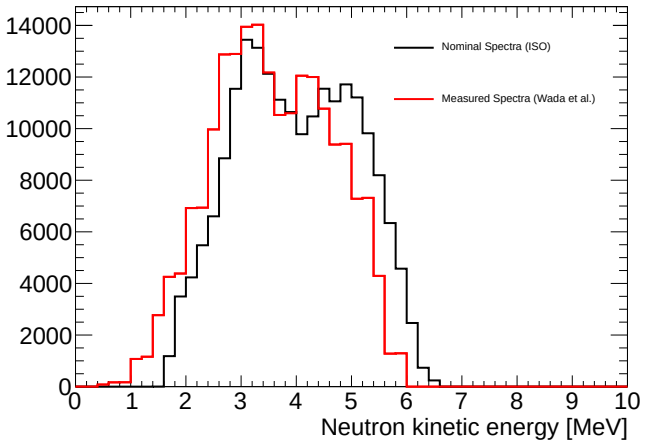

FIGURE 6.31: Neutron kinetic energy spectra from the first state of ^{12}C based on ISO (black) and measured (red).

efficiency shifts to 38.10%. This yields a relative discrepancy of 0.53%, incorporated as a systematic uncertainty.

6.5.4 Position Dependence

The potential variability in tagging efficiency based on position mandates inclusion in the systematic uncertainty assessment. Efficiencies across nine measured points are evaluated and illustrated in Figure 6.32.

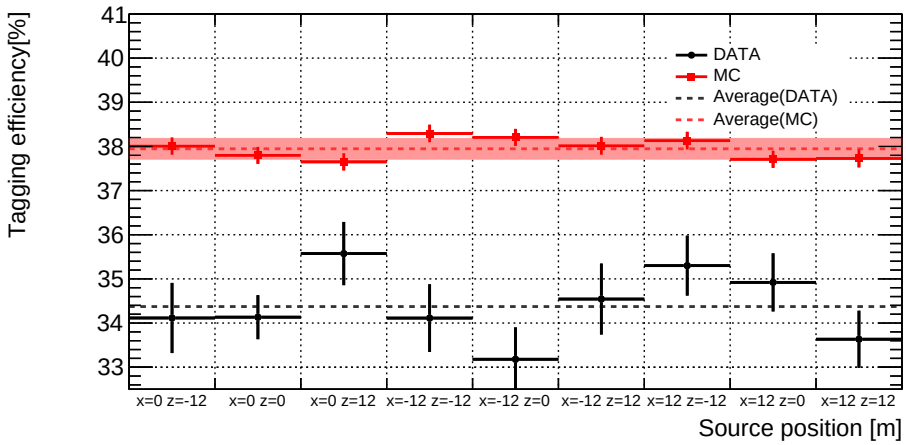

FIGURE 6.32: Neutron tagging efficiency for each measured point.

On average, the efficiency levels were 34.4% for data and 37.4% for MC. The considerable statistical uncertainty associated with the data points complicated the position dependence estimation. As such, the variability is gauged via MC deviations, resulting in a 0.47% value attributed to position dependence.

6.5.5 Total Systematic Uncertainty

The section culminates with an amalgamation of all systematic uncertainties concerning tagging efficiency — these are combined using a quadrature method. For this analysis, systematic uncertainties tied to the dummy prompt event estimation are deemed negligible. The systematic uncertainty of this measurement is presented in Table 6.11. In total, 2.22% of systematic uncertainty is considered for the tagging efficiency of MC.

6.6 Result

6.6.1 Neutron Tagging Efficiency

The representative value of neutron tagging efficiency is evaluated using both the center point data and MC at this time. For the center point, the efficiency without any surrounding apparatus (0BGO) is solely assessed for MC. The efficiencies, along with their respective errors, are summarized in Table 6.12. Figure 6.33 visualizes the tagging efficiency in relation to the quantity of surrounding BGOs. The efficiency of MC consistently surpasses the data, evident in both the 1BGO and 8BGO scenarios. Efficiency reveals a negative correlation with the BGO count. Moreover, the discrepancy between data and MC is more pronounced in the 8BGO scenario compared to the 1BGO setup. This suggests potential inaccuracies in understanding the influence of BGO and acrylic cases on efficiency, with the implications becoming less

TABLE 6.11: Summary of systematic uncertainty on AmBe measurement.

Content	Systematic uncertainty	
Prompt event selection	0.47%	0.47%
Timing goodness g_{vtx}	0.94%	1.06%
Direction goodness g_{dir}	0.03%	
Reconstructed energy	0.23%	
Vertex resolution	0.44%	
Gd concentration	0.17%	1.83%
Gd(n, γ)Gd model	1.70%	
Neutron excited state	0.39%	
Neutron energy spectrum	0.53%	
Position dependence	0.47%	0.47%
Total	2.22%	

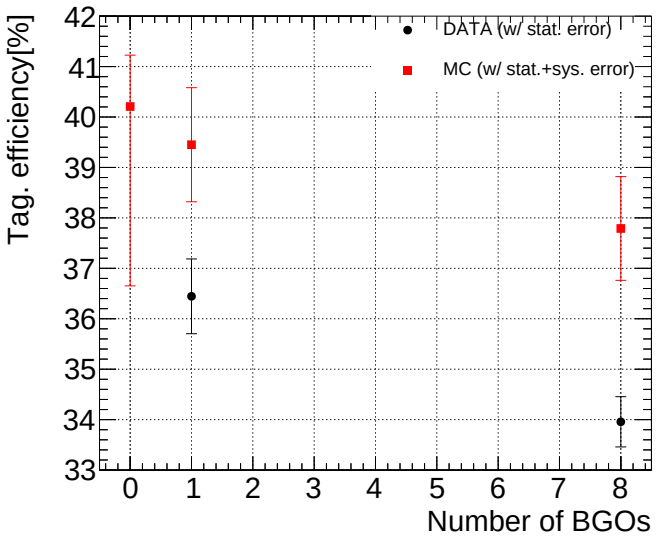

FIGURE 6.33: Neutron tagging efficiency as a function of the surrounding BGOs. Efficiency without BGO (0BGO) is only estimated by MC because it cannot be estimated for actual data.

pronounced as the number of BGOs decreases. Consequently, the divergence observed in the 1BGO scenario when comparing data and MC is recognized as an added systematic uncertainty for the MC in the 0BGO context. The final assessment pegs the neutron tagging efficiency for 0BGO at $40.2 \pm 0.1\,(stat.)\,^{+0.1}_{-3.4}\,(syst.)\,\%$.

6.6.2 Time variation

Monthly inspections, each spanning 30 minutes, are conducted at the center point to monitor potential fluctuations in tagging efficiency. This rigorous monitoring, which covered the entirety of the SK-VI period — from January 2021 through January 2022 — relies on the monthly AmBe source measurement at the center point. Figure 6.34 depicts variation in tagging efficiency with the data-taking date. On average, the

TABLE 6.12: Summary of neutron tagging efficiencies for the DATA and MC for each BGO geometry.

	1BGO	8BGO
Data	$36.4 \pm 0.7(stat.)\%$	$34.0 \pm 0.5(stat.)\%$
MC	$39.5 \pm 1.2(stat. + syst)\%$	$37.8 \pm 1.0(stat. + syst.)\%$
(Data-MC)/Data	-0.08 ± 0.03	-0.10 ± 0.03

efficiency values are $33.7 \pm 0.7\%$ for the 8BGO configuration and $36.8 \pm 0.3\%$ for the 1BGO setup. This data underscores the stability of neutron tagging efficiency throughout the SK-VI period.

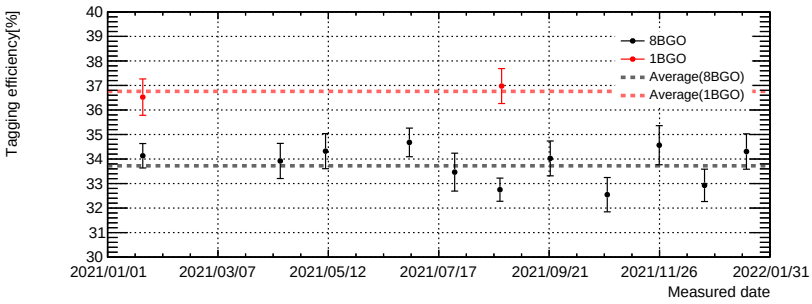

FIGURE 6.34: Neutron tagging efficiency as a function of the surrounding BGOs.

6.6.3 Conclusion

The neutron tagging algorithm to detect neutron capture on Gd is newly developed for the SK-Gd experiment. Using this method, the study of AmBe neutron measurement is carried out for the first time in SK-Gd. Alongside the measurement using the 8BGO geometry, an additional study using the 1BGO geometry was conducted to comprehend the effect of the BGO and acrylic apparatus. Also, this marks the first time to evaluate neutron tagging efficiency in MC with BGO geometry. Notably, the data and MC reveal a relative discrepancy of about 10%. The magnitude of the divergence varies based on the specific BGO configuration. In light of these findings, an additional uncertainty, mirroring the efficiency disparity for 1BGO between data and MC, is factored into the neutron tagging efficiency. The newly acquired understanding of the relationship between the apparatus configurations and neutron tagging efficiency has contributed to refining the margin of the uncertainty, shrinking it from the SK-IV pure-water study. The relative error derived for the 0BGO efficiency is applicable to the SRN analysis, as described in Chapter 7.

Chapter 7

Search for Diffuse Supernova Neutrino Background in SK-Gd

Using the data observed during July 2020 and May 2022, the first SRN search in the SK-Gd experiment is operated. This chapter provides an overview of the analysis, in terms of the data set, search energy window, and background sources.

7.1 Data Set

In this analysis, all SHE-triggered data linked to AFT-triggered events in the normal physics runs during SK-VI are utilized. From the middle of SK-V, tracking the AFT events after the OD-triggered event (primarily muons) became feasible, making post-muon neutron searches a potent method for spallation identification as described below. The trigger conditions are detailed in Chapter 2.

With the upgraded trigger system during SK-VI, AFT trigger event downtimes saw a significant decline. Until the mid-SK-VI, only one AFT event could be triggered once every 21 ms. However, post-March 3rd, 2022, the rate tripled, allowing three AFT triggers within the same timeframe. Consequently, the AFT trigger efficiency soared from around 97% to over 99.9%. The trigger conditions and live time during SK-VI are summarized in Table 7.1. Although SK-VI commenced on July 14th, 2020, the water and trigger conditions were stable on August 26th, 2020. Accordingly, the live time was accounted for from that date, and in total, operated for 552.2 days, which was 18.6% of the previous SK-IV SRN search (2970 days) [20]. As observed in Table 7.1, the SHE threshold decreased for about 11 days, but given the optimization of the energy window to 60 hits, this alteration does not affect the analysis.

Table 7.1: Trigger conditions and live-time during SK-VI.

Start date	End date	SHE threshold	Live time [day]	AFT rate limit
Aug. 26, 2020	Aug. 26, 2021	60	305.6	1/21 ms
Aug. 26, 2021	Sep. 12, 2021	52	10.97 day	1/21 ms
Sep. 12, 2022	Mar. 3, 2022	60	157.49 day	1/21 ms
Mar. 3, 2022	Jun. 1, 2022	60	78.15 day	3/21 ms

7.2 Signal Energy Window

This study targets the SRN signal within the 7.49–29.49 MeV energy region for the positron kinetic energy. The lower threshold stems from the energy level where SHE efficiency is sufficiently high, while the upper limit aligns with traditional analysis

windows. The side-band region exceeding 29.49 MeV aids in calibrating the atmospheric neutrino MC flux. For background evaluation, the energy spectrum is parsed into 2 MeV segments.

7.3 Overview of Background Events

Chapter 6 elucidates the achievement of a low misidentification rate for neutrons. Consequently, several low-energy events without neutron emission — solar neutrinos, most isotopes decay from muon spallation, radioactivity, etc. — are discounted. This chapter centers on events featuring neutron accompaniments, with primary background sources delineated in subsequent sections. The major background sources are characterized as follows:

1. Radioisotope decays originating from cosmic-ray spallation.
2. Atmospheric neutrinos.
3. Reactor neutrinos.
4. Accidental coincidence of low-energy event and neutron-like signal.

Other low-energy events, such as solar neutrinos and radioactivity, are adequately eliminated by neutron tagging. The modeling for each background source is described later in this chapter.

7.3.1 Radioisotope Decays from Muon Spallation and Lithium-9

Despite a 2700 m.w.e. overburden, the SK detector is exposed to the cosmic-ray muons at ~ 2 Hz. Certain of the muons break the oxygen nuclei of water, resulting in 'muon spallation.' The case of breaking the gadolinium and sulfur nuclei is ignored because of the small amount relative to the water. The muon spallation produces daughter isotopes and hadrons, such as neutrons and pions, as well as photons. The hadrons produced by this reaction cause subsequent spallation reactions, and eventually, the radioactive isotopes remain. Their radioactive decay emits γ and β rays, occasionally even neutrons. Since these visible electromagnetic (electron-like) particles have an energy below 20 MeV, they could pose as major backgrounds in the SRN analysis. Their counts in this energy region are 10^6 times the expected flux of SRN.

For each isotope in water, Li et al. [144, 145, 146] studied the half-life, decay mode, yield, and primary process with FLUKA [35], summarized in Table 7.2. Furthermore, the end-point energies of the electron-like particles, the half-lives, and the yield above 3.5 MeV for the electron-like particles, are presented in Figure 7.1. Although these are significantly reduced by neutron tagging because most spallation isotope decays do not produce neutrons, the decays with neutron production are not reduced. Moreover, spallation isotope decay acts as a major source of the accidental coincidence background, as described later in this section. Thus, a detailed understanding and efficient reduction of spallation isotope events are essential to be considered in this analysis. The reduction is dedicated to tuning below 24 MeV since the highest energy from ^{14}B and ^{11}Li amounts to 20.4 MeV.

Isotopes accompanied by neutron

The decays resulting $\beta + n$ emission are indistinguishable from the $\bar{\nu}_e$ signals, even with neutron tagging, because SK cannot discern between electrons and positrons.

TABLE 7.2: Summary of the muon spallation products in the water. This table is taken from Ref. [35].

Isotope	Half-life [s]	Decay mode	Yield $[\times 10^{-7}\mu^{-1}g^{-1}\mathrm{cm}^2]$	Primary process
n			2030	
^{18}N	0.624	β^-	0.02	$^{18}\mathrm{O}(n,p)$
^{17}N	4.173	$\beta^- + n$	0.59	$^{18}\mathrm{O}(n,n+p)$
^{16}N	7.13	$\beta^- + \gamma(66\%), \beta^-(28\%)$	18	(n,p)
^{16}C	0.747	$\beta^- + n$	0.02	$(\pi^-, n+p)$
^{15}C	2.449	$\beta^- + \gamma(63\%), \beta^-(37\%)$	0.82	$(n,2p)$
^{14}B	0.0138	$\beta^- + \gamma$	0.02	$(n,3p)$
^{13}O	0.0086	β^+	0.26	$(\mu^-, p+2n+\mu^-+\pi^-)$
^{13}B	0.0174	β^-	1.9	$(\pi^-, 2p+n)$
^{12}N	0.0110	β^-	1.3	$(\pi^+, 2p+2n)$
^{12}B	0.0202	β^+	0.02	$(n,\alpha+p)$
^{12}Be	0.0236	β^-	12	$(n,\alpha+p+n)$
^{11}Be	13.8	$\beta^-(55\%), \beta^-(31\%)$	0.10	$(n,\alpha+2p)$
^{11}Li	0.0085	$\beta^- + n$	0.01	$(\pi^+, 5p+\pi^++\pi^0)$
^{9}C	0.127	β^+	0.89	$(n,\alpha+4n)$
^{9}Li	0.178	$\beta^- + n(51\%), \beta^-(49\%)$	1.9	$(\pi^-, \alpha+2p+n)$
^{8}B	0.77	β^+	5.8	$(\pi^-, \alpha+2p+2n)$
^{8}Li	0.838	β^-	13	$(\pi^-, \alpha+{}^2\mathrm{H}+p+n)$
^{8}He	0.119	$\beta^- + \gamma(84\%), \beta^- + n(16\%)$	0.23	$(\pi^-, {}^3\mathrm{H}+4p+n)$
^{15}O			351	$(\gamma+n)$
^{15}N			773	$(\gamma+p)$
^{14}O			13	$(n,3n)$
^{14}N			295	$(\gamma, n+p)$
^{14}C			64	$(n,n+2p)$
^{13}N			19	$(\gamma, {}^3\mathrm{H})$
^{13}C			225	$(n, {}^2\mathrm{H}+p+n)$
^{12}C			792	(γ,α)
^{11}C			105	$(n,\alpha+2n)$
^{11}B			174	$(n,\alpha+p+n)$
^{10}C			7.6	$(n,\alpha+3n)$
^{10}B			77	$(n,\alpha+p+2n)$
^{9}Be			24	$(n,\alpha+2p+n)$
^{9}Be			38	$(n,2\alpha)$
sum			3015	

Although the energy of neutrons is not identical to the IBD signal, SK is not so sensitive to such a minor variation in the order of MeV. Therefore, these decays should be inspected. From Table 7.2, the major isotopes accompanying the neutrons include ^{8}He, ^{9}Li, ^{11}Li, and ^{16}C. However, ^{8}He, ^{11}Li, and ^{16}C do not form the dominant backgrounds owing to their low yield and the low branching ratio of $\beta+n$. As reported earlier, ^{11}Li has a short lifetime, and thus, its signal should be strongly correlated with the parent muon track and easy to eliminate.

Compared to other isotopes, ^{9}Li has a relatively long lifetime ($\sim$ 0.26 s) and provides a large yield. As ^{9}Li decays into $\beta + n$ channel with a branching ratio of 50.8% (Figure 7.2), the total yield is $1.9 \times 50.8\% \times 10^{-7}\mu^{-1}\mathrm{g}^{-1}\mathrm{cm}^2$. In addition, the energy of β is contained in the signal energy window. Therefore, in this analysis, only ^{9}Li will form a nonnegligible background.

The previous measurement result of the ^{9}Li rate at SK [48]: $0.86 \pm 0.12(stat.) \pm 0.15(syst.)$ kton^{-1}day^{-1} is utilized to estimate the amount of ^{9}Li in this analysis.

The spectrum of β from ^{9}Li decay is modeled by the BESTIOLE code [147] as depicted in Figure 7.3 with the reconstructed electron energy.

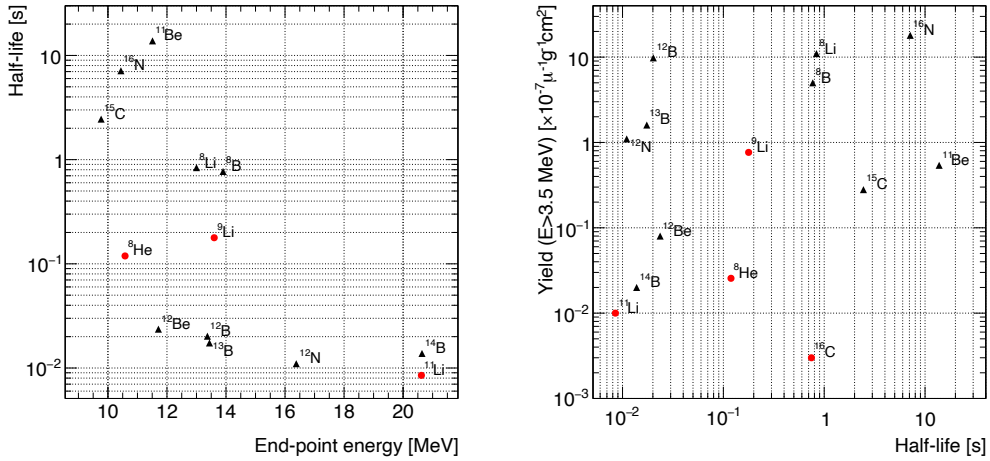

FIGURE 7.1: Correlation between end-point energies and half-lives (left) and that between half-lives and yield (right) for spallation isotopes detected in the DSNB search window and generated by cosmic-ray muons in water. Red circles in both figures represent undergoing beta decay with neutrons. For the isotopes undergoing decay with neutrons, the yield includes the fraction of decay with neutrons. The fraction of these plots referred from [48].

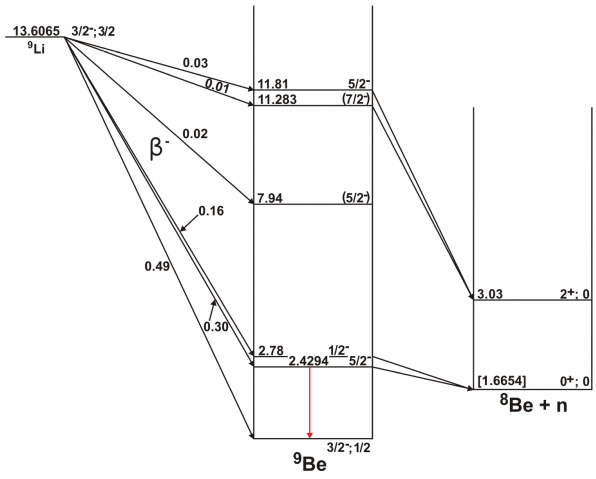

FIGURE 7.2: Decay scheme of ^{9}Li based on PDG [49].

7.3.2 Atmospheric Neutrinos

In this analysis, signals of a few tens of MeV from the atmospheric neutrinos significantly contribute to the background. Specifically, the events described below can be identified as a source of background:

- **Decay electron from muons:**
  Muons with energy below the Cherenkov threshold, known as 'invisible muons.' decay into electrons or positrons with a lifetime of 2.2 μs(decay-e). This kind of event cannot be identified by the parent muon event. Therefore, when atmospheric neutrino interactions yield invisible muons accompanied by neutrons, these interactions become indistinguishable from IBD interactions. Figure 7.4

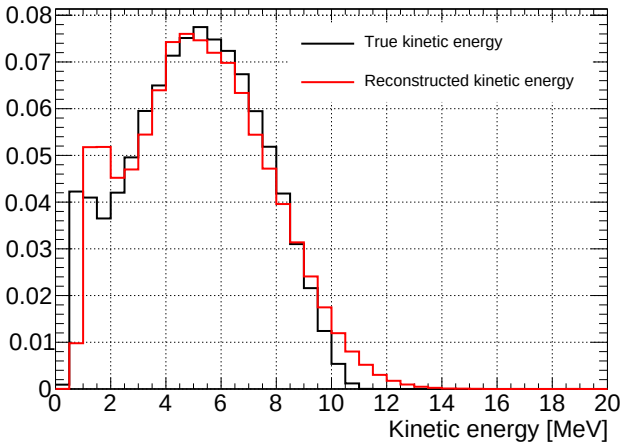

FIGURE 7.3: True and reconstructed electron kinetic energy for the β-decay of ^{9}Li.

provides a visual representation of this electron decay background. The decay-e event might also arise from the decay of pions into muons when both the muon and pion remain invisible. Since the decay-e event exhibits the familiar Michel spectrum, one can estimate the occurrence of such events by examining the side-band region data.

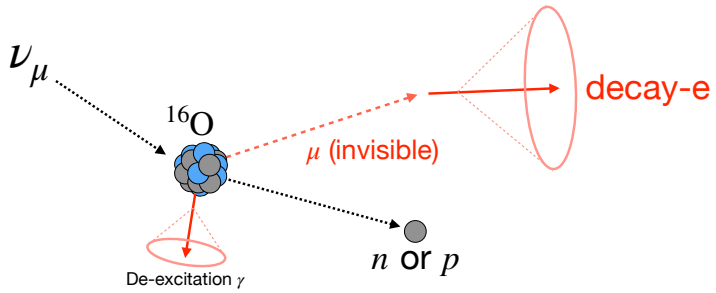

FIGURE 7.4: Illustration of decay electron background. In the figure, the decay electron from an invisible muon produced via CCQE interaction of atmospheric neutrino is displayed.

- **Visible pions and muons:**
  For pions and muons with energy surpassing their Cherenkov threshold, their light pattern observed by SK aids in their identification. If these particles decay within the ID, the double coincidence of their signals can be harnessed. Figure 7.5 displays a graphical representation of a visible muon background followed by a decay-e event.

- **Electrons from CC ν_e interactions:**
  Electrons emitted from ν_e interaction with neutrons cannot be separated from signals. The cross-section increases with energy, and these electrons mirror the energy of the original neutrino. The frequency of such events is similarly

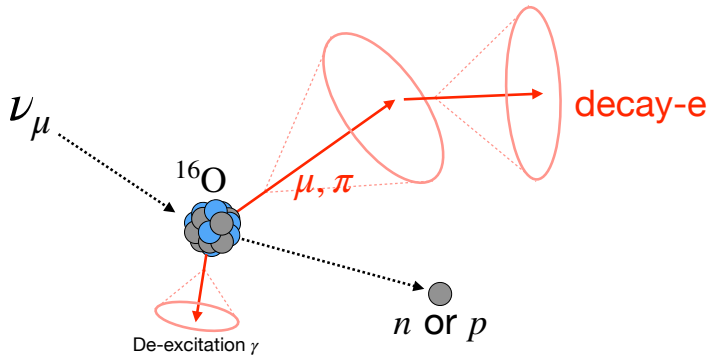

FIGURE 7.5: Illustration of the visible muon and pion background. In the figure, the visible muon and the decay electron produced via the CCQE interaction of atmospheric neutrino are displayed.

estimated using side-band data. Figure 7.6 depicts an electron event stemming from the CC interaction.

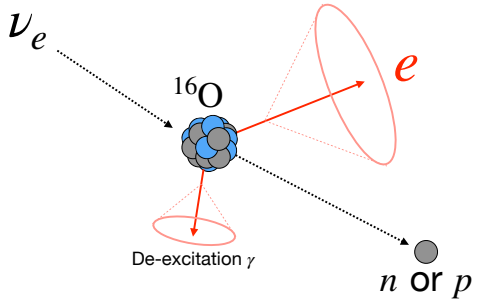

FIGURE 7.6: Illustration of the electron background event via CCQE interaction of the atmospheric electron neutrinos.

- **NCQE interaction events:**
  During NC interaction with a high-energy neutrino, if one or more nucleons are knocked out, and the remaining nuclei nucleus transitions to an excitation state, it emits a de-excitation gamma-ray. The final state particles of this interaction are the knocked-out nuclei and the de-excitation gamma-ray. Often, these knocked-out nucleons cause another hadronic interaction in the water. This results in the generation of multiple gamma rays. Although these can be minimized by the procedures mentioned in Chapter 8, the behavior of such events at low energies is poorly understood, leading to substantial uncertainties. Figure 7.7 exhibits an example of the de-excitation gamma-ray event from NCQE interaction.

7.3.3 Reactor Neutrinos

During the reactor activity, $\bar{\nu}_e$ are abundantly created via β^- decay as follows:

$$^{A}_{Z}X \rightarrow {}^{A}_{Z+1}X' + e^- + \bar{\nu}_e, \tag{7.1}$$

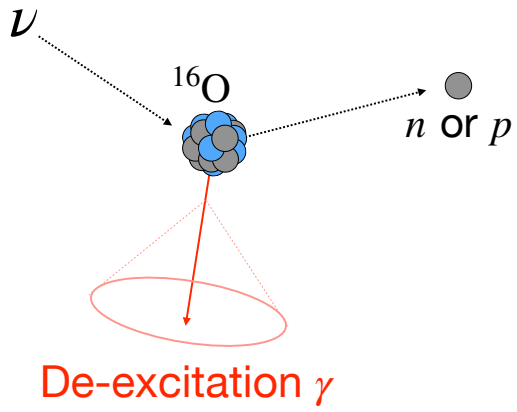

FIGURE 7.7: Illustration of the NCQE background event.

where $X(X')$ represents a specific nuclei. The neutrino flux from reactors fluctuates based on the reactor operations near the SK location. To determine the reactor neutrino flux at the SK, data on the activity of each reactor and neutrino emissions information is essential. The anticipated flux is calculated using SKReact [148], which is a tool for calculating the $\bar{\nu}_e$ flux from reactors. The situation for each reactor in Japan is referenced for the input reactor activity. The activities of the Japanese reactor are presented in Figure 7.8. Considering the neutrino oscillation, the neutrino

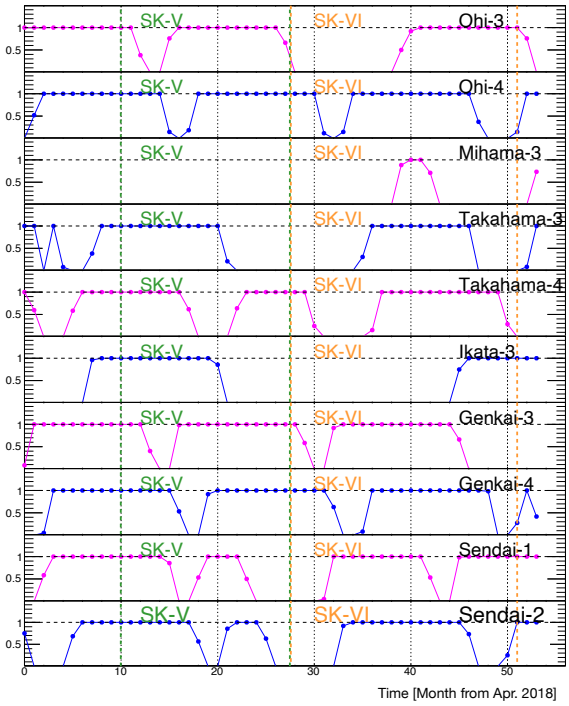

FIGURE 7.8: Activities of Japanese reactor from Apr. 2018 to Sep. 2022; dashed line indicates 100% operation time.

flux at the SK site per year is computed as depicted in Figure 7.9.

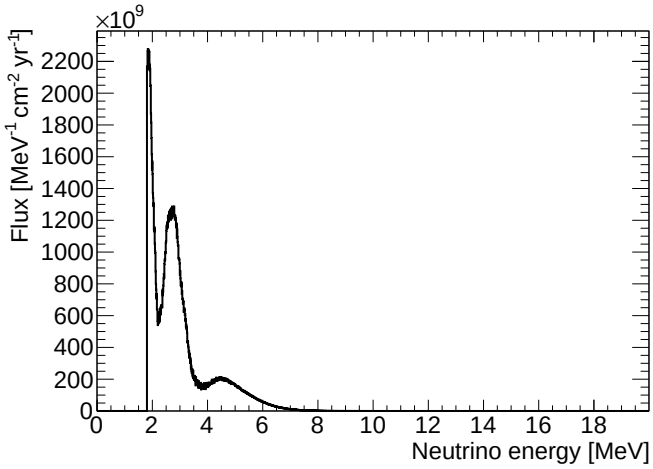

FIGURE 7.9: Expected neutrino energy flux from Japanese reactors at the SK site, considering the neutrino oscillation effect.

7.3.4 Accidental Coincidence background

In this analysis, 'accidental coincidence background' refers to events accidentally formed by pairing electron-like events with true or fake neutrons. If the pairing involves a true neutron, primarily a byproduct of muon spallation, differentiating these backgrounds from true signals becomes challenging.

Fake neutron signals can arise from low-energy radioactive backgrounds, clustered PMT dark noise, and other low-energy signals. The noise cluster of PMT hits can be substantially reduced by leveraging Gd-capture as an indicator for neutron signals since a typical Gd-capture signal results in a considerably higher count of PMT hits than one from the noise clusters. Other sources of fake neutron signals are meticulously investigated using neutron tagging, as detailed in Chapter 6.

7.4 MC Creation

To evaluate reduction efficiency and determine the final samples for both background and signal, Signal and Background MC are employed. The foundational principles of atmospheric neutrino MC production, covering aspects like flux and interactions in the tank, are outlined in Section 3.1. In this study, atmospheric neutrino MC events are simulated equivalent to the 497 years using the SKG4.

As explained in Section 3.2, the signal MC is designed with a uniform positron spectrum. This is used to estimate not only the various SRN spectra but also the backgrounds from ^{9}Li and the reactor. Appropriate flux weights are applied to the signal MC, and the methodology for this application is elucidated in Section 9. Signal MC events are created on the assumption of one event taking place every minute during the whole live time, amounting to $\sim 800,000$ events in total. The event vertex is uniformly distributed throughout the ID with an isotropic direction. Additionally, energies are presumed to be consistently distributed between 1–90 MeV.

To emulate a realistic noise environment for the neutron tagging, genuine noise hits are injected into the MC 1.7 μs post the initial generated time. The procedure for this data integration mirrors the one detailed in Section 6.1.3.

Chapter 8

Event reduction

The data undergoes the four reduction stages to reduce the background events. The first reduction removes non-physical and poor-quality events. The second reduction targets the minimization of muon spallation events. The third reduction selects the IBD prompt events while removing atmospheric neutrino and radioactivity events, and the fourth reduction implements neutron tagging. This chapter delves into the specifics of each reduction method, detailing the criteria and associated efficiencies.

8.1 First Reduction: Pre-cut

8.1.1 Nonphysical Event and Invalid Triggered Event Cut

In this analysis, the events should at least trigger the SHE. Moreover, the events triggered by OD are disregarded, as they are typically associated with muon activities. Initially, nonphysical events as listed below, are eliminated:

- Calibration trigger event
- Pedestal event
- Badly processed and incomplete event
- Runs that something unsolvable issue occurs
- Periodic trigger event
- T2K beam trigger event

In addition to the above cut, additional criteria were applied to remove the events triggered by PMT noise hit. The number of hits caused by PMT noise is smaller than those caused by the light from the actual physical signal in the physical event. Additionally, the PMT charge stemming from noise hits tends to be smaller. Thus, the condition $N(Q < 0.5 \text{ p.e.})/N_{\text{all}} < 0.55$ is applied to eliminate events influenced by PMT noise. Here, $N(Q < 0.5 \text{ p.e.})$ represents the number of hits where the PMT charge is below 0.5 p.e., and N_{all} denotes the number of total hits.

8.1.2 Cosmic-ray muon-induced event cut

Cosmic-ray muons arrive at SK at a rate of ~ 2 Hz. These muons typically issue the OD trigger. Some muons result in decay-e events with a lifetime of 2.2 μs. However, if a considerable time difference exists between the muon and decay-e, leading them to be identified as separate events, then decay-e is not triggered by OD. Any events occurring within 50 μs post muon event are discarded as a precaution. This reduction additionally filters out short-lived isotopes resulting from muon spallation, as outlined in Section 7.3.1.

8.1.3 Fiducial volume cut

Numerous low-energy events emanate from the radioactivity surrounding the wall of the tank. To eliminate these events, standard fiducial volume (FV) cuts that remove events within 200 cm from the tank wall are applied.

8.1.4 Fit-quality cut

At times, low-energy events exhibit subpar reconstruction quality. To counteract this, events are filtered using the fit goodness parameter, g_{vtx}. Events that have a g_{vtx} less than 0.5 are removed. Figure 8.1 illustrates the relationship between reconstructed kinetic energy (E_{rec}) and fit goodness (g_{vtx}) after applying the above-mentioned noise reduction cut for both data and signal MC. For energies above 8 MeV, the $g_{\mathrm{vtx}} > 0.5$ criterion does not adversely affect the signal, as depicted in the right panel of Figure 8.1. The pronounced event peak at $g_{\mathrm{vtx}} \sim 0.4$ below 8 MeV region appears to stem from radioactive backgrounds near the tank wall, lingering despite the FV cut. These should be further removed using subsequent cuts. The g_{vtx} criterion effectively removes events with poor fit quality related to radioactivity while retaining over $> 99.9\%$ of signal MC.

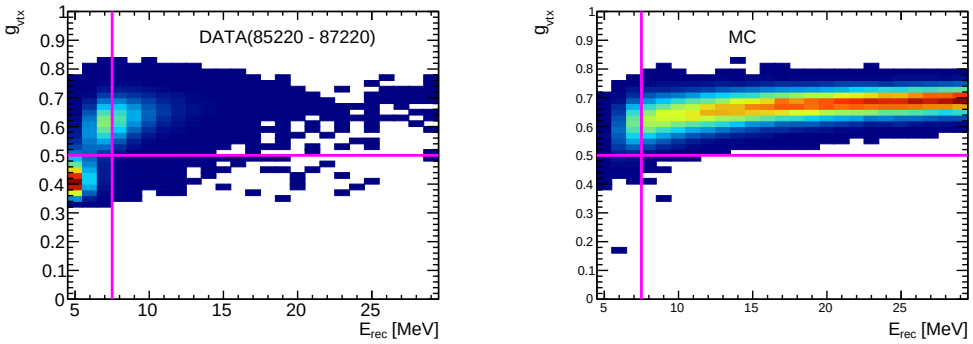

FIGURE 8.1: Reconstruction goodness and reconstructed energy distribution for data (left) and signal MC (right). Vertical magenta line exhibits the energy threshold of 7.49 MeV, and the horizontal magenta line presents the g_{vtx} threshold.

8.1.5 Trigger Requirement

As described in Chapter 2, the SHE and AFT triggers are required to search for the delayed neutron signals in this analysis. Furthermore, events must not trigger the OD in the quest for neutrino signals. Events meeting this criterion, i.e., SHE-triggered but OD-untriggered, are henceforth labeled as 'SHE event.' However, owing to the AFT trigger rate being limited to once every 21 ms until the middle of SK-VI, SHE triggers can occur without a subsequent AFT. This discrepancy needs to be assessed using real data and factored into the normalization of MC. The AFT efficiency $\varepsilon_{\mathrm{AFT}}$ is evaluated for each reconstructed energy bin of 2 MeV, as follows:

$$\varepsilon_{\mathrm{AFT}} = \frac{N_{\mathrm{AFT}}}{N_{\mathrm{SHE}}}, \tag{8.1}$$

where N_{AFT} denotes the number of AFT-triggered events and the N_{SHE} indicates the number of SHE-triggered events for each 2 MeV bin. The values of $\varepsilon_{\mathrm{AFT}}$ for each bin are summarized in Table 8.1.

TABLE 8.1: AFT trigger efficiency calculated using 2 MeV energy bins. These values are calculated by considering the average of the entire SK-VI period.

Energy bin [MeV]	After-trigger efficiency [%]
8–10	85.3%
10–12	80.4%
12–14	74.3%
14–16	70.0%
16–18	67.9%
18–20	63.4%
20–22	89.7%
22–24	90.0%
24–26	90.0%
26-28	100.0%
28–30	90.5%
>30	93.7%

8.2 Second Reduction: Spallation Cut

Following the first reduction, the isotope decay events stemming from the cosmic muon spallation become the dominant background within the signal energy region. Currently, no reliable simulation can reproduce muon spallation. Thus, a data-driven muon spallation is developed, for the present analysis, called the spallation cut. The core idea behind the spallation cut is to explore the relationship between the SHE events and muons observed close in time to the SHE events to potential events produced by earlier muons.

Muon spallation also prominently contributes to the prompt event of the accidental coincidence background. Events resulting from muon spallation are anticipated to outnumber those from SRN by a factor of $\mathcal{O}(10^6)$. The efficacy of the spallation cut should sufficiently reduce the muon spallation by a $\mathcal{O}(10^{-6})$, when combined with the neutron misidentification to offer a meaningful constraint on the SRN flux.

To prove the correlation between SHE events and the muons, nearby muon events to the SHE occurrences in time are identified, specifically those that trigger both HE and OD. For every SHE event, muons within a ±60-second window of the SHE event are compiled. Since the muon rate is $\sim$ 2 Hz at SK, $\sim$ 240 muons for each SHE event are found. For this analysis, the muon information included the time difference from SHE events, track information including the number of tracks estimated by Muboy fitter (Section 4.2), and the deposited energy dE/dx along with the track.

Muons surrounding the SHE event are categorized into 'pre-' and 'post-' regions. If we consider the timing of the SHE event, any time prior to it is designated as the 'pre-' region, while the time posterior is labeled the 'post-' region. Figure 8.2 illustrates this definition and the conceptual distinction between 'pre-' and 'post-' regions. A vital feature of this categorization is that while a muon from the pre-region might give rise to a SHE event, a muon from the post-region cannot, especially if the SHE event is

due to spallation. All muon events from these two regions are compiled for all SHE occurrences and labeled as 'pre-' and 'post-' samples.

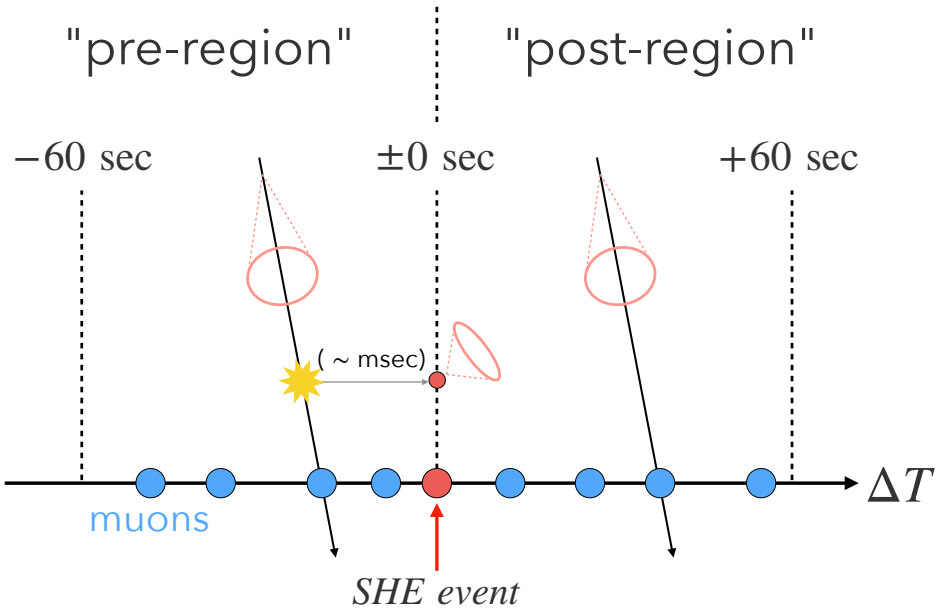

FIGURE 8.2: Illustration of muon concept for the spallation.

The spallation cut consists of five reduction contents.

- **1-ms cut:** Filters out hadronic interaction events resulting from the particles induced by muon spallation.
- **Neutron cloud cut:** Assess muon spallation events that occurred with neutrons along with the muon track.
- **Multiple Spallation cut:** Detects the presence of clustered low-energy events in both space and time.
- **Spallation likelihood cut:** Compute the likelihood of a SHE event originating from muon spallation.
- **Spallation Box cut:** A more stringent cut than others, utilizing muon goodness, time variance, and spatial difference to eliminate sufficiently high-energy spallation events.

8.2.1 1-ms cut

Muon spallation yields a cascade of particles, sometimes numbering in the thousands. These particles, being highly energetic, can instigate subsequent hadronic nuclear reactions, emitting gamma rays, neutrons, and more. Occasionally, these particles might activate the SHE triggers, with neutrons potentially causing a delayed signal due to neutron capture.

To filter out evident SHE events induced by the muon spallation, any SHE events within 1 ms muon occurrences are excluded. Factoring in the 2 Hz muon rate, the impact of this cut on signal efficiency is calculated as 1 ms/0.5 s = 0.2%.

8.2.2 Multiple Spallation Cut

Energetic muons occasionally produce multiple radioactive isotopes. If one such instance is a SHE event, another low-energy event should be observed close to the SHE event both in time and space. To identify correlated low-energy events with the SHE event, the selection criteria from the solar neutrino analysis [38] are employed on all low-energy events with a reconstructed energy range of 6–25 MeV. Spatial correlations between a specific SHE event and any selected low-energy events within a ±60 s window are subsequently investigated. Figure 8.3 visualizes the shortest distance between a given SHE event and its neighboring low-energy events. The contribution of spatially correlated events is clearly apparent when contrasted against a randomized distance distribution. Consequently, SHE events with a minimum distance of less than 4.0 m from the low-energy event are excluded. The efficiency of random events is gauged using a randomized vertex and stands at 98%.

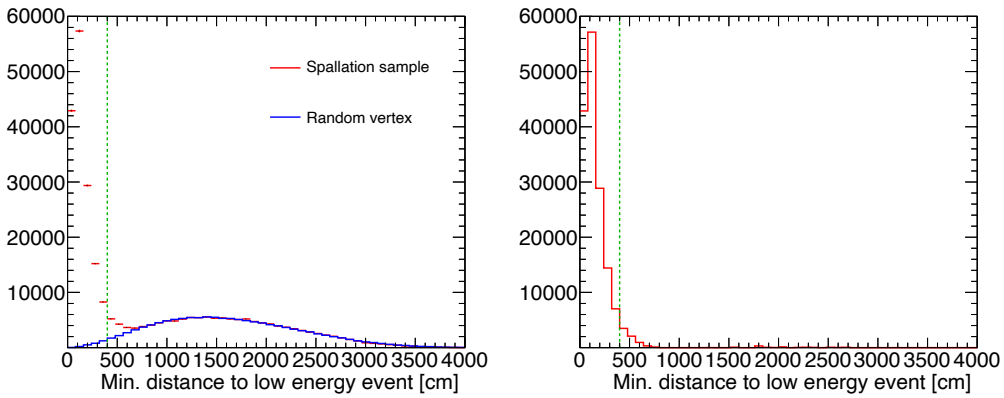

FIGURE 8.3: Minimum distance between the SHE event and the low-energy event within ±60 s, obtained from the SHE event and randomized vertex (left) and the subtracted distribution (right).

8.2.3 Neutron Cloud Cut

Muon spallation produces thousands of hadronic particles, including neutrons. These neutrons get captured by the nuclei, notably Gd in SK-Gd, within a timescale of $\mathcal{O}(100)$ μs. Such events generate neutron event clusters near the spallation origin point. This characteristic helps discerning muon spallation events, a phenomenon termed 'Neutron cloud.' The neutron events accompanying each identified muon are subsequently sought. The selection parameters for these neutrons mirror the methods of the cosmogenic neutron yield analysis [149] as follows:

- triggered with 25 hits/200 ns
- timing within [35, 535] μs from the muon
- $g_{\mathrm{vtx}} > 0.4$ and $g_{\mathrm{dir}} < 0.4$
- Distance from the muon is within 5 m.

If two or more neutrons are detected, the muon is considered to possess a neutron cloud. Figure 8.4 displays the count of accompanying neutrons for pre and post-muon samples, emphasizing the prominence of neutron clouds in the pre-sample.

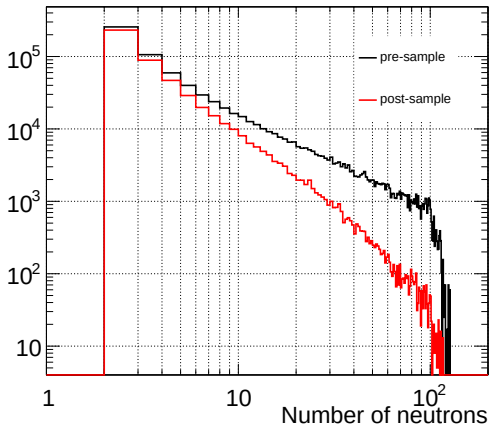

FIGURE 8.4: Number of neutrons after muons for pre (black) and post (red) samples.

Figure 8.5 plots the muon timing using the SHE event time as a reference. Muons with an increased neutron count show a timing correlation with SHE events. Expectedly, a spatial relationship exists between the neutron cloud and the SHE event. The vertex of the neutron cloud $\vec{r}_c$ denotes the weighted averaged vertex of the selected neutrons for each muon. Figure 8.6 demonstrates the distance separating the SHE event and the neutron cloud vertex, underscoring a spatial correlation only in the pre-sample. This relationship assists in pinpointing muon spallation.

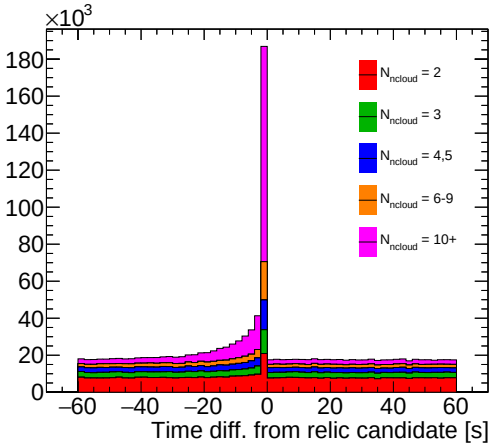

FIGURE 8.5: Time difference between muons and the SHE event. Each color exhibits the number of neutrons after muons.

To refine the cut criteria targeting muon spallation, a new coordinate system is introduced where the z-axis aligns with the muon track. Vertex difference along with this new coordinate system, labeled Δ_x, Δ_y, Δ_z, and the vertex difference Δl as $\Delta l = \Delta_x^2 + \Delta_y^2 + \Delta_z^2$ is calculated. The characterization of muon spallation with the neutron cloud incorporates these variables alongside the time difference between the muon and SHE event (ΔT). Figure 8.7 illustrates the definition of the newly

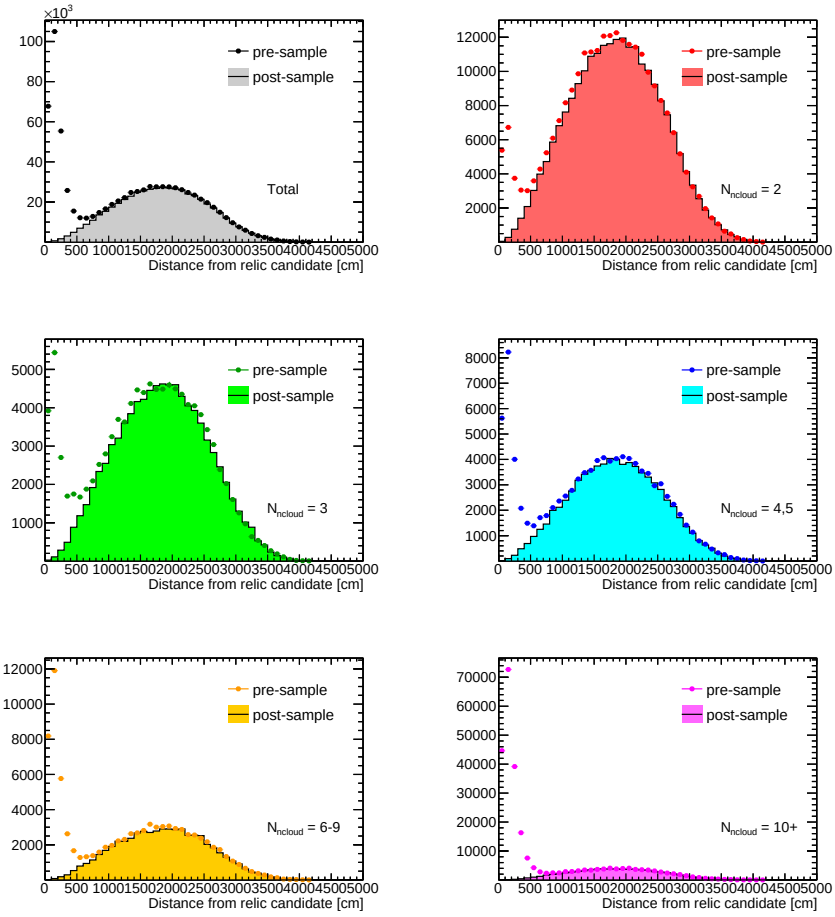

FIGURE 8.6: Distance between neutron cloud position and the SHE event. Each panel exhibits the difference in N_{ncloud}.

defined axis and variables. Given the varying dependence of the cloud on the muon,

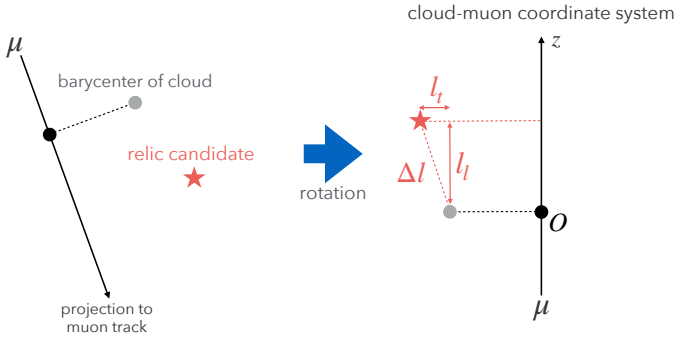

FIGURE 8.7: Illustration of definition for the variables used in the neutron cloud cut.

as illustrated in Figures 8.5 and 8.6, the cut criteria for the neutron cloud can be distinguished by N_{ncloud}.

Figure 8.8 displays the 2D distribution for each spatial variable Δ_x, Δ_y, Δ_z, including the cut criteria in this plane. The event cluster observed around $\log(\Delta t) = 1$ will be later removed based on the elliptical shape cut. Moreover, the correlation with the Δl and ΔT is depicted in Figure 8.9. Considering these distributions and taking into account the elliptical shape of cloud distribution, the cut criteria are determined.

The criteria are consolidated in Table 8.2 with reference to the previous analysis [20]. The neutron cloud cut reduces about 68% of the spallation events following Equation 8.8 while maintaining 98% of random efficiency defined by Equation 8.5.

TABLE 8.2: Cut criteria of neutron cloud cut. The signature (+) in the multiplicity column signifies equal or more than the value.

N_{ncloud}	Time [sec]	Spatial [cm]
2+	$\Delta T < 0.1$	$\Delta l < 1200$
2+	$\Delta T < 1$	$\Delta l < 800$
2	$\Delta T < 30$	$(\Delta_x^2 + \Delta_y^2)/200^2 + \Delta_z^2/400^2 > 1.2$
3	$\Delta T < 60$	$(\Delta_x^2 + \Delta_y^2)/(6 \times 10^4) + \Delta_z^2/500^2 > 1.2$
4, 5	$\Delta T < 60$	$(\Delta_x^2 + \Delta_y^2)/(1.2 \times 10^5) + \Delta_z^2/550^2 > 1.2$
6–9	$\Delta T < 60$	$(\Delta_x^2 + \Delta_y^2)/(2 \times 10^5) + \Delta_z^2/650^2 > 1.2$
10+	$\Delta T < 60$	$(\Delta_x^2 + \Delta_y^2)/500^2 + \Delta_z^2/700^2 > 1.2$

8.2.4 Spallation Likelihood Cut

The 1-ms cut, combined with the multiple spallation cut and neutron cloud cuts, eliminates roughly 70% of muon spallation events. To further minimize these events, a statistical method employing log-likelihood is explored. This approach aims to derive a single cut variable termed 'spallation likelihood,' which includes information concerning the correlation between the muon and SHE event. The spallation likelihood $\mathcal{L}_{\text{spall}}$ is defined as follows:

$$\mathcal{L}_{\text{spall}} = \log \prod_i \left(\frac{\text{PDF}^i_{\text{spall}}(x)}{\text{PDF}^i_{\text{random}}(x)} \right), \tag{8.2}$$

where the $\text{PDF}^i_{\text{spall}}$ denotes the Probability Density Function (PDF) of the spallation sample, and $\text{PDF}^i_{\text{random}}$ represents the PDF of the random sample, comprising the post-muon samples. i indicates the i-th variable used in the calculation, and x denotes the value of the i-th variable. The procedure for creating the PDF will be detailed subsequently.

Spallation variables

Key variables integral to the spallation likelihood (termed spallation variables) include:

- dt: Time difference between the SHE event and muon (same as the definition described in Section 8.2.3).
- ℓ_t: Transverse distance separating the SHE event from the muon track. For spallation occurrences, this typically does not exceed a few meters.
- ℓ_l: Longitudinal distance between the SHE event and sites of peak energy deposition (dE/dx) on the muon track. When a muon instigates spallation, this

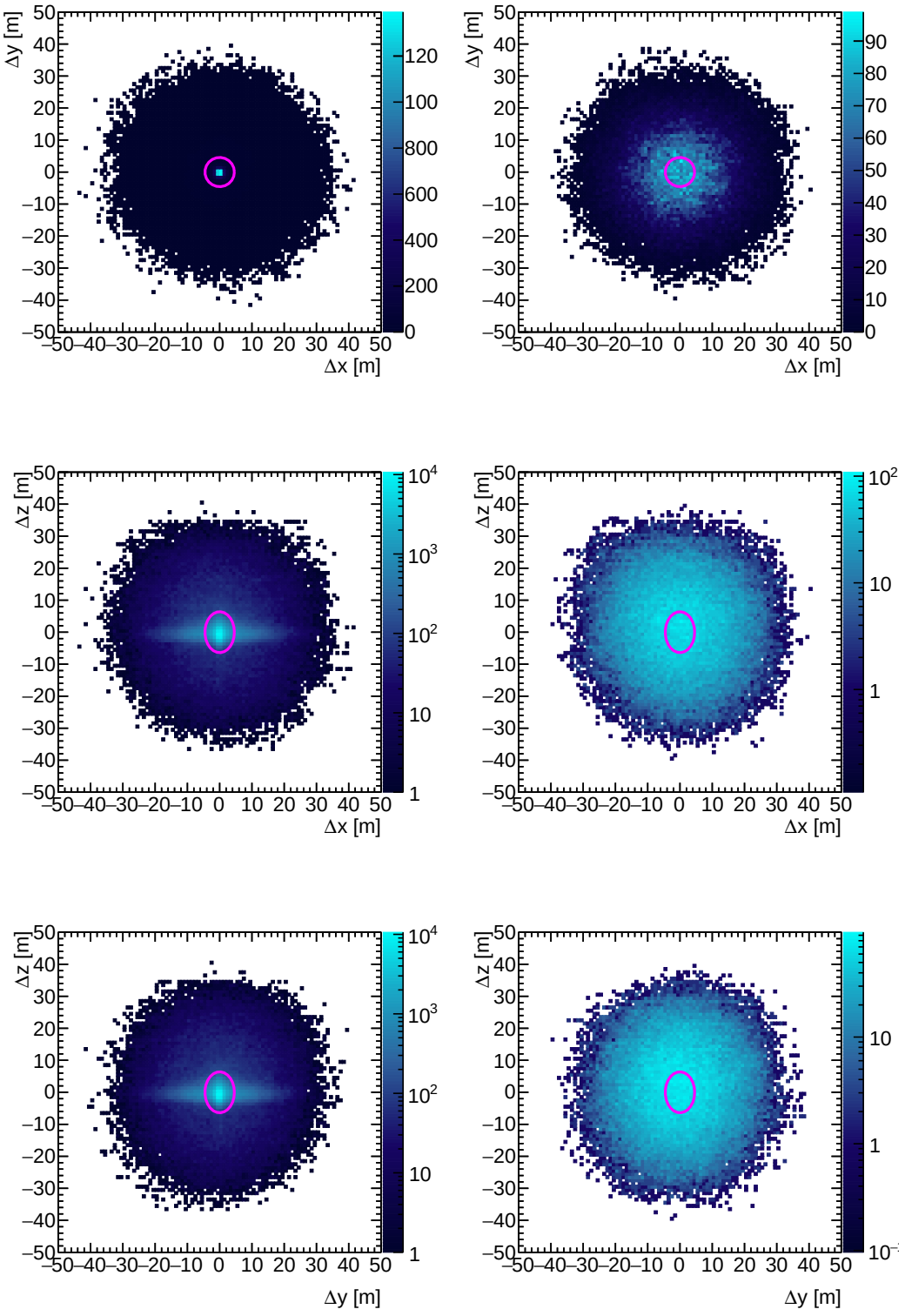

FIGURE 8.8: Two-dimensional distribution of Δ_x, Δ_y, and Δ_z. Left column represents the pre-samples, and right column indicates the post-samples. Magenta lines indicate the cut criteria. These are clouds with $N_{\mathrm{ncloud}} \geq 10$.

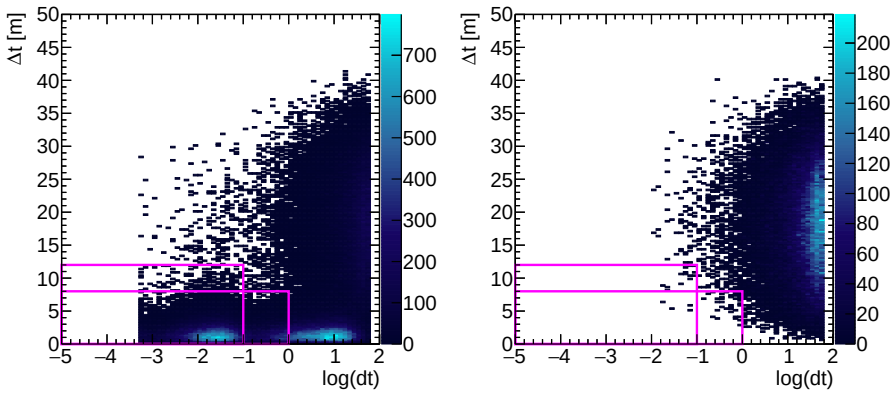

FIGURE 8.9: Two-dimensional distribution of $\log|dt|$ and Δl for the pre-sample (left) and the post-sample (right). Magenta lines are cut criteria in this plane. These are for clouds with $N_{\text{ncloud}} \geq 10$.

peak energy point tends to be proximate to the spallation side. Consequently, for such events, ℓ_l should remain within a few meters.

- Q_μ: Cumulative charge deposition of the muon within the ID of the tank. In instances where a muon triggers spallation, the energy deposition typically surpasses that of the Minimum Ionization Particle (MIP).

- Q_{res}: Residual charge deposition relative to the expected MIP value, expressed as:

$$Q_{\text{res}} = Q_\mu - Q_{\text{MIP}} \times L \tag{8.3}$$

where Q_{MIP} denotes the number of photoelectrons per centimeter expected from the MIP, and L indicates the track length of the muon. For multiple muons, the L represents the sum of the tracks since the Q_μ denotes the sum of charge deposition of all muons. Q_{res} is independent of the SHE event; however, it indicates the probability of muon to induce spallation.

The spallation variables are defined in Figure 8.10.

PDF and Likelihood

For likelihood computations, two area-normalized histograms are generated as PDFs; one for spallation ($\text{PDF}^i_{\text{spall}}$), and another for random ($\text{PDF}^i_{\text{random}}$). To derive the spallation component from the pre-muon sample for constructing $\text{PDF}^i_{\text{spall}}$, distributions of post-muon samples are subtracted from those of the pre-muon sample for each respective variable. Subsequently, all resulting distributions undergo area normalization. Separate PDFs are established for each likelihood variable, tailored to the muon type. Additionally, the PDFs for ℓ_l, Q_{res}, and Q_μ are segmented by dt (0–0.05 s, 0.05–0.5 s, 0.5–60 s) and ℓ_t (0–300 cm, 300-1000 cm, 1000–5000 cm) to optimize the removal of spallation events.

Given that the post-sample distribution is subtracted from the pre-sample to form $\text{PDF}^i_{\text{spall}}$, it is more susceptible to statistical variations compared to $\text{PDF}^i_{\text{random}}$. To mitigate these potential discrepancies, a Kernel Density Estimation (KDE) method is employed.

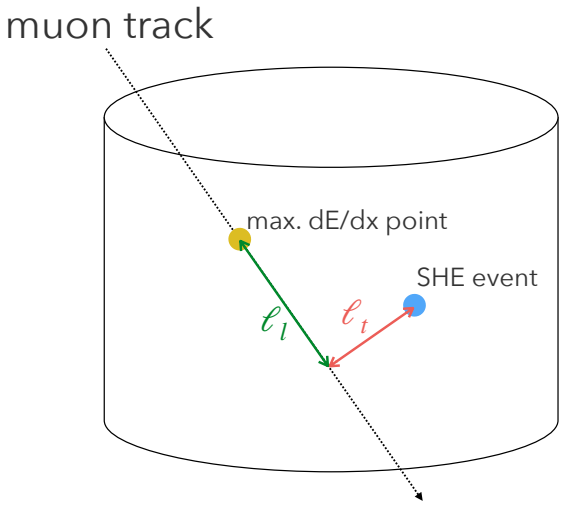

FIGURE 8.10: Illustration for variables related to spatial correlation

Estimated PDF $\hat{f}(x)$ is described as:

$$\hat{f}(x) = \frac{1}{nh}\sum_{i=1}^{n} k\left(\frac{x - X_i}{h}\right) \tag{8.4}$$

where the $k(x)$ denotes Kernel function, n indcates the number of total entries, i denotes the entry number, X_i represents the center value of the bin at i-th entry, and h indicates the bin width of PDF histograms. A Gaussian function, characterized by a mean of 0 and a variance of 1, utilized the Kernel function. The KDE methodology is implemented, resulting in new PDFs for all variables. Figure 8.11 shows PDFs of these variables for the single-through muon with $dt < 0.05$ s and $\ell_t < 300$ cm for ℓ_l, $Q_{\rm res}$, and Q_μ, as an example. The clear contributions are seen as the difference between spallation and random samples.

$\mathcal{L}_{\rm spall}$ value for all muons are calculated for each SHE event. $\mathcal{L}_{\rm spall}$ distributions are organized into bins based on the energy of the SRN candidate (reconstructed energy = 8–10, 10–12, 12–14, 14–16, 16–18, 18–20, 20–24 MeV) because the spallation event rate from each isotope is highly correlated with its energy. Furthermore, as the single-through and multiple muons are major types and it is required to review more carefully, the cut criteria of $\mathcal{L}_{\rm spall}$ are determined for each dt and ℓ_t binning; dt binning is common for two muon types: 0–0.05, 0.05–0.5, 0.5–60 s, whereas ℓ_t binning is divided for two types: 0–200, 200–300, 300–500, 500–1000, 1000–5000 cm for single-through muon and 0–100, 100–200, 200–300, 300–500, 500–700, 700–1000, 1000–5000 cm for multiple muons, respectively. For the misfitted muon, only dt is used to calculate $\mathcal{L}_{\rm spall}$, as the other variables are unreliable. Figure 8.12 presents the likelihood distributions for different muon types, showcasing the dt = 0–0.05 s and ℓ_t = 0–200 cm region for single-through muons, and dt = 0–0.05 s and ℓ_t = 0–100 cm region for multiple muons are shown as examples.

8.2.5 Spallation Box Cut

The muon spallation sample is drastically decreased at the high-energy region beyond 16 MeV. Therefore, the accurate optimization of spallation likelihood criteria is difficult. Thus, a series of strict cuts is applied primarily above 16 MeV.

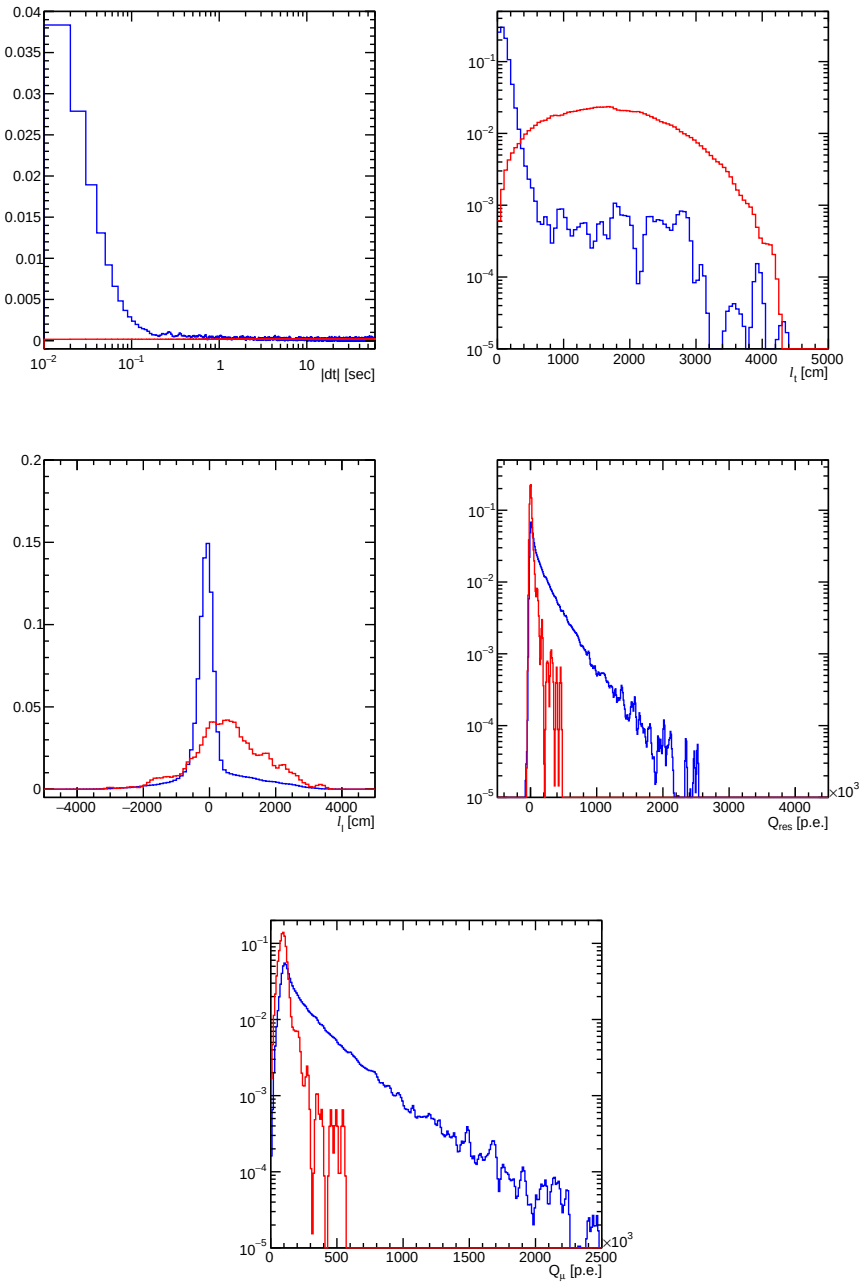

FIGURE 8.11: Random (red) and spallation (blue) PDFs for dt (top, left), ℓ_t (top, right), ℓ_l (middle, right), Q_{res} (middle, right), and Q_μ (bottom). These muons belong to the single through-going muons with the dt region of 0–0.05 s and the ℓ_t region of 0–300 cm.

Isotopes with relatively higher end-point energy, such as ^{12}N, ^{14}B, and ^{11}Li,typically have a very short lifetime as shown in Figure 7.1. Therefore, these events can be removed with more simple and robust cuts. Thus, a series of rectangular cuts for events mainly above 16 MeV and events with shorter ℓ_t and dt for each muon type. Table 8.3 summarizes the criteria for cuts.

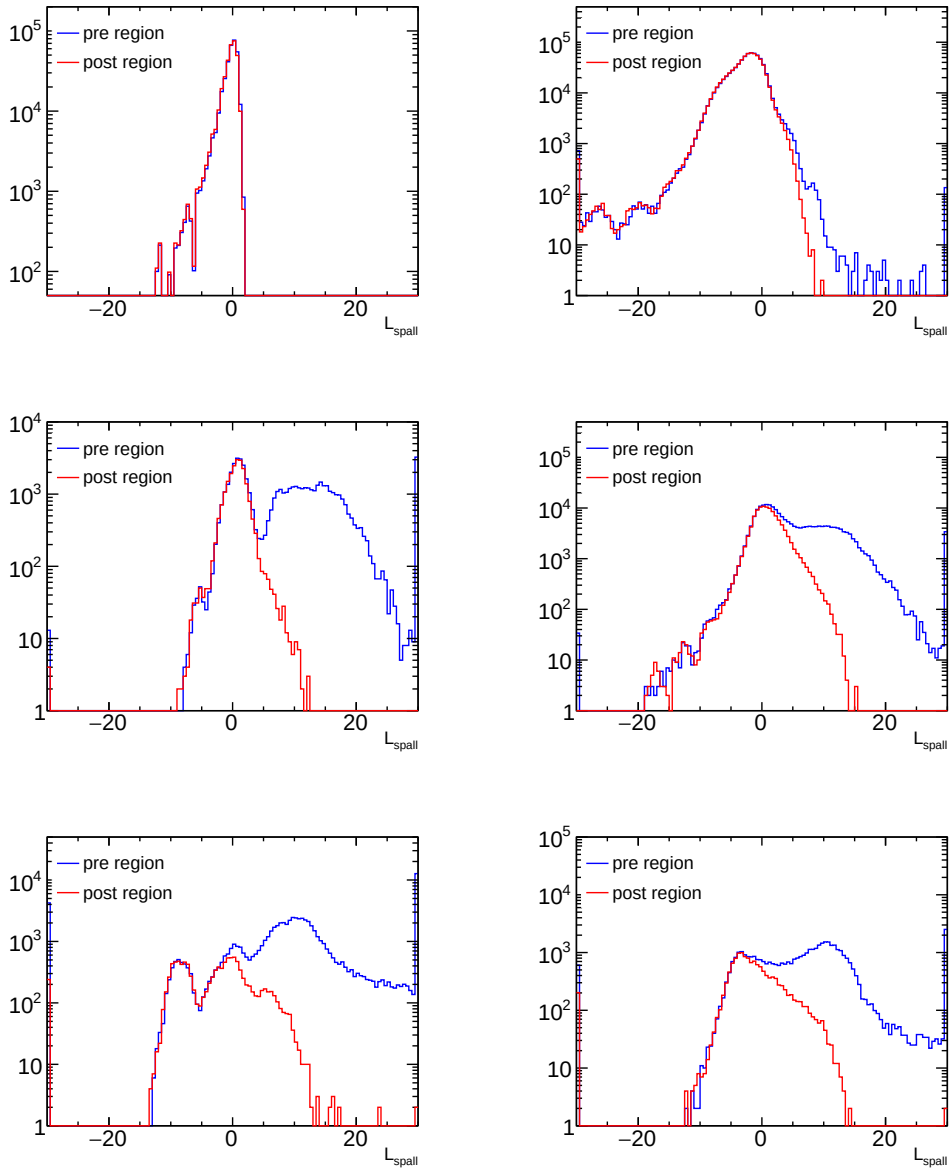

FIGURE 8.12: Spallation likelihood distributions of pre (blue) and post (red) samples, for misfit (top, left), stop (top, right), single through-going with dt = 0–0.05 sec (middle, left), and ℓ_t = 0–200 cm (middle, right), and multiple muons with dt = 0–0.05 sec (bottom left), and ℓ_t = 0–100 cm (bottom, right). These findings correspond to the reconstructed energy in the 8–10 MeV region.

8.2.6 Spallation Cut Efficiency Estimation

Survival probabilities after whole spallation cuts are estimated for the remaining background and signal events. In this study, four types of efficiencies that the events remaining rate after spallation cut are evaluated: spallation event ($\varepsilon_{\rm spall}$), random event ($\varepsilon_{\rm random}$), solar event ($\varepsilon_{\rm solar}$), and ^{9}Li event ($\varepsilon_{\rm li9}$).

TABLE 8.3: Summary of cut criteria of spallation box cuts for each reconstructed energy E region.

Energy region	Muon type	Cut criteria
$E < 24$ MeV	–	$dt < 0.1$ s and $\ell_t < 400$ cm
$16 < E < 20$ MeV	misfit	$dt < 1.5$ s
$16 < E < 18$ MeV	single	$g_\mu < 0.4$ and $dt < 7$ s and $\ell_t < 150$ cm
$16 < E < 18$ MeV	stopping	$g_\mu < 0.3$ and $dt < 6$ s
$16 < E < 20$ MeV	stopping	$dt < 0.05$ s
$16 < E < 20$ MeV	multiple	$dt < 0.1$ s and $\ell_t < 400$ cm

Efficiency for random event

As earlier outlined, efficiencies of the multiple spallation and neutron cloud cuts for random events stand at approximately 98%. The impact of a 1-ms cut on these events is negligible. Subsequent references to these three cuts collectively label them as the spallation pre-cut.

The spallation cut efficiency for a random event $\varepsilon_{\text{random}}$, which is equivalent to the signal efficiency after the spallation cut, can be calculated as follows:

$$\varepsilon_{\text{random}} = \frac{N_{\text{post,after}}}{N_{\text{before}}}, \tag{8.5}$$

where N_{before} denotes the number of SHE events before cuts. $N_{\text{post,after}}$ indicates the number of remaining SHE events after applying likelihood cut and box cut, considering the spallation pre-cut efficiency. Here, the likelihood and box cut use the correlation only with post-sample muons.

Efficiency for solar neutrino event

Given that solar neutrino events should not correlate to any muons, they offer a valuable benchmark to verify the randomness of the post-sample. By examining the correlation between the solar neutrino event direction and the sun's direction, the number of solar SHE events N_{sol} is calculated as follows:

$$N_{\text{sol}} = N_{\cos\theta_\odot > 0.5} - N_{\cos\theta_\odot < -0.5}, \tag{8.6}$$

where the $N_{\cos\theta_\odot > 0.5}$ denotes the number of SHE events from the solar direction, and $N_{\cos\theta_\odot < -0.5}$ (N_{nonsol}) indicates the number of SHE events from the opposite direction of the sun. Figure 8.13 illustrates the schematic of the definition of solar neutrino events. To cross-check independently from the post-muon sample, the spallation cut is applied to the solar neutrino events using only pre-muon samples. After that, spallation cut efficiency for the solar neutrino event $\varepsilon_{\text{solar}}$ is evaluated.

The definition of $\varepsilon_{\text{solar}}$ is stated as follows:

$$\varepsilon_{\text{solar}} = \frac{N_{\text{sol,pre,after}}}{N_{\text{sol,before}}}, \tag{8.7}$$

where $N_{\text{sol,pre,after}}$ denotes the number of solar SHE events after the spallation cut using only the pre-muon sample, and $N_{\text{sol,before}}$ refers to the number of solar SHE events before the spallation cut.

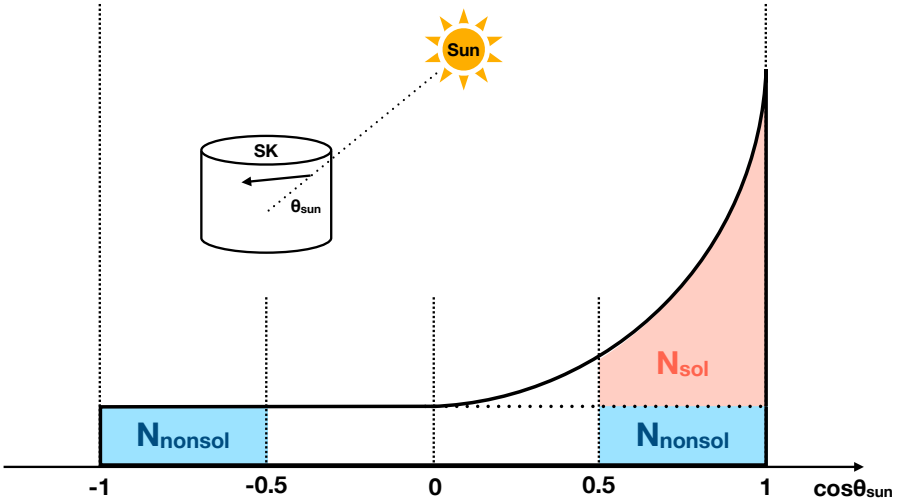

FIGURE 8.13: Schematic of definition of $\theta_{\rm sun}$ and $\cos\theta_{\rm sun}$.

Figure 8.14 portrays the correlation between the random and solar event efficiency for events in the 8–10 MeV range as likelihood cut threshold shift. A linear correlation between the two efficiencies is clearly seen, confirming that $\varepsilon_{\rm random}$ can be used in our analysis. The post-sample is used to evaluate $\varepsilon_{\rm random}$ rather than the solar SHE sample because the statistic of the post-sample is much larger than the solar sample. Moreover, $\varepsilon_{\rm random}$ is unreliable at the higher energy region owing to drastically decreased statistics of the solar neutrino event in the higher energy region.

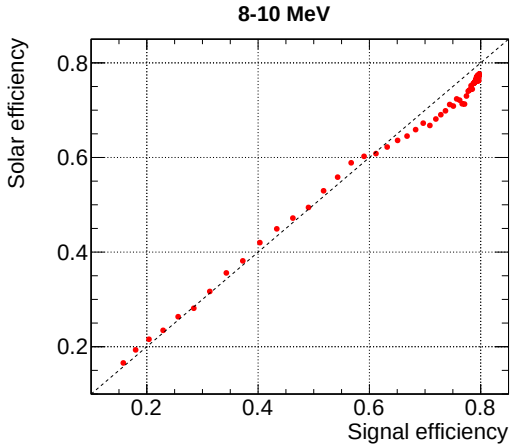

FIGURE 8.14: Correlation between $\varepsilon_{\rm random}$ and $\varepsilon_{\rm solar}$.

Spallation remaining rate

To evaluate spallation cut performance, the spallation remaining rate must be calculated. Below 16 MeV, solar neutrino events primarily predominate before neutron

tagging, except for the spallation event. To circumvent the solar neutrino event contamination, the spallation remaining rate employs non-solar events:

$$\varepsilon_{\text{spall}} = \frac{N_{\cos\theta_\odot<0,\text{pre,after}} - N_{\text{atm,after}}}{N_{\cos\theta_\odot<0,\text{before}} - N_{\text{atm,before}}}, \tag{8.8}$$

where the $N_{\cos\theta_\odot<0,\text{pre,after}}$ and $N_{\cos\theta_\odot<0,\text{before}}$ denote the number of events before and after all likelihood cuts using only pre-sample muons with $\cos\theta_\odot < 0$, and $N_{\text{atm,before}}$ and $N_{\text{atm,after}}$ indicate the number of atmospheric neutrino events before and after likelihood cut. Because a second major event above 14 MeV is an atmospheric neutrino event, $\varepsilon_{\text{spall}}$ is estimated by subtracting atmospheric neutrino events. $N_{\text{atm,before}}$ denotes estimated by the atmospheric neutrino MC, and the $N_{\text{atm,after}}$ can be calculated by $N_{\text{atm,before}} \times \varepsilon_{\text{random}}$.

Efficiency for the Lithium-9

^{9}Li survival probability ε_{li9} should be estimated as the spallation events from ^{9}Li decay remain dominantly after even all cuts are applied. As estimating the e the number of ^{9}Li events is challenging, ε_{li9} is evaluated by combining certain survival probabilities. In principle, muon events in the pre and post-samples for a given SHE are classified into three types: (a) a muon that produces the given SHE event, (b) muons that produce other SHE events, and (c) muons that do not produce any SHE events. The survival probabilities after spallation cut by these muons (a), (b), and (c) are defined as ε_{a}, ε_{b}, and ε_{c}, respectively. The survival probabilities after spallation cut using pre and post-muon samples ε_{pre} and $\varepsilon_{\text{post}}$ can be described as follows:

$$\varepsilon_{\text{pre}} = \varepsilon_{\text{a}} \times \varepsilon_{\text{b}} \times \varepsilon_{\text{c}} \tag{8.9}$$

$$\varepsilon_{\text{post}} = \varepsilon_{\text{b}} \times \varepsilon_{\text{c}}, \tag{8.10}$$

because ε_{a}, ε_{b}, and ε_{c} are independent of each other. Therefore, ε_{a} can be computed by $\varepsilon_{\text{a}} = \varepsilon_{\text{pre}}/\varepsilon_{\text{post}}$. As the ε_{li9} is equivalent to the ε_{pre} for the ^{9}Li event, it can be evaluated in the same manner as follows:

$$\varepsilon_{\text{li9}} = \varepsilon_{\text{a,li9}} \times \varepsilon_{\text{random}} \times \varepsilon_{\text{multi+ncloud}}, \tag{8.11}$$

$$\varepsilon_{\text{multi+ncloud}} = \varepsilon_{\text{spall}}/\varepsilon_{\text{1-ms+likeli+box}}, \tag{8.12}$$

where $\varepsilon_{\text{a,li9}}$ denotes the same definition as ε_{a} for the ^{9}Li event, $\varepsilon_{\text{multi+ncloud}}$ indicates the efficiency after the multiple spallation and neutron cloud cuts, and $\varepsilon_{\text{1-ms+likeli+box}}$ denotes the efficiency after the 1-ms, likelihood, and box cuts.

In order to estimate $\varepsilon_{\text{a,li9}}$, ^{9}Li likelihood should be computed considering the ^{9}Li property. In this analysis, we assumed that only dt is unique to the isotope among the spallation variables. Therefore, the ^{9}Li likelihood can be calculated by replacing only dt with the random number based on the ^{9}Li lifetime ($\tau = 0.26$ s).

ROC curve

The Receiver Operating Characteristic(ROC) curve serves as a good indicator to evaluate reduction performance and optimize spallation cuts. For energy levels exceeding 16 MeV, the estimation of ε_{li9} becomes unnecessary, given its end-point energy. Additionally, any spallation remaining rate above 16 MeV is unreliable because the atmospheric event becomes the dominant factor, and the statistical uncertainty tied to the spallation event becomes substantially pronounced.

The ROC curve for the 8–10 MeV events is plotted in Figure 8.15. In the 8–10 MeV region which is the most affected by the spallation event, the spallation remaining rate can be reduced to be $\mathcal{O}(1)\%$. Other distributions are discussed in Chapter B. Furthermore, the correlation with the spallation remaining rates $\varepsilon_{\text{spall}}$ and ε_{li9} is illustrated in Figure 8.16. As a portion of ^{9}Li can be reduced by spallation, the remaining rate of ^{9}Li should have a positive correlation with the remaining rate of spallation. Other distributions are discussed in Chapter B.

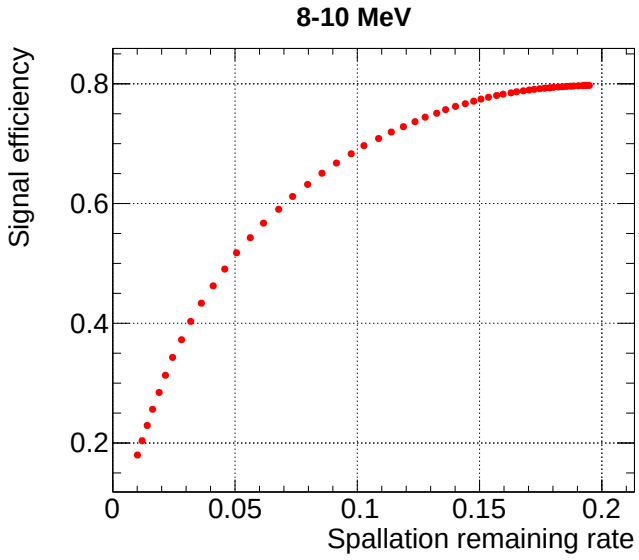

FIGURE 8.15: ROC curve representing the correlation between spallation remaining rate and random event efficiency for 8–10 MeV region.

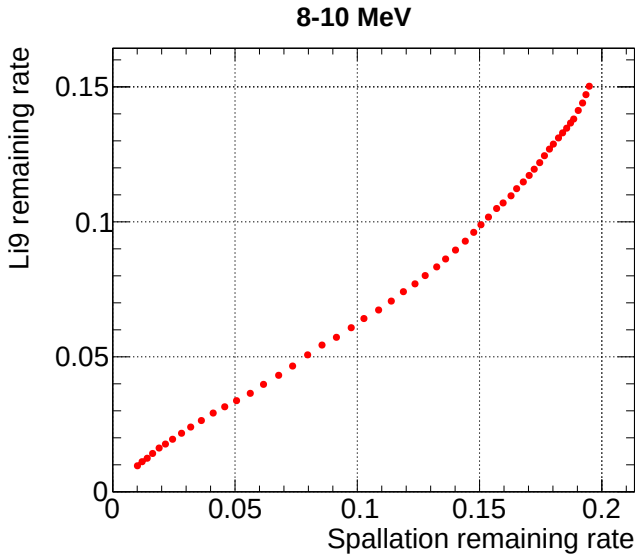

FIGURE 8.16: Correlation between spallation remaining rate and lithium-9 event efficiency for 8–10 MeV region.

Optimization of the spallation cut criteria below 16 MeV energy region focuses on maximizing significance. This is achieved by evaluating the composite of all potential backgrounds and expected signals. The specifics of this optimization process are elaborated upon in the concluding segment of this chapter (Section 8.5.1).

Efficiencies above 16 MeV

Constructing a ROC curve to optimize the likelihood cut for the events above 16 MeV presents a challenge because the limited statistics at this energy region compromise the precision of the PDF. As a result, the threshold for the likelihood cut is set at the point where random efficiency maximizes after the box cut. The random event efficiencies and spallation remaining rates for the cut point with separated energy binning are summarized in Table 8.4.

TABLE 8.4: Summary of the cut efficiency of spallation cut above 16 MeV.

Energy region	Spallation remaining rate	Random event efficiency
$16 - 18$ MeV	0.010	73.4%
$18 - 20$ MeV	< 0.001	81.8%
$20 - 24$ MeV	< 0.001	86.1%

8.3 Third Reduction: Positron Event Selection

For energy regions above 16 MeV, most all spallation byproducts have minimal impact on the results. In this energy range, the dominant background stems from atmospheric neutrino events. An electron-like event triggered by an atmospheric neutrino is virtually indistinguishable from an IBD signal in the absence of neutron tagging. However, events involving muons, pions, and gamma rays — resulting from the interaction of atmospheric neutrinos with Oxygen nuclei — can be differentiated and eliminated based on certain characteristic variables. These events include the Cherenkov angle, the ratio of charge to the number of hits, pion likeness, and additional PMT activities. Additionally, to further reduce residual radioactivity following the fiducial volume cut, a distance-from-the-wall cut, aligned with the reconstructed event direction d_{eff} is applied. Except for d_{eff} cut, the cut criteria and selection efficiencies are derived from signal and atmospheric neutrino MC simulations.

8.3.1 Cherenkov angle

The Cherenkov angle θ_{C} is primarily determined by its mass and velocity. As described in Section 2.1, the Cherenkov angle of electrons is about 42°, whereas heavier particles such as muons and pion exhibit smaller Cherenkov angles. As each of the multiple gamma rays cannot be distinguished in SK, these events should have large Cherenkov angles by mis-reconstruction of the angle, as depicted in Figure 8.17.

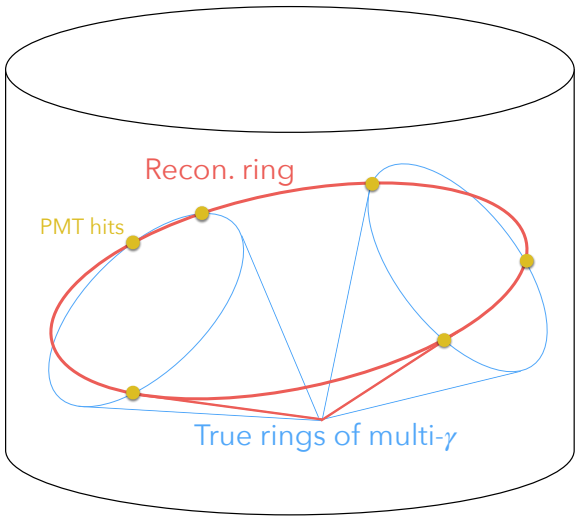

FIGURE 8.17: Mis-reconstruction of the Cherenkov ring owing to the multiple Cherenkov ring.

Consequently, the Cherenkov angle cut emerges as an effective variable for filtering out heavier particles and multiple photon events. Figure 8.18 reveals the distributions of the reconstructed Cherenkov angles. Notably, events resulting from the NC interaction tend to exhibit larger angles. On the other hand, low-energy muons and pions from the CC interaction, peak at an angle lower than the angle of electron signals. For this analysis, the reconstructed angle θ_{C} is restricted within $\theta_{\text{C}} \in [38°, 53°]$.

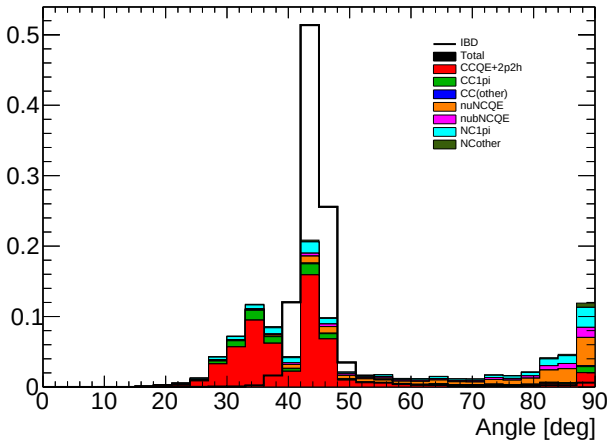

FIGURE 8.18: Distribution of the Cherenkov angle. Color plot describe the type of atmospheric neutrino interaction, and black line denotes the DSNB signal MC assuming the Horiuchi+09 flux model [10]. These are obtained from the events after only passing the first reductions.

8.3.2 Ratio of charge over the number of hits

Energetic muons deposit more charge on a single PMT compared to electrons in the MeV scale. This characteristic can be harnessed to filter out muons by calculating the ratio of charge to the number of hits in a 50 ns time-of-flight subtracted window centered on the primary activity peak. Figure 8.19 displays the $q50/n50$ distribution for the atmospheric and signal MC. Typically, low-energy events are assumed to produce

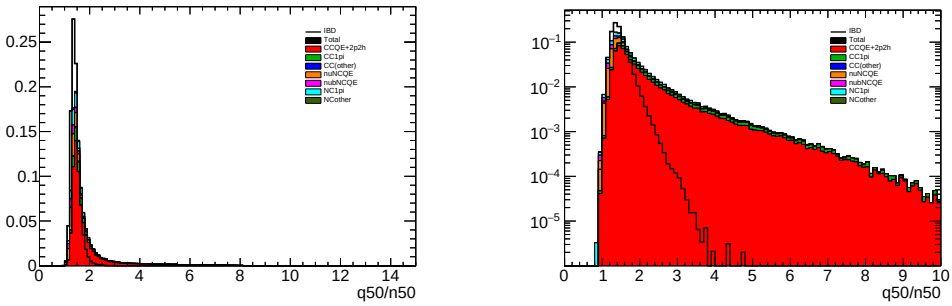

FIGURE 8.19: Distribution of the $q50/n50$ with the linear (left) and logarithmic (right) for the vertical axis. Color plot exhibits the type of atmospheric neutrino interaction, and black line denotes the DSNB signal MC assuming the Horiuchi+09 flux model [10]. These are made from the events after passing only the first reductions.

one photo-electron per PMT. Therefore, a selection criteria of $q50/n50 < 2$ effectively identifies the low-energy positron events.

8.3.3 Pion likeness

Electron rings appear diffused due to their multiple scattering in the tank, whereas pions produce a distinct ring pattern. This difference is exploited by computing

the 'fuzziness' of the ring pattern. To compute this fuzziness, PMT hits in a 15 ns time-of-flight subtracted window centered on the main activity peak are used. The opening angles for all possible three-hit combinations are then calculated using the same method described in Section 4.1.5. Based on the peak of these opening angle distributions θ_0, the fuzziness of the ring pattern is evaluated as follows:

$$\mathcal{L}_{\text{pion}} = \frac{N_{\text{triplets}}(\theta_0 \pm 3^\circ)}{N_{\text{triplets}}(\theta_0 \pm 10^\circ)}, \tag{8.13}$$

where $N_{\text{triplets}}(\theta_0 \pm \theta)$ denotes the number of three-hits combinations within $\theta_0 \pm \theta$. $\mathcal{L}_{\text{pion}}$ tends to be proximate to one for pions. Figure 8.20 displays the $\mathcal{L}_{\text{pion}}$ distribution for the atmospheric MC and signal MC. The contribution from the pion-producing interaction events is seen at the larger $\mathcal{L}_{\text{pion}}$. Therefore, the events require $\mathcal{L}_{\text{pion}} < 0.37$.

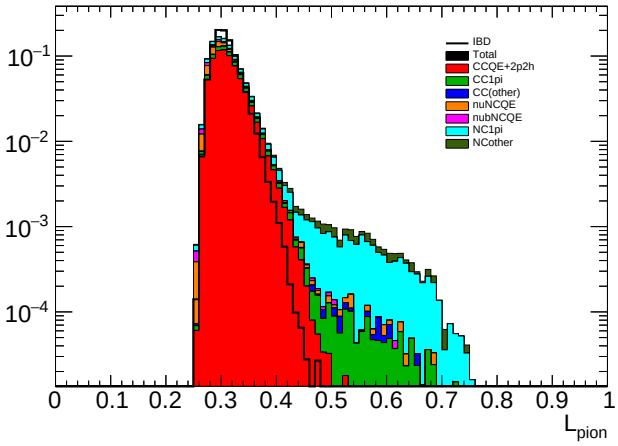

FIGURE 8.20: Distribution of $\mathcal{L}_{\text{pion}}$. Color plot denotes the type of atmospheric neutrino interaction, and black line exhibits the DSNB signal MC assuming the Horiuchi+09 flux model [10]. These are made from the events after passing only the first reductions.

8.3.4 Pre-PMT activities and post-PMT activities

Events arising from visible muon decays to electrons result in two signal activities within the same event trigger window of $[-5, 35]$ μs. Depending on which signal is designated as the primary trigger, in other words, which signal most deposits charge, another activity is seen before or after the triggered time.

To search additional activity before the main peak (pre-activity), the time-of-flight subtracted timing window is scanned to search the hit clusters using a 15 ns window from the start of the event window until 12 ns before the main peak. Figure 8.21 displays the number of maximum hits within 15 ns ($N_{\text{pre}}^{\text{max}}$). Compared with the IBD MC, the $N_{\text{pre}}^{\text{max}}$ should be less than 12 hits.

The primary cause of the additional PMT activities after the main event peak (post-activity) is the decay-e from the muons or pions. To quantify this, the number of additional events from the decay electron $N_{\text{decay-e}}$ is searched utilizing an algorithm used in previous SK analyses to search and reconstruct decay-e from muon or pion [150]. Figure 8.22 presents the count of decay electron-like hit clusters within

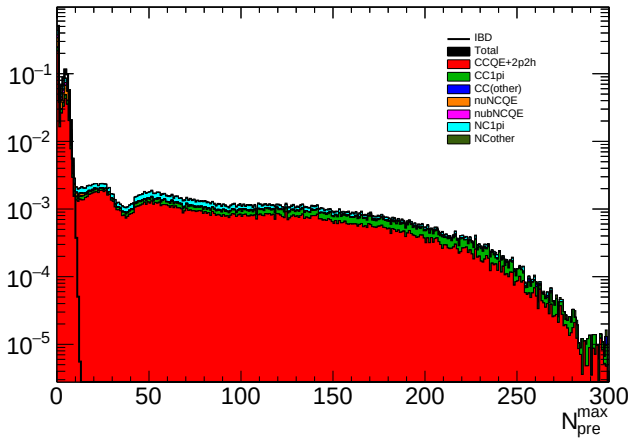

FIGURE 8.21: Distribution of $N_{\text{pre}}^{\text{max}}$. Color plot exhibits the type of atmospheric neutrino interaction. These are made from the events after passing only the first reductions.

the 35 μs of the event window ($N_{\text{decay-e}}$). As there should be no decay electron-like event after IBD, the events are required to be $N_{\text{decay-e}} = 0$.

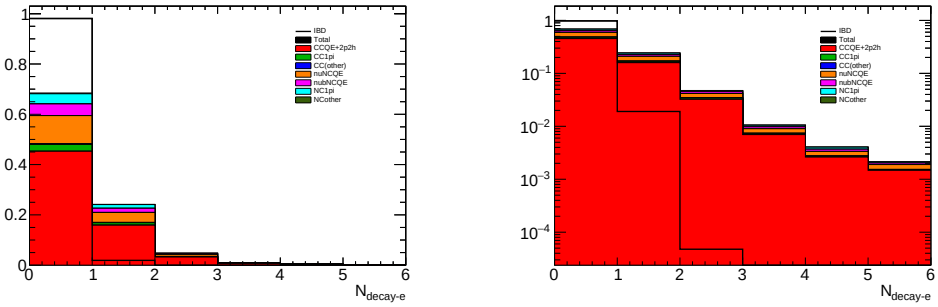

FIGURE 8.22: Distribution of $N_{\text{decay-e}}$ with the linear (left) and logarithmic (right) for the vertical axis. Color plot exhibits the type of atmospheric neutrino interaction. These are made from the events after passing only the first reductions.

8.3.5 Remaining Radioactivity cut using Effective wall distance

The cut using d_{eff} enables the removal of the remaining radioactive events around the wall while maximizing effective volume. Figure 8.23 illustrates the definition of the d_{eff}.

The d_{eff} distribution after the first reduction for the data and signal MC is plotted in Figure 8.24. In the bottom panel of Figure 8.24, a clear excess at a small d_{eff} region in the data over MC can be observed.

The cut criteria are considered by the data and signal MC (Fig. 8.24). The criteria are optimized between 300–500 cm following the same approach as the previous SK-IV search:

$$d_{\text{eff}} > \max[300\text{ cm}, 500\text{ cm} - 50(E_{\text{rec}} - 16\text{ MeV})] \tag{8.14}$$

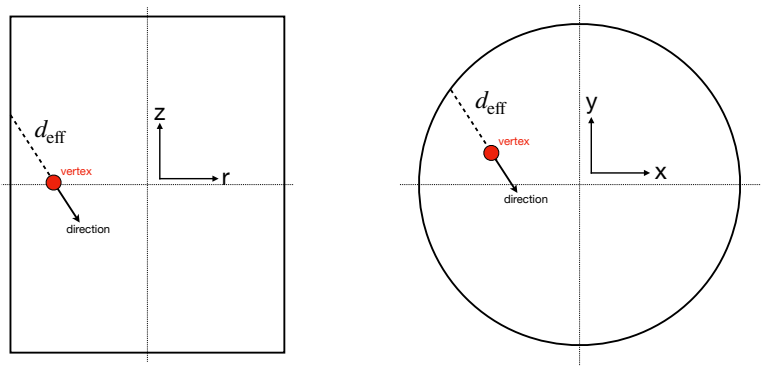

FIGURE 8.23: Illustration of definition of d_{eff}.

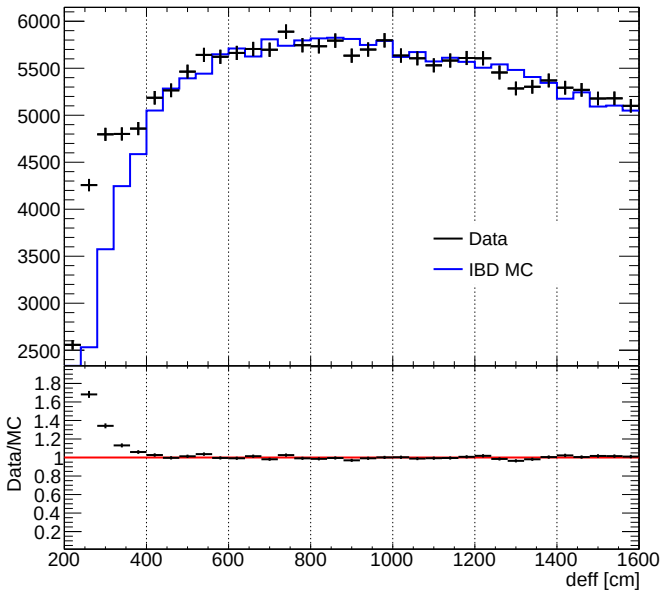

FIGURE 8.24: Comparison of d_{eff} after 1st reduction between data and MC.

Other distributions are exhibited in Chapter C.

8.3.6 Systematic Uncertainty Estimation with LINAC data

The event produced by LINAC is the mono-energetic electron, as detailed in Section 5.3. Consequently, this data can mirror the likeness of the positron signature in the IBD signal at each beam energy. Some of the systematic uncertainties related to the selection of positron-like events can be estimated using LINAC data and MC. The target energy and position of the beam edge of the LINAC data operated in SK-VI are listed in Table 8.5. There are 10 data samples, and the energy is between 6–15 MeV and z-position −12, 0, 12 m. Major systematic uncertainties on the reduction

TABLE 8.5: LINAC positions and target energies used in the evaluation

Target energy [MeV]	x-position [m]	z-position [m]
8.0	−12	12
12.0	−12	12
15.0	−12	12
6.0	−12	0
8.0	−12	0
12.0	−12	0
15.0	−12	0
8.0	−12	−12
12.0	−12	−12
15.0	−12	−12

originate from the variables associated with the Cherenkov light signature, such as the Cherenkov angle, $\mathcal{L}_{\text{pion}}$, and $q50/n50$ cuts.

Cherenkov angle

Figure 8.25 demonstrates the angle distribution for LINAC data and MC. The distribution for data slightly skews toward larger angles. Nevertheless, this skewness only marginally impacts the cut efficiency since the skewed region falls within the selection criteria. A comparison of cut efficiency between data and MC indicates that the largest discrepancy is 1.1% for energies above 12 MeV, with 0.5% for other values. The 1.1% is conservatively assigned as a systematic error. Additional distributions are available in Chapter C.

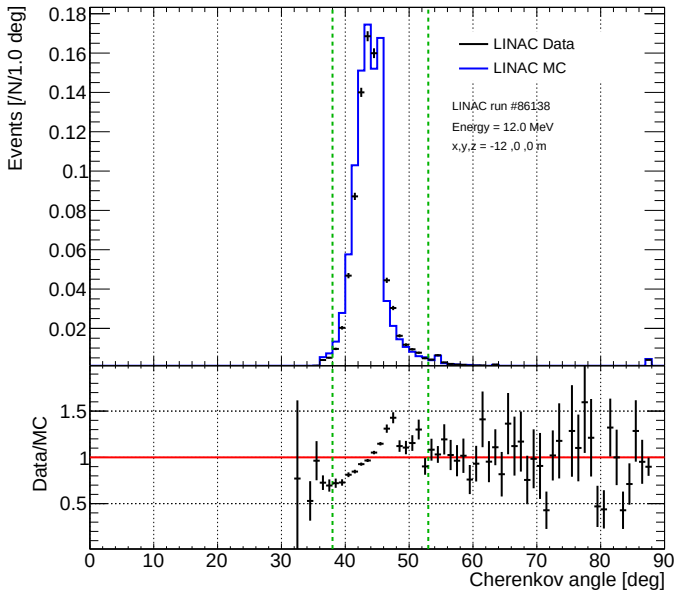

FIGURE 8.25: Comparison of Cherenkov angle distribution between data and MC (top) and the data/MC ratio (bottom) for the E =12 MeV LINAC run.

Pion likeness

Figure 8.26 displays the angle distribution of LINAC data and MC, highlighting discrepancies around the cut criteria. However, these cut criteria are robust enough to select a positron signal, given the low statistics in the vicinity of the cut criteria. The efficiency is therefore not significantly affected by these criteria. Upon comparing the cut efficiency between data and MC, the largest discrepancy noted is 1.1% for those above 12 MeV in Figure 8.26 and 0.6% for others. The 1.1% discrepancy is conservatively assigned as the systematic error. Details on other distributions can be found in Chapter C.

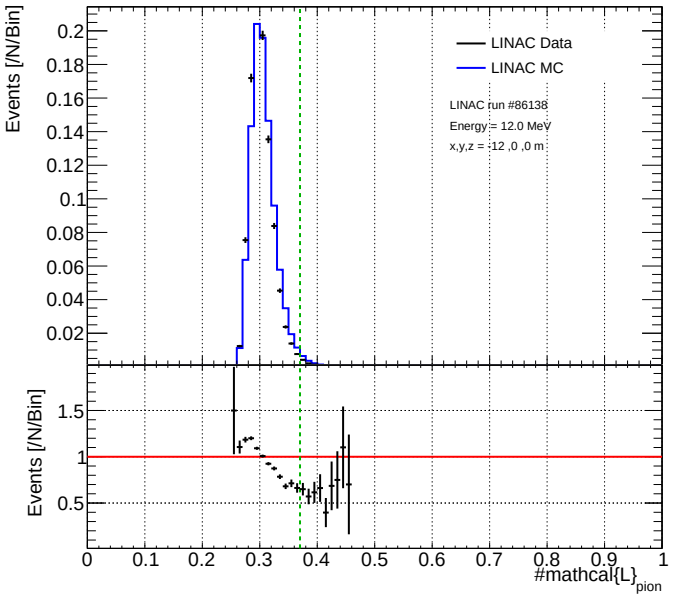

FIGURE 8.26: Comparison of $\mathcal{L}_{\text{pion}}$ distribution between data and MC (top) and the data/MC ratio (bottom) for the E =12 MeV LINAC run.

q50/n50

Figure 8.27 depicts the angle distribution of LINAC data and MC. As portrayed in Figure 8.27, this cut criterion adequately selects the positron signal. By comparing the cut efficiency between data and MC, the largest discrepancy is 0.5%. Thus, 0.5% is assigned as a systematic error. Other distributions are detailed in Chapter C.

8.3.7 Reduction summary

The cut criteria and signal efficiency are summarized in Table 8.6. The total uncertainty on the third cut is estimated by summing the quadrature of these uncertainties to be 1.6%.

8.4 Forth Reduction: Neutron Tagging

The final reduction step involves neutron tagging, utilizing a method nearly identical to that detailed in Section 6 for neutron signal identification. For the IBD interaction, only one neutron is consistently generated. Given their low energy, these neutrons

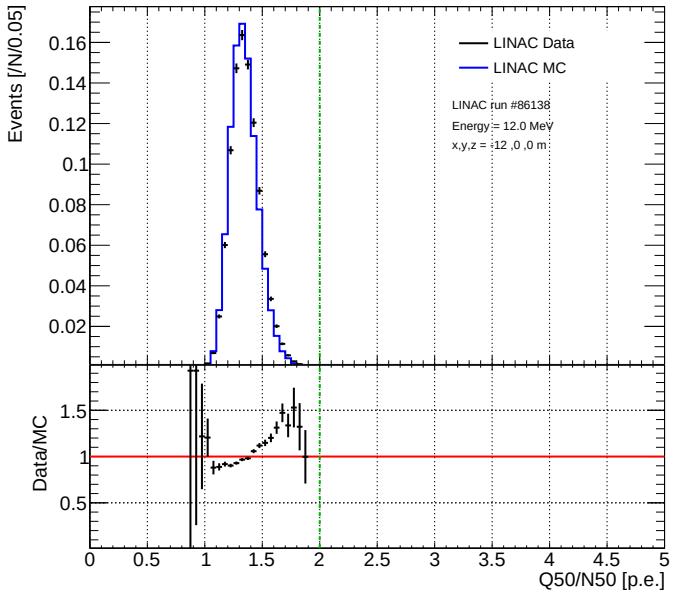

FIGURE 8.27: Comparison of $q50/n50$ distribution between data and MC (top) and the ratio of data/MC (bottom) for the E =12 MeV LINAC run.

TABLE 8.6: Summary of the cut criteria and efficiencies.

Variable	Cut criteria	Efficiency (Syst. unc.)
Cherenkov angle θ_c	$\theta_c \in [38°, 53°]$	94.4 (1.1)%
Charge/Hit ratio $q50/n50$	$q50/n50 < 2.0$	98.6 (0.5)%
Pion likeness $\mathcal{L}_{\text{pion}}$	$\mathcal{L}_{\text{pion}} < 0.37$	98.6 (1.1)%
Pre-PMT activities $N_{\text{pre}}^{\text{max}}$	$N_{\text{pre}}^{\text{max}} < 12$	99.8 (< 0.1)%
Post-PMT activities $N_{\text{decay-e}}$	$N_{\text{decay-e}} < 1$	99.8(< 0.1)%
Effective distance from wall d_{eff}	(Equation 8.14)	95.0 (< 0.1)%

seldom yield secondary neutrons through nuclear interactions. Consequently, this analysis requires a single tagged neutron after the SHE events. This cut powerfully reduces events lacking neutron emissions, including most decay events induced by muon spallation decay and electron scattering events of solar neutrinos. Additionally, it can eliminate some events involving multiple neutron emissions, such as those from atmospheric neutrinos.

8.4.1 Neutron misidentification rate

As described in Section 7.3.1, muon spallation events at SK occur at a rate 10^6 greater than that of SRN. Despite a significant reduction to $\mathcal{O}(1)$% level due to the spallation cut is achieved as discussed in Section 8.2, the remaining $\sim 10^4$ higher rate is problematic for the SRN search. The neutron tagging cut can further diminish spallation events since most spallation isotopes do not produce any neutrons. Thus, in order to make neutron tagging effective, a sufficiently low misidentification rate is needed for neutron selection. This ensures the effective identification of events devoid of neutron

emission, thereby reducing accidental coincidence background events. To reduce accidental coincidence background events from muon spallation to the same level as the SRN, a misidentification rate $\varepsilon_{\mathrm{mis}}$ is required to achieve $\mathcal{O}(10^{-4})$.

To achieve this low rate, parameters such as the distance from the prompt event d_{prompt} and reconstructed energy E_{delayed}, which are the most effective for neutron selection, are investigated. Figure 8.28 depicts the $\varepsilon_{\mathrm{mis}}$ per prompt-event as a function of cut criteria for d_{prompt} and E_{delayed} obtained by the data taken on Jan. 21, 2021, which was the closest day to the AmBe data measurement. The nominal criteria for the AmBe measurement were $(1.8 \pm 0.6) \times 10^{-3}$ per prompt event. Based on this inspection, although changing the d_{prompt} criteria does not alter $\varepsilon_{\mathrm{mis}}$, the effect of varying E_{delayed} can pose a relatively large impact. Consequently, $E_{\mathrm{delayed}} > 3.5$ MeV is required to achieve $\mathcal{O}(10^{-4})$ of $\varepsilon_{\mathrm{mis}}$. Based on the new criteria, $\varepsilon_{\mathrm{mis}}$ is re-evaluated throughout the entire SK-VI period, following the same approach as Section 6.7. Figure 8.29 depicts the time variation of ϵ_{mis} to be $(2.75 \pm 0.15) \times 10^{-4}$ per event.

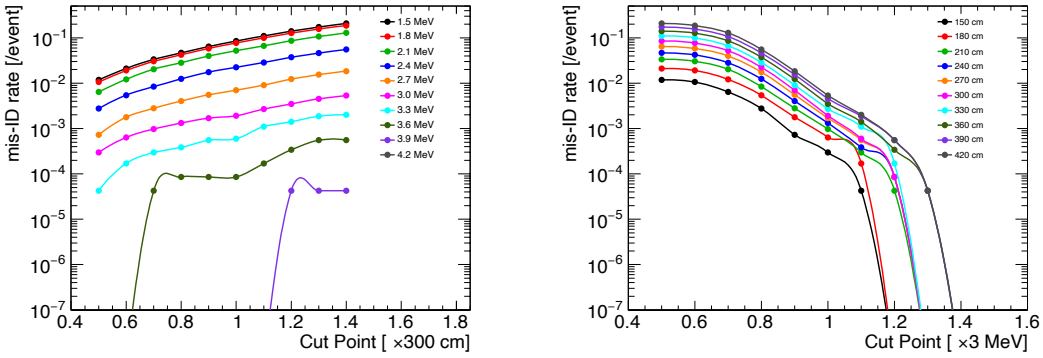

FIGURE 8.28: Distribution of ϵ_{mis} as a function of the cut criteria for the d_{prompt} (left) and the E_{delayed} (right). Color for the left (right) plot exhibits the cut criteria of E_{delayed} (d_{prompt}).

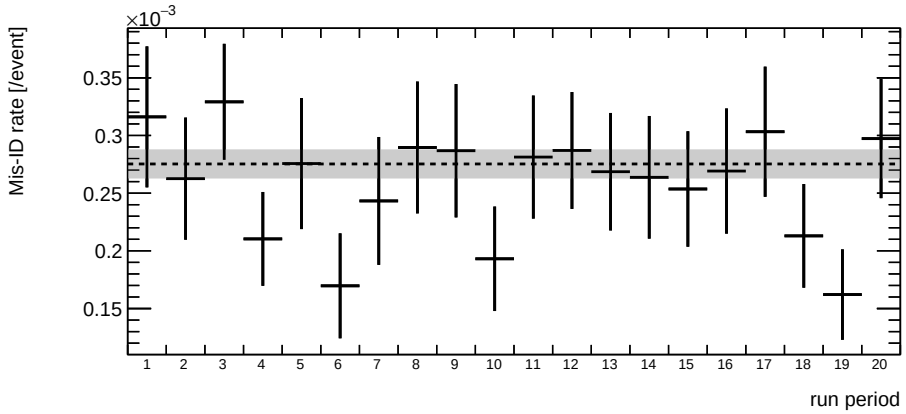

FIGURE 8.29: Time variation of ϵ_{mis}. Black-dotted line depicts the weighted mean value for the entire period, and the gray-shaded region indicates the standard deviation. Horizontal axis represents the same factor as that in Figure 6.7.

8.4.2 Neutron tagging efficiency

Neutron tagging efficiency is re-evaluated by altering the energy threshold for the delayed signal search. Consequently, the efficiency for the Am/Be MC with 0BGO is $35.6 \pm 2.5\%$. The relative systematic uncertainty can be assumed to be the same as that described in Section 6.5.

8.4.3 Tagged neutron multiplicity

Tagged neutron multiplicity is reviewed from the signal MC and atmospheric neutrino MC. Figure 8.30 depicts the number of tagged neutrons N_{tagged}, which is definitely 0 or 1 for the signal MC owing to the absence of a secondary neutron because of its low energy. In contrast, the atmospheric neutrinos, especially the NCQE events, tend to contain multiple N_{tagged} due to the subsequent interaction of emitted nucleons. Thus, the neutron tagging reduction requiring $N_{\text{tagged}} = 1$ can power to reduce these atmospheric neutrino background events.

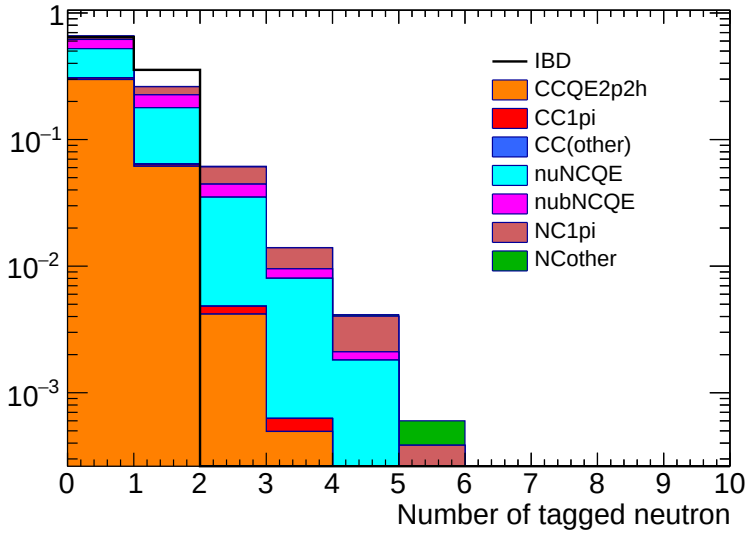

FIGURE 8.30: Distribution of number of tagged neutrons for the IBD MC and atmospheric neutrino MC, after first to third reductions, in the signal energy region. Histograms of atmospheric neutrino MC are stacked with each other.

8.5 Reduction Summary

8.5.1 Optimization of Spallation Cut Criteria

The most dominant background in the absence of neutron tagging stems from spallation. Therefore, the number of accidental coincidence background events largely hinges on the residual spallation events after neutron tagging. The spallation likelihood cut criteria for energies below 16 MeV are refined after the neutron tagging, with the defining criteria being the point where signal significance is maximized. This significance is computed using the approach outlined in [151]. To determine significance, the expected background for all sources is required. Thus, the number of ^{9}Li, reactor

neutrino, and atmospheric neutrino background events are estimated by MC and its flux. In particular, $\varepsilon_{\mathrm{li9}}$ is also put into the computation. The accidental coincidence background is derived by the spallation remaining rate and $\varepsilon_{\mathrm{mis}}$. Thus, the signal efficiency, spallation remaining rate, and $\varepsilon_{\mathrm{li9}}$ of the spallation cut are optimized as summarized in Table 8.7

TABLE 8.7: Summary of the signal efficiencies at each cut stage for energy $E = 8$–16 MeV.

Energy region	Signal efficiency	Spallation remaining rate	$\varepsilon_{\mathrm{li9}}$
$8 < E < 10$ MeV	51.8%	5.1%	3.4%
$10 < E < 12$ MeV	78.2%	6.8%	5.0%
$12 < E < 14$ MeV	86.0%	6.8%	5.9%
$14 < E < 16$ MeV	93.1%	5.3%	5.5%

8.5.2 Signal Efficiency

The signal efficiency is estimated by applying all the above cuts to the signal MC. Figure 8.31 displays the signal efficiency after each cut stage at each 2 MeV bin for reconstructed kinetic energy E_{rec}. The cut was initiated after recording 100% of the events in the first reduction. The efficiency plot displayed in Figure 8.31 refers to the efficiency from the black line.

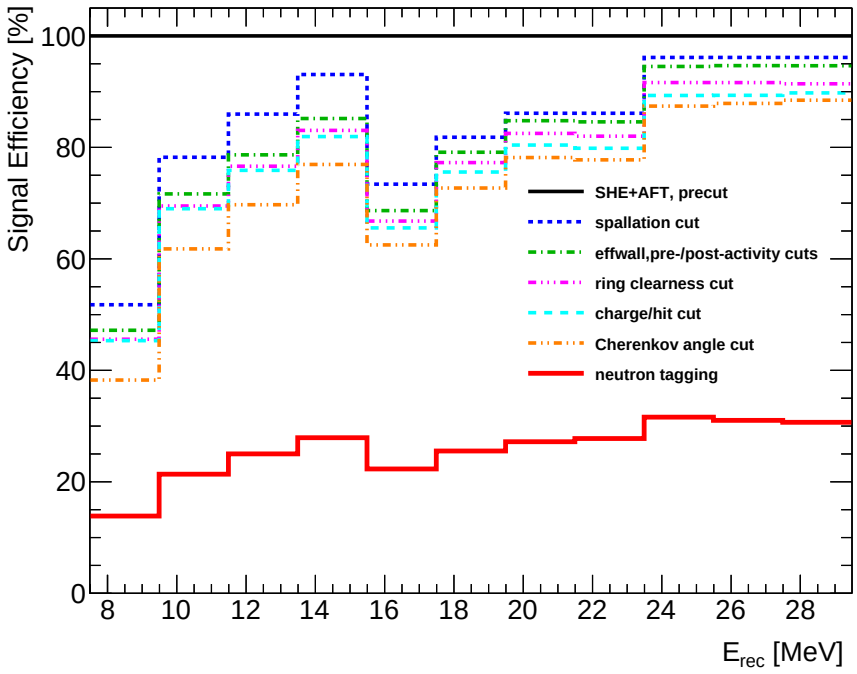

FIGURE 8.31: Signal efficiency as a function of kinetic energy E_{rec}.

Efficiencies for signals at each cut stage are summarized in Tables 8.8, 8.9, and 8.10. After the spallation cut, the signal efficiency dwindles in the lower energy spectrum due to an abundance of spallation events in that range. Nevertheless, since the muon spallation event frequently diminishes at elevated energies, the spallation cut efficiency

rebounds, attributed to reduced owing to the low $\varepsilon_{\mathrm{mis}}$ and accidental coincidence background rates when E_{rec} <15.49 MeV. However, for $E_{\mathrm{rec}} > 15.49$ MeV, the reliability of the spallation likelihood cut wanes due to limited data statistics. Therefore, a stringent box cut is implemented to entirely purge the spallation event, circumventing potential systematic errors from misjudging the spallation background in that region. This rigorous cut criterion results in diminished signal efficiency within the E_{rec} =15.49–23.49 MeV.

TABLE 8.8: Summary of the signal efficiencies at each cut stage for the E_{rec} = 7.49–15.49 MeV.

Energy region [MeV]	7.49–9.49	9.49–11.49	11.49–13.49	13.49–15.49
Spallation cut	0.518	0.782	0.86	0.931
d_{eff} cut	0.912	0.916	0.915	0.915
$N_{\mathrm{pre}}^{\mathrm{max}}$ cut	> 0.999	> 0.999	> 0.999	> 0.999
$N_{\mathrm{decay\text{-}e}}$ cut	> 0.999	> 0.999	> 0.999	> 0.999
$\mathcal{L}_{\mathrm{pion}}$ cut	0.966	0.97	0.974	0.975
$q50/n50$ cut	0.994	0.993	0.99	0.987
Cherenkov angle cut	0.844	0.896	0.919	0.939
Neutron tagging	0.362	0.346	0.359	0.363

TABLE 8.9: Summary of the signal efficiencies at each cut stage for E_{rec} =15.49–23.49 MeV.

Energy region [MeV]	15.49–17.49	17.49–19.49	19.49–21.49	21.49–23.49
Spallation cut	0.734	0.818	0.861	0.861
d_{eff} cut	0.936	0.967	0.985	0.982
$N_{\mathrm{pre}}^{\mathrm{max}}$ cut	> 0.999	> 0.999	> 0.999	> 0.999
$N_{\mathrm{decay\text{-}e}}$ cut	> 0.999	> 0.999	> 0.999	> 0.999
$\mathcal{L}_{\mathrm{pion}}$ cut	0.973	0.977	0.973	0.97
$q50/n50$ cut	0.982	0.978	0.975	0.974
Cherenkov angle cut	0.953	0.962	0.972	0.974
Neutron tagging	0.357	0.351	0.348	0.357

TABLE 8.10: Summary of the signal efficiencies at each cut stage for E_{rec} = 23.49–29.49 MeV.

Energy region [MeV]	23.49–25.49	25.49–27.49	27.49–29.49
Spallation cut	0.961	0.961	0.961
d_{eff} cut	0.983	0.985	0.985
$N_{\mathrm{pre}}^{\mathrm{max}}cut$	> 0.999	> 0.999	> 0.999
$N_{\mathrm{decay\text{-}e}}$ cut	> 0.999	> 0.999	> 0.999
$\mathcal{L}_{\mathrm{pion}}$ cut	0.969	0.968	0.966
$q50/n50$ cut	0.975	0.975	0.982
Cherenkov angle cut	0.979	0.984	0.985
Neutron tagging	0.362	0.353	0.347

Chapter 9

Background Estimation

In this chapter, we evaluate the remaining background events after the reduction for each category. As detailed in Chapter 7, Lithium-9 and reactor neutrino background events are modeled using IBD MC and later weighted by each expected flux. The atmospheric neutrino background is already weighted, being derived directly from the neutrino flux. Conversely, the accidental coincidence background must be derived from the real data.

9.1 Atmospheric neutrinos

The atmospheric neutrino background is deduced using MC as outlined in Section 7.3.2. From now on, events are bifurcated into two categories: NCQE events and other non-NCQE events.

9.1.1 NCQE event

The prevailing atmospheric neutrino background for energies below 16 MeV is primarily due to NCQE interactions. This encompasses the NC-2p2h interaction, where two nucleons are dislodged from the nucleus. The cross-section of the NCQE interaction in SK, as measured by the T2K beam [51], enables the evaluation of the scaling factor for each ν and $\bar{\nu}$ cross-section is evaluated as:

$$f_{\nu\text{-NCQE}} = 0.80 \pm 0.08(\text{stat})^{+0.24}_{-0.18}(\text{syst}), \tag{9.1}$$

$$f_{\bar{\nu}\text{-NCQE}} = 1.11 \pm 0.18(\text{stat})^{+0.29}_{-0.22}(\text{syst}). \tag{9.2}$$

Thus, the number of NCQE events from ν-NCQE and $\bar{\nu}$-NCQE are renormalized by 0.80 for ν and 1.11 for $\bar{\nu}$, respectively.

Systematic uncertainties related to the NCQE-like events can be split into pre- and post-neutrino interactions in SK. The pre-interaction uncertainties are sourced from:

- Atmospheric neutrino flux and spectrum shape.
- NCQE-like interaction cross-section.

In contrast, post-interaction uncertainties arise from:

- Neutron-related aspects.
- Observed event spectrum shape.

Neutrino flux and flux shape

Flux uncertainty originates from the absolute uncertainty and the flux shape variance between atmospheric neutrinos and the T2K neutrino beam (since the cross-section uses the scale of the T2K neutrino beam). The former is approximated at 15%, as per references [33, 29]. The latter is deduced by determining the ratio of flux-averaged events between the T2K beam and atmospheric neutrino fluxes, denoted as R^i_ν and $R^i_{\bar{\nu}}$, for various cross-section models i:

$$R^i_\nu = \frac{\int \phi^{\mathrm{T2K}}_\nu \sigma^i_{\nu\text{-NCQE}} dE_\nu}{\int \phi^{\mathrm{ATM}}_\nu \sigma^i_{\nu\text{-NCQE}} dE_\nu}, \tag{9.3}$$

$$R^i_{\bar{\nu}} = \frac{\int \phi^{\mathrm{T2K}}_{\bar{\nu}} \sigma^i_{\bar{\nu}\text{-NCQE}} dE_\nu}{\int \phi^{\mathrm{ATM}}_{\bar{\nu}} \sigma^i_{\bar{\nu}\text{-NCQE}} dE_\nu}, \tag{9.4}$$

where the ϕ^{T2K}_ν ($\phi^{\mathrm{T2K}}_{\bar{\nu}}$) denotes the ν ($\bar{\nu}$) neutrino flux of the T2K beam, ϕ^{ATM}_ν ($\phi^{\mathrm{ATM}}_{\bar{\nu}}$) indicates the ν ($\bar{\nu}$) neutrino flux of the atmospheric neutrinos, $\sigma^i_{\nu\text{-NCQE}}$ ($\sigma^i_{\bar{\nu}\text{-NCQE}}$) represents the ν ($\bar{\nu}$) cross-sections on oxygen from model i, respectively. In this analysis, seven cross-section models such as Spectral Function (SF) [152, 153], Relativistic Mean Field (RMF) [154], SuperScaling (SUSA) [155], Relativistic Green Function (RGF) with two types of the functional forms (EDAI, Democratic) [154, 156], and Relativistic Wave Impulse Approximation (RPWIA) [154], as depicted in Figure 9.1, are investigated to extract uncertainty. The maximum difference of all models for each R^i_ν and $R^i_{\bar{\nu}}$ are assigned as systematic errors, which is set to 7%.

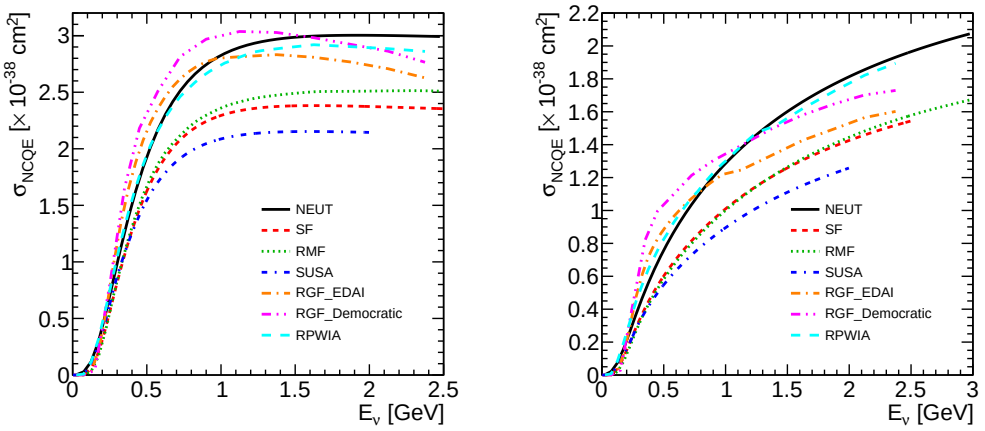

FIGURE 9.1: Total cross-section for neutrino (left) and antineutrino (right) for $^{16}\mathrm{O}(\nu, \nu'\mathrm{N})$ interaction.

Cross-section

The systematic uncertainty before interaction comes from the neutrino interaction cross-section and flux. The cross-section uncertainty is extracted from the scaling factor of the T2K measurement, which is set to 44%.

Neutron tagging efficiency and neutron multiplicity

After neutrino interaction, some uncertainties remain at the detector. Neutrons originating from the NCQE interaction and following secondary interaction are important for the SRN search as neutron tagging is utilized. Thus, the uncertainty related to the neutron, such as the neutron tagging efficiency and the neutron multiplicity at the final state, should be considered. Figure 9.2 displays the averaged tagged neutron multiplicity as a function of reconstructed four-dimension momentum Q^2, measured by the T2K experiment with the CC-dominant samples [50]. These are separately obtained for ν-mode (FHC) and $\bar{\nu}$-mode (RHC). The ratio of the predicted and observed tagged neutrons multiplicity is summarized in Table 9.1. The values in Table 9.1 exhibit combined multiplicity for ν and $\bar{\nu}$, which is calculated by $N_{\rm obs}^{\rm T2K} = N_{\rm obs}^{\rm FHC} + N_{\rm obs}^{\rm RHC}$ and $N_{\rm pred}^{\rm T2K} = N_{\rm pred}^{\rm FHC} + N_{\rm pred}^{\rm RHC}$. Moreover, Figure 9.3 illustrates the number of tagged neutrons of atmospheric neutrino MC for each Q^2 region. Assuming the multiplicity for the atmospheric neutrino MC is also higher than the actual data, which is analogous with the fact of T2K, the corrected multiplicity that should reproduce the data can be evaluated as

$$N_{\rm data}^{\rm atm} = N_{\rm MC}^{\rm atm} \times N_{\rm obs}^{\rm T2K}/N_{\rm pred}^{\rm T2K}, \tag{9.5}$$

where $N_{\rm data}^{\rm atm}$ denotes the expected mean tagged neutron multiplicity of the atmospheric neutrino data, and $N_{\rm MC}^{\rm atm}$ denotes that of the atmospheric neutrino MC. The uncertainty is estimated by moving the number of tagged neutrons for a given event in Figure 9.3 to a lower multiplicity bin. The probability of shifting one lower multiplicity bin is defined as $\epsilon_{\rm trans}$. The best $\epsilon_{\rm trans}$ is determined to correspond to the mean multiplicity to $N_{\rm data}^{\rm atm}$ by varying $\epsilon_{\rm trans}$. Subsequently, after smearing the neutron multiplicity, the variation of $N_{\rm tagged} = 1$ bin is calculated. The maximum variance in all Q^2 regions is assigned to the systematic errors, set to 30% for both the ν and $\bar{\nu}$.

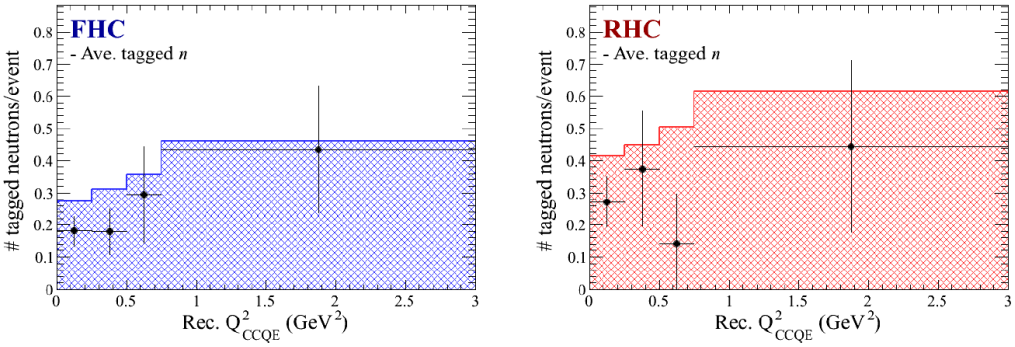

FIGURE 9.2: Average of the number of tagged neutrons in the T2K CC-dominant samples, as a function of reconstructed Q^2, for FHC (left) and RHC (right). Plots are taken from [41], and the original work was done by [50].

Spectrum shape of the observed event

Knocked-out nucleon from NCQE interaction causes subsequent secondary interaction in the water, as depicted in Figure 9.4. NCQE spectrum shapes highly rely on the secondary interaction because the gamma rays from both primary and secondary

TABLE 9.1: Ratio of the number of observed neutrons $N_{\text{obs}}^{\text{T2K}}$ over the predicted by MC $N_{\text{pred}}^{\text{T2K}}$ in each Q^2 region.

Q^2 region	$N_{\text{obs}}/N_{\text{pred}}$
0.00–0.25 GeV^2	0.65
0.25–0.50 GeV^2	0.72
0.50–0.75 GeV^2	0.51
0.75–3.00 GeV^2	0.82

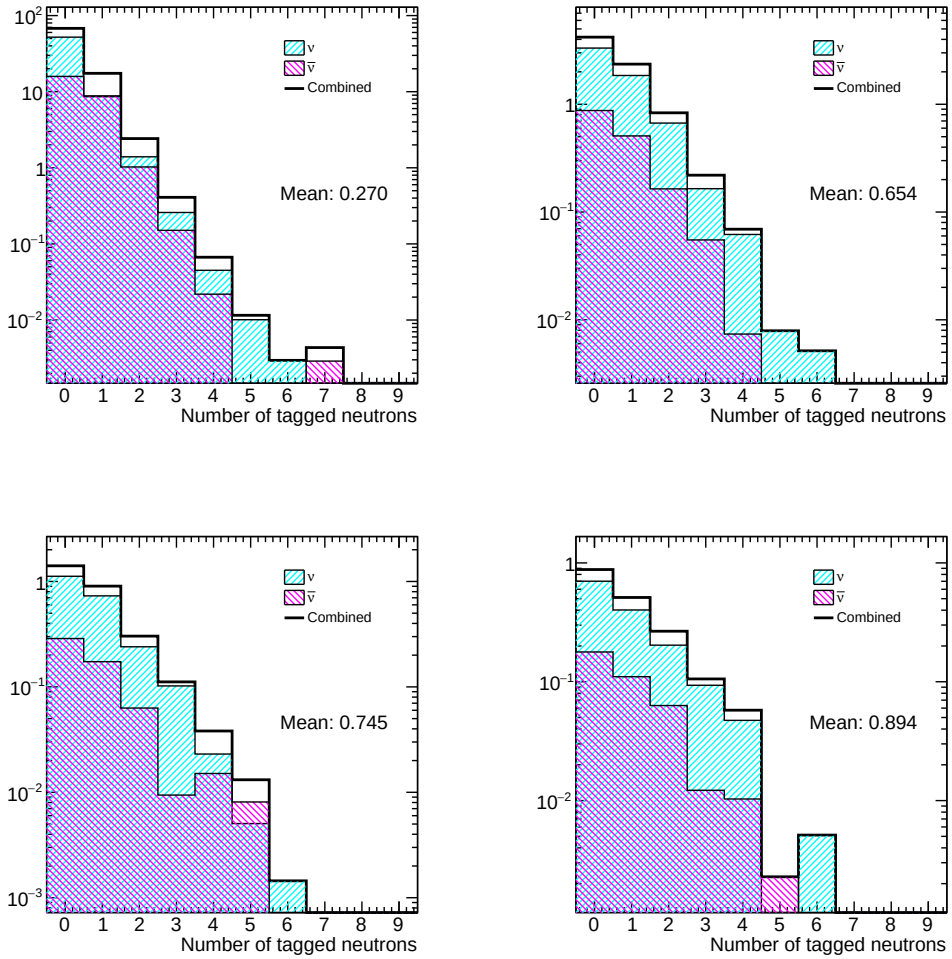

FIGURE 9.3: Neutron multiplicity distribution for $Q^2 < 0.25$ GeV^2 (upper left), $Q^2 = 0.25$–0.5 GeV^2 (upper right), $Q^2 = 0.5$–$0.0.75$ GeV^2 (bottom left), and $Q^2 = 0.75$–3.0 GeV^2.

interactions, caused within the nano sec-scale, are considered one event in SK. These de-excited gamma rays have a typical energy range within 6–8 MeV [157].

The recent T2K NCQE cross-section measurement highlighted a distortion in the reconstructed Cherenkov angle distribution of the measured data relative to the MC for the reconstructed kinetic energy range of $\in [7.49, 29.49]$ MeV, as depicted in Figure 9.5. Notably, within the signal θ_{C} region for this study, specifically $\theta_{\text{C}} \in [38°, 53°]$, the FHC sample data exceeded the MC predictions. However, the actual

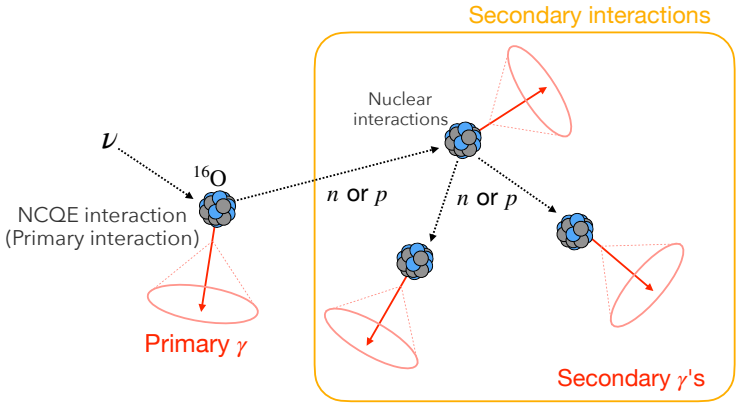

FIGURE 9.4: Illustration of the NCQE interaction and subsequent nuclear interactions.

data falls short of the MC for larger angle regions, which are likely dominated by multiple gamma-ray events from NCQE interactions. This discrepancy underscores potential modeling inaccuracies for secondary interactions and gamma-ray emissions. Therefore, the uncertainty stemming from the spectrum shape inaccuracies should be considered.

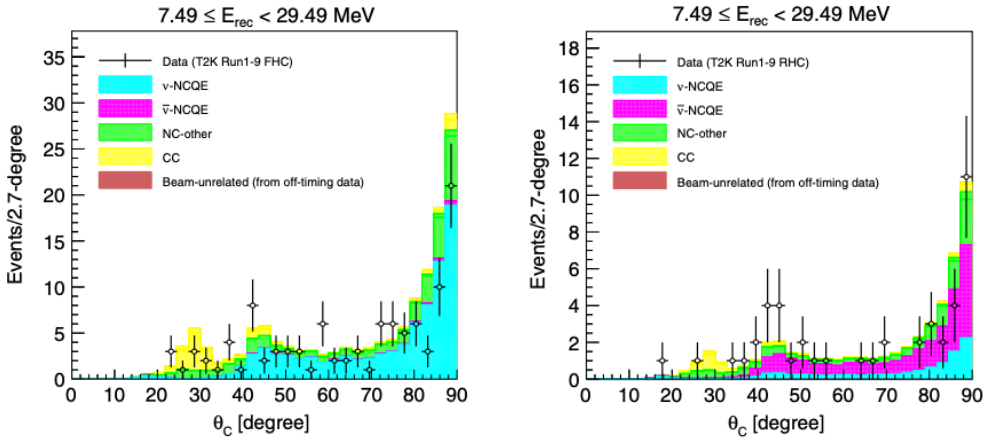

FIGURE 9.5: Reconstructed Cherenkov angle distribution in the T2K FHC (left) and RHC (right) measurements. These plots are recited from [51].

Because the energy spectrum in multiple gamma-ray regions for Cherenkov angle distribution is profoundly model-dependent, straightforward scaling for this domain is challenging when estimating systematic uncertainty. To address this, an energy spectrum is smeared using a pseudo-Gaussian distribution with an energy-dependent standard deviation $\sigma(E_{\mathrm{rec}})$. By employing this method, a new effective spectrum $\mathcal{S}'(E_{\mathrm{rec}})$ is obtained from the simulated atmospheric NC event spectrum $\mathcal{S}(E_{\mathrm{rec}})$ as follows:

$$\mathcal{S}'(E_{\mathrm{rec}}) = \mathcal{N} \int \mathcal{S}(E) \times \exp\left[-\frac{(E - E_{\mathrm{rec}})^2}{2\sigma(E)^2}\right] dE, \tag{9.6}$$

where $\mathcal{N}$ denotes the overall normalization of the pseudo-Gaussian. In this analysis, the deviation $\sigma(E)$ was determined to 3 MeV with reference to [20], sufficient to cover the discrepancy about θ_C of the T2K result. Systematic uncertainty is gauged by reweighting the NCQE atmospheric MC after the third cut, using reweighting factors ε_ν and $\varepsilon_{\bar{\nu}}$, defined as follows:

$$\varepsilon_{\nu(\bar{\nu})} = \frac{\mathcal{S}'_{\nu(\bar{\nu})}(E_{\rm rec})}{\mathcal{S}_{\nu(\bar{\nu})}(E_{\rm rec})} \tag{9.7}$$

As the efficiency of the third cut depends on the energy, the $\varepsilon_{\nu(\bar{\nu})}$ is calculated immediately after the first reduction. Figure 9.6 depicts the calculated $\varepsilon_{\nu(\bar{\nu})}$ distribution for each 2 MeV bin. $\varepsilon_{\nu(\bar{\nu})}$ is larger beyond 16 MeV, where the NCQE event with multiple gamma-rays becomes dominant. Moreover, the difference increases with every 2 MeV, which may indicate the effect of NCQE multiple gamma-ray events.

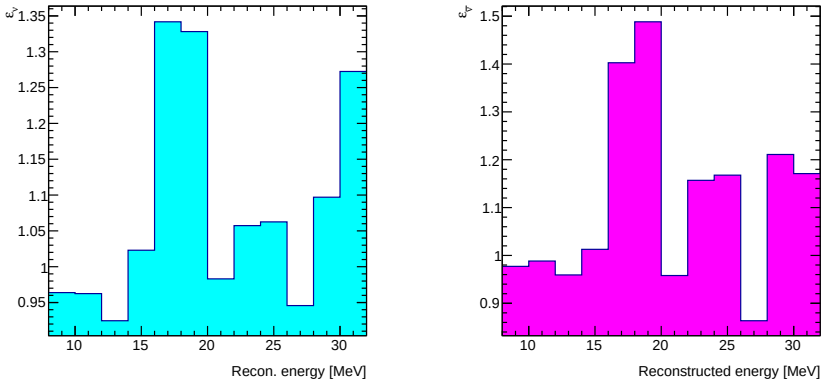

FIGURE 9.6: Weighting factor $\varepsilon_{\nu(\bar{\nu})}$ of neutrino (left) and antineutrino (right), each 2 MeV bin.

The energy-dependent systematic uncertainty $\varepsilon_{\rm sys}(E_{\rm rec})$ is deduced from the relative mean difference between the reweighted and original spectrum after post the cuts as follows:

$$\varepsilon_{\rm sys}(E_{\rm rec}) = \frac{\mathcal{S}_{\nu+\bar{\nu}}(E_{\rm rec}) - \mathcal{S}'_{\nu+\bar{\nu}}(E_{\rm rec})}{\mathcal{S}_{\nu+\bar{\nu}}(E_{\rm rec})}. \tag{9.8}$$

Figure 9.7 displays the $\nu + \bar{\nu}$ combined weighting factor depending on the reconstructed energy, and Figure 9.8 depicts the reconstructed energy spectrum before and after reweighting, after the third reduction. The resultant systematic uncertainty, determined by comparing these two energy distributions, is conservatively set at 37%.

Total systematic uncertainty

The breakdown of systematic uncertainty for the NCQE interaction event is consolidated in Table 9.2. Being mutually exclusive, the total systematic error is calculated by quadratically summing individual uncertainties, amounting to 68%.

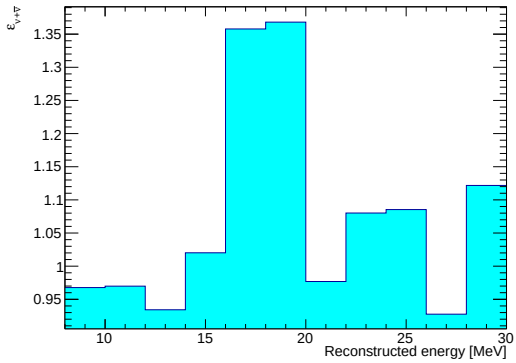

FIGURE 9.7: Weighting factor $\varepsilon_{\nu+\bar{\nu}}$ each 2 MeV bin.

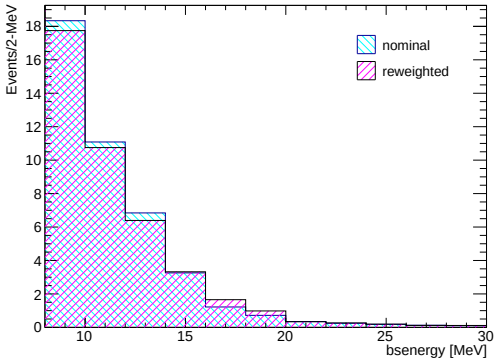

FIGURE 9.8: Energy distribution before and after reweighting by $\varepsilon_{\nu+\bar{\nu}}$, after the third reduction.

TABLE 9.2: Break down the systematic uncertainty on the NCQE interaction events.

T2K cross-section	44%
Atmospheric neutrino flux	15%
Flux difference	7%
Reductions	2%
Neutron tagging efficiency	9%
Neutron multiplicity	30%
Spectral shape	37%
Total	68%

9.1.2 Non-NCQE like interactions

After the third reduction, the dominant background source from non-NCQE interactions in the 8–30 MeV region is the decay electrons/positrons from the decay of invisible muon, which is produced by the ν_μ CC interaction and decay from pions originating from atmospheric neutrino interactions. The shape of the spectrum aligns

with the well-known Michel spectrum from muon decay, reliably gauged using cosmic-ray muon data over many years. While significant systematic uncertainty exists for heavy particle production rates, such as muon, pion, and neutrons, these only impact the scaling of the Michel spectrum. Thus, the number of non-NCQE-like events is estimated by comparing the spectrum in the side-band region of 30–80 MeV between observed data and MC before neutron tagging. The scaling factor is determined to the minimum χ^2 value, estimated to be 0.846. Figure 9.9 illustrates the energy spectrum for the data and MC before and after scaling.

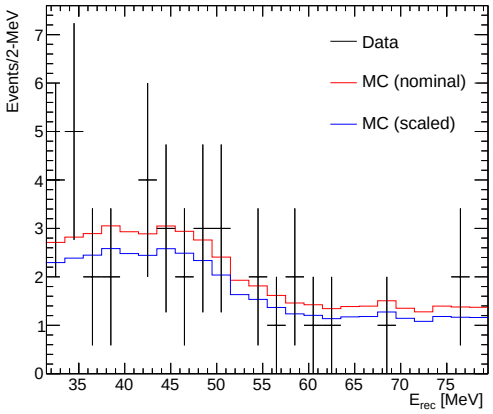

FIGURE 9.9: Energy spectrum in the side-band region of 31.49–79.49 MeV for the reconstructed kinetic energy.

Figure 9.10 displays χ^2 distribution as a function of the scaling factor. All uncertainties associated with the non-NCQE events, except for the neutron tagging and neutron multiplicity, are contained in the statistical uncertainty for the scaling factor tuning, which is 17% by the 1σ regions of χ^2 distribution. Upon considering the

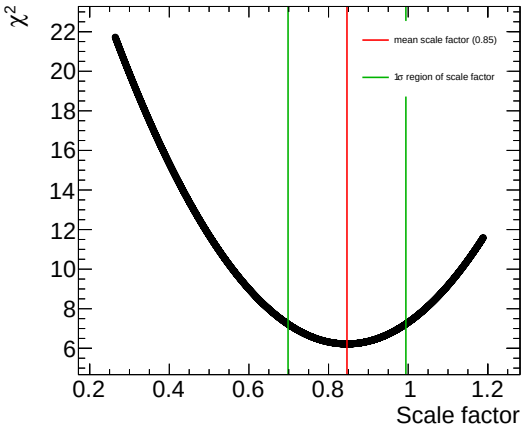

FIGURE 9.10: χ^2 distribution as a function of the scaling factor.

neutron-related uncertainty, such as the neutron multiplicity and tagging efficiency,

the total uncertainty associated with the non-NCQE interaction is estimated to be 36%.

9.2 Lithium-9

The number of remaining ^{9}Li events ($B_{^9\mathrm{Li}}$) can be estimated as follows:

$$\begin{aligned} B_{^9\mathrm{Li}} =& R_{^9\mathrm{Li}} \times T_{\mathrm{live}} \times 22.5 \\ & \times \mathrm{Br}[^9\mathrm{Li} \to \beta + n] \times f_{\mathrm{window}} \times \epsilon_{\mathrm{reduc}}, \end{aligned} \tag{9.9}$$

where the $R_{^9\mathrm{Li}}$ denotes the production rate of ^{9}Li by spallation, T_{live} denotes the live time of this measurement (552.2 days), $\mathrm{Br}[^9\mathrm{Li} \to \beta + n]$ indicates the branching fraction for the β+n decay of ^{9}Li, f_{window} indicates the fraction of the energy spectrum for ^{9}Li event above the search energy threshold, and $\epsilon_{\mathrm{reduc}}$ represents the reduction efficiency.

The two types of uncertainty on the ^{9}Li are assumed in this analysis; one is based on the production rate, and the other is from the reduction efficiency. The production rate of ^{9}Li is estimated to be $0.86 \pm 0.12\,(\mathrm{stat.}) \pm 0.15\,(\mathrm{sys.})$ kton$^{-1} \cdot$ day^{-1}, by [158], and this value is used in this analysis. This estimation results in 22% uncertainty in total.

The ^{9}Li efficiency is evaluated by assuming that only the dt is isotope dependent, as discussed in Section 8.2.6. This is caused by the absence of the accurate spallation MC for the SK. However, the assumption is approximate and probably incorrect. Thus, the uncertainty depending on that assumption is conservatively assigned to be 50%, similar to the previous SK-IV analysis. Therefore, the other uncertainty based on the reduction efficiency primarily emerges from neutron tagging, which is 10% in total. The total uncertainty on the $B_{^9\mathrm{Li}}$ is assigned to be 55%.

9.3 Reactor Neutrinos

The reactor neutrino event is estimated by scaling the IBD signal MC to the reactor neutrino spectrum. This background forms the lowest energy in all considered backgrounds, and these populate only the lowest energy bin. Conservatively, the systematic uncertainty for the reactor neutrino backgrounds is assigned to 100%. Owing to the low rate of this background in the signal energy region, the effect is quite small for the result.

9.4 Accidental Fake background

The remaining accidental fake coincidence background B_{acc} can be calculated as:

$$B_{\mathrm{acc}} = \varepsilon_{\mathrm{mis}} \times N^{\mathrm{data}}_{\text{pre-ntag}}, \tag{9.10}$$

where the $\varepsilon_{\mathrm{mis}}$ denotes the misidentification rate at the neutron selection, and $N^{\mathrm{data}}_{\text{pre-ntag}}$ indicates the remaining data event after the first to the third reduction, described in Section 8. The contribution from the multiple misidentifications can be ignored at this instant because the effect can obviously be ignored. The uncertainty, depending on the estimation from the $\varepsilon_{\mathrm{mis}}$, is estimated as 5%.

9.5 Expected Background Spectrum

Figure 9.11 displays the estimated background across the entire SK-VI period with 552.2 days of live time. To compensate for the small statistic of SK-VI, the energy bin is merged based on the type of background, such as 7.49–9.49 MeV, 9.49–11.49 MeV, 11.49–15.49 MeV, 15.49–23.49 MeV, and 23.49–29.49 MeV. Figure 9.12 exhibits the bin-merged background energy spectrum, wherein the first and second bins are not merged because of their relatively large statistic. The third bin is the highest energy bin among including ^{9}Li background. The almost NCQE background is contained below the fourth bin. The final bin is dominated by an atmospheric non-NCQE background. The breakdown of each background and these systematic errors for each merged bin is depicted in Table 9.3.

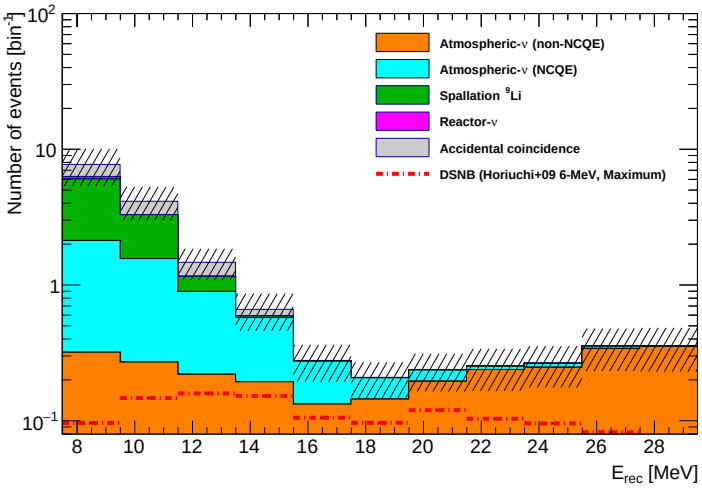

FIGURE 9.11: Expected background spectrum with these total systematic uncertainties (hatched) for each 2 MeV bin. Dotted-dashed red line denotes the expected SRN signal based on [10].

TABLE 9.3: Breakdown of the expected background events and these systematic errors at each merged bin.

E_{rec} bin [MeV]	7.49–9.49	9.49–11.49	11.49–15.49	15.49–23.49	23.49–29.49
Non-NCQE	0.32 ± 0.12	0.27 ± 0.10	0.41 ± 0.15	0.71 ± 0.26	0.94 ± 0.34
NCQE	1.81 ± 0.00	1.30 ± 1.74	1.06 ± 1.25	0.26 ± 1.02	0.03 ± 0.25
^{9}Li	3.92 ± 2.16	1.73 ± 0.95	0.28 ± 0.15	0.00 ± 0.00	0.00 ± 0.00
Reactor	0.25 ± 0.25	0.01 ± 0.01	0.00 ± 0.00	0.00 ± 0.00	0.00 ± 0.00
Accidental	1.43 ± 0.07	0.83 ± 0.04	0.38 ± 0.02	0.01 ± 0.00	0.00 ± 0.00
Total	7.73 ± 2.35	4.14 ± 1.15	2.13 ± 0.57	0.98 ± 0.29	0.98 ± 0.34

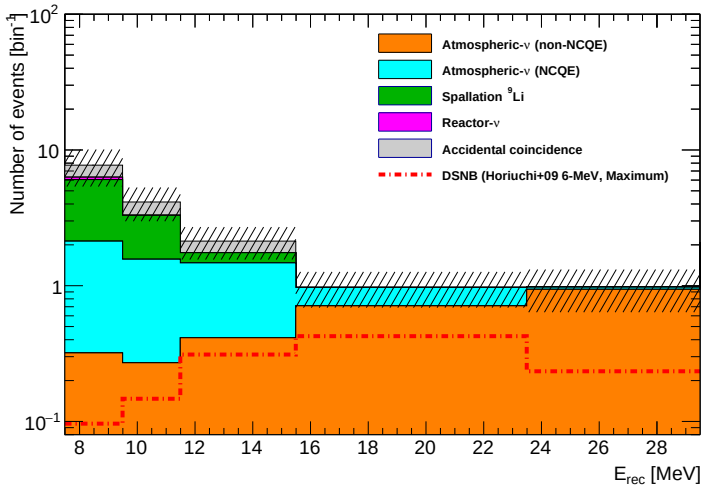

FIGURE 9.12: Expected background spectrum with these total systematic uncertainty (hatched) for each merged bin (hatched). Dotted-dashed red line portrays the expected SRN signal based on [10].

Chapter 10

Results

10.1 Search Result

All reduction criteria were applied to the data from 552.2 days of the SK-VI operation. The reduction efficiency for each energy bin is summarized in Table 10.1.

TABLE 10.1: Breakdown the event reduction and signal efficiency at each merged bin.

E_{rec} bin	7.49–9.49	9.49–11.49	11.49–15.49	15.49–23.49	23.49–29.49
First reduction	204328	58993	18292	630	54
Spallation cut	13352	5778	1982	115	47
d_{eff} cut	9581	4606	1628	101	47
$N_{\mathrm{pre}}^{\mathrm{max}}$	9521	4582	1613	96	43
$N_{\mathrm{dacay\text{-}e}}$	9492	4563	1593	56	14
$\mathcal{L}$	8740	4293	1541	41	8
$q50/n50$ cut	8713	4280	1538	35	8
θ_{c} cut	5003	2924	1334	21	5
Neutron tagging	5	5	3	2	1

After all reductions, 16 events remain in the signal energy region. The energy spectrum for these observed events, alongside the expected background, is presented in Figure 10.1. The error for these observed events is assigned as the square root of the number of events.

To investigate the significance of the observed events (N_{obs}) relative to the expected background events (N_{bkg}) for each bin, a p-value, indicating the probability of obtaining the number of observed events under the assumption that all events are background, is utilized. The p-value across each energy bin is calculated via the toy-MC as follows:

1. Estimate the expected background using a Gaussian probability, adopting the expected mean value and the mean and systematic error as the deviation.

2. Generate the number of events based on a Poisson probability with the earlier deduced background as the mean. This set is one toy MC.

3. Interactively perform the prior step a million times, curating a Poisson-like toy MC.

4. Count the number of toy MC instances exceeding the number of observed events.

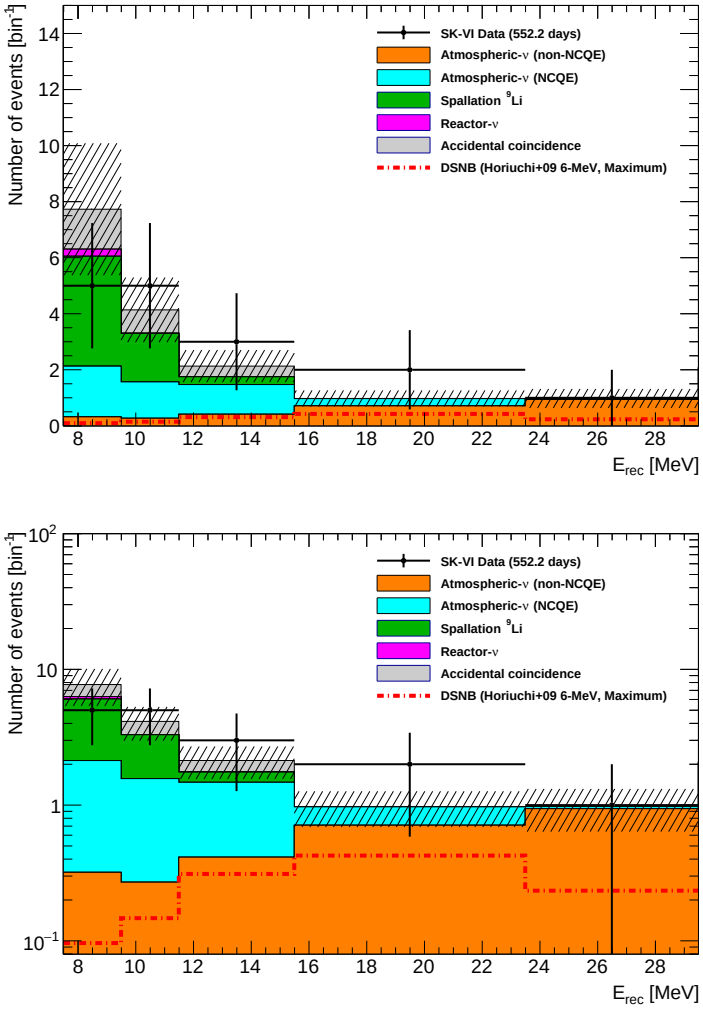

FIGURE 10.1: Observed and expected background spectrum with these total systematic uncertainties (hatched) with linear scale (top) and logarithmic (bottom). The dot-dashed red line shows the expected SRN signal based on [10].

5. The p-value is defined as

$$p\text{-value} = \frac{\text{The number of counts}}{\text{The number of generated toy MC}} \tag{10.1}$$

Figure 10.2 visualizes the derived toy MC distribution and the consequent p-value for each bin. The result of the p-value test were: 80.7% (7.49–9.49 MeV), 39.8% (9.49–11.49 MeV), 35.8% (11.49–15.49 MeV), 25.6% (15.49–23.49 MeV), 60.2% (23.49–29.49 MeV). Specifically, the p-value for the energies above 15.49 MeV, almost released from the NCQE and ^{9}Li background, is 32.6%. For all cases, the p-value surpassed 5%, concluding that no significant excess can exist over the expected background.

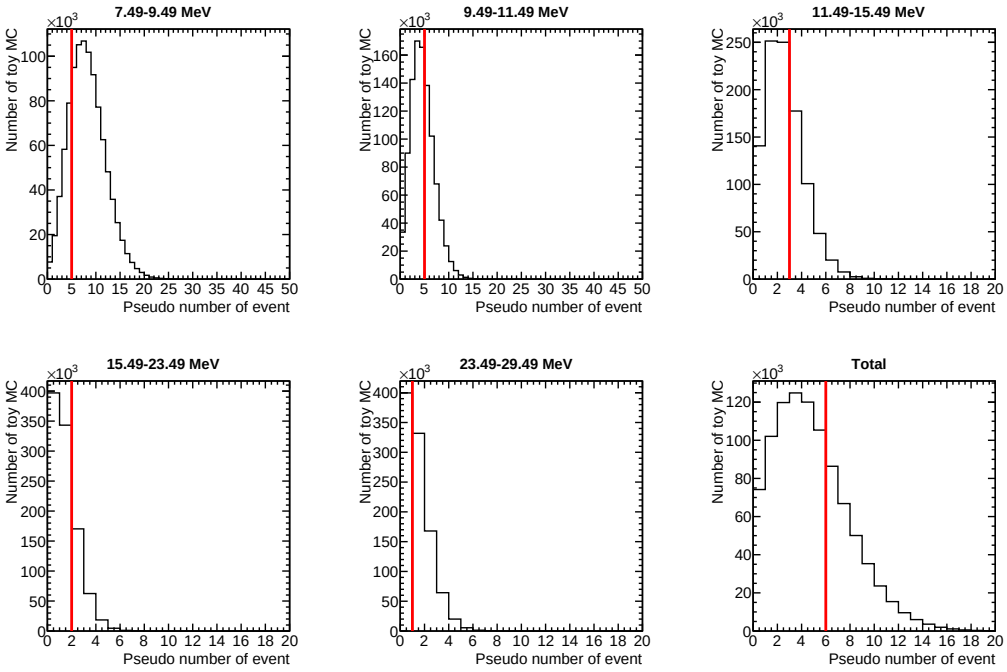

FIGURE 10.2: Toy MC result for calculating the p-value for each energy bin above 11.49 MeV (bottom, right). Red line exhibits the actual observed event in this analysis.

10.2 Upper Limit Extraction

10.2.1 Upper limit on the number of signal events

No significant excess is observed in data over the expected background prediction for all energy bins. Therefore, the upper limit of $\bar{\nu}_e$ flux is extracted in the signal energy region. First, the 90%-confidence level (C.L.) upper limit on the number of signal events $N_{90}^{\rm limit}$ is calculated by operating a pseudo experiment as the following procedure.

1. Number of observed events $N_{\rm obs}^{\rm toy}$ and the expected events $N_{\rm bkg}^{\rm toy}$ in a toy data set are calculated by the Gaussian probability, with random variations of the statistical error on $N_{\rm obs}$ and the systematic error on $N_{\rm bkg}$.

2. The number of signal events $N_{\rm sig}^{\rm toy}$ is calculated by subtracting $N_{\rm obs}^{\rm toy}$ from $N_{\rm bkg}^{\rm toy}$.

3. Make $N_{\rm sig}^{\rm toy}$ distribution by 10^6 times iteration of the prior pseudo test.

4. Calculate $N_{90}^{\rm limit}$ as the number through integration between zero and $N_{\rm sig}$, containing 90% of the integration above zero.

Figure 10.3 exhibits the $N_{\rm sig}$ distribution as the pseudo-experiment results for the 9.49–11.49 MeV bin.

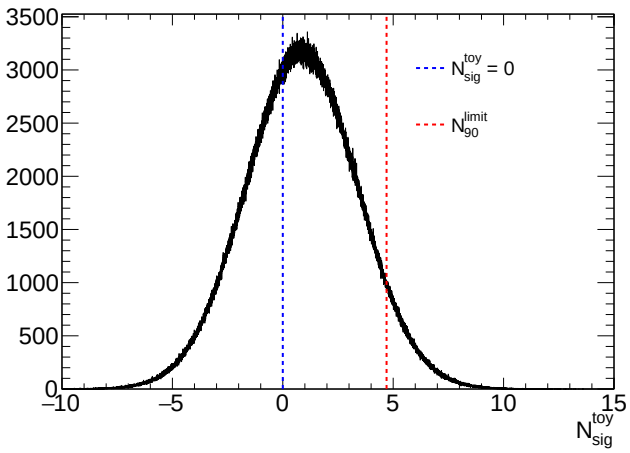

FIGURE 10.3: $N_{\rm sig}$ distribution for $E_{\rm rec}$ = 9.49–11.49 MeV bin as an example of $N_{90}^{\rm limit}$. The region between $N_{\rm sig} = 0$ and $N_{\rm sig} = N_{90}^{\rm limit}$ contains 90% of the total of $N_{\rm sig} > 0$ events.

10.2.2 Flux Upper Limit Calculation

The flux upper limit $\phi_{90}^{\rm limit}$ [$\rm cm^{-2}\,sec^{-1}\,MeV^{-1}$] is calculated based on the following formula:

$$\phi_{90}^{\rm limit} = \frac{N_{90}^{\rm limit}}{\bar{\sigma}_{\rm IBD} \cdot N_p \cdot T \cdot \varepsilon_{\rm sig}}, \tag{10.2}$$

where $\bar{\sigma}_{\rm IBD}$ [$\rm cm^2$] illustrates the averaged cross-section of IBD interaction for the mean neutrino energy (E_ν) for the corresponding energy region, N_p denotes the number of target protons in SK, T [sec] indicates the live-time for SK-VI (552.2 days), and $\varepsilon_{\rm sig}$ denotes the averaged signal efficiency, as indicated in Figure 8.31. E_ν is obtained by the $E_{\rm rec} + 1.8$ MeV for IBD interaction.

To calculate the expected sensitivity $\phi_{90}^{\rm exp}$ [$\rm cm^{-2}\,sec^{-1}\,MeV^{-1}$], $N_{\rm obs}$ in the calculation of $N_{90}^{\rm limit}$ is replaced by $N_{\rm bkg}$.

Figure 10.4 exhibits the observed and expected flux upper limit on the $\bar{\nu}_e$ flux, including certain flux limits estimated by other searches and some theoretical flux predictions (caption of Figure 10.4). These values are also summarized in Table 10.2.

TABLE 10.2: Summary table of upper limits, sensitivity.

Neutrino energy [MeV]	9.29–11.29	11.29–13.29	13.29–17.29	17.29–25.29	25.29–31.29
Live time T	552.2 days				
Number of Target N_p	1.5×10^{33} protons				
$N_{90}^{\rm limit}$	3.94	4.70	3.59	3.09	1.75
$N_{90}^{\rm exp}$	5.99	3.85	2.58	1.69	1.72
$\phi_{90}^{\rm limit}$ [$/\rm cm^2\,/sec\,/MeV$]	32.32	18.21	3.75	0.89	0.32
$\phi_{90}^{\rm exp}$ [$/\rm cm^2\,/sec\,/MeV$]	49.16	14.89	2.70	0.49	0.32

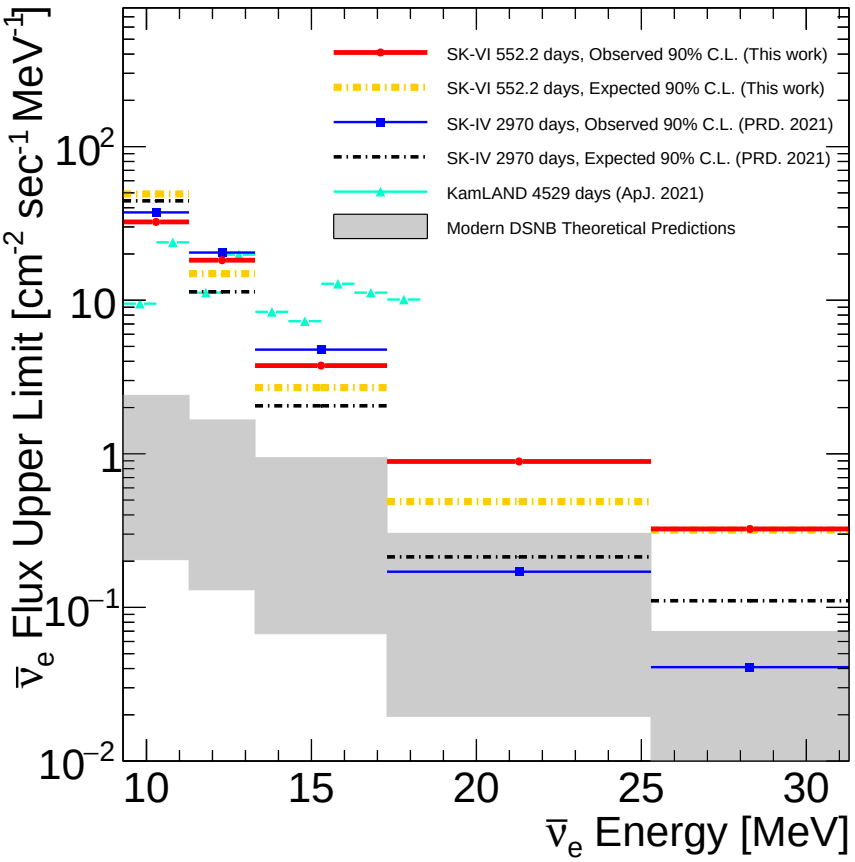

FIGURE 10.4: Upper limits on the $\bar{\nu}_e$ flux. Solid lines denote the observed upper limit for SK-IV (blue), SK-VI (red), and KamLAND (green), respectively. Dot-dashed lines represent the expected sensitivity based on the expected background for SK-IV (black) and SK-VI (yellow). Gray-shaded region represents the range of the modern theoretical expectation. The expectation drawn in the figure includes DSNB flux models [15, 16, 14, 12, 11, 10, 9, 3, 8, 6, 5, 4, 52]. Ando+03 model was updated in [13].

Chapter 11

Discussion and Conclusion

11.1 Future Prospects on the SRN Search

The additional Gd is loaded into the SK tank to achieve the Gd concentration of approximately 0.03% for SK-VII. This process started at the beginning of June 2022 and was completed at the beginning of July 2022. The Gd capture fraction is about 75% for the SK-VII, leading to an anticipated 1.5 times higher neutron tagging efficiency and keeping $\varepsilon_{\mathrm{mis}}$ consistent with SK-VI. Additionally, a machine-learning approach to neutron identification, inspired by previous SK-IV searches, is under development. Current projections suggest that this will enhance neutron tagging efficiency by a factor of 1.2. Moreover, with the complete implementation of AFT trigger improvement discussed in Section 2.4.2, an AFT efficiency $\varepsilon_{\mathrm{AFT}}$ exceeding 99% is expected. Based on considerations of advancements and certain analysis improvements, the expected sensitivity for running SK-VII can be estimated.

The first improvement concerns the NCQE interaction background, predominantly evident below the $E_{\mathrm{rec}} = 15.49$ MeV region. Efforts are underway to reduce this NCQE interaction further. For instance, leveraging machine-learning-based characterization to differentiate the PMT hit patterns of NCQE from IBD interactions could potentially diminish NCQE interaction events [159]. Thus, an assumption is assigned that 30% of NCQE events are removed by additional reduction. Because it is difficult to estimate the effect of neutron tagging with multiple neutron events on the amount of NCQE background, the effect is ignored at this time.

Moreover, the systematic uncertainty on the NCQE event, currently assigned to about 70%, is expected to be reduced by refining the physics model of the detector simulations, validated by external measurement with neutron-oxygen interaction. The dominant uncertainty arises from the spectrum shape originating from the gamma-ray multiplicity. External measurements promise a deeper insight into proton interaction around $\mathcal{O}(10)$ GeV, offering a clearer understanding of the systematic uncertainty associated with atmospheric neutrino flux. These efforts may halve the current uncertainty.

In addition to the NCQE events, ^{9}Li events resulting from the muon spallation are key contributions to the major background in the lowest two energy bins. Most systematic uncertainties associated with the ^{9}Li event stem from the belief that the timing from muon is only an isotope-dependent variable in the spallation cut. In the future, accurate muon spallation MC models will validate the accuracy of this assumption, aiming to reduce uncertainty by half. As estimating the potential reduction in ^{9}Li is challenging, its projected event rate remains unchanged.

As a further improvement, the atmospheric non-NCQE event should be reduced. In this analysis, the non-NCQE event is scaled using the side-band data before neutron tagging. It causes additional systematic uncertainty on the neutron multiplicity.

In addition, given that the current MC displays an augmented neutron signal (Section 9.1.1), more events with one neutron signal are expected. It makes an overestimation of non-NCQE events. In the future, these effects should be reduced by $\sim 60\%$ by scaling from the comparison after neutron tagging. The systematic uncertainty on non-NCQE events, estimated from side-band region fitting uncertainties, is assumed to be reduced by the increasing statistic by $\sim 60\%$.

11.2 Future Sensitivity Calculation

Factoring these conditions, the prospective model-independent sensitivity for the $\bar{\nu}_e$ is derived, following the methodology outlined in Section 10.2. Considering various assumptions, Figure 11.1 visualizes the expected 90% C.L. sensitivity for future SK-Gd operations in the two lowest energy bins. These assumptions, pivotal for sensitivity estimations, are cataloged in Table 11.1. Due to significant contamination from the reactor, ^{9}Li, and accidental background in these bins, which are challenging to mitigate effectively, the sensitivity in these areas is restricted.

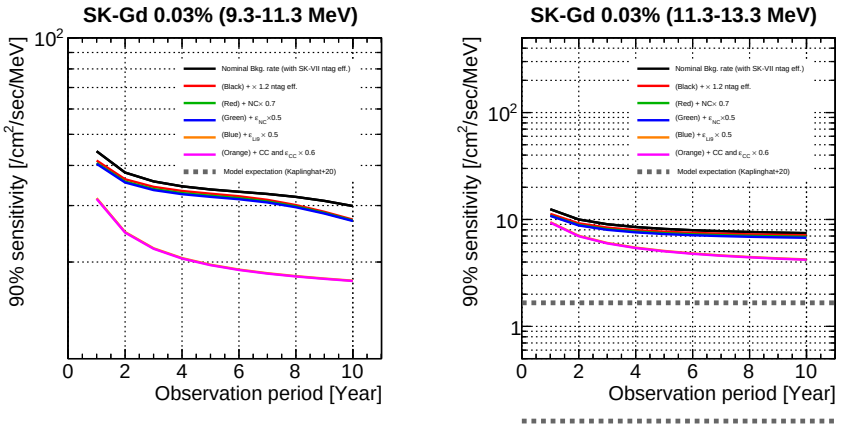

FIGURE 11.1: Expected future sensitivity for 9.3–11.3 MeV (left) and 11.3–13.3 MeV energy bins with various background conditions, such as nominal case (black), and further higher neutron tagging efficiency (red), 70% of NCQE background (green), 50% of the error on the NCQE background (blue), 50% of the error on the ^{9}Li (Orange), 50% of the CCQE background and their error (Magenta). Thick-dotted line denotes the most optimistic theoretical expected flux. In the 9.3–11.3 MeV region, the theoretical expectation is excluded from this figure as it is smaller than the sensitivity.

Conversely, future sensitivities for higher energy bins — 13.3–17.3 MeV, 17.3–25.3 MeV, and 25.3–31.3 MeV — are depicted in Figure 11.2, the optimistic flux models, such as Kaplinghat+00 [14], stand to be validated with 3σ precision through intensified background reductions efforts discussed above section. As events above 17.3 MeV are largely devoid of NCQE and ^{9}Li contamination, the sensitivity fluctuates chiefly based on assumptions regarding neutron tagging efficiency and CCQE backgrounds.

TABLE 11.1: Assumptions for calculating future sensitivity. Titles about color indicate the line color for each panel shown in Figure 11.1.

	Neutron tag. eff.	NC bkg.	NC unc.	^{9}Li unc.	CC bkg. and unc.
(1) Black	×1.5	100%	100%	100%	100%
(2) Red	×1.8	100%	100%	100%	100%
(3) Green	×1.8	70%	100%	100%	100%
(4) Blue	×1.8	70%	50%	100%	100%
(5) Orange	×1.8	70%	50%	50%	100%
(6) Magenta	×1.8	70%	50%	50%	50%

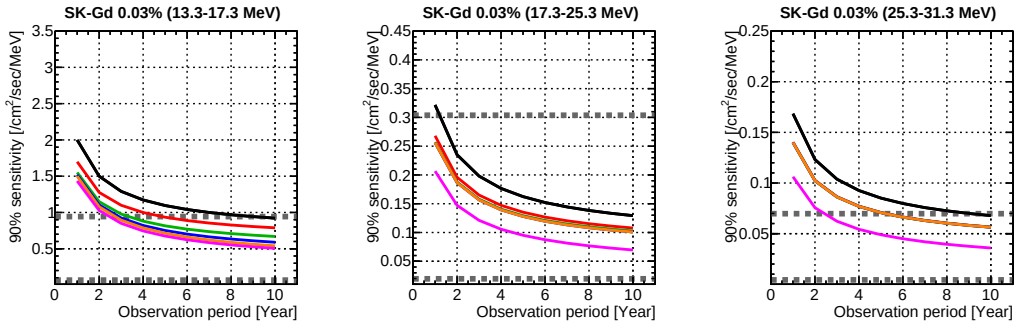

(A) 90% C.L. sensitivity with the same assumption as Figure 11.1.

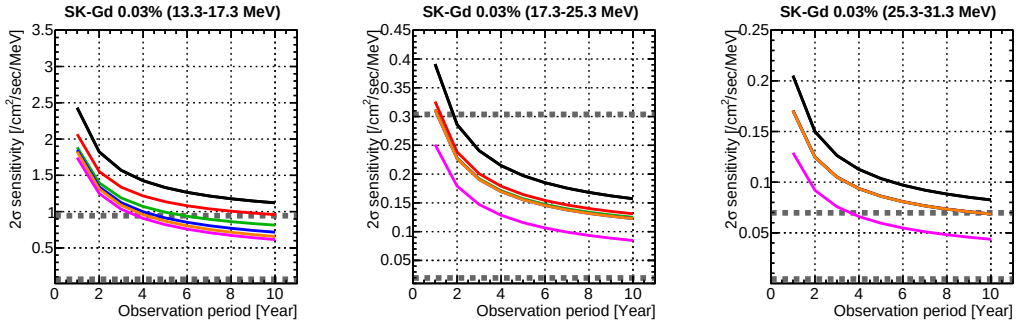

(B) 2σ C.L. sensitivity with the same assumption as Figure 11.1.

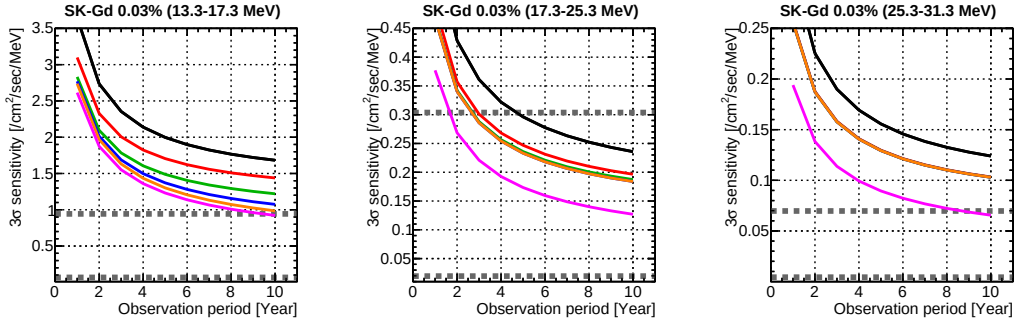

(C) 3σ C.L. sensitivity with the same assumption as Figure 11.1.

FIGURE 11.2: Expected future sensitivity for 13.3–17.3 MeV (left) 17.3–25.3 MeV (middle), and 25.3–31.3 MeV (right) energy bins with the same assumption as Figure 11.1; colors represent the assumptions listed in Table 11.1. Two thick-dotted lines exhibit the range of model expectations.

11.3 Limitation to the Failed Supernova Rate

The failed supernova rate, a fraction that the supernova forms the black hole (BH) before successfully exploding and forming a neutron star (NS), can be estimated using the flux upper limit on the SRN. According to [53], the supernova neutrino spectrum and total neutrino emission energy from a supernova depend on its fate, i.e., its remnant, low-mass NS (Canonical-mass NS; CNS), high-mass NS (High-mass NS; HNS), and failed supernova. The distinction between low- and high-mass NS is based on a baryon mass of $M_{\mathrm{NS,b}} = 1.6 M_{\odot}$. Furthermore, it is assumed that the explosion does not occur, and in the case of the failed supernovae, only continuous mass accretion occurs which results in a BH. Introducing the failed supernova fraction f_{BH} and the high-mass NS forming supernova fraction f_{HNS} to the SNe with NS, the neutrino number density term dN/dE_{ν} in Equation 1.35 can be rewritten as

$$\begin{aligned}\left\langle \frac{dN(E'_{\nu})}{dE'_{\nu}} \right\rangle =& f_{\mathrm{BH}} \frac{dN_{\mathrm{BH}}(E'_{\nu})}{dE'_{\nu}} + (1 - f_{\mathrm{BH}}) \\ & \times \left[f_{\mathrm{HNS}} \frac{dN_{\mathrm{HNS}}(E'_{\nu})}{dE'_{\nu}} + (1 - f_{\mathrm{HNS}}) \frac{dN_{\mathrm{CNS}}(E'_{\nu})}{dE'_{\nu}} \right],\end{aligned} \tag{11.1}$$

where the $dN_{\mathrm{BH}}(E'_{\nu})/dE'_{\nu}$, $dN_{\mathrm{CNS}}(E'_{\nu})/dE'_{\nu}$ denote the number spectrum for the failed SN, SN with creating HNS, and SN with creating CNS, respectively. The event rate spectrum is shifted to higher energy depending on the remnant mass, as depicted in Figure 11.3. The total energy of neutrino emission depends on the condition of NS formed after the explosion, and the nuclear Equation Of State (EOS) is responsible for the final state of the remnant. At this time, the three EOS models, such as Togashi [160], LS220 [161], and Shen [162], as following [53] are considered.

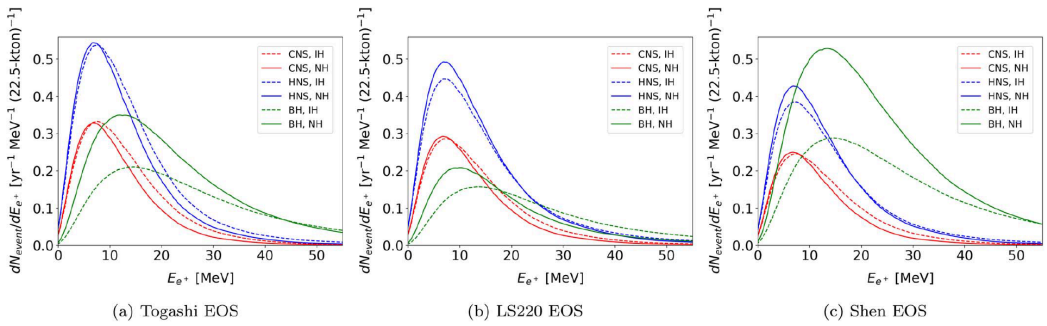

(a) Togashi EOS (b) LS220 EOS (c) Shen EOS

FIGURE 11.3: Event rate spectra of DSNB $\bar{\nu}_e$ for SK 22.5 kton water per year. The EOS model is assumed to be (a) Togashi EOS, (b) LS220 EOS, (c) Shen EOS, respectively. Colors correspond to the remnant types and mass hierarchy of the neutrino oscillation. These plots are sourced from [53].

The HNS contributes more to the flux than the CNS, although their spectrum shapes are similar. However, the neutrino spectrum from BH-forming supernovae varies based on the EOS model. Differences in the event rate spectrum become significant above ~ 15 MeV, especially between Togashi EOS and Shen EOS. On the other hand, for the LS220 EOS, the spectrum contributions from BH-forming supernovae are similar to those from NS-forming ones. Thus, the parameters f_{BH} and f_{HNS} can

be investigated based on the flux upper limit, considering such differences in the contribution of BH-forming SN to the DSNB flux. In this thesis, the expected fluxes for various f_{BH} and f_{HNS} are compared with the future sensitivity under assumption (6) in Table 11.1. The strategy for the evaluation is the same as [53]. The two energy regions, namely, $13.3 < E_\nu < 31.3$ MeV and $17.3 < E_\nu < 31.3$ MeV, are investigated as the integrated flux.

The formulation of the expected neutrino flux is stated in Equation 1.34. Moreover, the flux of $\bar{\nu}_e$ at SK is described by Equation 1.40, and the CCSN rate adopts the definition of Equation 1.42. The minimum progenitor mass that causes the core collapse is set to $8M_\odot$, with other settings and assumptions detailed in [53]. The expected integrated flux limit in 10 years of SK-Gd observations is 2.12 $\mathrm{cm}^{-2}\,\mathrm{sec}^{-1}$ for the $13.3 < E < 31.3$ MeV range and 0.78 $\mathrm{cm}^{-2}\,\mathrm{sec}^{-1}$ for the $17.3 < E < 31.3$ MeV range with 3σ, respectively. Using this information, the limit is assigned for the f_{BH} and f_{HNS} parameter-space. Figures 11.4 and 11.5 display comparisons between future sensitivities and expected fluxes for nominal (NH) and inverted (IH) mass hierarchies, respectively. Flux values exceeding the dot-dashed line are expected to be inspected in the upcoming decade. Exclusion areas vary depending on EOS models, mass hierarchy, and search energy region. Notably, for the NH case (Figure 11.4), the higher energy threshold sets stricter limits on f_{HNS} and f_{BH}, deviating from the finding in [53]. This change is mainly attributed to the improved estimation of CCQE events, which dominate above the 17.3 MeV bins. Specifically, the limit for f_{BH} is harsher than for f_{HNS} in the Shen model, as this model has the characteristic BH flux shape. In contrast, the sensitivity for f_{BH} is limited for all f_{HNS} regions in the LS220 model since the BH spectrum is similar to the HNS and CNS spectrum. The tendency is similar in the IH case (Figure 11.5).

The overlaid exclusion areas of three EOS models for each energy range are depicted in Figures 11.6 and 11.7. Since more neutrinos are emitted from HNS than CNS, detecting neutrinos at larger f_{HNS} for all models is easier. However, specifically in LS220 models, the tendency for BH is dissimilar to that for HNS flux since the flux from the BH is less than that of HNS and CNS with even higher energy threshold regions. Thanks to the CCQE improvement, $f_{\mathrm{HNS}} > 0.8$ region with any f_{BH} can be investigated for both NH and IH cases. Specifically, the Shen model can be verified for almost all parameters in the IH case. Although the result is model-dependent, 10 years of SK-Gd operation can explore the higher f_{HNS} and lower f_{BH} regions for all three models based on these tendencies.

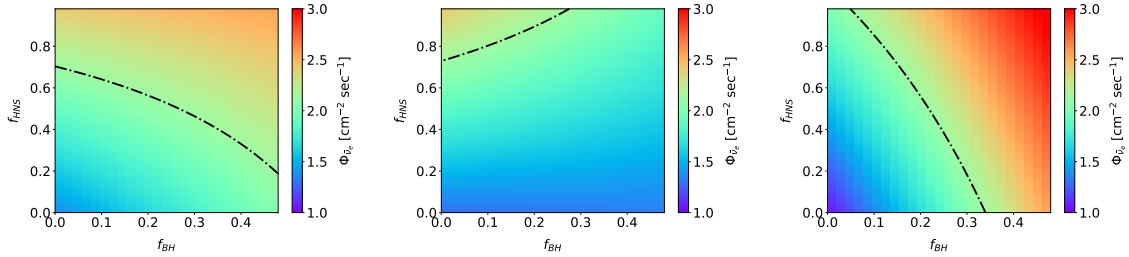

(1a) Togashi EOS
$13.3 < E_\nu < 31.3$ MeV

(1b) LS220 EOS
$13.3 < E_\nu < 31.3$ MeV

(1c) Shen EOS
$13.3 < E_\nu < 31.3$ MeV

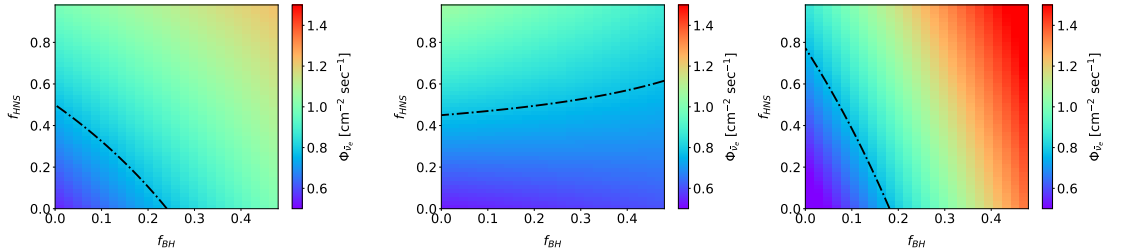

(2a) Togashi EOS
$17.3 < E_\nu < 31.3$ MeV

(2b) LS220 EOS
$17.3 < E_\nu < 31.3$ MeV

(2c) Shen EOS
$17.3 < E_\nu < 31.3$ MeV

FIGURE 11.4: Two-dimensional map of the DSNB $\bar{\nu}_e$ flux as a function of $f_{\rm BH}$ and $f_{\rm HNS}$ in normal mass hierarchy. Dotted-dashed line reports the 3σ expected sensitivity derived from the 10 years of future SK-Gd operation. These are estimated as the integrated flux for the neutrino energy $13.3 < E_\nu < 31.3$ MeV (top) and $17.3 < E_\nu < 31.3$ MeV (bottom) with distinct EOS models such as Togashi EOS (left), LS220 EOS (middle), and Shen EOS (right), respectively.

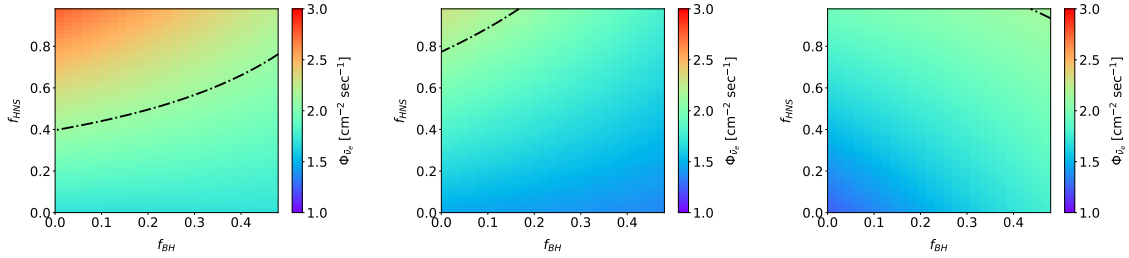

(1a) Togashi EOS
$13.3 < E_\nu < 31.3$ MeV

(1b) LS220 EOS
$13.3 < E_\nu < 31.3$ MeV

(1c) Shen EOS
$13.3 < E_\nu < 31.3$ MeV

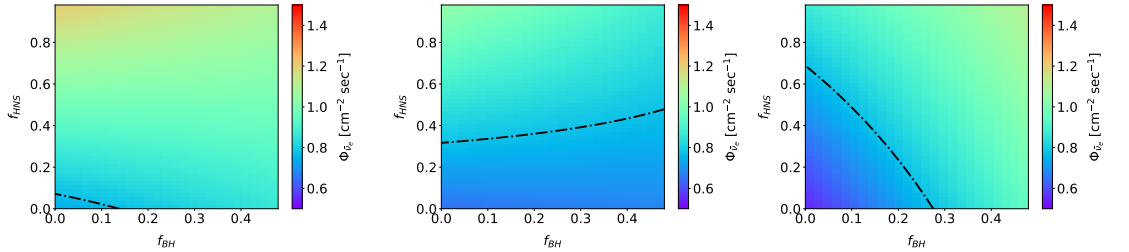

(2a) Togashi EOS
$17.3 < E_\nu < 31.3$ MeV

(2b) LS220 EOS
$17.3 < E_\nu < 31.3$ MeV

(2c) Shen EOS
$17.3 < E_\nu < 31.3$ MeV

FIGURE 11.5: Distributions with the same manners as Figure 11.4, in case of inverted mass hierarchy.

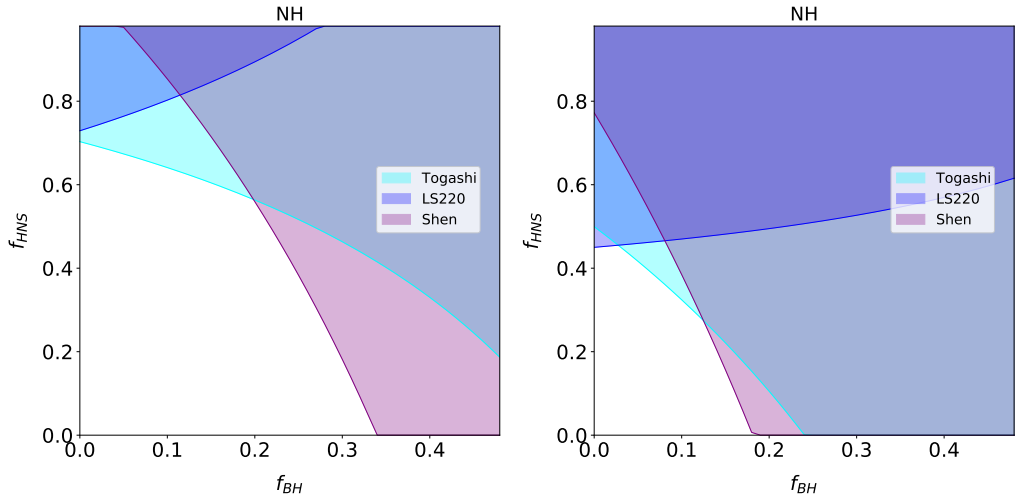

FIGURE 11.6: 3σ detectable areas on the f_{BH}-f_{HNS} plane assuming NH for three distinct EOS models in the energy range of 13.3–31.3 MeV (left) and 17.3–31.3 MeV (right) according to the future flux limit at 10 year of the SK-Gd observation.

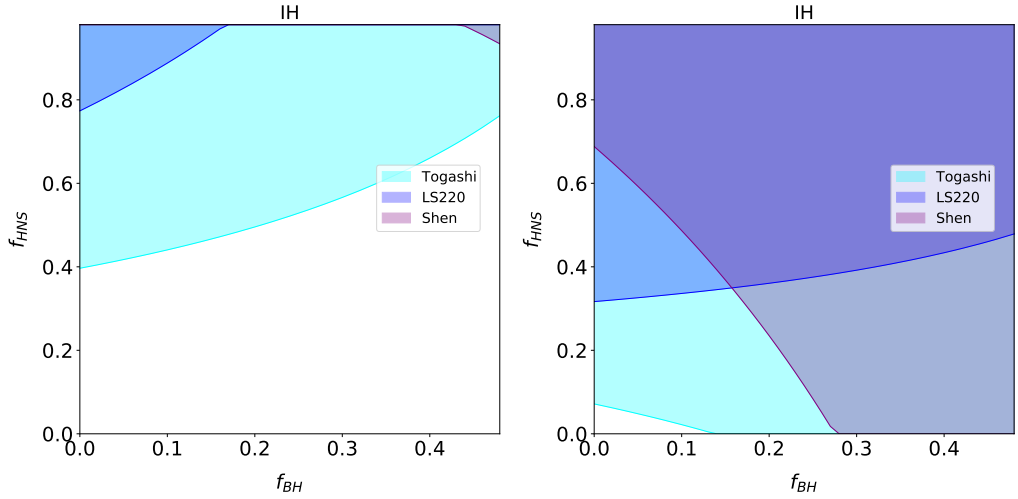

FIGURE 11.7: Distributions with the same manners as Figure 11.6 but assuming IH.

11.4 Conclusion

In this thesis, the data from the recent SK-Gd phase was analyzed to search for supernova relic neutrinos. Initially, a novel algorithm was formulated to detect neutron capture on Gd. This involved evaluating fit quality, analyzing reconstructed energy, and gauging the distance from a given prompt event to the delayed candidates. The performance of this neutron identification was evaluated using the newly taken AmBe data. For this, the AmBe calibration geometry was established in detector simulation for the first time to compare it with the measurement. The subsequent neutron tagging efficiency in the SK-Gd is estimated at $40.2^{+1.0}_{-3.5}$%. When evaluating the efficiency of neutron tagging with two distinct BGO shapes, the outcomes aligned with the MC simulation within 10% of the actual data. Given that disparities between actual data and MC simulations depend on the BGO geometry, it was deduced that an unidentified BGO effect might impact neutron interaction. Thus, the uncertainty on the neutron tagging in SK-Gd is estimated to be 8.8%, including position dependence.

After evaluating neutron tagging efficiency, the first search for SRN using 552 days of SK-Gd data is performed. All simulations used in this analysis were based on a newly constructed MC, termed SKG4. Cut criteria for removing spallation events, atmospheric neutrinos, and radioactive background are optimized. Consequently, the signal efficiency was estimated to range between 13.9–31.6% in the signal energy region. Notably, this efficiency is significantly improved from the previous SRN searches in SK below the 16 MeV energy regions, attributable to high neutron tagging efficiency while keeping sufficiently low misidentification probability in the neutron tagging.

Background events estimation for individual components, along with their systematic uncertainties were newly determined using SKG4. Not that this is the first time to evaluate the atmospheric neutrinos event MC via SKG4. The observed data was also passed through a reduction, and finally, 16 events remained within the signal energy region. However, following a p-value test, it was discerned that there was no significant excess over the background. In the absence of a marked event surplus over the expected background across energy bins, a 90% confidence level upper limit was set. The observed and expected upper limits of SRN flux are 0.32–32.32 and 0.32–49.16 $\mathrm{cm}^{-2}\,\mathrm{sec}^{-1}\,\mathrm{MeV}^{-1}$, depending on energy bins. A pivotal observation was that owing to the enhanced signal efficiency stemming from Gd-induced neutron capture, the flux upper limit based on 552.2 days in the SK-VI period is comparable to the outcomes from a 2970 days exploration in a previous pure-water phase, which is the world's stringent upper limit in the energy regions above 15.3 MeV. This proves the SK-Gd experiment is the most sensitive to the SRN search, considering 20% of the live time as the previous search.

Peering into future prospects, the estimations were made for the expected performance for future SK-Gd observations, grounded on the meticulous actual data analysis and validation with the expected backgrounds. Pragmatic assumptions concerning background reductions and related systematic uncertainties were incorporated. Additionally, a Gd concentration of 0.03% was assumed, mirroring current levels in the SK-VII operation. The expected sensitivity with a decade of SK-Gd operation indicates that several DSNB models are validated.

Lastly, by applying these findings to pertinent physics parameters, proportions of failed supernovae and those associated with high-mass neutron stars over 10 years of SK-Gd operations were explored. These insights accentuate how future DSNB observations of SK-Gd illuminate our understanding of the fate of Supernova.

Appendix A

Theoretical prediction of SRN flux with integrated bins

TABLE A.1: Summary of model projections of average flux and obtained sensitivity in each bin. The future sensitivity in SK-VII represents the magenta line in Figure 11.1. The unit of each value is $\mathrm{cm}^{-2}\,\mathrm{sec}^{-1}\,\mathrm{MeV}^{-1}$.

Neutrino energy [MeV]	9.29–11.29	11.29–13.29	13.29–17.29	17.29–25.29	25.29–31.29
Present results in SK-VI	49.16	14.89	2.70	0.49	0.32
Future sensitivity in SK-VII	17.46	4.20	0.51	0.07	0.04
Horiuchi+21 [4]	1.71	1.01	0.51	0.14	0.04
Galais+10 [9]	1.03	0.72	0.42	0.15	0.04
Tabrizi+20 [5]	0.69	0.46	0.29	0.09	0.02
Kresse+20 [6]	1.31	0.87	0.48	0.15	0.04
Nakazato+15 (IH, Max) [3]	0.47	0.30	0.16	0.05	0.01
Nakazato+15 (NH, Min) [3]	0.20	0.13	0.07	0.02	< 0.01
Horiuchi+18 ($\xi_{2.5,\mathrm{crit}} = 0.1$) [8]	0.77	0.53	0.32	0.12	0.03
Horiuchi+18 ($\xi_{2.5,\mathrm{crit}} = 0.5$) [8]	0.75	0.46	0.24	0.06	0.01
Horiuchi+09 (6 MeV, Max) [10]	1.11	0.81	0.49	0.18	0.05
Ando+03 [12, 13]	0.57	0.38	0.20	0.06	0.02
Lunardini09 [11]	0.55	0.37	0.20	0.07	0.02
Malaney97 [15]	0.26	0.17	0.09	0.03	0.01
Hartmann+97 [16]	0.47	0.33	0.19	0.06	0.02
Kaplinghat+00 [14]	2.40	1.66	0.94	0.30	0.07

Appendix B

Spallation Distributions

B.1 Neutron cloud distributions

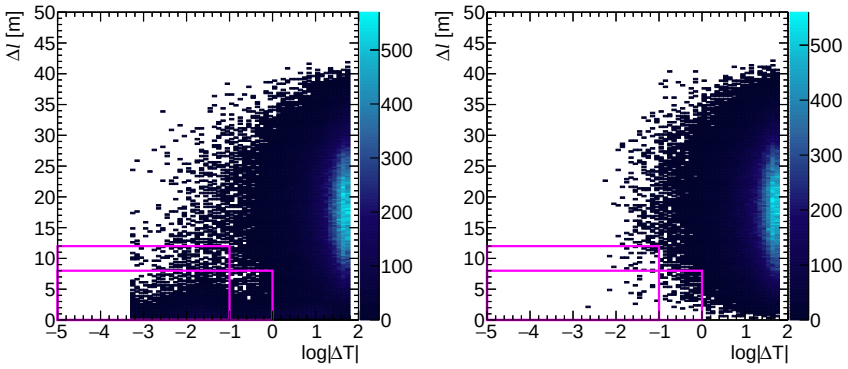

FIGURE B.1: Two-dimensional distribution of $\log|dt|$ and Δl for the pre-sample (left) and the post-sample (right). Magenta lines are cut criteria in this plane. These are for clouds with $N_{\mathrm{ncloud}} = 2$.

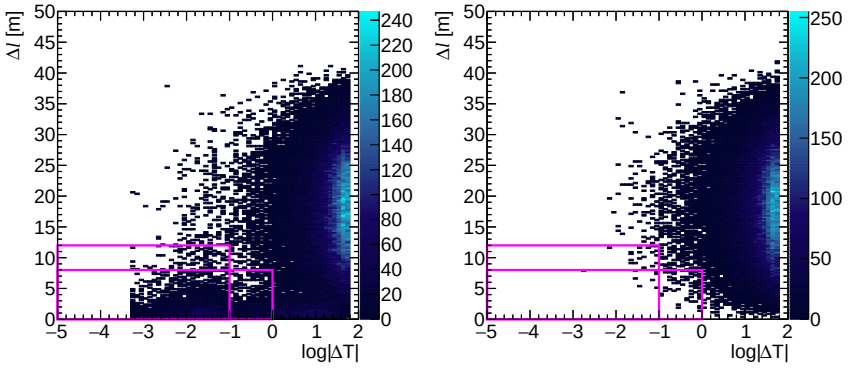

FIGURE B.2: Two-dimensional distribution of $\log|dt|$ and Δl for the pre-sample (left) and the post-sample (right). Magenta lines are cut criteria in this plane. These are for clouds with $N_{\mathrm{ncloud}} = 3$.

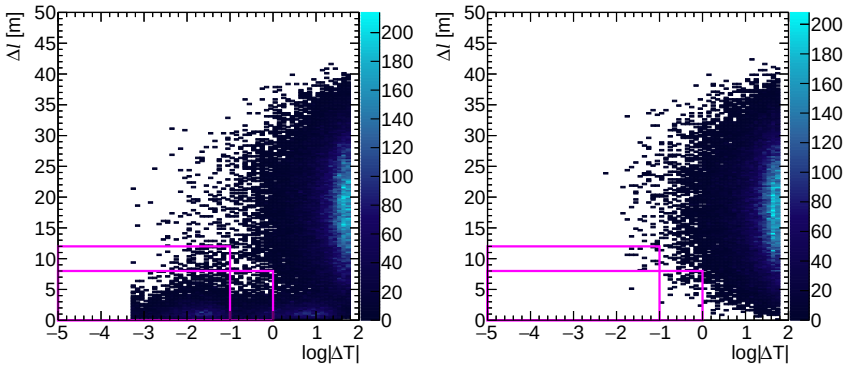

FIGURE B.3: Two-dimensional distribution of $\log|dt|$ and Δl for the pre-sample (left) and the post-sample (right). Magenta lines are cut criteria in this plane. These are for clouds with $N_{\mathrm{ncloud}} = 4$-5.

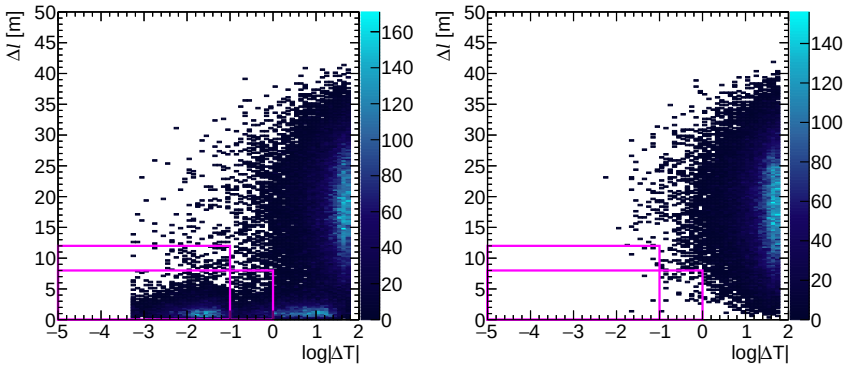

FIGURE B.4: Two-dimensional distribution of $\log|dt|$ and Δl for the pre-sample (left) and the post-sample (right). Magenta lines are cut criteria in this plane. These are for clouds with $N_{\mathrm{ncloud}} = 6$-9.

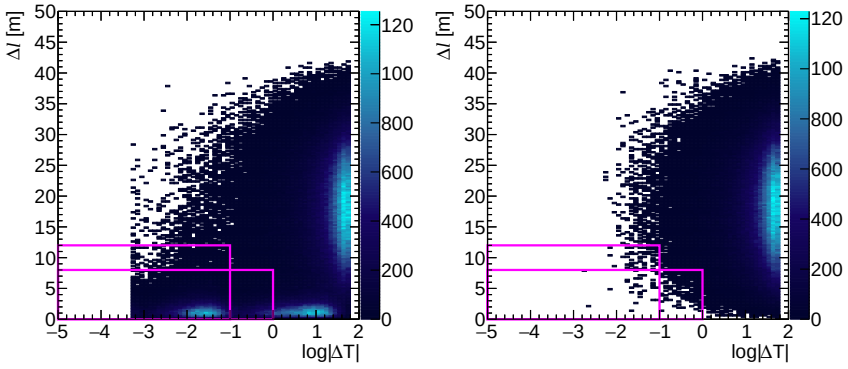

FIGURE B.5: Two-dimensional distribution of $\log|dt|$ and Δl for the pre-sample (left) and the post-sample (right). Magenta lines are cut criteria in this plane. These are for clouds with $N_{\mathrm{ncloud}} \geq 2$.

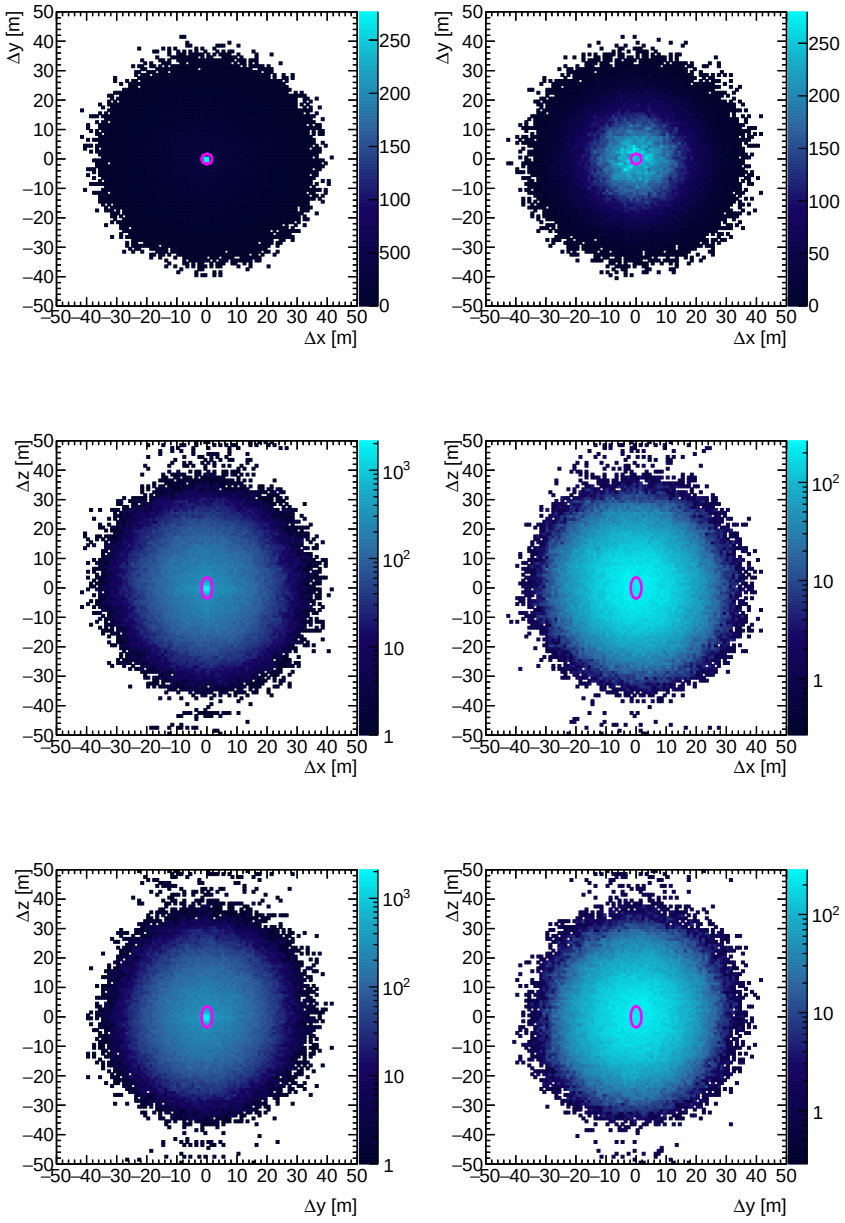

FIGURE B.6: Two-dimensional distribution of Δ_x, Δ_y, and Δ_z. The left column shows the pre-samples and the right column shows the post-samples. Magenta lines are cut criteria. These are clouds with $N_{\text{ncloud}} = 2$.

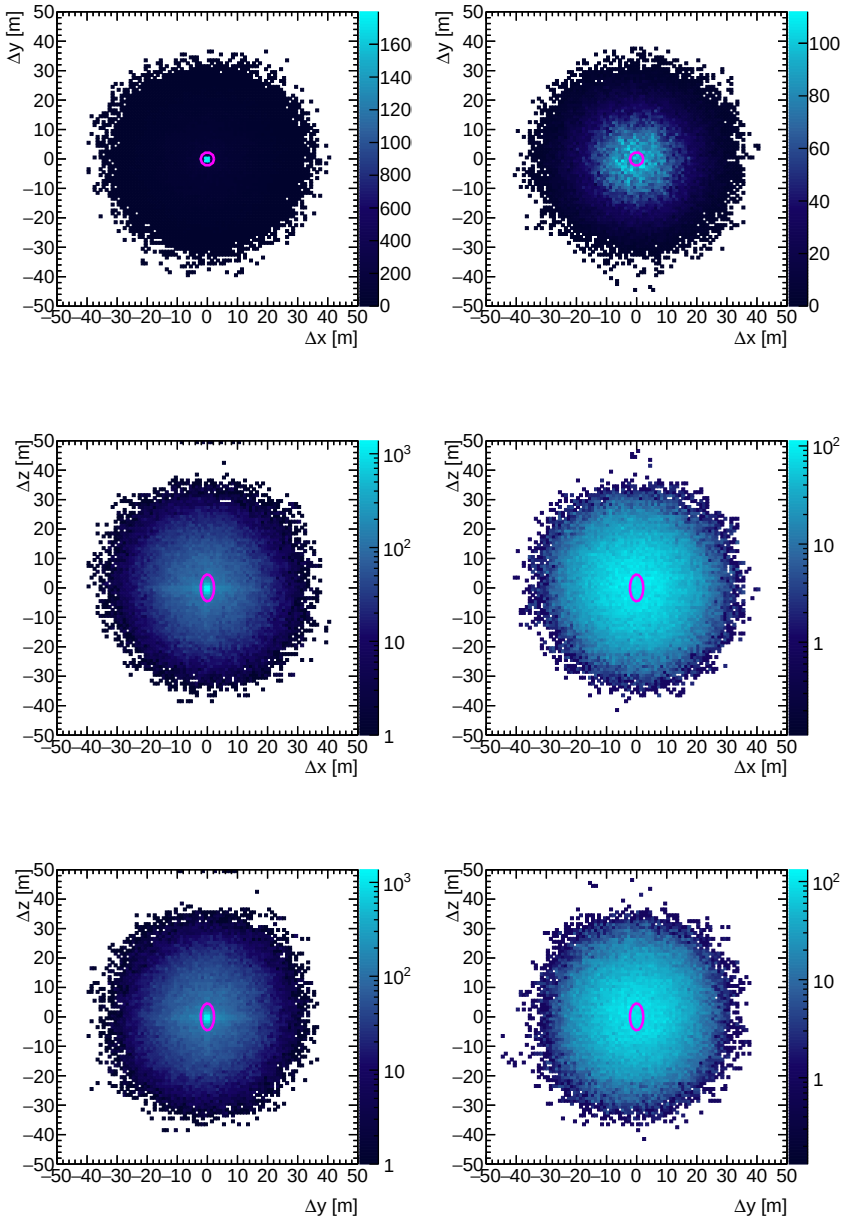

FIGURE B.7: Two-dimensional distribution of Δ_x, Δ_y, and Δ_z. The left column shows the pre-samples and the right column shows the post-samples. Magenta lines are cut criteria. These are clouds with $N_{\text{ncloud}} = 3$.

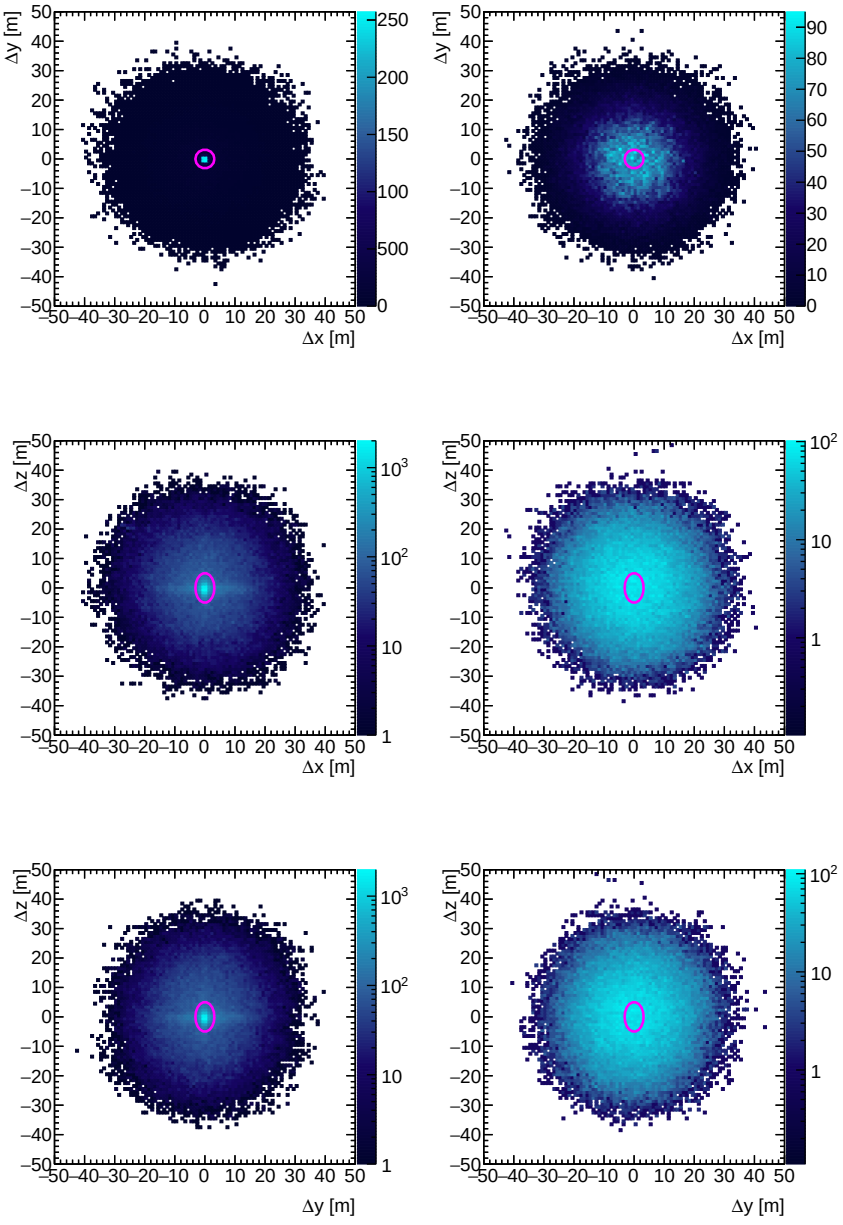

FIGURE B.8: Two-dimensional distribution of Δ_x, Δ_y, and Δ_z. The left column shows the pre-samples and the right column shows the post-samples. Magenta lines are cut criteria. These are clouds with $N_{\mathrm{ncloud}} = 4\text{-}5$.

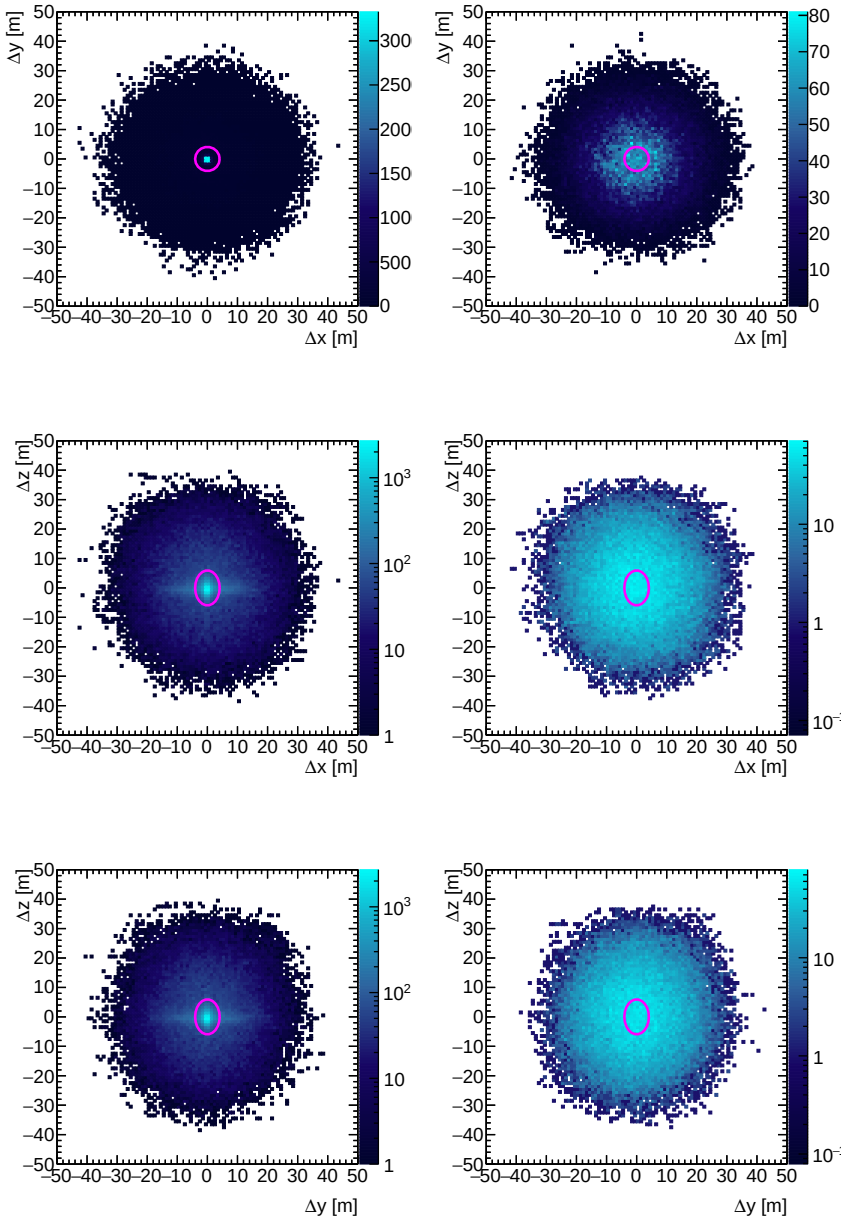

FIGURE B.9: Two-dimensional distribution of Δ_x, Δ_y, and Δ_z. The left column shows the pre-samples and the right column shows the post-samples. Magenta lines are cut criteria. These are clouds with $N_{\text{ncloud}} = 6\text{-}9$.

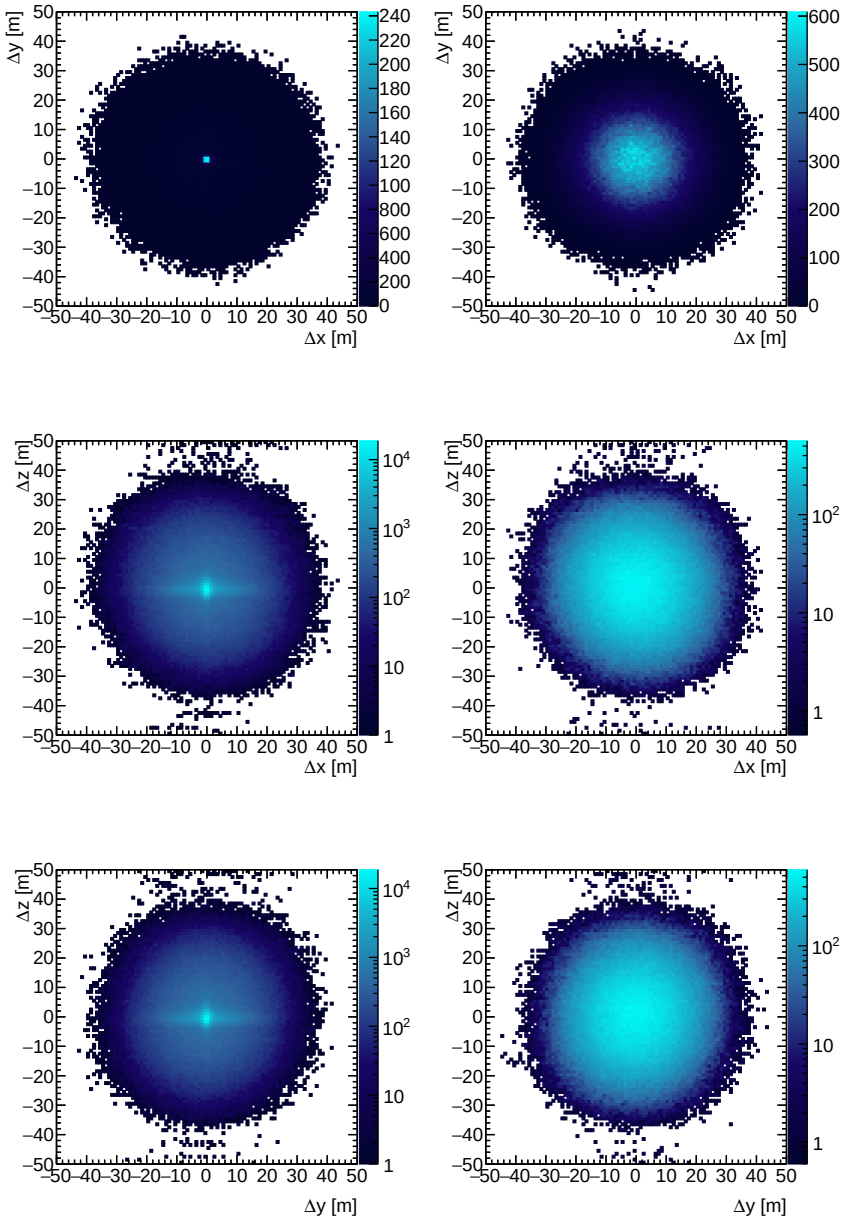

FIGURE B.10: Two-dimensional distribution of Δ_x, Δ_y, and Δ_z. The left column shows the pre-samples and the right column shows the post-samples. Magenta lines are cut criteria. These are clouds with $N_{\mathrm{ncloud}} \geq 2$.

B.2 PDF distributions

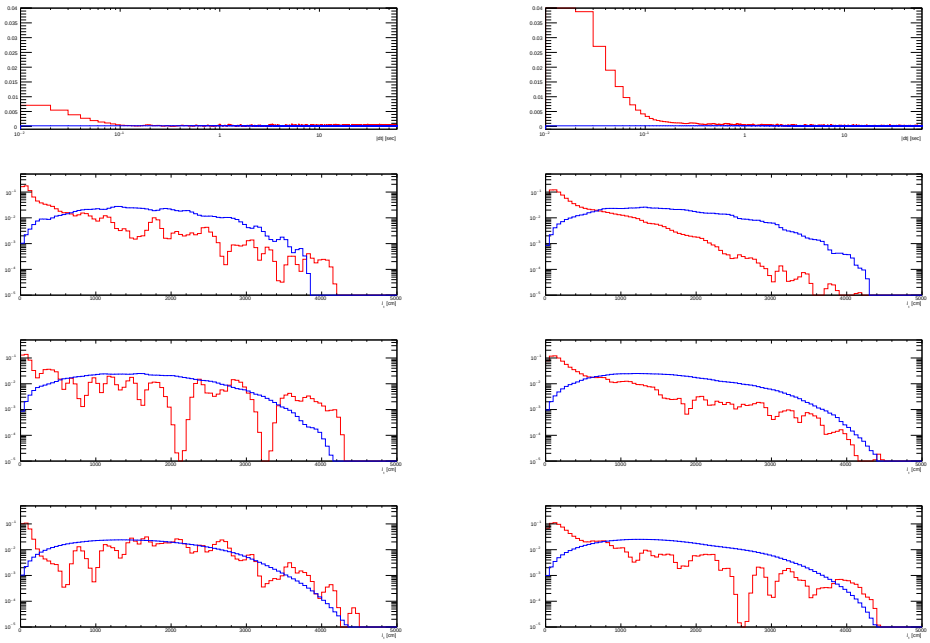

FIGURE B.11: Random (blue) and spallation (red) PDFs for dt (top), and ℓ_t (second from the top to bottom). ℓ_t PDF distributions are separated for the muon with dt region of 0–0.05 sec (second from top), 0.05–0.5 sec (third from top), and 0.5-60 sec (bottom). These muons belong to the stopping (left) and multiple (right) muons.

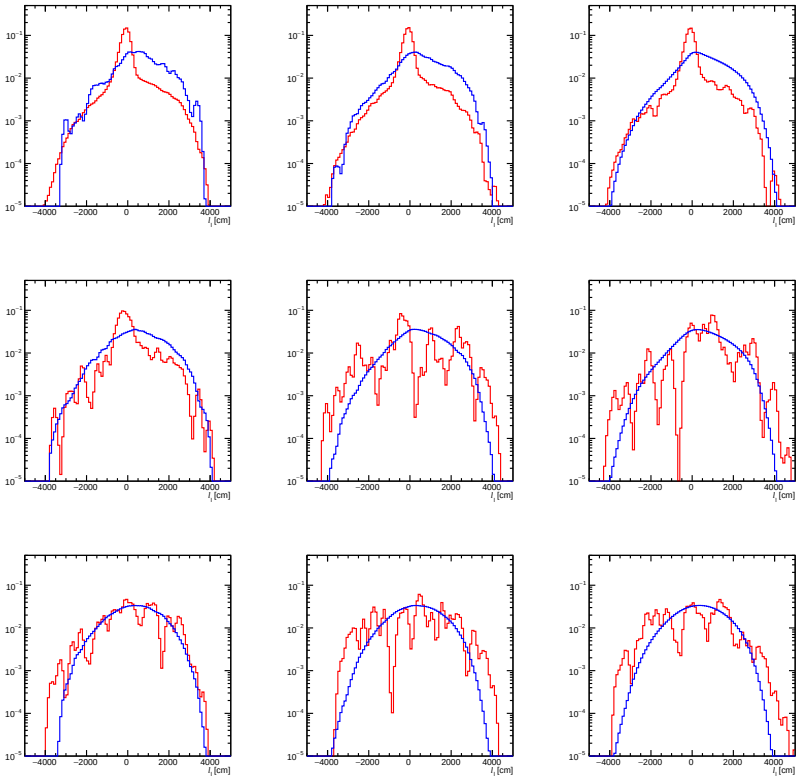

FIGURE B.12: Random (blue) and spallation (red) PDFs for ℓ_l with dt region of 0–0.05 sec (top), 0.05–0.5 sec (middle), 0.5-60 sec (bottom), and ℓ_t region of 0–300 cm (left), 300–1000 cm (middle), and more than 1000 cm (right). These muons belong to the single through-going muons.

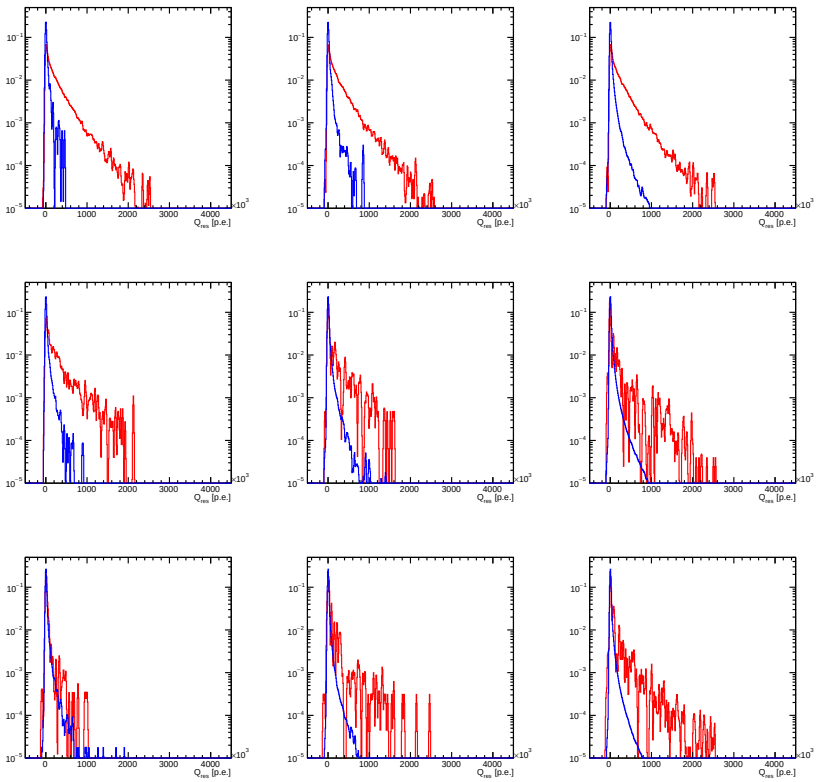

FIGURE B.13: Random (blue) and spallation (red) PDFs for Q_{res} with dt region of 0–0.05 sec (top), 0.05–0.5 sec (middle), 0.5-60 sec (bottom), and ℓ_t region of 0–300 cm (left), 300–1000 cm (middle), and more than 1000 cm (right). These muons belong to the single through-going muons.

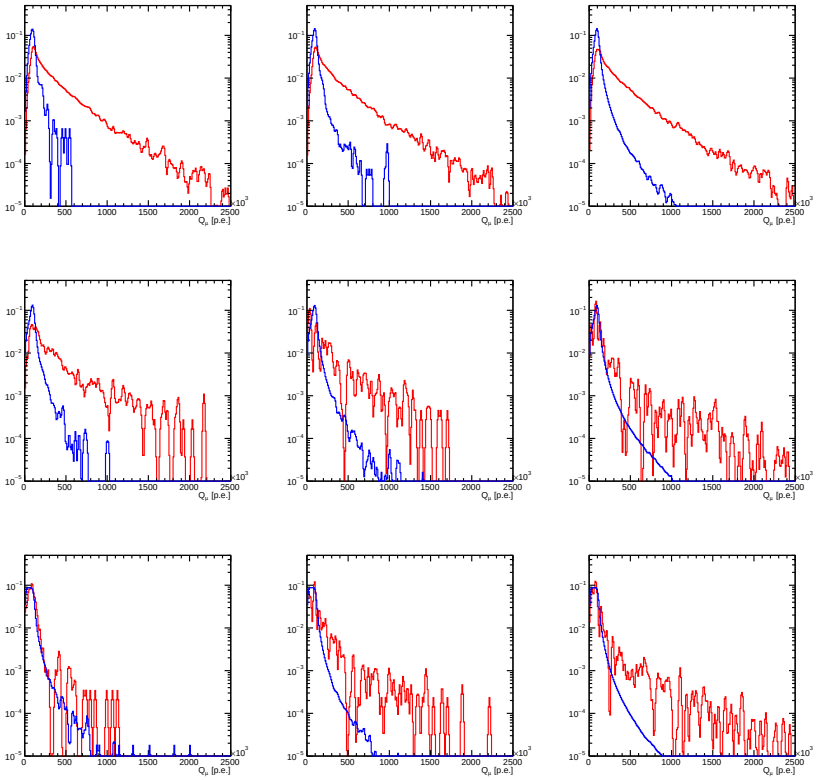

FIGURE B.14: Random (blue) and spallation (red) PDFs for Q_{mu} with dt region of 0–0.05 sec (top), 0.05–0.5 sec (middle), 0.5-60 sec (bottom), and ℓ_t region of 0–300 cm (left), 300–1000 cm (middle), and more than 1000 cm (right). These muons belong to the single through-going muons.

B.3 ROC Curves for each energy bin

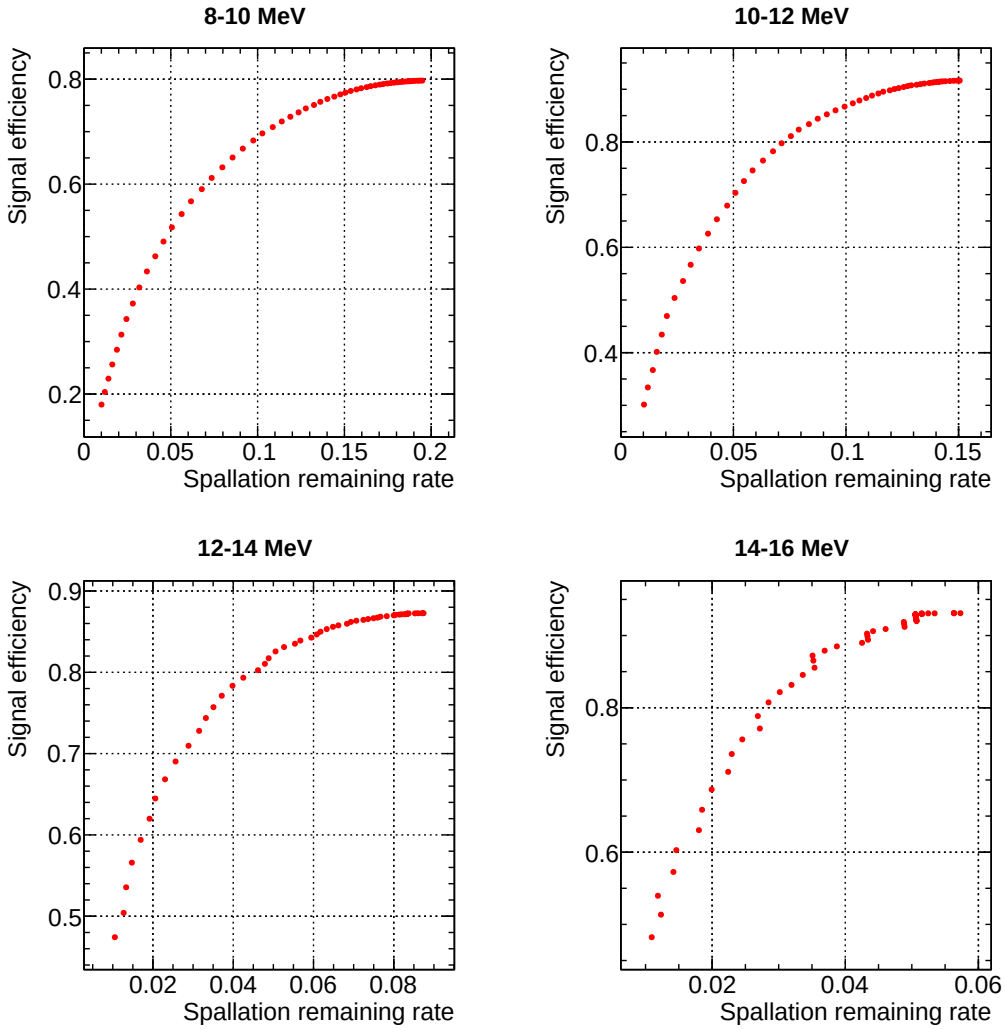

FIGURE B.15: ROC curve for each 2 MeV bin below 16 MeV.

B.4 Correlation between Spallation and Li9 efficiency

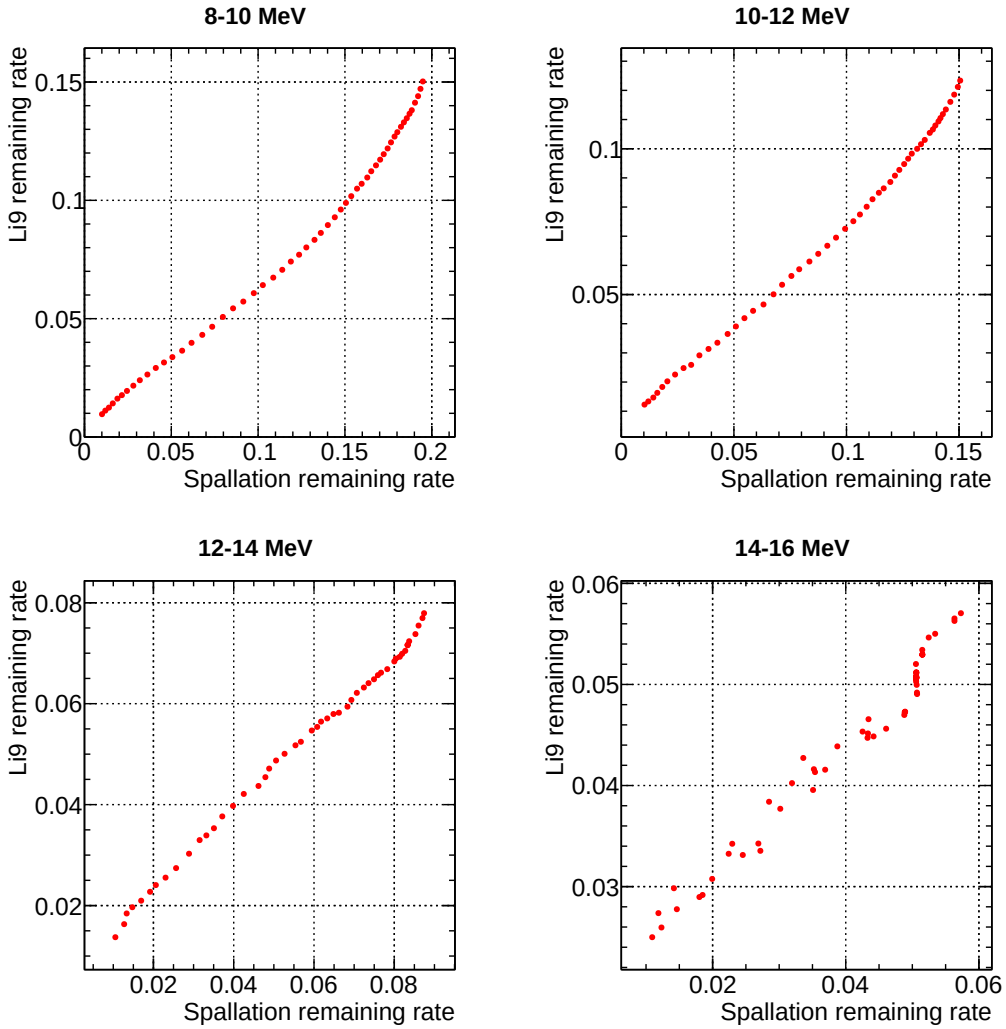

FIGURE B.16: Correlation between spallation remaining rate and ^9Li efficiency for each 2 MeV energy bin below 16 MeV.

Appendix C

Third Reduction Cut Variables

C.1 Effective wall distance distribution

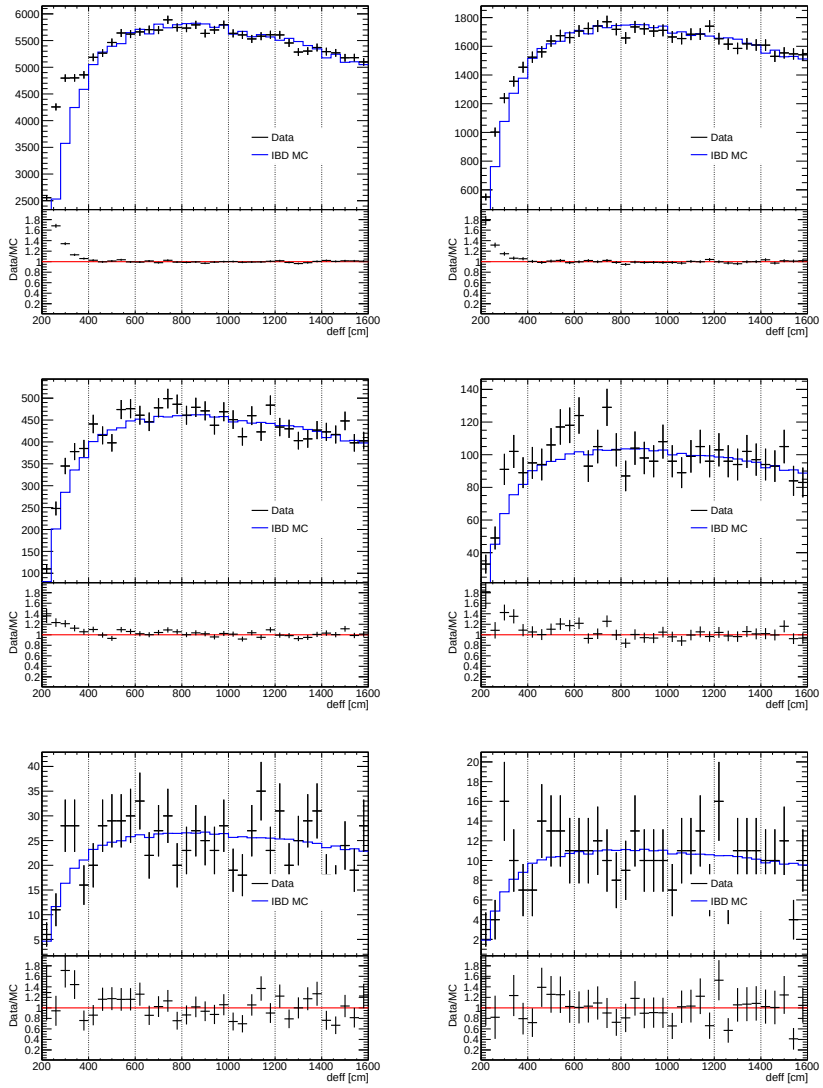

FIGURE C.1: d_{eff} wall distribution for the data (black) and MC (blue). Each panel show the reconstructed energy E for $E > 8$ MeV (left-top), $E > 10$ MeV (right-top), $E > 12$ MeV (left-middle), $E > 14$ MeV (right-middle), $E > 16$ MeV (left-bottom), and $E > 20$ MeV (right-bottom).

C.2 Third reduction variables in LINAC data

C.2.1 Cherenkov Angle

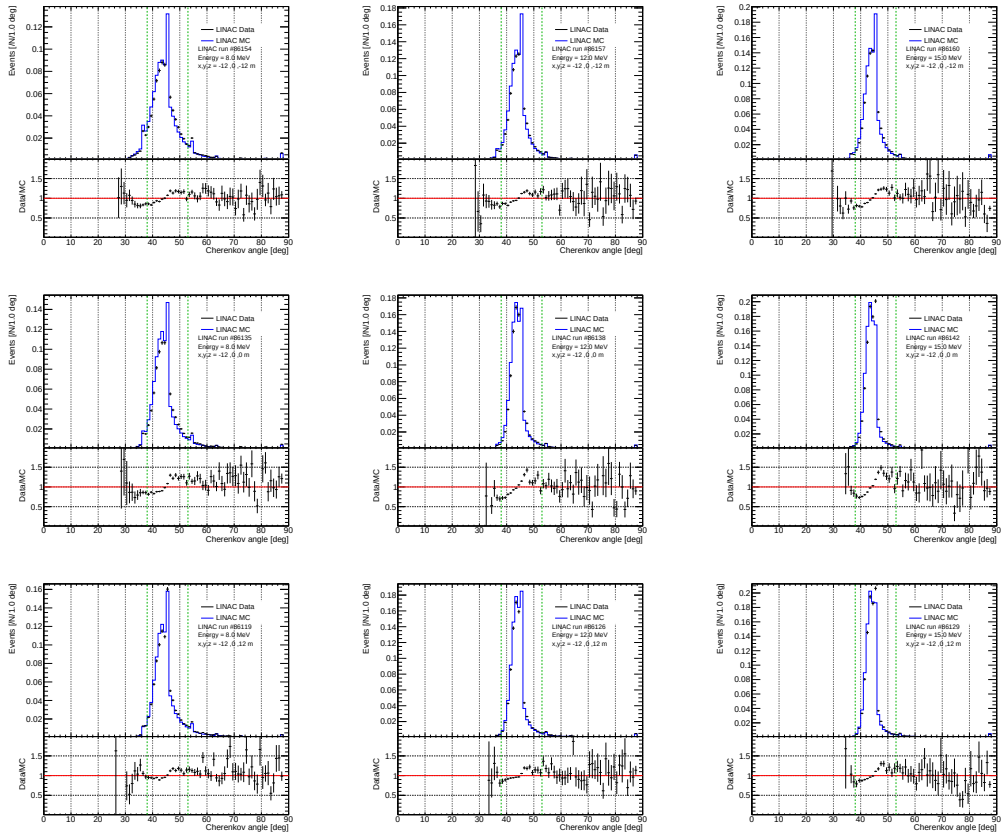

FIGURE C.2: Reconstructed Cherenkov angle distribution for LINAC data (black) and MC (blue). For each plot, the lower panel shows the ratio of data over MC. For the LINAC position, figures show the $z = -12$ m (top), $z = 0$ m (middle), and $z = 12$ m (bottom). For the LINAC energy, figures show the $E = 8$ MeV (left), $E = 12$ MeV (middle), and $E = 15$ MeV (right).

C.2.2 Cherenkov Angle

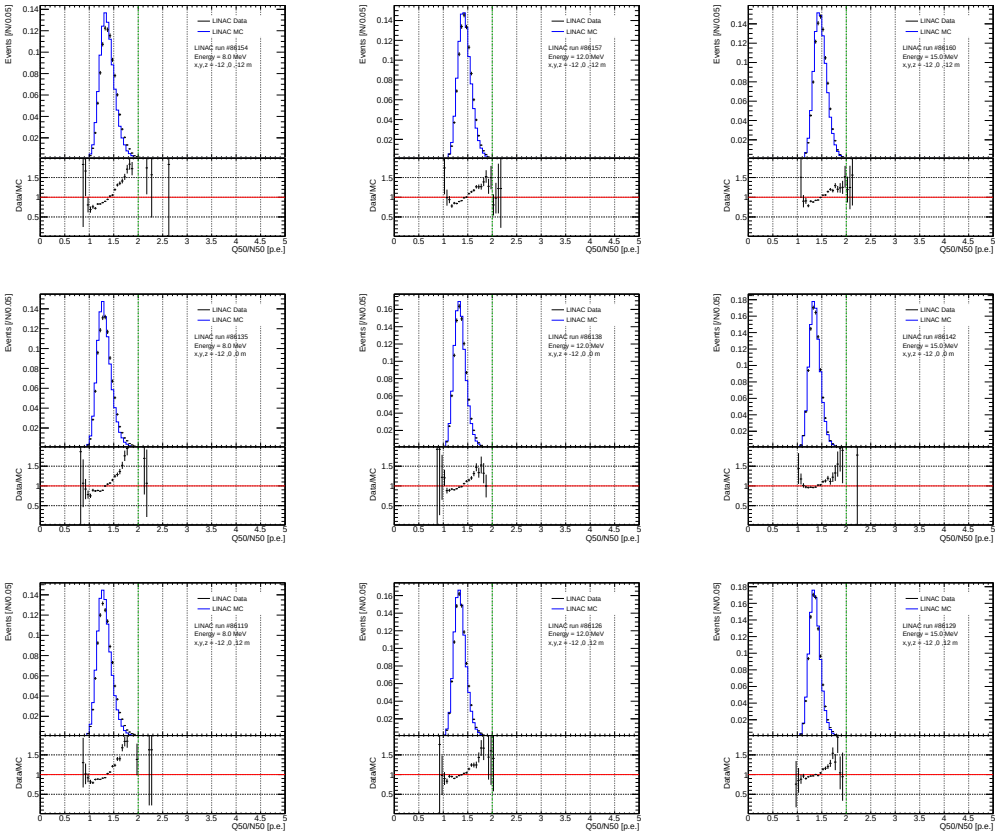

FIGURE C.3: Ratio of charge over number of hits in 50 ns distribution for LINAC data (black) and MC (blue). For each plot, the lower panel shows the ratio of data over MC. For the LINAC position, figures show the $z = -12$ m (top), $z = 0$ m (middle), and $z = 12$ m (bottom). For the LINAC energy, figures show the $E = 8$ MeV (left), $E = 12$ MeV (middle), and $E = 15$ MeV (right).

C.2.3 Pion likeness

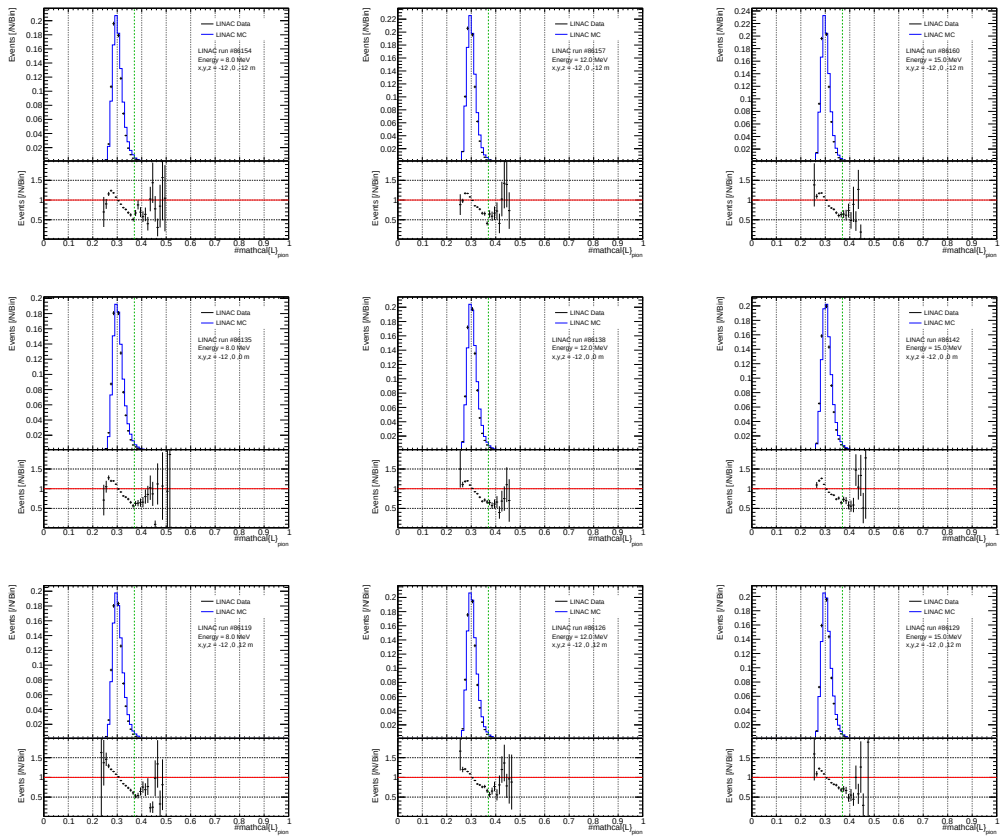

FIGURE C.4: Pion likeness distribution for LINAC data (black) and MC (blue). For each plot, the lower panel shows the ratio of data over MC. For the LINAC position, figures show the $z = -12$ m (top), $z = 0$ m (middle), and $z = 12$ m (bottom). For the LINAC energy, figures show the $E = 8$ MeV (left), $E = 12$ MeV (middle), and $E = 15$ MeV (right).

Bibliography

[1] K. Nakazato *et al.*, "SUPERNOVA NEUTRINO LIGHT CURVES AND SPECTRA FOR VARIOUS PROGENITOR STARS: FROM CORE COLLAPSE TO PROTO-NEUTRON STAR COOLING," *The Astrophysical Journal Supplement Series*, 205(1):2, feb 2013.

[2] K. S. Hirata *et al.*, "Observation in the kamiokande-ii detector of the neutrino burst from supernova sn1987a," *Phys. Rev. D*, 38:448–458, Jul 1988.

[3] K. Nakazato *et al.*, "Spectrum of the supernova relic neutrino background and metallicity evolution of galaxies," *The Astrophysical Journal*, 804(1):75, May 2015.

[4] S. Horiuchi *et al.*, "Impact of binary interactions on the diffuse supernova neutrino background," *Phys. Rev. D*, 103:043003, Feb 2021.

[5] Zahra Tabrizi and Shunsaku Horiuchi, "Flavor triangle of the diffuse supernova neutrino background," *Journal of Cosmology and Astroparticle Physics*, 2021(05):011, may 2021.

[6] Daniel Kresse, Thomas Ertl, and Hans-Thomas Janka, "Stellar collapse diversity and the diffuse supernova neutrino background," *The Astrophysical Journal*, 909(2):169, mar 2021.

[7] H. de Kerret *et al.*, "Double chooz θ_{13} measurement via total neutron capture detection," *Nature Physics*, 16(5):558–564, 2020.

[8] S. Horiuchi *et al.*, "Diffuse supernova neutrino background from extensive core-collapse simulations of 8–100 $M_\odot$ progenitors," *Monthly Notices of the Royal Astronomical Society*, 475(1):1363–1374, 12 2017.

[9] S. Galais *et al.*, "Shock waves in supernovae: New implications on the diffuse supernova neutrino background," *Phys. Rev. D*, 81:053002, Mar 2010.

[10] Shunsaku Horiuchi, John F. Beacom, and Eli Dwek, "Diffuse supernova neutrino background is detectable in super-kamiokande," *Phys. Rev. D*, 79:083013, Apr 2009.

[11] Cecilia Lunardini, "Diffuse neutrino flux from failed supernovae," *Phys. Rev. Lett.*, 102:231101, Jun 2009.

[12] S. Ando, K. Sato, and T. Totani, "Detectability of the supernova relic neutrinos and neutrino oscillation," *Astroparticle Physics*, 18(4):307–318, 2003.

[13] S. I. Ando Relic supernova neutrino background: Current status and prospects of future detectors In Jacques Dumarchez, editor, *Proceedings of the Next Generation of Nucleon Decay and Neutrino Detectors, Aussois, Savoie, France*, number C0504071 in SLAC eConf, April 2005.

[14] M. Kaplinghat, G. Steigman, and T. P. Walker, "Supernova relic neutrino background," *Phys. Rev. D*, 62:043001, Jul 2000.

[15] R.A. Malaney, "Evolution of the cosmic gas and the relic supernova neutrino background," *Astroparticle Physics*, 7(1):125–136, 1997.

[16] D.H. Hartmann and S.E. Woosley, "The cosmic supernova neutrino background," *Astroparticle Physics*, 7(1):137–146, 1997.

[17] G. L. Fogli *et al.*, "Probing supernova shock waves and neutrino flavour transitions in next-generation water cherenkov detectors," *Journal of Cosmology and Astroparticle Physics*, 2005(04):002, apr 2005.

[18] S. Appel M. Agostini, K. Altenmüller *et al.*, "Search for low-energy neutrinos from astrophysical sources with borexino," *Astroparticle Physics*, 125:102509, 2021.

[19] S. Abe *et al.*, "Limits on astrophysical antineutrinos with the kamland experiment," *The Astrophysical Journal*, 925(1):14, jan 2022.

[20] K. Abe *et al.*, "Diffuse supernova neutrino background search at super-kamiokande," *Phys. Rev. D*, 104:122002, Dec 2021.

[21] K. Abe *et al.*, "The T2K experiment," *Nucl. Instruments Methods Phys. Res. Sect. A Accel. Spectrometers, Detect. Assoc. Equip.*, 659(1):106–135, dec 2011.

[22] S. Fukuda *et al.*, "The super-kamiokande detector," *Nuclear Instruments and Methods in Physics Research Section A: Accelerators, Spectrometers, Detectors and Associated Equipment*, 501(2):418 – 462, Apr 2003.

[23] Z.Conner *A Study of Solar Neutrinos Using the Super-Kamiokande Detector* PhD thesis, University of Maryland, http://www-sk.icrr.u-tokyo.ac.jp/sk/_pdf/articles/zoa-thesis.pdf, 1997.

[24] T.Yamaguchi *Observation of 8B solar neutrinos from 300-day data at super-kamiokande* PhD thesis, The University of Osaka, 1998.

[25] Y. Nakano *et al.*, "Measurement of the radon concentration in purified water in the super-kamiokande iv detector," *Nuclear Instruments and Methods in Physics Research Section A: Accelerators, Spectrometers, Detectors and Associated Equipment*, 977:164297, 2020.

[26] K. Abe *et al.*, "First gadolinium loading to super-kamiokande," *Nuclear Instruments and Methods in Physics Research Section A: Accelerators, Spectrometers, Detectors and Associated Equipment*, 1027:166248, 2022.

[27] H. Ishino *et al.*, "High-speed charge-to-time converter ASIC for the Super-Kamiokande detector," *Nuclear Instruments and Methods in Physics Research A*, 610(3):710–717, Nov 2009.

[28] S. Yamada *et al.*, "Commissioning of the new electronics and online system for the super-kamiokande experiment," *IEEE Transactions on Nuclear Science*, 57(2):428–432, 2010.

[29] M. Honda *et al.*, "Improvement of low energy atmospheric neutrino flux calculation using the jam nuclear interaction model," *Phys. Rev. D*, 83:123001, Jun 2011.

[30] O. Allkofer *et al.*, "Cosmic ray muon spectra at sea-level up to 10 tev," *Nuclear Physics B*, 259(1):1–18, 1985.

[31] S. Matsuno *et al.*, "Cosmic-ray muon spectrum up to 20 tev at 89° zenith angle," *Phys. Rev. D*, 29:1–23, Jan 1984.

[32] T. Sanuki *et al.*, "Study of cosmic ray interaction model based on atmospheric muons for the neutrino flux calculation," *Phys. Rev. D*, 75:043005, Feb 2007.

[33] M. Honda *et al.*, "Calculation of atmospheric neutrino flux using the interaction model calibrated with atmospheric muon data," *Phys. Rev. D*, 75:043006, Feb 2007.

[34] G. D. Barr *et al.*, "Three-dimensional calculation of atmospheric neutrinos," *Phys. Rev. D*, 70:023006, Jul 2004.

[35] G. Battistoni *et al.*, "The FLUKA code: description and benchmarking," *AIP Conference Proceedings*, 896(1):31–49, 03 2007.

[36] Y. Hayato, "A Neutrino Interaction Simulation Program Library NEUT," *Acta Physica Polonica B*, 40(9):2477, Sep 2009.

[37] T. Tanaka *et al.*, "Gamma-ray spectra from thermal neutron capture on gadolinium-155 and natural gadolinium," *Progress of Theoretical and Experimental Physics*, 2020(4), 04 2020 043D02.

[38] K. Abe *et al.*, "Solar neutrino measurements in super-kamiokande-iv," *Phys. Rev. D*, 94:052010, Sep 2016.

[39] J. Hosaka *et al.*, "Solar neutrino measurements in super-kamiokande-i," *Phys. Rev. D*, 73:112001, Jun 2006.

[40] M. Shinoki *Master thesis* PhD thesis, Tokyo University of Science, March 2020.

[41] Y. Ashida *Measurement of Neutrino and Antineutrino Neutral-Current Quasielastic-like Interactions and Applications to Supernova Relic Neutrino Searches* PhD thesis, Kyoto University, Feb 2020.

[42] H.Kitagawa *Measurement of the charge ratio of cosmic-ray muons in Super-Kamiokande* PhD thesis, Okayama University, https://www-sk.icrr.u-tokyo.ac.jp/sk/_pdf/articles/2022/Master_Thesis_Kitagawa.ver8_.pdf, March 2022.

[43] K. Abe *et al.*, "Calibration of the super-kamiokande detector," *Nuclear Instruments and Methods in Physics Research Section A: Accelerators, Spectrometers, Detectors and Associated Equipment*, 737:253 – 272, 2014.

[44] F De Guarrini and R Malaroda, "Two different technique measurements of the neutron spectrum of an am–be source.," *Nucl. Instrum. Methods 92: 277-84(1971).*, 1 1971.

[45] ISO *ISO 8529-1:2021 Neutron reference radiations fields — Part 1: Characteristics and methods of production* pub-ISO, 2021.

[46] W. Wolszczak *et al.* Temperature properties of scintillators for pet detectors: A comparative study In *2014 IEEE Nuclear Science Symposium and Medical Imaging Conference (NSS/MIC)*, pages 1–4, 2014.

[47] M. Chadwick *et al.*, "Endf/b-vii.1 nuclear data for science and technology: Cross sections, covariances, fission product yields and decay data," *Nuclear Data Sheets*, 112(12):2887–2996, 2011 Special Issue on ENDF/B-VII.1 Library.

[48] Y. Hayato H. Zhang, K. Abe *et al.*, "Supernova relic neutrino search with neutron tagging at super-kamiokande-iv," *Astroparticle Physics*, 60:41–46, 2015.

[49] D. Tilley *et al.*, "Energy levels of light nuclei a=8,9,10," *Nuclear Physics A*, 745(3):155–362, 2004.

[50] R. Akutsu *A Study of Neutrons Associated with Neutrino and Antineutrino Interactions on the Water Target at the T2K Far Detector* PhD thesis, University of Tokyo, December 2019.

[51] K. Abe *et al.*, "Measurement of neutrino and antineutrino neutral-current quasielasticlike interactions on oxygen by detecting nuclear deexcitation γ rays," *Phys. Rev. D*, 100:112009, Dec 2019.

[52] N. Ekanger *et al.*, "Impact of late-time neutrino emission on the diffuse supernova neutrino background," *Phys. Rev. D*, 106:043026, Aug 2022.

[53] Yosuke Ashida and Ken'ichiro Nakazato, "Exploring the fate of stellar core collapse with supernova relic neutrinos," *The Astrophysical Journal*, 937(1):30, sep 2022.

[54] I. Esteban *et al.*, "The fate of hints: updated global analysis of three-flavor neutrino oscillations," *Journal of High Energy Physics*, 2020(9):178, 2020.

[55] G. A. Tammann, W. Loeffler, and A. Schroeder, "The Galactic Supernova Rate," *The Astrophysical Journal Supplement Series*, 92:487, June 1994.

[56] H. A. Bethe and J. R. Wilson, "Revival of a stalled supernova shock by neutrino heating," *The Astrophysical Journal*, 295:14–23, August 1985.

[57] K. Sumiyoshi *et al.*, "Postbounce evolution of core-collapse supernovae: Long-term effects of the equation of state," *The Astrophysical Journal*, 629(2):922, aug 2005.

[58] Tomoya Takiwaki, Kei Kotake, and Yudai Suwa, "THREE-DIMENSIONAL HYDRODYNAMIC CORE-COLLAPSE SUPERNOVA SIMULATIONS FOR AN 11.2$M_\odot$ STAR WITH SPECTRAL NEUTRINO TRANSPORT," *The Astrophysical Journal*, 749(2):98, mar 2012.

[59] T. Foglizzo *et al.*, "Instability of a stalled accretion shock: Evidence for the advective-acoustic cycle," *The Astrophysical Journal*, 654(2):1006, jan 2007.

[60] Y. Fukuda *et al.*, "Evidence for oscillation of atmospheric neutrinos," *Phys. Rev. Lett.*, 81:1562–1567, Aug 1998.

[61] Q. R. Ahmad *et al.*, "Measurement of the rate of $\nu_e + d \rightarrow p + p + e^-$ interactions produced by ^8b solar neutrinos at the sudbury neutrino observatory," *Phys. Rev. Lett.*, 87:071301, Jul 2001.

[62] B. Pontecorvo, "Mesonium and Antimesonium," *Sov. Phys. JETP*, 33(2):549, 2 1957 [Zh. Eksp. Teor. Fiz.53,1717(1967)].

[63] B. Pontecorvo, "Inverse beta processes and nonconservation of lepton charge," *Zh. Eksp. Teor. Fiz.*, 34:247, 1957.

[64] Ziro Maki, Masami Nakagawa, and Shoichi Sakata, "Remarks on the Unified Model of Elementary Particles," *Prog. Theor. Phys.*, 28(5):870–880, nov 1962.

[65] B. Pontecorvo, "Neutrino Experiments and the Problem of Conservation of Leptonic Charge," *Sov. Phys. JETP*, 26:984–988, 1968 [Zh. Eksp. Teor. Fiz.53,1717(1967)].

[66] L. Wolfenstein, "Neutrino oscillations in matter," *Phys. Rev. D*, 17:2369–2374, May 1978.

[67] L. Wolfenstein, "Neutrino oscillations and stellar collapse," *Phys. Rev. D*, 20:2634–2635, Nov 1979.

[68] S. P. Mikheyev and A. Yu. Smirnov, "Resonance Amplification of Oscillations in Matter and Spectroscopy of Solar Neutrinos," *Sov. J. Nucl. Phys.*, 42:913–917, 1985 [Yad. Fiz.42,1441(1985); ,305(1986)].

[69] Yasuhiro Nakajima Recent results and future prospects from super-kamiokande, Jun 2020.

[70] B. Aharmim *et al.*, "Combined analysis of all three phases of solar neutrino data from the sudbury neutrino observatory," *Phys. Rev. C*, 88:025501, Aug 2013.

[71] A. Gando *et al.*, "Reactor on-off antineutrino measurement with kamland," *Phys. Rev. D*, 88:033001, Aug 2013.

[72] K. Abe *et al.*, "Atmospheric neutrino oscillation analysis with external constraints in super-kamiokande i-iv," *Phys. Rev. D*, 97:072001, Apr 2018.

[73] M. Jiang *et al.*, "Atmospheric neutrino oscillation analysis with improved event reconstruction in Super-Kamiokande IV," *Progress of Theoretical and Experimental Physics*, 2019(5), 05 2019 053F01.

[74] K. Abe *et al.*, "Constraint on the matter–antimatter symmetry-violating phase in neutrino oscillations," *Nature*, 580(7803):339–344, 2020.

[75] Patrick Dunne Latest neutrino oscillation results from t2k, July 2020.

[76] M. A. Acero *et al.*, "First measurement of neutrino oscillation parameters using neutrinos and antineutrinos by nova," *Phys. Rev. Lett.*, 123:151803, Oct 2019.

[77] Alex Himmel New oscillation results from the nova experiment, July 2020.

[78] D. Adey *et al.*, "Measurement of the electron antineutrino oscillation with 1958 days of operation at daya bay," *Phys. Rev. Lett.*, 121:241805, Dec 2018.

[79] Y. Suwa *et al.*, "Observing supernova neutrino light curves with super-kamiokande: Expected event number over 10 s," *The Astrophysical Journal*, 881(2):139, aug 2019.

[80] K. Nakazato *et al.*, "Observing supernova neutrino light curves with super-kamiokande. ii. impact of the nuclear equation of state," *The Astrophysical Journal*, 925(1):98, jan 2022.

[81] Y. Suwa *et al.*, "Observing supernova neutrino light curves with super-kamiokande. iii. extraction of mass and radius of neutron stars from synthetic data," *The Astrophysical Journal*, 934(1):15, jul 2022.

[82] K. Hirata *et al.*, "Observation of a neutrino burst from the supernova sn1987a," *Phys. Rev. Lett.*, 58:1490–1493, Apr 1987.

[83] R. M. Bionta *et al.*, "Observation of a neutrino burst in coincidence with supernova 1987a in the large magellanic cloud," *Phys. Rev. Lett.*, 58:1494–1496, Apr 1987.

[84] E. N. Alekseev *et al.*, "Possible Detection of a Neutrino Signal on 23 February 1987 at the Baksan Underground Scintillation Telescope of the Institute of Nuclear Research," *JETP Lett.*, 45:589–592, 1987 [,739(1987)].

[85] H. A. Bethe, "Supernova mechanisms," *Rev. Mod. Phys.*, 62:801–866, Oct 1990.

[86] Amol S. Dighe and Alexei Yu. Smirnov, "Identifying the neutrino mass spectrum from a supernova neutrino burst," *Phys. Rev. D*, 62:033007, Jul 2000.

[87] H. Sana *et al.*, "Binary interaction dominates the evolution of massive stars," *Science*, 337(6093):444–446, 2012.

[88] Zapartas, E. *et al.*, "Effect of binary evolution on the inferred initial and final core masses of hydrogen-rich, type ii supernova progenitors," *A&A*, 645:A6, 2021.

[89] P. Madau *et al.*, "High-redshift galaxies in the Hubble Deep Field: colour selection and star formation history to $z \sim 4$," *Monthly Notices of the Royal Astronomical Society*, 283(4):1388–1404, 12 1996.

[90] J. R. WILSON *et al.*, "Stellar core collapse and supernovaa,b," *Annals of the New York Academy of Sciences*, 470(1):267–293, 1986.

[91] Andrew M. Hopkins and John F. Beacom, "Erratum: "on the normalization of the cosmic star formation history" (apj, 651, 142 [20067])," *The Astrophysical Journal*, 682(2):1486, aug 2008.

[92] A. de Gouvêa *et al.*, "Fundamental physics with the diffuse supernova background neutrinos," *Phys. Rev. D*, 102:123012, Dec 2020.

[93] M. Malek *et al.*, "Search for supernova relic neutrinos at super-kamiokande," *Phys. Rev. Lett.*, 90:061101, Feb 2003.

[94] K. Bays *et al.*, "Supernova relic neutrino search at super-kamiokande," *Phys. Rev. D*, 85:052007, Mar 2012.

[95] Tomonori Totani and Katsuhiko Sato, "Spectrum of the relic neutrino background from past supernovae and cosmological models," *Astroparticle Physics*, 3(4):367–376, 1995.

[96] R. Becker-Szendy *et al.*, "Imb-3: a large water cherenkov detector for nucleon decay and neutrino interactions," *Nuclear Instruments and Methods in Physics Research Section A: Accelerators, Spectrometers, Detectors and Associated Equipment*, 324(1):363 – 382, 1993.

[97] M. Honda *et al.*, "Calculation of the flux of atmospheric neutrinos," *Phys. Rev. D*, 52(9):4985–5005, Nov 1995.

[98] M. Honda *et al.*, "Comparison of 3-dimensional and 1-dimensional schemes in the calculation of atmospheric neutrinos," *Phys. Rev. D*, 64:053011, Aug 2001.

[99] M. Honda *et al.*, "New calculation of the atmospheric neutrino flux in a three-dimensional scheme," *Phys. Rev. D*, 70:043008, Aug 2004.

[100] T. Sanuki *et al.*, "Precise measurement of cosmic-ray proton and helium spectra with the BESS spectrometer," *The Astrophysical Journal*, 545(2):1135–1142, dec 2000.

[101] S. Haino *et al.*, "Measurements of primary and atmospheric cosmic-ray spectra with the bess-tev spectrometer," *Physics Letters B*, 594(1):35 – 46, 2004.

[102] J. Alcaraz *et al.*, "Cosmic protons," *Physics Letters B*, pages 27–35, 01 2020.

[103] T. Gaisser *et al.*, "Primary spectrum to 1 tev and beyond," *Proceedings of the 27th International Cosmic Ray Conference.*, page 1643, 08 2001.

[104] T. K. Gaisser and M. Honda, "Flux of atmospheric neutrinos," *Annual Review of Nuclear and Particle Science*, 52(1):153–199, 2002.

[105] Y. Nara *et al.*, "Relativistic nuclear collisions at 10a gev energies from $p+$Be to au+au with the hadronic cascade model," *Phys. Rev. C*, 61:024901, Dec 1999.

[106] S. Roesler, R. Engel, and J. Ranft The monte carlo event generator dpmjet-iii In A. Kling *et al.*, editors, *Advanced Monte Carlo for Radiation Physics, Particle Transport Simulation and Applications*, pages 1033–1038, Berlin, Heidelberg, 2001. Springer Berlin Heidelberg.

[107] K. Niita *et al.*, "Phits—a particle and heavy ion transport code system," *Radiation Measurements*, 41(9):1080 – 1090, 2006 Space Radiation Transport, Shielding, and Risk Assessment Models.

[108] A. Capella *et al.*, "Dual parton model," *Physics Reports*, 236(4):225 – 329, 1994.

[109] M. Catanesi *et al.*, "Measurement of the production cross-sections of $\pi\pm$ in p–c and $\pi\pm$–c interactions at 12gev/c," *Astroparticle Physics*, 29:257–281, 05 2008.

[110] M. Catanesi *et al.*, "Forward $\pi\pm$ production in p–o2 and p–n2 interactions at 12gev/c," *Astroparticle Physics*, 30:124–132, 10 2008.

[111] T. Sanuki *et al.*, "Measurements of atmospheric muon spectra at mountain altitude," *Physics Letters B*, 541(3):234 – 242, 2002.

[112] P. Achard *et al.*, "Measurement of the atmospheric muon spectrum from 20 to 3000 gev," *Physics Letters B*, 598(1):15 – 32, 2004.

[113] Yoshinari Hayato and Luke Pickering, "The neut neutrino interaction simulation program library," *The European Physical Journal Special Topics*, 230(24):4469–4481, 2021.

[114] S. Jadach *et al.*, "The τ decay library tauola, version 2.4," *Computer Physics Communications*, 76(3):361 – 380, 1993.

[115] C.H. Llewellyn Smith, "Neutrino reactions at accelerator energies," *Physics Reports*, 3(5):261 – 379, 1972.

[116] R.A. Smith and E.J. Moniz, "Neutrino reactions on nuclear targets," *Nuclear Physics B*, 43:605 – 622, 1972.

[117] A. A. Aguilar-Arevalo *et al.*, "First measurement of the muon neutrino charged current quasielastic double differential cross section," *Phys. Rev. D*, 81:092005, May 2010.

[118] J. Nieves, I. Ruiz Simo, and M. J. Vicente Vacas, "Inclusive charged-current neutrino-nucleus reactions," *Phys. Rev. C*, 83:045501, Apr 2011.

[119] Dieter Rein and Lalit M Sehgal, "Neutrino-excitation of baryon resonances and single pion production," *Annals of Physics*, 133(1):79 – 153, 1981.

[120] Ch. Berger and L. M. Sehgal, "Lepton mass effects in single pion production by neutrinos," *Phys. Rev. D*, 76:113004, Dec 2007.

[121] K. M. Graczyk *et al.*, "C_5^A axial form factor from bubble chamber experiments," *Phys. Rev. D*, 80:093001, Nov 2009.

[122] D. Rein, "Angular distribution in neutrino-induced single pion production processes," *Zeitschrift für Physik C Particles and Fields*, 35(1):43–64, Mar 1987.

[123] Torbjorn Sjostrand Pythia 5.7 and jetset 7.4 physics and manual, 1995.

[124] M. Glück, E. Reya, and A. Vogt, "Dynamical parton distributions of the proton and small-x physics," *Zeitschrift für Physik C Particles and Fields*, 67(3):433–447, Sep 1995.

[125] A. Bodek and U. K. Yang Modeling neutrino and electron scattering inelastic cross sections, 2003.

[126] Dieter Rein and Lalit M. Sehgal, "Coherent π_0 production in neutrino reactions," *Nuclear Physics B*, 223(1):29 – 44, 1983.

[127] Ch. Berger and L. M. Sehgal, "Partially conserved axial vector current and coherent pion production by low energy neutrinos," *Phys. Rev. D*, 79:053003, Mar 2009.

[128] Alessandro Strumia and Francesco Vissani, "Precise quasielastic neutrino / nucleon cross-section," *Physics Letters B*, 564:42–54, 2003.

[129] R. Brun *et al. GEANT 3: user's guide Geant 3.10, Geant 3.11; rev. version* CERN, Geneva, 1987.

[130] R. Brun *et al. GEANT: Detector Description and Simulation Tool; Oct 1994* CERN Program Library. CERN, Geneva, 1993 Long Writeup W5013.

[131] S. Agostinelli *et al.*, "Geant4—a simulation toolkit," *Nuclear Instruments and Methods in Physics Research Section A: Accelerators, Spectrometers, Detectors and Associated Equipment*, 506(3):250–303, 2003.

[132] J. Allison *et al.*, "Geant4 developments and applications," *IEEE Transactions on Nuclear Science*, 53(1):270–278, 2006.

[133] J. Allison *et al.*, "Recent developments in geant4," *Nuclear Instruments and Methods in Physics Research Section A: Accelerators, Spectrometers, Detectors and Associated Equipment*, 835:186–225, 2016.

[134] M. Nakahata *et al.*, "Atmospheric neutrino background and pion nuclear effect for kamioka nucleon decay experiment," *Journal of the Physical Society of Japan*, 55(11):3786–3805, 1986.

[135] E. Bracci Compilation of cross sections, 1972.

[136] A. S. Carroll *et al.*, "Pion-nucleus total cross sections in the (3,3) resonance region," *Phys. Rev. C*, 14:635–638, Aug 1976.

[137] K. Hagiwara *et al.*, "Gamma-ray spectrum from thermal neutron capture on gadolinium-157," *Progress of Theoretical and Experimental Physics*, 2019(2), 02 2019 023D01.

[138] S. Desai *High Energy Neutrino Astrophysics With Super-Kamiokande* PhD thesis, Boston University, 2004.

[139] Robin M. Pope and Edward S. Fry, "Absorption spectrum (380–700 nm) of pure water. ii. integrating cavity measurements," *Appl. Opt.*, 36(33):8710–8723, Nov 1997.

[140] Guangyuan Zhao and Xianming Sun Error analysis of using henyey-greensterin in monte carlo radiative transfer simulations In *In Progress In Electromagnetics Research Symposium Proceedings*, 2010.

[141] M. Stockhoff *et al.*, "Advanced optical simulation of scintillation detectors in gate v8.0: first implementation of a reflectance model based on measured data.," *Phys Med Biol*, 62(12):L1–L8, Jun 2017.

[142] Glenn F. Knoll *Radiation detection and measurement / Glenn F. Knoll* Wiley New York, 2nd ed. edition, 1989.

[143] H. Ito *et al.* Analyzing the neutron and γ-ray emission properties of an americium-beryllium tagged neutron source, 2023.

[144] Shirley Weishi Li and John F. Beacom, "First calculation of cosmic-ray muon spallation backgrounds for mev astrophysical neutrino signals in super-kamiokande," *Phys. Rev. C*, 89:045801, Apr 2014.

[145] Shirley Weishi Li and John F. Beacom, "Spallation backgrounds in super-kamiokande are made in muon-induced showers," *Phys. Rev. D*, 91:105005, May 2015.

[146] Shirley Weishi Li and John F. Beacom, "Tagging spallation backgrounds with showers in water cherenkov detectors," *Phys. Rev. D*, 92:105033, Nov 2015.

[147] Thomas Mueller *Expérience double Chooz : simulation des spectres antineutrinos issus de réacteurs* PhD thesis, IRFU, SPhN, Saclay, 2010 2010PA112124.

[148] SKReact Skreact-git hub.

[149] M. Shinoki *et al.*, "Measurement of the cosmogenic neutron yield in super-kamiokande with gadolinium loaded water," *Phys. Rev. D*, 107:092009, May 2023.

[150] K. Abe *et al.*, "Measurement of neutrino and antineutrino oscillations by the T2K experiment including a new additional sample of veinteractions at the far detector," *Phys. Rev. D*, 96(9):1–50, 2017.

[151] J. Lundberg *et al.*, "Limits, discovery and cut optimization for a poisson process with uncertainty in background and signal efficiency: Trolke 2.0," *Computer Physics Communications*, 181(3):683–686, 2010.

[152] O. Benhar *et al.*, "Spectral function of finite nuclei and scattering of gev electrons," *Nuclear Physics A*, 579(3):493–517, 1994.

[153] O. Benhar *et al.*, "Electron- and neutrino-nucleus scattering in the impulse approximation regime," *Phys. Rev. D*, 72:053005, Sep 2005.

[154] R. González-Jiménez *et al.*, "Relativistic description of final-state interactions in neutral-current neutrino and antineutrino cross sections," *Phys. Rev. C*, 88:025502, Aug 2013.

[155] J. E. Amaro *et al.*, "Superscaling and neutral current quasielastic neutrino-nucleus scattering," *Phys. Rev. C*, 73:035503, Mar 2006.

[156] Andrea Meucci and Carlotta Giusti, "Final-state interaction effects in neutral-current neutrino and antineutrino cross sections at miniboone kinematics," *Phys. Rev. D*, 89:057302, Mar 2014.

[157] A. M. Ankowski *et al.*, "Analysis of γ-ray production in neutral-current neutrino-oxygen interactions at energies above 200 mev," *Phys. Rev. Lett.*, 108:052505, Feb 2012.

[158] Y. Zhang *et al.*, "First measurement of radioactive isotope production through cosmic-ray muon spallation in super-kamiokande iv," *Phys. Rev. D*, 93:012004, Jan 2016.

[159] D. Maksimović, M. Nieslony, and M. Wurm, "Cnns for enhanced background discrimination in dsnb searches in large-scale water-gd detectors," *Journal of Cosmology and Astroparticle Physics*, 2021(11):051, nov 2021.

[160] H. Togashi *et al.*, "Nuclear equation of state for core-collapse supernova simulations with realistic nuclear forces," *Nucl. Phys. A*, 961:78–105, May 2017.

[161] James M. Lattimer and Douglas F. Swesty, "A generalized equation of state for hot, dense matter," *Nucl. Phys. A*, 535(2):331–376, December 1991.

[162] H. Shen *et al.*, "Relativistic equation of state for core-collapse supernova simulations," *The Astrophysical Journal Supplement Series*, 197(2):20, nov 2011.